ELECTRICAL TRANSMISSION SYSTEMS FOR LARGE OFFSHORE WIND FARMS

A THESIS SUBMITTED TO CARDIFF UNIVERSITY FOR THE DEGREE OF
DOCTOR OF PHILOSOPHY

Rosemary Louise King

February 2011

UMI Number: U567155

Dissertation Publishing

UMI U567155

ProQuest LLC
789 East Eisenhower Parkway
P.O. Box 1346
Ann Arbor, MI 48106-1346

For Abigail

ABSTRACT

The large area required for an offshore wind farm along with its location results in extensive cable systems with a large number of radial feeders and step-up transformers. These transmission systems are very different to traditional onshore networks.

Offshore wind farms above around 100MW capacity and over 20km from shore will have either AC or DC transmission, at above 132 kV. The capital costs were compared for AC and DC submarine transmission in order to find a break-even point. Over the lifetime of the wind farm, the cost of losses, maintenance and constrained energy was important. A loss-load factor was determined to enable a quick estimation of the annual cost of losses.
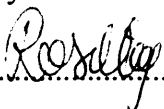
Suitable models for the simulation of switching transients in offshore wind farms were identified. Simulations of Nysted offshore wind farm were compared with measurements provided by DONG Energy. A Vacuum Circuit Breaker model was developed and validated against the measurements. It was required in order to represent pre-strikes which caused successive waves and increased the overvoltage. The input data for the cable model was validated by examining the cable charging current and propagation speed of the transients. It was shown that the actual insulation thickness and semiconductor thickness of the cable were each 1mm thicker than that stated in the manufacturer's data sheets.

Simulations of switching transients were carried out in EMTP-RV. Overvoltages in offshore wind farms ranged from temporary over voltages to very fast front transients. Transient Recovery Voltages of the offshore circuit breakers exceeded IEC 62271 requirements in some situations. The disconnection of an array following a single phase fault at a wind turbine produced the most severe overvoltages, exceeding IEC 60071 requirements. The overvoltages in the array remained at a very serious level until the wind turbines stopped generating.

DECLARATION

This work has not previously been accepted in substance for any degree and is not concurrently submitted in candidature for any degree.

Signed...(candidate)   Date: 24/02/2011

STATEMENT 1

This thesis is being submitted in partial fulfilment of the requirements for the degree of PhD.

Signed...(candidate)   Date: 24/02/2011

STATEMENT 2

This thesis is the result of my own independent work/investigation, except where otherwise stated. Other sources are acknowledged by explicit references.

Signed...(candidate)   Date: 24/02/2011

STATEMENT 3

I hereby give consent for my thesis, if accepted, to be available for photocopying and for inter-library loan, and for the title and summary to be made available to outside organisations.

Signed...(candidate)   Date: 24/02/2011

ACKNOWLEDGEMENTS

LIST OF PUBLICATIONS

King, R., Moore, F., Jenkins, N., Haddad, A., Griffiths, H., Osborne, M., *"Switching transients in offshore wind farms – impact on the offshore and onshore networks"*, International Power Systems Transients Conference (IPST2011), Delft, the Netherlands, June 14-17, 2011

Chukaluri, E. K., Barker, C., **King, R.**, *"A study on some of the important aspects related to feasibility of HVDC grid"*, CIGRE International Symposium "The Electric Power System of the Future – integrating supergrids and microgrids", Bologna, Italy, September 13-15, 2011

King, R., Yao, L., Kang, H., Rasolonjanahary, J. L., Jenkins, N., *"Transient Recovery Voltages in Offshore Wind Farms"*, 9th International Workshop on Large Scale Integration of Wind Power and on Transmission Networks for Offshore Wind Farms; Quebec City, Quebec, Canada, October 18–19, 2010; *ISBN:* 978-3-9813870-2-5; *Publisher:* Energynautics

Gomis-Bellmunt, O., Liang, J., Ekanayake, J., **King, R.**, Jenkins, N., *"Topologies of multiterminal HVDC-VSC transmission for large offshore wind farms"*, Electrical Power Systems Research; Article in Press; Accepted; 8 Sept 2010, Available online; 27 Oct 2010; *DOI:* 10.1016/j.epsr.2010.09.006; *Publisher:* Elsevier Ltd

King, R., Ekanayake, J. B., *"Harmonic modelling of offshore wind farms"*, IEEE PES General Meeting "Power Systems Engineering in Challenging Times", Minneapolis, Minnesota, USA, July 25-29, 2010; *Organiser:* IEEE

King, R., Jenkins, N., *"Switching Transients in Large Offshore Wind Farms"*, 7th International Workshop on Large Scale Integration of Wind Power and on Transmission Networks for Offshore Wind Farms, Madrid, Spain, May 26-27, 2008; *ISBN:* 978-3-9813870-0-1; *Publisher:* Energynautics

CONTENTS

LIST OF TABLES

LIST OF FIGURES

1. INTRODUCTION

1.1. OFFSHORE WIND ENERGY

Offshore wind energy is a key element of many countries programmes to reduce the emission of carbon dioxide [1-4]. Offshore wind will also increase the energy security of countries such as the UK [5]. Although more developed renewable technologies such as onshore wind and hydropower are cheaper, many of the suitable sites have already been taken and planning permission for new onshore sites takes a significant time. Offshore wind has higher mean wind speeds and is less turbulent than onshore wind which enables an offshore wind farm to generate more energy than an equivalent onshore wind farm. This, along with the reduced time-scales for obtaining planning permission offshore, makes offshore wind farms particularly attractive.

1.2. OFFSHORE WIND FARMS

The development of worldwide offshore wind farm capacity is shown in Fig. 1-1. Further details of these offshore wind farms are given in Appendix A1.
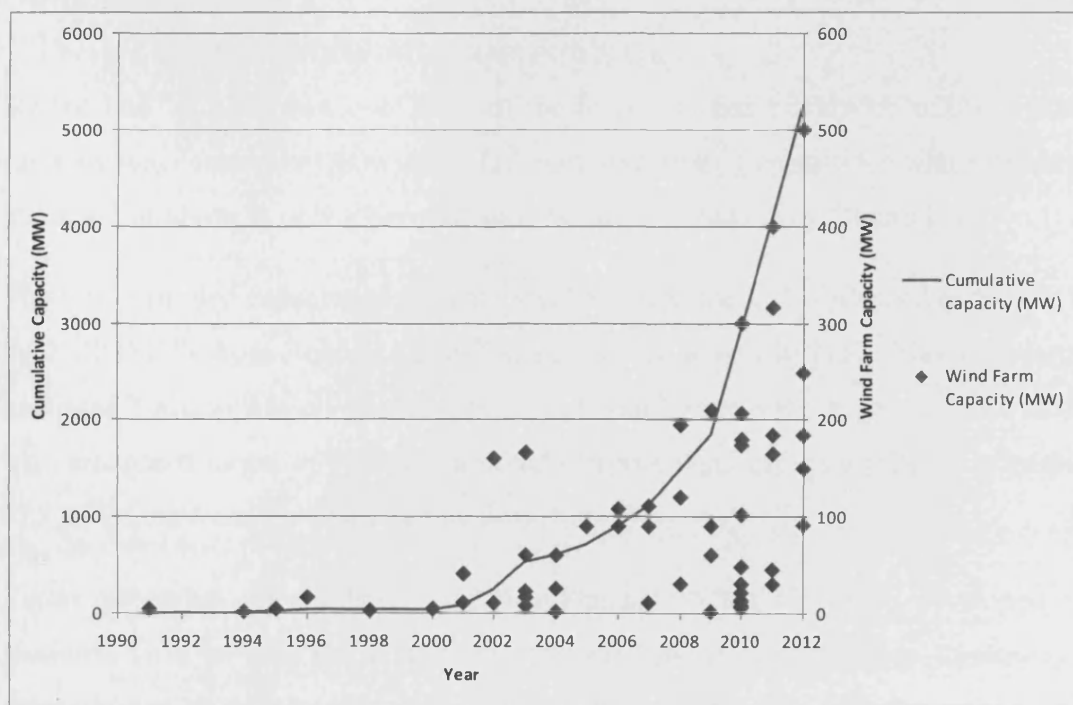
Fig. 1-1. Development of Worldwide offshore wind farm capacity. The wind farms shown after 2010 are currently under construction.

By the end of 2010 there was 3GW of offshore wind farm capacity in operation. The offshore wind farms were located up to 45km from shore and had wind turbine ratings of up to 5MW. All of the 44 offshore wind farms were connected by AC to shore, of which twelve had an offshore substation to allow High Voltage AC (HVAC) transmission to shore.

Greater Gabbard is the largest offshore wind farm currently in construction. It has 140 wind turbines, a capacity of 500MW and two HVAC offshore substations [6].

BARD Offshore 1 is the first offshore wind farm to be connected by High Voltage Direct Current (HVDC) to shore and is expected to be in full operation in 2011 [7]. BARD Offshore 1 is over 100km from shore and has a rating of 400MW.

The majority of offshore wind farms built to date are located in Northern Europe. A number of other countries around the world are now starting to develop offshore wind farms. In 2010 the first offshore wind farm in China (Shanghai Donghai Bridge) started operation, with a rating of just over 100MW. The installed capacity of offshore wind farms in China is expected to exceed 32GW by 2020 [8]. The US is currently developing its first offshore wind farm, Cape Wind, which will be just under 500MW [9]. A number of other projects in the US are under development [4].

1.2.1. OFFSHORE WIND FARMS IN THE UK

By the end of 2010, just over 40% of the total installed worldwide offshore wind capacity was located in UK waters. Offshore electricity transmission which operates at 132kV or above is now a licensed activity and is regulated by Ofgem [10].

The total installed capacity of offshore wind farms in the UK is planned to be 32GW by 2020 (8GW from Rounds 1 and 2 and 25GW in Round 3) [11]. The wind farms in Round 3 are split into 9 zones. The Dogger Bank zone is the largest of these zones with an agreed target of 9GW of installed offshore wind capacity [12]. It is located 125 to 195km from the east coast of Yorkshire.

Future scenarios for offshore wind development in the UK were developed by National Grid to provide a basis for the analysis of how offshore transmission networks can be developed to interconnect offshore generation with the onshore grid and to identify areas of the onshore transmission network which need to be reinforced in order to support the connection of offshore transmission. These future scenarios covered an anticipated range of offshore generation capacity of nearly

17GW in 2025 in the 'Slow Progression' scenario to over 47GW in 2025 in the 'Sustainable Growth' scenario [13].

1.3. TRANSMISSION OPTIONS FOR LARGE OFFSHORE WIND FARMS

There are three main transmission options for offshore wind farms; Medium Voltage AC (MVAC, typically 33kV), High Voltage AC (HVAC, typically 132kV) and High Voltage DC (HVDC). These three transmission options are shown in Fig. 1-2. The decision on which scheme to use depends on a variety of factors such as cable route length, the number of cables required to transmit the wind farm output, acceptable losses and capital costs.
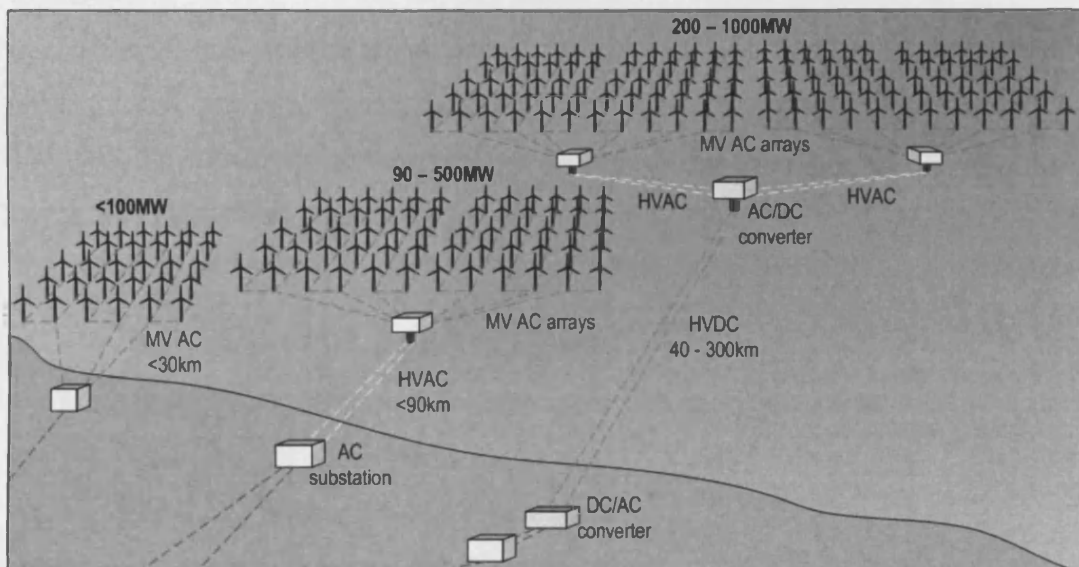
Fig. 1-2. Transmission Options for Offshore Wind Farms

As shown in Fig. 1-2, all three options involve the use of MVAC. For the larger wind farms with either HVAC or HVDC transmission to shore, MVAC is utilized to collect the power from the wind turbines to the offshore HVAC or HVDC connection point.

The high capital costs of offshore transmission systems means that they do not have total redundancy built in to the design. Instead, redundancy is sometimes provided for components that have low investment costs with a high chance of failure and/or a high impact of failure. Examples include cooling pumps, secondary systems and communications. Partial redundancy is provided when there are multiple export cables and transformers. An example of this is where two transformers, each rated at

50% nominal capacity of the wind farm are installed. In this case there is still some capacity available if one transformer is taken out of service.

1.3.1. MEDIUM VOLTAGE AC TRANSMISSION

Medium Voltage AC transmission is typically used for projects below 100MW in size. The voltage level is around 33kV and is restricted by the size of transformer which can be fitted into the wind turbine structure. A three-core 33kV cable (630mm² Cu conductors) has a capacity of just over 40MVA [14]. This means that a 90MW offshore wind farm would require three 33kV cables to connect to the onshore grid. The cable route lengths are generally less than 30km, so the losses are low.

In this thesis, a string of wind turbines which are connected in a radial fashion, either to shore or to an offshore substation is called an array. The size of the turbine in terms of rated power and rotor diameter will determine the spacing between turbines and also the maximum number of turbines per array. The choice of array cable rating will also affect losses. The probability of array cable failure is small, so it is not likely that redundancy would be required allowing the cables to be tapered.

1.3.2. HIGH VOLTAGE AC TRANSMISSION

High Voltage AC transmission is preferred when the cable route length is above around 20km and for wind farms above around 90MW rating. Fig. 1-3 shows a typical HVAC connection for an offshore wind farm.

An offshore substation that transforms the array voltage up to a higher voltage is required for HVAC transmission, since the maximum voltage in the wind farm array is currently around 33kV. The substation adds considerable capital costs; however HVAC has the benefit of having lower transmission losses. The maximum rating of an offshore substation is around 500MW. It is limited by the size and weight of the platform, which is dictated by the transportation methods available, and number of cables which can connect to the platform.

Current offshore wind farms with HVAC transmission have either a 132kV or 150kV transmission voltage. The transmission voltage is restricted by the availability of three-core XLPE cables. There are very limited manufacturing facilities able to produce three-core XLPE cables of this voltage, with the highest voltage level being 275kV [15] but this is extremely heavy to install. Higher voltage XLPE cables are

available, but only as single-core, so the lay-and-bury costs for these would be greater.

Three-core XLPE HVAC cables (800mm² Cu conductors) have capacities of approximately 200MVA at 132kV and 330MVA at 220kV [16]. This means that a 200MW wind farm for example would require only one HVAC cable to shore whereas a 33kV option results in at least 5 cables to shore. This reduction in cables results in lower capital and installation costs. There may also be a limit on the amount of cables allowed to connect wind farms due to environmental concerns.
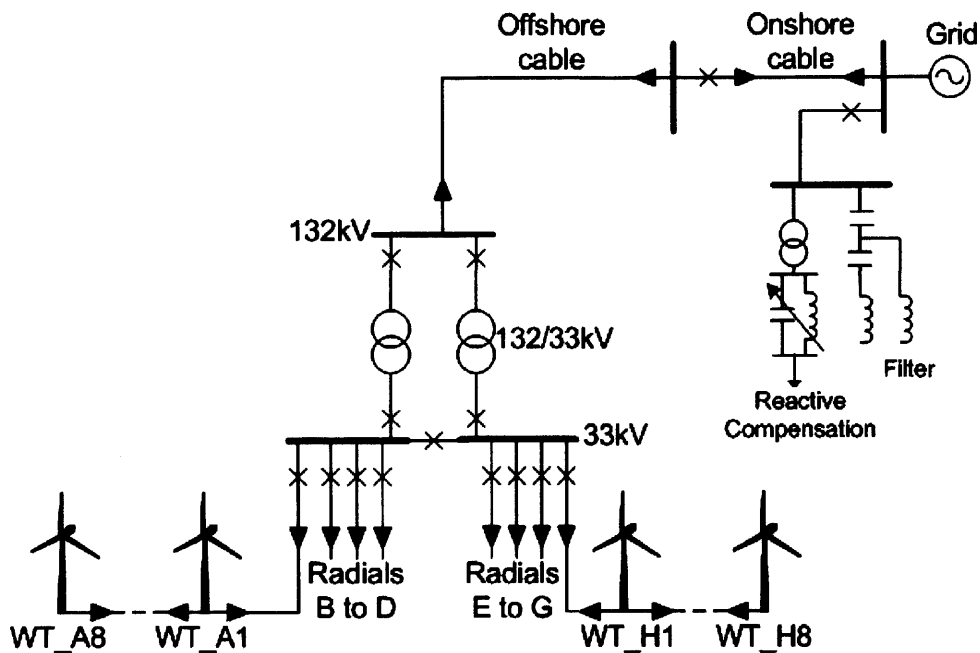
Fig. 1-3. Example HVAC connection of an offshore wind farm.

The first offshore substations had a single two- or three-winding transformer. Offshore substations built after 2008 tend to have two transformers (each with around 50% nominal capacity of the wind farm). Having multiple transformers on the offshore substation allows the weight of individual items of equipment to be reduced and also allows the wind farm to continue to export power when one transformer is out of service.

High voltage cables have a much larger capacitance than overhead lines, which results in large amounts of reactive power being generated along the cable's length. This reduces the ability of the cable to transmit active power, especially at longer distances. Reactive compensation is required to increase the amount of active power that can be transmitted and also to help reduce losses.

The reactive power, Q_C, (in MVAr) generated in a cable due to its capacitance is calculated using the following equation:

$$Q_C = 2\pi f l C V^2$$

Where f is the power frequency (Hz), V is the rated voltage (kV), l is the length of the cable (km) and C is the capacitance of the cable per unit length (F/km).

Filters are usually required at the onshore point of connection in order to ensure that the injection of harmonics into the grid is limited to acceptable levels and to ensure that resonant frequencies within the wind farm network are not excited by the onshore grid [17].

1.3.3. HVDC TRANSMISSION

For cable route lengths above 50km, HVDC transmission becomes a viable option [18]. The particular cable length above which HVDC transmission becomes more economic than HVAC transmission is called the AC/DC break-even point. Above around 100km HVDC is the only option since there will be a length limit of HVAC transmission due to the high amounts of reactive power generated. For wind farms above around 200MW in size, the HVDC option tends to have the least amount of cables connecting the wind farm to shore.

There are two distinct HVDC technologies, Line-Commutated Current Source Converters (CSC) and Self-Commutated Voltage Source Converters (VSC). CSC technology is based on line-commutated thyristors that are switched on by a pulse and switched off when the current flowing through them reduces to zero. The converters have a requirement to be connected to a reliable AC system, since the AC system voltage forces the current to commutate from one phase to another. The current must always flow in the same direction through a thyristor which means that in order to reverse the power flow the voltage polarity of the DC link must be reversed.

HVDC VSC employs semiconductor switches that can be turned on and off in a controlled manner which means that HVDC VSC is able to operate when there is no local generation and it can control the AC system voltage and frequency. The majority of HVDC VSC converters in operation at present are based on either a two or three level design which enables switching between two or three different voltage

levels to the AC terminal of the converter. Multilevel HVDC VSC converters have now been developed which allow lower switching frequencies, resulting in lower converter losses compared to two or three level converters. The first multilevel converter (the Trans Bay Cable project) was installed in 2010 and is rated at 400MW, ±200kV DC [19].

Only VSC HVDC technology is being considered for offshore wind farms. Whilst the conventional CSC HVDC technology is well developed with lower capital costs and losses compared to the VSC technology, there would be a significantly higher requirement for space onshore for the filters. The VSC technology offers greater flexibility in terms of real and reactive power control. The ongoing advances in HVDC VSC technology along with market growth and competition between manufacturers are likely to drive down both capital and operational costs.

The largest HVDC VSC scheme currently being developed (called the BorWin2 project) will connect two offshore wind farms in Germany (Global Tech 1 and Veja Mate, located 125km from shore), to shore with 800MW, ±300kV HVDC Voltage Source Converters. It is expected to be in operation by 2013. Both the AC (155/33kV) and DC substations for the BorWin2 project will be self-floating, self-installing platforms [20, 21].

1.4. RESEARCH OBJECTIVE

1.4.1. MAIN OBJECTIVES OF THE THESIS

The objectives of the thesis were to:

- Determine AC/DC break-even points for offshore wind farm capacities from 300 to 2600MW
- Develop a method for assessing the annual cost of losses in the offshore transmission system
- Determine suitable models for the simulation of switching transients in offshore wind farms
- Develop a suitable Vacuum Circuit Breaker model for switching transient studies
- Verify switching transient simulations against measurements at an offshore wind farm

- Identify the types and magnitude of overvoltages which may occur in offshore wind farms

- Determine whether Transient Recovery Voltage standards for circuit breakers in offshore wind farms will be exceeded

1.4.2. THE STRUCTURE OF THE THESIS

This thesis contains 8 chapters. A list of abbreviations is included in Appendix 1.

Chapter 2 is a study of the **Costs and Losses of Offshore Transmission Systems**. The work in this Chapter was carried out for BP Alternative Energy. It starts with an assessment of electrical losses in AC and DC offshore transmission systems. A method for evaluating the cost of losses is described. The break-even points for AC and DC transmission for wind farm capacities of between 300MW to 2600MW are found. The assessment of the break-even point includes the cost of capital, losses, maintenance and constrained energy. The Chapter ends with a review of offshore grids and multiterminal HVDC networks and the requirement for HVDC circuit breakers.

Chapter 3 is a **Review of Switching Transients**. It starts with some concepts which have relevance to switching transients in offshore wind farms. The types of switching transients are described. The importance of switching transient studies in offshore wind farms is highlighted, including the difference to onshore networks and impact of switching transients on offshore transformers. The Chapter ends with a review of switching transient studies (carried out by ABB Corporate Research and DONG Energy) in offshore wind farms.

The **Modelling of Offshore Wind Farms for Switching Transient Studies** is described in Chapter 4. Suitable models for the simulation of switching transients in offshore wind farms are determined, which include a review of models for circuit breakers, cables, transformers and wind turbines. A Vacuum Circuit Breaker model which is able to represent pre-strikes and re-strikes is developed. The methods used to convert the cable data provided in manufacturer's data sheets to suitable input parameters for the cable models in EMTP-RV are described and the effect of changing input parameters is investigated.

Chapter 5 is a **Comparison of Simulations with Switching Transient Measurements at Nysted Offshore Wind Farm**. The work described in this

Chapter involved collaboration with DONG Energy who provided the measurement results. Transient simulations in EMTP-RV are compared with the measurements at Nysted offshore wind farm in order to validate the models used in switching transient studies. The representation of the VCB model (described and developed in Chapter 4) is verified against the measurements. The difficulties in modelling cables accurately due to the small geometries involved are highlighted.

Transient Recovery Voltages of circuit breakers in a typical offshore wind farm are assessed in Chapter 6. Five fault locations are considered and the resulting Transient Recovery Voltages are compared against requirements specified in IEC 62271-100:2001 in order to determine if the requirements were exceeded. The effect of array cable length, 132kV export cable length and the addition of reactive compensation on the Transient Recovery Voltage are investigated. The effect of wind turbine fault current contribution on TRVs is investigated.

Chapter 7 is a study of **Energisation and Disconnection Transients** in a typical offshore wind farm. The different options for the energisation of the HVAC export cable are investigated and simulated. The disconnection of an unloaded export cable is simulated. Switching transients in the medium voltage arrays are studied. The disconnection of an array following a single phase fault is simulated. A summary of the magnitudes of overvoltages which occurred in the typical offshore wind farm is included at the end of the Chapter.

The **Conclusions and Recommendations for Further Work** are given in Chapter 8. The main contributions resulting from the research in this thesis are stated. Research questions which arose from the conclusions and further work which complements the studies in this thesis are described.

2. COSTS AND LOSSES OF OFFSHORE TRANSMISSION SYSTEMS

Due to the location and radial nature of offshore windfarms, the capital costs for the electrical transmission system form a large proportion of the total costs. The design and choice of the transmission system have implications on the capital costs and on the electrical losses. The most economic solution depends both on the wind farm size and the distance that it is from shore [22]. The cost of grid connection for an offshore wind farm is typically around 25% of the total cost and is a much higher fraction than for connections of onshore projects [23].

The specifications of the cables and transformers used in this chapter are given in Appendix 2A.

2.1. AC FULL-LOAD LOSSES

The main contributors to electrical losses in a wind-farm with HVAC transmission to shore are the HVAC cables to shore, transformers, and the MVAC array cabling. Load flow calculations were carried out in IPSA in order to calculate the losses in the system.

2.1.1. LOAD FLOW CALCULATIONS

Load flow studies were carried out in IPSA to determine the full-load losses of a 200MW wind farm with 132kV transmission to shore. Three types of model were simulated, the PQ model where the offshore generator was set to generate P = 200MW and Q = 0MVAr, the PV model where the offshore generator was set to 200MW and 1p.u voltage, and a 'transformer plus cable' model where the 132/33kV transformer was included with the 33kV offshore busbar set to 200MW and 1p.u. voltage.

Table 2-1 gives the results of simulations for a 200MW wind farm with 132kV transmission to shore. Three 'transformer plus cable' models were considered; a single 250MVA transformer, two parallel 90MVA transformers and three parallel 90MVA transformers. The two parallel 90MVA transformers configuration is suggested by the Great Britain Supply Quality and Security Standards (SQSS).

As shown in Table 2-1 the full load losses increased considerably with distance to shore.

Table 2-1. Full Load Losses for a 200MW Wind Farm with 132kV Transmission to shore via a single 800mm² XLPE cable. Values in red (italic) show that the cable is over-loaded.

Full Load Losses (%)	Distance to Shore (km)								
	20	30	40	50	60	70	80	90	100
PQ – Cable Losses only	1.060	1.576	2.086	2.590	3.093	*3.595*	*4.102*	*4.616*	*5.142*
PV – Cable Losses only	*1.2505*	*1.8645*	*2.472*	*3.072*	*3.667*	*4.256*	*4.839*	*5.417*	*5.989*
250MVA Transformer plus cable	1.3705	1.881	2.3805	2.876	3.372	*3.8705*	*4.364*	*4.8825*	*5.3995*
Three parallel 90MVA Transformers plus cable	1.3465	1.8565	2.3565	2.853	3.3495	*3.849*	*4.3435*	*4.862*	*5.3795*
Two parallel 90MVA Transformers (SQSS suggestion) plus cable	1.488	1.996	2.493	2.9855	3.478	*3.9745*	*4.466*	*4.9805*	*5.495*

For the PV model, a large amount of reactive power was required at the offshore busbar in order to maintain the voltage at 1p.u. For example, 104MVAR was absorbed at the offshore busbar for a 50km cable length, resulting in 225MVA being transmitted (at the offshore end of the cable) which is above the rating (203MVA) of the 132kV (800mm² Cu) cable. The higher amount of reactive power in the PV model compared to the PQ model meant that the losses were higher in the PV model than the PQ model, which can be seen in Table 2-1.

It is unlikely that there will be such a high amount of reactive power injected into the offshore busbar as that in the PV case. Doubly Fed Induction Generator (DFIG) and Fully Rated Converter (FRC) wind turbine control systems are likely to try to keep their output at unity power factor. This means that the losses will be closer to those obtained in the PQ model. Fixed Speed Induction Generator (FSIG) wind turbines on the other hand will only output unity power factor when the reactive power output of the capacitor matches the inductive power of the generator, which is at a particular rated output power. At output powers of a lower value the FSIG will generate reactive power (due to the capacitors), and at higher output powers the FSIG will absorb reactive power.

The losses varied slightly depending on the number or type of transformers that were used in the model. As shown in Table 2-1, the highest losses were for the two parallel 90MVA transformers and the high voltage cable. This was because their

combined rating was 180MVA, which was 90% of the wind farm rating, meaning that they were over-loaded when the wind farm operated at full-load. This configuration was suggested by the SQSS sub-group of the Offshore Transmission Expert Group (OTEG) as being the most economic option overall [24]. It follows that the configuration with 3 parallel 90MVA transformers with a combined rating of 270MVA had lower losses because the transformers were not loaded to such a high extent.

2.1.2. TRANSMISSION VOLTAGE LEVEL

Two transmission voltages were assessed, 132kV and 220kV (at the time of this work, 220kV was the highest voltage available for three-core XLPE cables. Although 275kV three-core XLPE are now available, their significant weight may limit their use for long offshore wind farm connections).

The 132kV cable losses were considerably higher than for the 220kV cable, as shown in Table 2-2. However, the reactive power generated in the 220kV cable was almost double that generated in the 132kV cable, so more reactive compensation is required for the 220kV transmission than for 132kV. There will be a trade-off between the cost of reactive compensation and the cost of losses. The results in Tables 2-1 to 2-3 do not include the addition of reactive compensation.

Table 2-2. The effect of Transmission voltage on Full Load Losses and Reactive power generated for a 200MW wind farm at various distances from shore.

		Distance (km)								
		20	**30**	**40**	**50**	**60**	**70**	**80**	**90**	**100**
132kV, single 800mm² cable with 2 90MVA Transformers	Full Load Losses (%)	1.49	2.00	2.49	2.99	3.48	3.97	4.47	4.98	5.50
	Reactive power generated in cable (MVAr)	18.96	28.75	38.77	49.03	59.56	70.40	81.51	93.00	104.82
220kV, single 500mm² cable with 2 90MVA Transformers	Full Load Losses (%)	0.98	1.25	1.54	1.83	2.13	2.46	2.83	3.22	3.67
	Reactive power generated in cable (MVAr)	39.62	59.67	79.89	100.31	120.93	141.79	162.90	184.29	205.98

2.1.3. EFFECT OF CABLE RATING

The choice of cable rating affects losses. For a given rated voltage, the cable rating increases as the conductor area increases. The full-load losses and reactive power generation for a 200MW wind farm were studied for a 132kV 800mm² three-core

cable and a 132kV 1000mm² three-core cable. The results are shown in Table 2-3 below.

Table 2-3. The effect of conductor area (and therefore cable rating) on Full Load Losses and Reactive power generation for a 200MW wind farm with cable route lengths of between 20 and 100km.

		Distance (km)								
		20	30	40	50	60	70	80	90	100
132kV, single 800mm², 203MVA cable with 2 90MVA Transformers	Full Load Losses (%)	1.49	2.00	2.49	2.99	3.48	3.97	4.47	4.98	5.50
	Reactive power generated in cable (MVAr)	18.96	28.75	38.77	49.03	59.56	70.40	81.51	93.00	104.82
132kV, single 1000mm², 217MVA cable with 2 90MVA Transformers	Full Load Losses (%)	1.40	1.87	2.33	2.79	3.25	3.71	4.18	4.67	5.16
	Reactive power generated in cable (MVAr)	21.21	32.13	43.27	54.87	66.34	78.30	90.57	103.23	116.23

The 132kV 1000mm² cable produced lower losses than the 132kV 800mm² cable. This was because the resistance per unit length of the 1000mm² cable was lower. The reactive power generated in the 1000mm² cable was slightly higher than the cable 800mm² cable. There will be a trade-off between cost of losses and cost of the cable and its installation, as the higher rated cables will cost more to buy and install. Further details of full-load losses for wind farms ratings of between 100MW to 350MW and with a single three-core cable connection to shore with cable route lengths of 20km to 100km can be found in tables 1 to 6 in Appendix 2B.

2.1.4. ARRAY CABLE LOSSES

The array cable losses were studied in IPSA. The effect of the wind turbine rating was assessed. The results in Fig. 2-1 show that the losses in an array of 3MW turbines were higher than in an array with 5MW turbines for a particular amount of MW being transmitted in an array. The difference became more apparent as the rated MW of the array increased. The losses were higher for the 3MW turbines because the overall distance of the array was longer due to the ratio of the wind turbine rotor diameter over the power rating being higher for the 3MW turbine (30m/MW for the 3MW turbine as opposed to 25.2m/MW for the 5MW turbine).

Further results for the full-load 33kV array losses are given in table 7 of Appendix 2B.
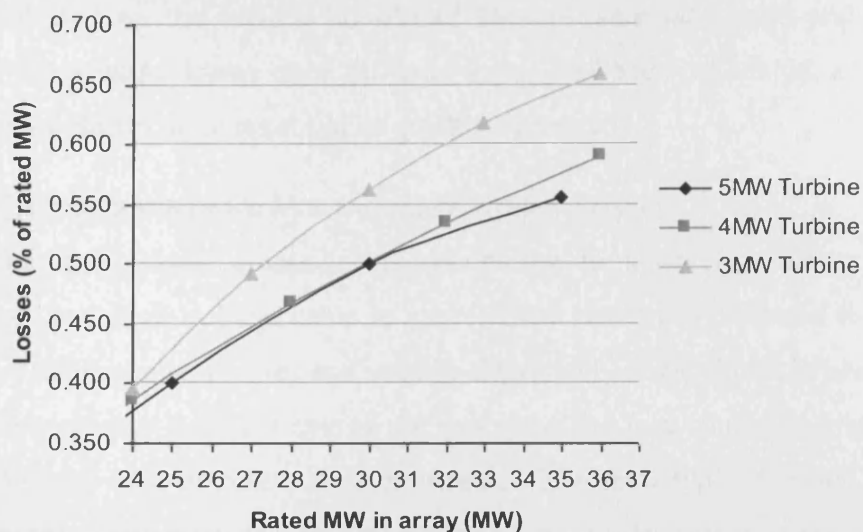
Fig. 2-1. Full-load losses in an array composed of turbines rated at 5MW, 4MW and 3MW respectively. The array cables were tapered.

2.1.5. OVERALL FULL-LOAD LOSSES

Fig. 2-2 shows how the array, cable and transformer full-load losses varied with transmission distance for a 200MW wind farm. It shows that the majority of the losses were due to high voltage cable losses, especially above 40km cable route lengths. The transformer and array cable losses remained around the same value for both voltage levels and over the range of transmission distances. A comparison in terms of full-load array, transformer and cable losses for a wider range of wind farm configurations located at 60km from shore is included in table 8 of Appendix 2B.
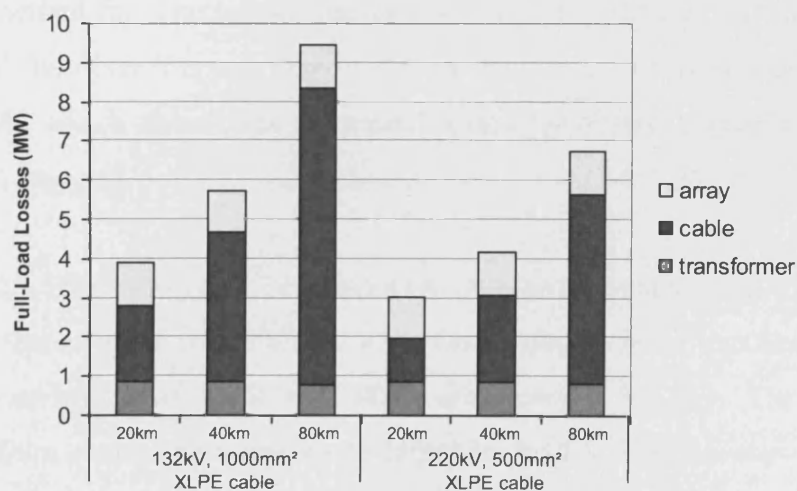
Fig. 2-2. Full-Load Losses for a 200MW offshore wind farm connected by a single XLPE cable with different lengths and voltage levels.

34

2.2. LOSS-LOAD FACTORS

The average losses in an offshore wind farm system are dependent on the fluctuating power generated by the wind. Loss-Load Factors were developed and used to determine the average losses once full-load losses had been calculated, so that the annual cost of electrical losses could be quickly estimated.

2.2.1. CURRENT AND VOLTAGE DEPENDENT LOSSES

Each of the three main components contributing to losses (the array cabling, transformers and high voltage cable to shore) have two types of losses associated with it; current-dependent losses and voltage-dependent losses. There is also a third type of electrical loss which is energy not generated due to a constraint imposed by electrical system unavailability, such as a fault. The third type of losses was not included in the calculation of loss-load factors. Current-dependent losses vary with the square of the load and include I^2R losses due to load currents. Voltage-dependent losses are constant and continuous during the whole time that the equipment is connected to the supply (as long as the voltage does not vary). This includes hysteresis and eddy-current loss in core laminations of a transformer and dielectric losses in a cable.

As the output of the wind farm varies, the part of the full-load losses (in MW) which is due to voltage-dependent losses remains the same, whereas the current-dependent losses vary with the square of the wind farm output. This means that the ratio of the losses to the wind farm output will not remain the same. In order to calculate the average value of losses over a year, a loss-load factor was applied to the full-load losses. A method for determining the cost of losses for offshore transmission was given in [53], however this only provided a loss factor which corresponded to a load factor of 40% which meant that the annual losses for different mean wind speeds could not be assessed.

2.2.2. THE VARIATION OF POWER OUTPUT AND LOSSES WITH WIND SPEED

The power characteristic of a 200MW wind farm along with the loss characteristics for cable route-lengths of 25, 50 and 100km are shown in Fig. 2-3. The wind farm with the 100km route-length had much larger no-load losses than the wind farms with shorter cable lengths. The increase in no-load currents did not vary linearly

with cable length, this is because the losses due to charging currents vary with the cube of the cable length, as shown in the Equations (2-1) and (2-2) below [25].

The charging current, I_c (A/m), is

$$I_c = 2\pi f C U_0 \qquad (2\text{-}1)$$

where f is the system frequency, U_0 is the phase-to-ground voltage, and C is the cable capacitance per unit length.

The charging current is not uniform along the cable, and in a cable with all the charging current flowing from one end (such as a cable with no reactive compensation), the charging current losses per phase, W_{ch} (W), are [26]:

$$W_{ch} = \frac{1}{3} I_C^2 \cdot l^3 \cdot R \qquad (2\text{-}2)$$

where l is the cable length, and R is the cable resistance per unit length.

The dielectric losses however are proportional to the cable length. The charging-current losses have a much larger effect for a longer cable length.
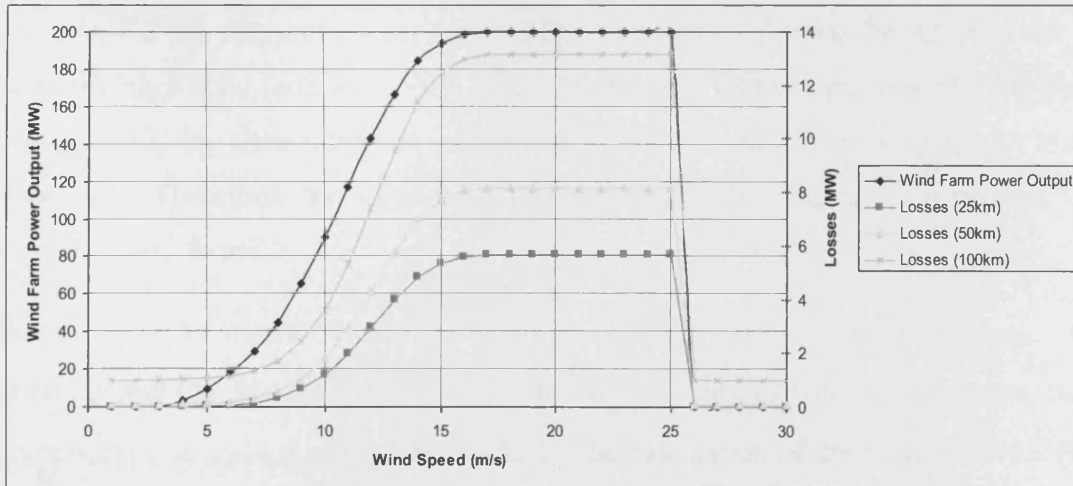
Fig. 2-3. Variation of Power output and Losses with Wind Speed for 132kV AC transmission via a single 3core 800mm^2 cable to shore.

2.2.3. ECONOMIC EVALUATION OF LOSSES

Voltage-dependent and Current-dependent losses affect the revenue of a wind farm in different ways [27]. When the wind farm is not generating, energy must be purchased to supply the no-load (voltage-dependent) losses of the wind farm. The price of the energy that must be purchased during the times of no generation is often

different to the price that the wind farm will obtain for the energy that it sells, and can include a demand charge [27]. Current-dependent losses on the other hand represent reduced output and do not have a requirement for purchased power.

2.2.4. LOSS-LOAD FACTOR DEFINITION

The losses depend upon the power output of the wind farm for any given period. The Loss-Load Factor, μ is defined as the ratio of the actual losses $W(t)$ over a period τ, to the losses obtained if the maximum load is maintained [28], as shown in (2-3):

$$\mu = \frac{1}{W_{max} \cdot \tau} \cdot \int_{t=0}^{\tau} W(t) \cdot dt \tag{2-3}$$

This can usually be approximated by [29]:

$$\mu_I = \frac{1}{I_{max}^2 \cdot \tau} \cdot \int_{t=0}^{\tau} I^2(t) \cdot dt \tag{2-4}$$

In engineering practice, the Loss Load Factor μ is approximated using the Neher/McGrath approach [30] from the known or assumed Load Factor (LF) as:

$$\mu_{LF} = p \cdot LF + (1-p) \cdot LF^2 \tag{2-5}$$

The value of the constant p can be taken as equal to 0.3 for transmission circuits and equal to 0.2 for distribution networks [25]. The value of p will be different for a large offshore wind farm due to the nature of the energy source and also the fact that power must be transmitted to shore via sub-sea cables over reasonably long distances. Therefore, the value of p was determined for transmission systems of offshore wind farms.

Equations (2-4) and (2-5) only take into account the current-dependent losses. In order to use the loss-load factor μ_{LF}, the full-load losses were split up into two components, as shown in equation (2-6) for the calculation of the average losses (in MW):

$$\overline{W} = W_{max,I} \cdot \mu_{LF} + W_V \tag{2-6}$$

where $W_{max,I}$ is the current-dependent losses at full-load, W_V is the voltage-dependent losses, and $W_{max} = W_{max,I} + W_V$, which is the total full-load losses.

In reality, the loss-load factor is also dependent on the operating temperature because the conductor resistance varies with temperature. In most rating calculations,

37

including the calculations carried out in this report, the loss-load factor was calculated from the load shape alone without consideration of the conductor temperature [29].

2.2.5. CALCULATION OF LOAD FACTOR

If the wind speed resource curve and the power characteristic of the turbines are known, a value of LF can be found.

The Load Factor is defined in equation (2-7) below.

$$LF = \frac{1}{P_{rated} \cdot \tau} \cdot \int_{t=0}^{\tau} P(t)dt \qquad (2\text{-}7)$$

The quantity of energy that can be produced annually (not taking into account turbine availability) depends upon the wind speed distribution at the wind farm site and the power characteristic of the wind turbine. The wind-speed distribution was represented by the Weibull probability density function (p.d.f) [31, 32]:

$$f(v) = \frac{k}{c}\left(\frac{v}{c}\right)^{k-1} \exp\left[-\left(\frac{v}{c}\right)^{k}\right] \qquad (2\text{-}8)$$

where c is the scale factor and is a characteristic speed related to the average wind speed at the site, and k is a shape parameter. The proportion of time for which the wind speed v will occur is given by (2-8). Fig. 2-4 illustrates the effect of the shape parameter on the Weibull distribution. When the shape parameter k is equal to 2, the p.d.f. is called the Rayleigh probability density function:

$$f(v) = \frac{2v}{c^2} \exp\left[-\left(\frac{v}{c}\right)^{2}\right] \qquad (2\text{-}9)$$

There is a direct relationship between the scaling factor c and the average wind speed $\bar{v}$:

$$\bar{v} = \int_{0}^{\infty} v \cdot f(v)dv = \int_{0}^{\infty} \frac{2v^2}{c^2} \exp\left[-\left(\frac{v}{c}\right)^{2}\right] = \frac{\sqrt{\pi}}{2} c \cong 0.886c \qquad (2\text{-}10)$$

Although equation (2-10) is derived for the Rayleigh function, it is quite accurate for a range of shape factors k from 1.5 to 4 [32].
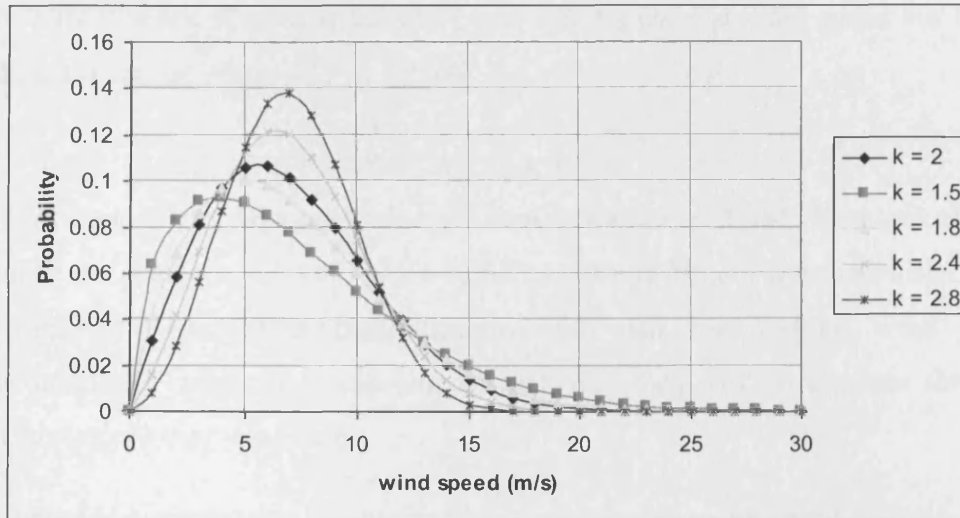
Fig. 2-4. Weibul distribution, with mean wind speed = 7.09m/s.

For a given wind regime probability distribution, $f(u)$, and a known wind turbine power curve, $P_W(u)$, the average wind turbine power, $\overline{P_W}$, is given by [33]:

$$\overline{P_W} = \int_0^\infty P_W(u) f(u) du \qquad (2\text{-}11)$$

The annual expected energy output is then equal to $\overline{P_W} \cdot 8760$, and the Load Factor equals $\overline{P_W} / P_{rated}$. Another way to calculate the annual energy output is to separate the curves into wind speed bins as shown in Fig. 2-5.
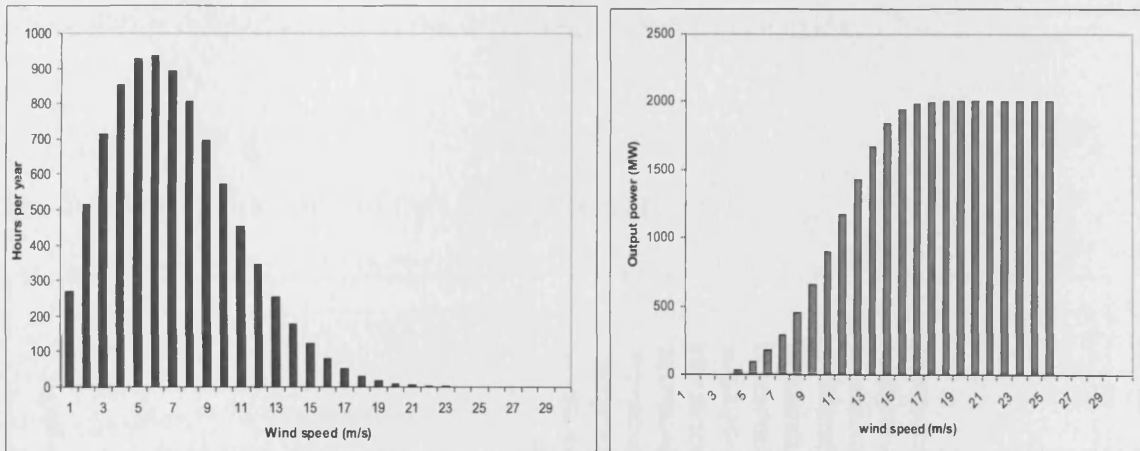
Fig. 2-5. Wind Speed resource curve (for k =2 and c = 8) and Power Characteristic for the Vestas V80 2MW wind turbine.

The annual energy output was obtained by combining the wind speed resource curve with the power curve of the turbine:

$$Energy = \sum_{i=1}^{i=n} H(i) \cdot P(i) \qquad (2\text{-}12)$$

39

where $H(i)$ = hours in wind speed bin i, and $P(i)$ = power at wind speed bin i. The Load Factor equals $Energy / (P_{rated} \cdot 8760)$.

2.2.6. LOSS LOAD FACTOR CALCULATIONS

The Loss Load Factor was calculated in a similar way to the Load Factor calculations shown in the previous section. Once some Loss Load factors were calculated for a few different wind farm configurations and also for varying wind speed characteristics, a value of p was found which was then used to estimate the Loss Load factors of other wind farms.

The annual lost energy can be obtained by combining the wind speed resource curve with the Losses Characteristic of the wind farm:

$$Lost\_Energy = \sum_{i=1}^{i=n} H(i) \cdot W(i) \qquad \textbf{(MWh)} \qquad (2\text{-}13)$$

where $W(i)$ = wind farm electrical losses at wind speed bin i. The Loss-Load factor equals $Lost\_Energy / (W_{max} \cdot 8760)$. However, since the voltage-dependent losses remained constant throughout the year, the current-dependent Loss-Load factor was calculated, such as in (2-5) and (2-6). This was calculated as follows:

$$\overline{W_I} = \sum_{i=1}^{i=n} F(i) \cdot W_I(i) \qquad \textbf{(MW)} \qquad (2\text{-}14)$$

where $F(i)$ is the probability of the wind speed in bin (i) occurring.

$$\mu_I = \frac{\overline{W_I}}{W_{max,I}} \qquad (2\text{-}15)$$

Fig. 2-6 shows an example of the Losses characteristic.
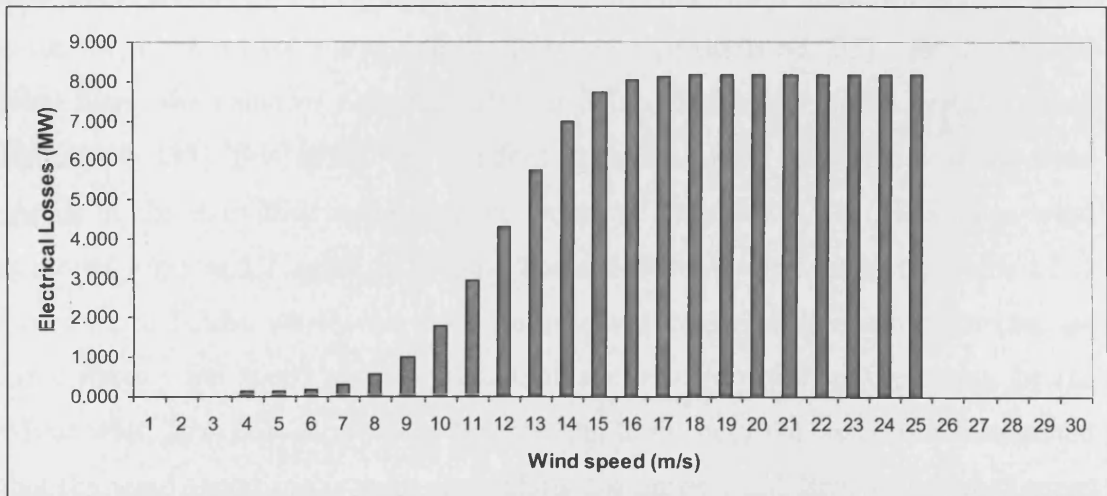
Fig. 2-6. Electrical Losses for a 200MW wind farm with 50km of 132kV transmission to shore via a 3 core cable with 800mm² conductors.

2.2.7. DETERMINATION OF A VALUE FOR P

Once the Load Factor and Loss Load Factor were found, a value of p was calculated using equation (2-16):

$$p = \frac{\mu_l - LF^2}{LF - LF^2} \tag{2-16}$$

In the following sections, values of p were calculated for wind farms with a range of cable route lengths and with varying wind speed characteristics.

2.2.8. AGGREGATED POWER CURVE FOR THE WHOLE WIND FARM

Large wind-farms are installed over a large area. In this report it was assumed that the wind had the same speed throughout the entire area of the wind farm. In practice however, this is not the case. For a given mean value of wind speed the actual wind speed in different locations within the wind farm will deviate, depending on D and I [34]. D is the length of the side of the wind farm that is perpendicular to the direction of the wind, and I is the turbulence intensity.

The deviation in wind speeds across the wind farm mean that the aggregated power curve for the whole wind farm will not follow the same shape as the power curve for a single wind turbine. The cut-in and cut-out wind speeds for the entire wind farm will be different to those for a single wind turbine. This is because the actual wind speed varies around the mean value, so in some locations the wind speed is above the cut-in wind speed for a single turbine, even if the mean wind speed is below this value.

The deviation of the simultaneous power outputs from the wind turbines is distributed around an average value, with the amount of deviation depending on the extent of the wind farm area and the turbulence of the wind [35]. For a 200MW wind farm, the value of D is around 5 to 10km, depending on the design. From figure 6 in [35], this means the standard deviation of the distribution of the wind speeds at the individual wind turbines would be only about 0.2 (for a mean wind speed of 7m/s and I equal to 10%). For a 1000MW wind farm, the value of D increases to 50km, which increases the standard deviation to roughly 0.6 (for the same mean wind speed and I). This results in an aggregated power curve for the whole wind farm that is only slightly different to the curve obtained if it is assumed that the wind speed is the same throughout the entire wind farm. The wind speed

deviations across the wind farm were not included in the calculation of a loss-load factor as they should only make a very small difference to the losses calculations.

2.2.9. EXAMPLE WIND FARMS FOR LOSS-LOAD FACTOR STUDY

The wind farms considered had a single High Voltage cable connection to shore. It was assumed that all turbines were of the Vestas V80 2MW design, since the power characteristic for this turbine was used for all calculations. For the 33kV array cable loss calculation, an average spacing of 500m between turbines was used. The rating of the array cabling varied depending on its position in the array (i.e. the conductor size increased as the amount of turbines connected along the array increased).

The configuration of the wind farm was similar to that shown in Fig. 1-3. For 132kV (200MW) wind farm configurations, 800mm^2 Cu 3 core cables were used. 500mm^2 Cu 3 core cables were used in the 220kV (250MW) wind farm configurations. There was no reactive compensation included. The losses were determined for the submarine cable, offshore transformers and array cabling only.

2.2.10. RESULTS

As the annual mean wind speed increased, so did the Load factor and the Loss-Load factor, as shown in Fig. 2-7. The Loss-Load factor was always lower than the Load factor for a given annual mean wind speed.
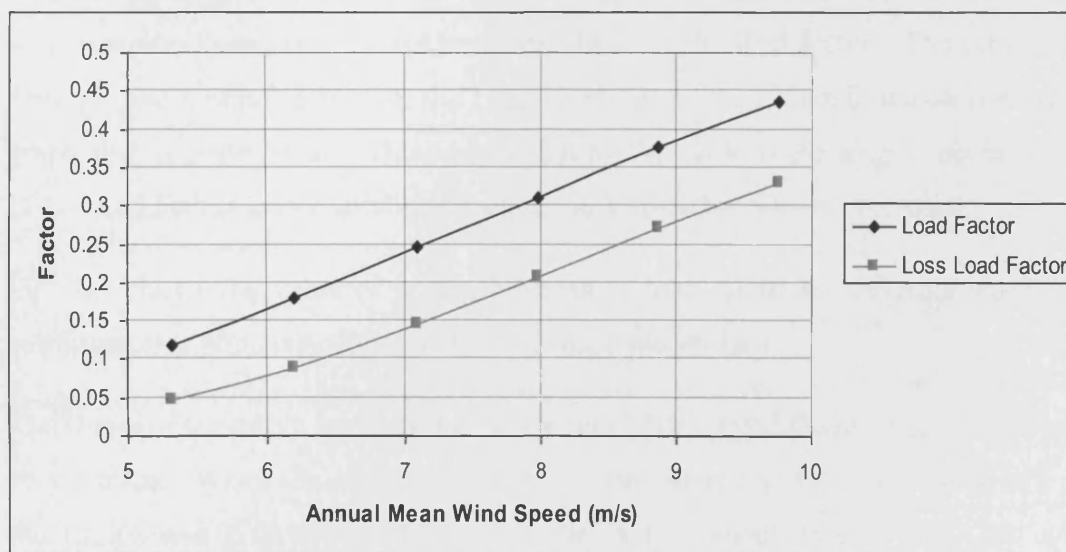
Fig. 2-7. Load Factor and Loss-Load factor as a function of annual mean wind speed for a 200MW 132kV Wind Farm with a cable route length of 50km. Weibull shape parameter, k = 2.

Fig. 2-8 shows the relationship between the wind farm load factor and loss-load factor for three 200MW 132kV wind farms located 25, 50 and 100km from shore.
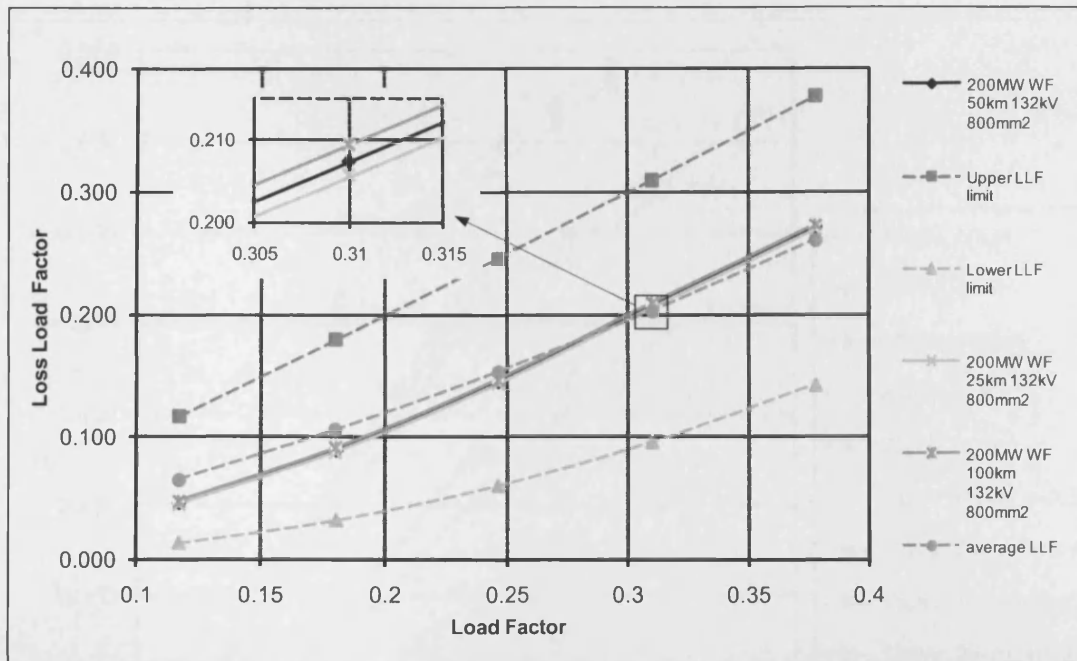
Fig. 2-8. Curves showing the effect of the wind farm Load factor upon the Loss-Load factor for various wind farm designs with a Weibull shape parameter, $k = 2$.

The green and pink dashed lines in Fig. 2-8 show the extreme limits for the Loss-Load factor. Using (2-5), the upper limit is reached when $p = 1$ and the lower limit is reached when $p = 0$. The average Loss-Load Factor (shown as a blue dashed line) is assumed to be when $p = 0.5$. The upper and lower limits and the average LLF are only included here to assess the range. Fig. 2-8 shows that as the load factor increases, the Loss-Load Factor becomes closer to the load factor. The cable route distance had a minor effect on the Loss-Load Factor, as shown in the section of the graph that is zoomed in. This shows that as the cable route length increases, the Loss-Load Factor increases slightly while the load factor remains the same.

Fig. 2-9 shows the value of p as a function of load factor for different wind farm configurations and also different Weibull shape parameters.

The shape of the curve for both the 132kV and 220kV wind farms (when $k = 2$) were very similar. When the cable route distance was 50km and $k = 2$, the value of p for the 132kV and 220kV wind farms only differed by about 0.02. The 132kV wind farm had a slightly higher value of p than the 220kV wind farm. This could be due to the fact that the 132kV cable will operate closer to its maximum rating at full-output (the full-output is 200MW and cable rating is 203MW) compared to the 220kV cable (the full-output in this case would be 250MW and the cable rating is 279MW) for the wind farm configurations considered in this report.
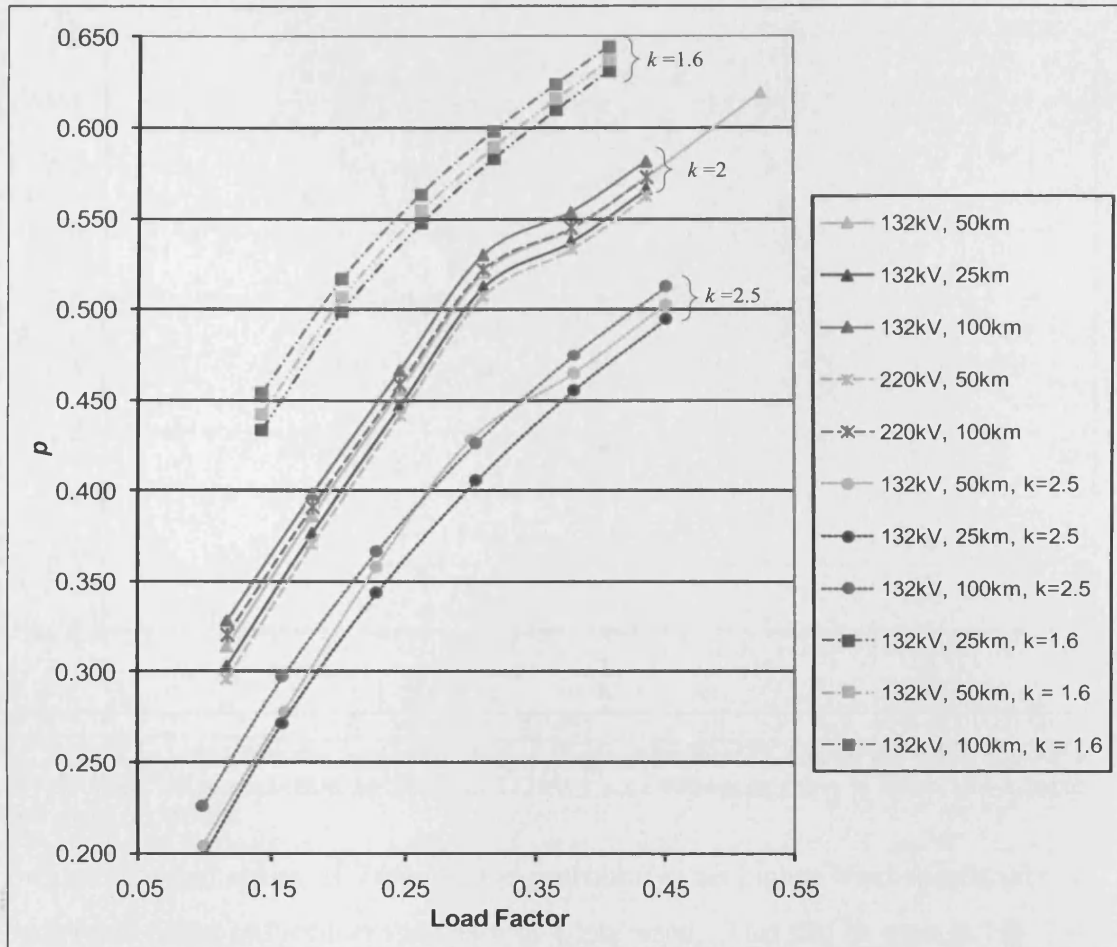
Fig. 2-9. Variation of *p* with Load Factor for Current-Dependent Losses

The Weibull shape parameter had a big effect on the value of *p* for a given Load factor, as shown in Fig. 2-9. This means that it is important that the correct shape parameters are used for a particular wind farm site, as it will affect the expected losses that are calculated. The variation of *p* with shape parameter is further explored in Fig. 2-10. The value of *p* varied inversely with the shape parameter, and although it was not linear over a large range, the relationship could be assumed linear over a smaller range, such as for values of *k* from 1.5 to 2.5. Values of *k* in this smaller range will be of most interest since the Weibull shape parameter for wind farms is often close to 2.
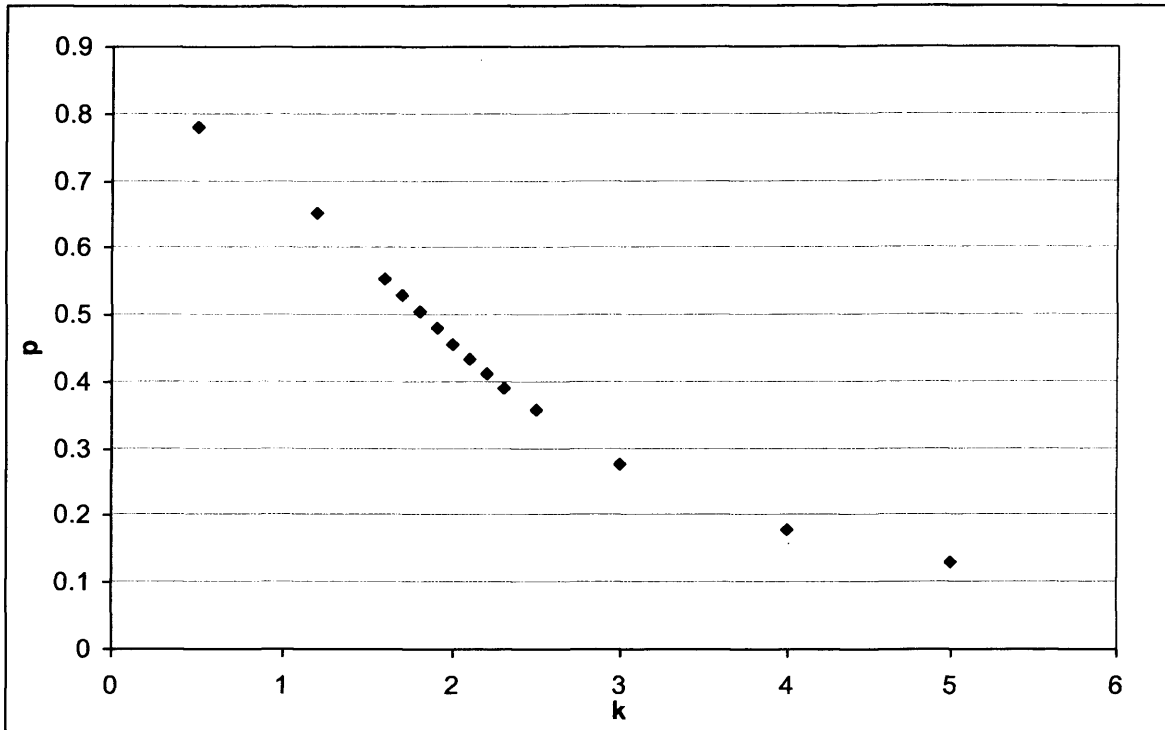
Fig. 2-10. The effect that the wind-distribution shape parameter, k, has on the value of p for a 200MW wind farm connected by 50km of 132kV 3 core 800sqmm cable to shore and a mean wind speed of 7.09m/s.

For a mean wind speed of 7.09m/s, the probability that higher wind speeds (above 13m/s) will occur reduced as the value of k increased. This can be seen in Fig. 2-4 and Table 2-4, and is the reason why the value of p was larger for smaller values of k. The reason for this can be explained by looking at equation (2-5).

Table 2-4. The probabilities that a wind speed occurs above 18m/s and below 4m/s for a mean wind speed of 7.09m/s, and the percent of time that the wind farm will spend operating at rated output while the wind speeds are within the cut-in and cut-out values.

k	1.8	1.9	2.1	2.2
Percent of time that a wind speed occurs above 18m/s (%)	1.66	1.19	0.56	0.36
Percent of time that a wind speed occurs below 4m/s (%)	19.65	18.35	15.90	14.76
Percent of time spent at rated output, while operating inside the cut-in and cut-out speeds (%)	2.07	1.46	0.67	0.42

Since the current-dependent losses only occur when the wind speeds are above cut-in and below cut-out values, the current-dependent loss-load factor will also be applicable within this range. As shown in Table 2-4, there was a larger percent of time spent at full-rated output for the smaller values of k.

2.2.11. GUIDELINE FOR THE CALCULATION OF LOSS-LOAD FACTORS

A method for the determination of the annual losses was developed and is given in Appendix 2C. This provides a guideline for the choice of p and the estimation of the loss-load factor.

2.3. HVDC LOSSES

It is generally accepted that for distances up to around 50km HVAC transmission has the lowest losses. Above 50km conventional HVDC LCC tends to have the lower losses [36]. For two- level HVDC VSC, higher switching frequencies are favourable because fewer harmonics are produced which results in a lower requirement for filtering of the resultant waveform. However, as the switching frequency increases, so do the losses. There will be a balance between the amount of losses and harmonics that can be tolerated in the system. A description of two-level HVDC VSC is given in Appendix 2D.

2.3.1. DEVICE LOSSES

The losses in a power semiconductor switch are composed of on-state conduction losses, off-state blocking losses, and turn-on and turn-off switching losses, as shown in Fig. 2-11. The on and off-state losses of a device are relatively easy to calculate. The on-state losses are calculated by multiplying the device current by the forward saturation voltage and the off-state loss is the product of the blocking voltage and the leakage current.

As shown in Fig. 2-11, the losses that occur during switching are considerably higher than the losses that occur during the on and off-state of the IGBT. The turn-on and turn-off switching losses are determined by the voltage and current waveforms, and although they are shown as a linear transition in Fig. 2-11, the waveforms are non-linear in a practical device. The switching waveforms of the device is governed by various factors such as DC bus voltage, current magnitude, gate voltage, gate resistance, junction temperature and the parasitic impedance of the circuit.
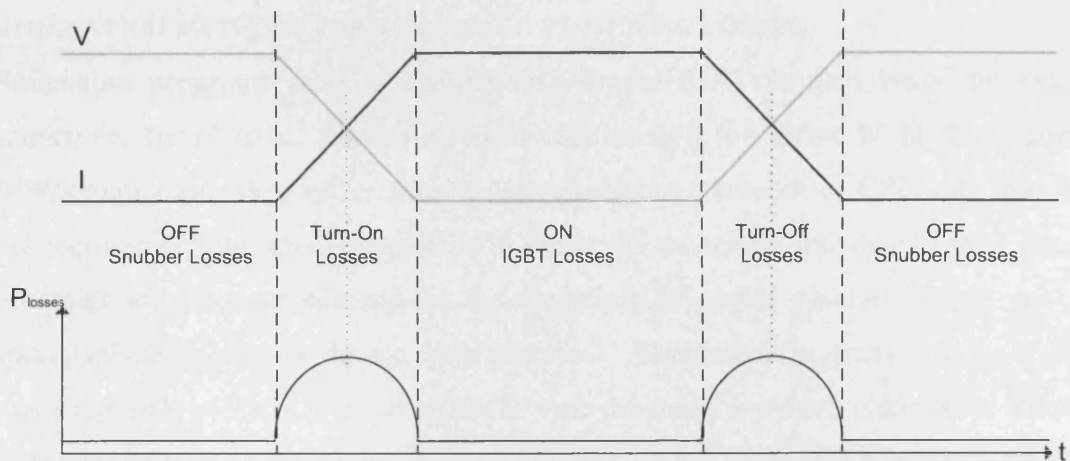
Fig. 2-11. An example of the losses that occur in an IGBT device with a snubber circuit.

DEVICE TURN-ON AND TURN-OFF

Typical waveforms that occur during turn-on and turn-off in a real IGBT device are shown in [39] with the characteristics of IGBT devices described in [40 - 42]. The turn-off losses can be reduced by increasing the doping impurities which helps to speed up recombination. However, increased doping will increase the on-state and turn-on losses [43].

The IGBT model in PSCAD consists as two state resistances. The state resistances are chosen by the user. Although this simple representation of an IGBT is sufficiently accurate for power system simulations, it is not adequate for the determination of switching losses which requires a consideration of the physics of the switching process [37, 38].

SNUBBER CIRCUIT

During switching, the semiconductor device may be subject to large amounts of stresses due to the high rate of rise of current and voltage during turn-on and turn-off respectively. In order to solve this problem, either a device whose ratings exceed the stresses should be chosen or a snubber circuit should be added to the device [44]. Snubber circuits protect semiconductor devices during switching transients by limiting current and voltage rise times and magnitudes. A snubber circuit can also reduce the turn-off losses. If a capacitive turn-off snubber is used the turn-off losses decrease exponentially as the capacitor value increases [43].

SIMULATION METHODS FOR MODELLING SWITCHING LOSSES

Simulation programs such as PSPICE can model IGBT devices based on exact semiconductor physics. However, when simulating a full Pulse Width Modulated (PWM) converter they suffer from an extremely large amount of CPU time due to the requirement for small time-steps to cover the switching transients [45]. Such programs are also not suitable for the modelling of power systems as they are a specialist semiconductor device simulation tool. Simulation programs using a fixed time-step such as PSCAD or other EMTP type programs are more likely to be suited to the modelling of switching losses in a large power electronic system; however there may still be an unacceptably large CPU time.

One approach to modelling switching losses in an EMTP type program is the use of a curve-fitting method combined with a point-by-point user defined function. This approach does not require any semiconductor device physics modelling so the simulation time is reduced compared to simulations carried out in programs such as PSPICE [46]. However, this method still requires the simulation to be carried out with very small time-steps (10ns time-steps for a 2.4kHz switching frequency) so the simulation time is large. Another method is the simple use of lookup tables or fitted curves as proposed in [39, 47], however such methods do not take into account the dependency of switching losses on various factors such as stray inductances and the reverse recovery process of the diode and so tend not to be accurate. A method that is more accurate involves the use of simple functions derived from typical switching waveforms to estimate the switching losses, as presented in [40, 48]. This method can take into account various factors that influence switching losses such as switching voltage and current and stray inductances which ensure that the predicted waveforms conform to the semiconductor physics. A refined model using this technique is presented in [37] and requires only a few parameters that can be extracted either from manufacturers data sheets or from measured waveforms.

2.3.2. CONVERTER LOSSES

The converter losses will depend on the switching scheme chosen and the converter topology used, both of which are continuously developing. The PWM method, shown in Appendix 2D, means that each IGBT will switch for a fixed number of times over the fundamental AC time period and so the switching losses will be high. In order to reduce these losses a switching scheme could be adopted which switches to the need rather than at a fixed switching frequency. This technique has been

adopted by ABB for their HVDC Light technology [49], and it can also be combined with the Selective Harmonic Elimination Method (SHEM) of switching so that certain harmonics can be reduced. ABB have also recently presented a cascaded two-level converter which consists of several smaller two-level converters (called cells) [50]. This technique reduces the losses to nearly 1% per converter. The modular multilevel HVDC VSC technology offered by Siemens (HVDC PLUS) allows the converters to be operated at a low switching frequency which results in lower converter losses than conventional 2 or 3-level converters. The new HVDC VSC being offered by ALSTOM Grid is a hybrid approach which combines series-connected IGBTs with multilevel converters based on individual and isolated half-bridge and full-bridge cells [51]. The overall converter losses for this hybrid HVDC VSC scheme are expected to be around 0.8%.

The operating costs could be reduced in two ways; through the reduced cost of losses and also through reduced maintenance costs due to the reduction in the number of components. These cost reductions will help to reduce the break-even point between HVAC and HVDC VSC transmission and are likely to make the HVDC VSC connection of offshore wind farms more attractive in future years.

2.3.3. CABLE LOSSES

The losses in HVDC cables are significantly lower than losses in HVAC cable transmission due to the additional charging current losses in AC cables. In DC cables the voltage distribution (electrical stresses) is dependent on the cable geometry and is highly dependent on the temperature drop across the insulation as the conductivity of the insulation increases exponentially with temperature. Usually it is these electrical stresses that limit the transmission capacity of DC cables and not the maximum allowable conductor temperature [52].

2.3.4. COMPARISON OF HVAC AND HVDC VSC LOSSES

The losses in a 200MW HVDC transmission system were compared to the losses in various 200MW HVAC transmission systems for cable route lengths ranging from 20km to 100km. The results are shown in Fig. 2-12. The increase of losses with increasing cable route length was much lower for the HVDC system than the HVAC system. However, the HVDC system losses at shorter cable route lengths were much higher when compared with the HVAC systems. This is due to the high HVDC converter losses (which was assumed to be 1.6% per converter based on ABB's

original HVDC Light technology) compared with the lower HVAC substation losses. As the switching methods and converter configurations are refined the converter losses will reduce and so the break-even point in terms of electrical losses will reduce. The additional requirement for harmonic filters and STATCOMs for the HVAC systems will increase the HVAC system losses and so decrease the break-even point further.
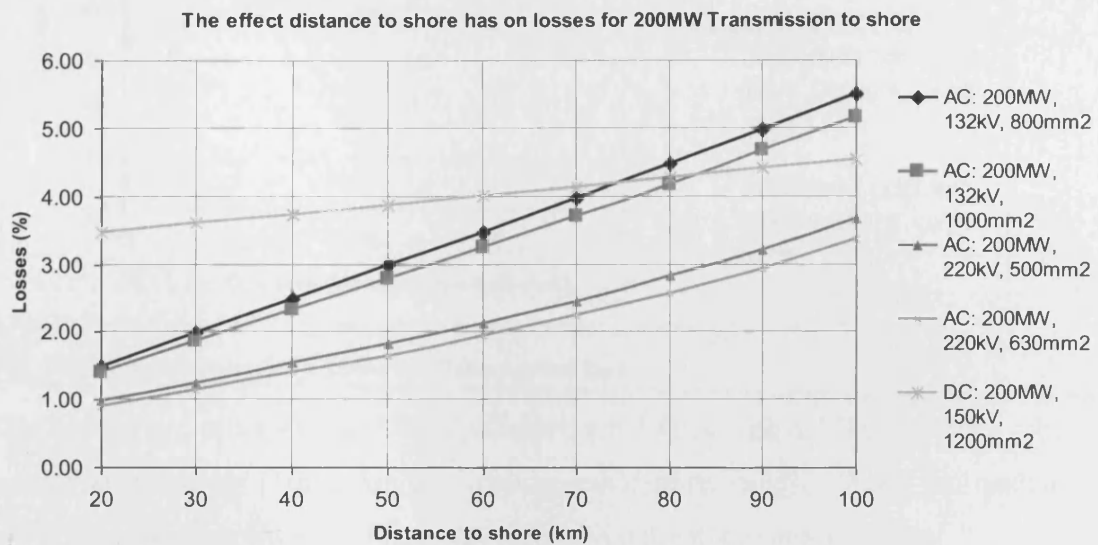
Fig. 2-12. Losses in HVDC transmission compared to HVAC transmission for cable lengths between 20 and 100km.

2.4. AC VERSUS DC BREAK-EVEN POINTS

The choice between AC or DC transmission is mainly determined by the wind farm rating and the cable route lengths connecting the offshore wind farm to the onshore grid. Since the capital costs represent the majority of the overall costs, they were compared for AC and DC schemes with varying cable route lengths in order to find a break-even point. In order to obtain a more reliable break-even point, the cost of losses, maintenance and constrained energy were included. Appendix 2E includes case studies for two Round 3 zones, the North West and Dogger Bank.

2.4.1. CAPITAL COSTS

The capital costs of a DC converter station are much higher than the capital costs of an AC substation. However, due to the lower number and cost of DC cables required to transmit the same quantity of energy, the capital cost of the DC cables are lower than AC cables. This resulted in DC schemes being more expensive for shorter cable routes but more economically viable as the cable route length increased, as shown in Fig. 2-13. The cost data used in this thesis was obtained from [53].

50
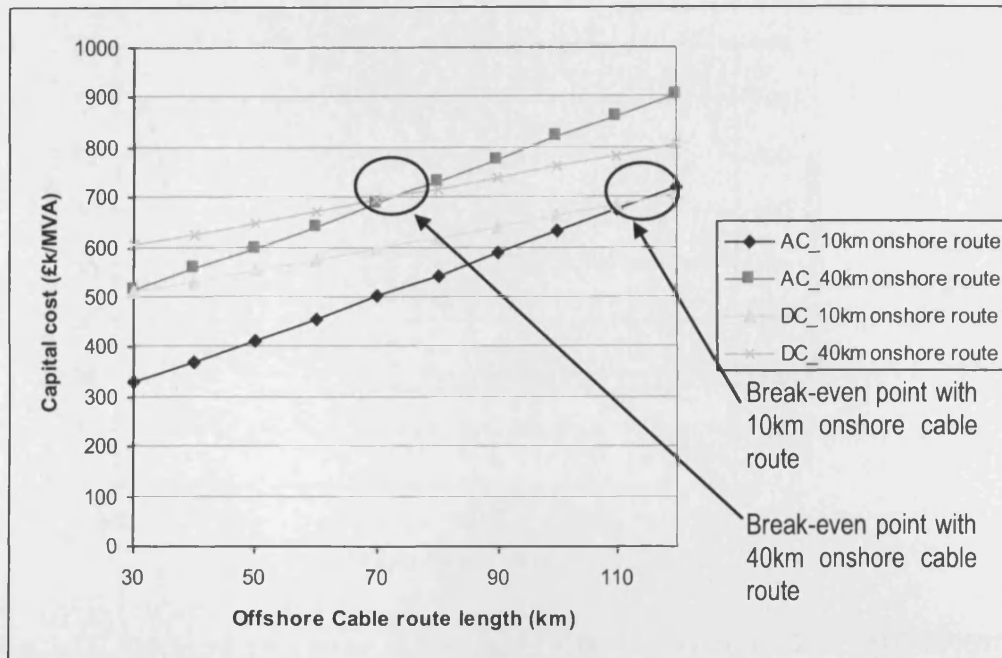
Fig. 2-13. Capital costs for a 300MW offshore wind farm.

The break-even point for a 300MW offshore wind farm with a 10km onshore cable route was just over 110km for the offshore cable route length. When the onshore cable route was increased to 40km, the break-even point was around 70km.

The break-even points and the corresponding capital cost for wind farm ratings from 300MW to 2400MW are shown in Fig. 2-14 and Fig. 2-15 for onshore cable routes of 10km and 40km respectively.
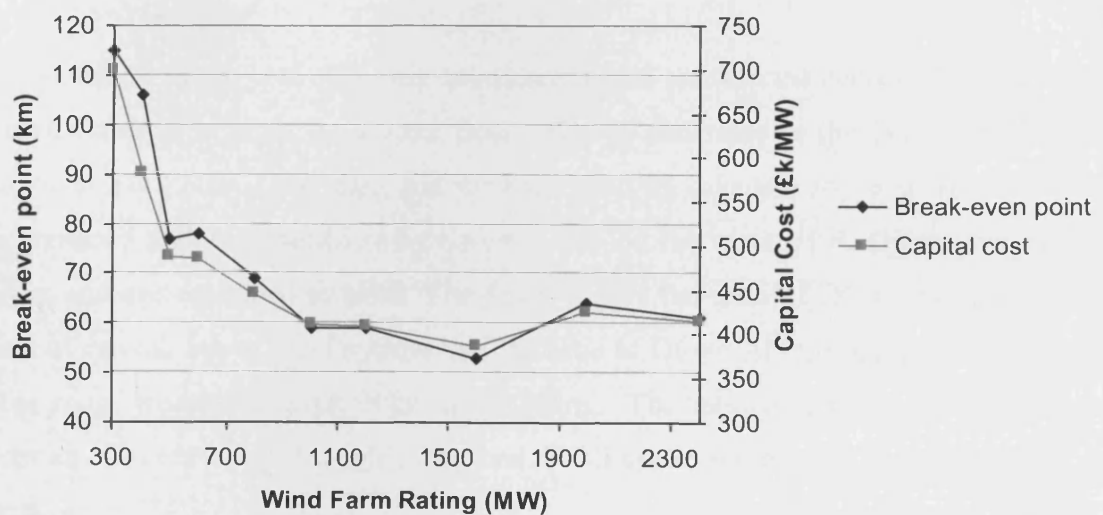
Fig. 2-14. The break-even points of wind farms with ratings ranging from 300 to 2400MW and their corresponding capital cost. An onshore cable route length of 10km was assumed.
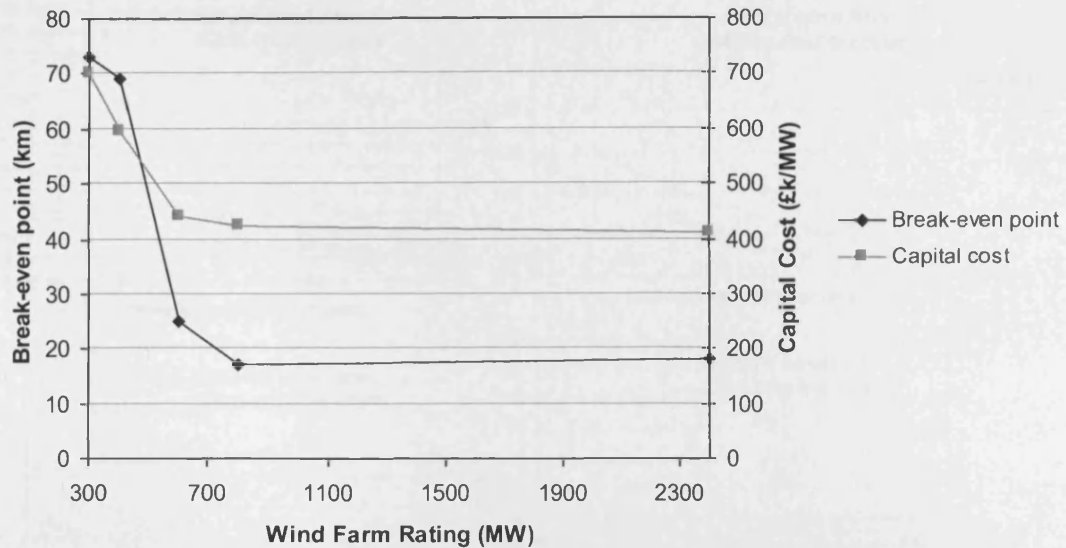
Fig. 2-15. The break-even points of wind farms with ratings ranging from 300 to 2400MW and their corresponding capital cost. An onshore cable route length of 40km was assumed.

As the wind farm rating increased, the break-even point reduced. The break-even point attained its lowest value when the maximum rating of a single HVDC converter station was reached (1600MW). The break-even point then settled at this point for larger wind farm ratings. The results show that for a 10km onshore cable route, the break-even point for wind farms above around 1000MW was 60km. When the onshore cable route was 40km, the break-even point was less than 20km.

2.4.2. CONSIDERATION OF LOSSES, MAINTENANCE AND CONSTRAINED ENERGY

The inclusion of the cost of losses, maintenance and constrained energy shifted the overall break-even point for a wind farm. This is illustrated in the four examples shown in Fig. 2-16. The data and methods used to calculate the cost of losses, maintenance and constrained energy were based on the work of P. Djapic and G. Strbac and are described in [53]. The figure shows the ratio of DC to AC for the costs of capital, losses, maintenance and the ratio of DC to AC for the total cost for cable route lengths between 30km and 120km. The ratio of DC to AC cost of constrained energy stayed roughly the same for all cable lengths so is not included in the figure.
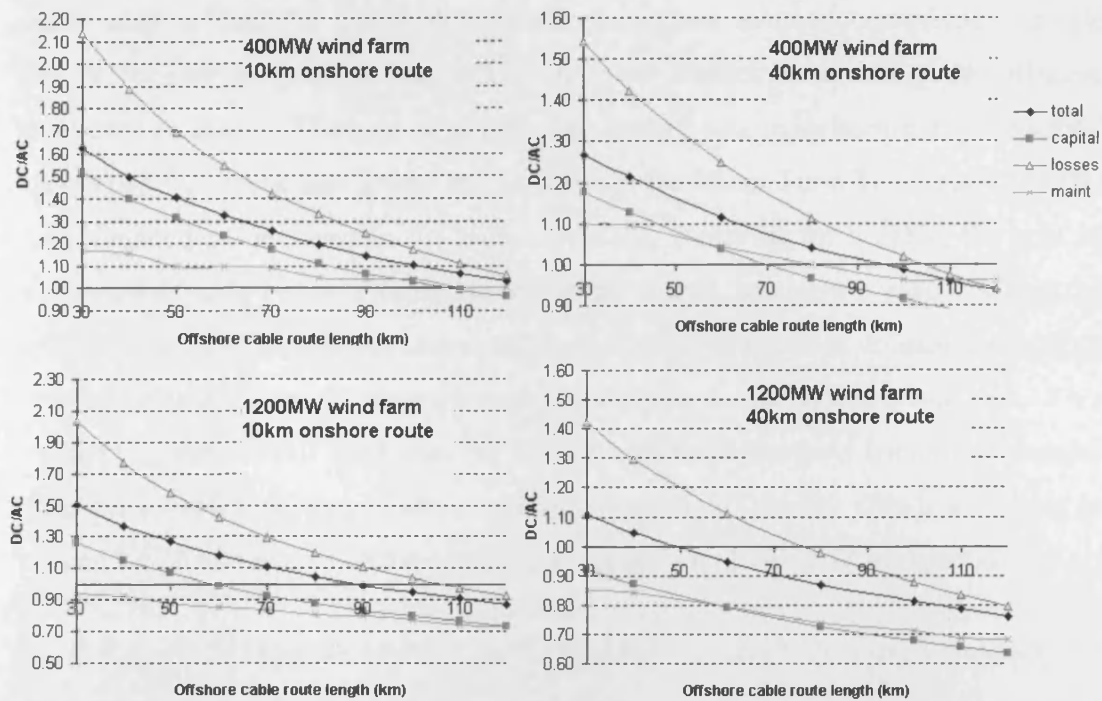
Fig. 2-16. The ratio of DC to AC costs for connections of wind farms with cable route lengths from 30 to 120km. The ratio of the DC to AC total costs includes the cost of capital, maintenance, losses and constrained energy.

The results show that the inclusion of losses, maintenance, and constrained energy had the combined effect of increasing the overall break-even point. For all four cases, the break-even offshore cable route length was increased by roughly 30km. The main reason for the increased break-even point was the significant cost of constrained energy for DC solutions when compared to AC solutions. For the 400MW wind farm, the cost of DC constrained energy was 2.5 times larger than for AC and represented roughly 10% of the total cost. For the 1200MW wind farm, the cost of DC constrained energy was around 10 times larger than for AC and represented 14% of the total cost. For all four examples, the cost of losses was around 10% of the total cost. The break-even point for the losses was higher than for the capital costs due to the high proportion of losses in the converter stations. If the losses in the converter station were lower the break-even point for the losses would reduce. The cost of maintenance represents around 1% of the total cost and did not have a significant effect on the overall break-even point.

HVDC CONNECTION STRATEGIES

Two different connection strategies were investigated for a 1600MW offshore wind farm with a submarine cable route of 190km and an onshore cable route of 70km. The first connection strategy comprised four separate HVDC converter platforms

each rated at 400MW whilst the second connection strategy comprised a single HVDC converter rated at 1600MW with two bipoles connecting the offshore converter to shore. The cost of constrained energy was calculated using a method developed by Djapic and Strbac in [53]. When the Mean Time To Repair (MTTR) was assumed to be 1 month for a converter and 2 months for a cable, the cost of constrained energy was 5 times more for the shared connection case. When the MTTR of the converters was increased to 4 months, the cost of constrained energy was 10 times more for the shared connection than for the individual connection. This resulted in the overall total cost for the individual connections becoming cheaper than the overall total cost of the combined connection. Further details are given in Appendix 2E and results of the comparison are shown in Table 18 of Appendix 2E.

2.5.   OFFSHORE GRIDS AND DC MULTITERMINAL NETWORKS

There have been a number of research projects carried out into the applicability and viability of offshore grids for the connection of offshore wind farms. Offshore grids may provide a more cost effective solution to the connection of offshore wind farms and could involve both AC and DC transmission systems. A few of these studies include:

- A HVDC grid study on the GB East Coast, by **Econnect** [54]. This study was commissioned by the Crown Estate in order to assess the technical and economic feasibility of using the east coast seabed for an offshore transmission network. In this study, HVDC VSC was chosen as the transmission medium because of its suitability for multi-terminal networks and ability to connect weak points on AC systems. The study included a longer term potential '2020 scenario' network which was designed to accommodate future Round 3 developments.

- A study by **PB Power** for grid extension on the GB West Coast [55]. The PB Power study examined the cost of building a 2GW HVDC offshore transmission system down the west coast of Great Britain to connect renewable generation in the north to the demand centres in the south.

- **ISET** study for German North Sea [56]. This study compared the concept of an offshore grid with the planned connections for offshore wind in Germany. The planned connections involve arranging the offshore wind farms into clusters then connecting them via separate cable traces to the German

Transmission system. It was shown that with separate connections, the loading of the Grid Connection Points were not balanced and that at two connection points the short circuit power ratio may not be high enough to ensure high grid stability. The use of cross-connections between clusters enabled the lower loaded grid connection points to take the excessive wind energy from the highly loaded points. The offshore grid solution also reduced the number of offshore platforms, equipment and cables.

• **Airtricity (Scottish and Southern)** proposed a Supergrid, which would connect offshore wind farms located in the Baltic Sea, the North Sea, the Atlantic, the Bay of Biscay and the Mediterranean [57]. They were putting plans in place for a 10GW Foundation Project which will consist of a number of projects in Dutch, German and UK waters. The offshore grid would consist of HVDC VSC connections. The 10GW Foundation Project would comprise 2000 turbines rated at 5MW, with an operational date of 2017 – 2019.

2.5.1. DC SWITCHGEAR

In order to minimise the interruption of power during a fault or outage in a multi-terminal HVDC system, HVDC circuit breakers would be a major advantage. The requirement of DC circuit breakers in multi-terminal HVDC systems would be to connect and disconnect substations and lines for both removal of faults and operational switching cases.

The absence of cyclic moments of current zero in a DC system inherently makes DC current switching more difficult than for AC systems, as arcs require a current zero in order to extinguish. There are two main types of HVDC circuit breaker; electromechanical and solid-state.

There have been many electromechanical HVDC circuit breakers developed over the past 5 decades. These can be grouped into three main interruption techniques; 1: Inverse voltage generating method, 2: Divergent Current Oscillating method, and 3: Inverse current injecting method [58]. Of these, the inverse-current injecting method is suitable for higher voltage and current ratings. This creates a current zero by superimposing a high frequency inverse current on the DC current by discharging a pre-charged capacitor through an inductor. A conventional AC circuit breaker can be

selectively utilised in this method and the cost of components required for such an electromechanical DC circuit breaker would not be significantly higher than that of an AC circuit breaker. Typical applications of electromechanical HVDC circuit breakers can be found in the neutral bus of bipolar HVDC-LCC schemes [59]. Electromechanical HVDC circuit breakers are available up to 500kV, 5kA and have a fault-clearing time of the order of 100ms [58, 60].

There are some cases where a clearing time which is much faster than possible with electromechanical HVDC circuit breakers is required. Example applications include pulsed power [61] and traction [62]. Solid-state circuit breakers are suitable and able to interrupt current within a couple of milliseconds [61, 63]. They are generally based on Integrated Gate Commutated Thyristors (IGCT) as they have lower on-state losses than IGBTs [64]. Current flows through the IGCT during on-state operation. In order to interrupt the current, the IGCTs are turned off and the voltage quickly increases until a varistor starts to conduct. The varistor is designed to block a voltage above the system voltage level. The main disadvantages of the solid-state circuit breakers are their high on-state losses and capital costs. Typical ratings of solid-state circuit breakers in operation are 4kV, 2kA [61, 62], although in [63] ratings of up to 150kV, 2kA were considered.

In a multiterminal HVDC system without HVDC circuit breakers the whole system voltage would have to be brought to zero in order to clear a fault. In the case of multiterminal HVDC-LCC systems, the overcurrent can be limited by its DC current control function and the fault can be cleared by the action of thyristor valve control and protection. After a de-ionisation period, the system can be restarted in 100ms to 300ms [65, 66]. In the case of multiterminal HVDC-VSC systems, such a fast re-start would be difficult without the use of HVDC circuit breakers. If a fault occurred on a multiterminal HVDC-VSC system, the free-wheeling diodes used in the VSC would cause DC current to continue to flow into the fault even if the IGBTs were blocked. If HVDC circuit breakers are not used, it would be necessary to open the AC circuit breakers at all converter terminals. It would take a relatively long time to restore the system since it would be necessary to charge the DC system to rated voltage before restarting.

In the case of a large multiterminal HVDC-VSC system it would not be feasible to allow the whole system voltage to go to zero in the event of a fault, as this would

result in a significant loss of power. DC circuit breakers which can clear the fault within a few milliseconds are required [67]. This is to meet the requirements of preventing the fault current rising very fast towards very high values due to the low system impedance and preventing voltage collapse of the whole HVDC system. A solid-state HVDC circuit breaker would be necessary since the operating time of an electromagnetic HVDC circuit breaker is too slow for this requirement. It is sensible to minimise the number of these solid-state HVDC circuit breakers in the system due to their very high costs and on-state losses. Faults are also rare on DC cables and on the DC side of converters, so investment in solid-state HVDC circuit breakers at the extremities of all circuits cannot be justified.

2.6.   SUMMARY

The long cable distances required for offshore wind farms means that electrical losses become a major issue when considering the cost implications of a particular wind farm. At cable route lengths over 40km, the high voltage cable losses represented a high proportion of the overall full-load losses. In order to reduce the losses in the high voltage cable, the conductor area or the voltage rating was increased. Although these two options reduced the cost of losses in the cable, the capital costs would increase. A trade-off between the cost of losses and capital costs would have to be made. The 33kV array cable losses were influenced by the size of the turbines being used. The total array losses were lower than the high voltage cable losses.

Although the full-load losses of an offshore wind farm were found relatively easily, it is the annual losses that are of the most use when calculating the costs of energy. In order to calculate annual losses, the full-load losses were first split into current and voltage dependent losses. Although the voltage dependent losses stayed virtually constant from no-load to full-load, the current dependent losses varied with the square of the current as the wind speed varied. A method for determining the annual losses in an offshore wind farm transmission system was developed which used a loss-load factor.

The load factor and the loss-load factor were both dependent on the wind speed characteristics of the site. The wind speed characteristics were represented by the Weibull curve, which was defined by the annual mean wind speed and a shape parameter. Both these values had an effect on the load and loss-load factors.

As the value of the shape parameter, k increased, the value of p (the constant which determines the loss load factor from the load factor) decreased. As the annual mean wind speed of a site increased for a given shape parameter, the value of p increased. A guideline for the estimation of the annual losses is included in Appendix 2C.

The main proportion of losses in HVDC VSC systems were in the converter stations. High frequency (typically around 1kHz) PWM operation resulted in high switching losses. The accurate modelling of these switching losses in a HVDC VSC power system is complicated due to the small time-steps required. There have been a few techniques developed to estimate the switching losses which do not require such a small time-step, however the simulation time is still relatively large. The switching losses are dependent on a variety of factors such as collector current, gate resistance and stray inductances. The losses in the converter were dependent on the switching frequency, converter configuration and the IGBT rating. Over the 10 years that HVDC VSC has been in operation, the technology has significantly developed. The ongoing advances in HVDC VSC technology along with market growth and competition between manufacturers are likely to drive down both capital and operational costs. This will improve the prospect for offshore wind farms connected by HVDC VSC as the system would become more economically competitive with HVAC transmission systems.

The use of offshore grids and international connections could greatly increase the amount of offshore wind generation that could be connected. There would however need to be clear rules for sharing the cost of development and associated revenues between countries. The offshore grids would most likely be connected by HVDC VSC as they are more suited to long distance transmission and to multi-terminal network operation. The development of HVDC circuit breakers would present a significant advantage to the operation of offshore grids. Furthermore, the use of offshore grids in the North Sea and in regions such as Dogger Bank could reduce the cost of constrained energy significantly.

3. REVIEW OF SWITCHING TRANSIENTS

3.1. INTRODUCTION

An electrical transient is a short lived oscillation in a system caused by a sudden change in voltage, current or load, such as when a fault occurs or during a switching operation. The time spent in the transient condition is insignificant compared to that spent in steady state. However, it is during the transient periods that network components are subjected to the greatest stresses from excessive currents or voltages. In extreme cases equipment can be permanently damaged.

The main source of transient overvoltages in overhead transmission systems is lightning, whereas in cable systems transient overvoltages are mainly caused by circuit breaker operations [68]. When a switching operation occurs, there will be a sudden change in the currents flowing in the network. Any inductances that are present in the system will oppose this change in current by inducing a voltage, due to the theory of constant flux linkage. For a faster change in current, there will be a larger resulting voltage. The energy stored in the inductance will oscillate between the inductive and capacitive components of the system at the resonant frequencies of the system until the energy is dissipated by any resistance present. There are several possible ways in which a transient overvoltage can occur due to switching operations [68].

Switching operations can cause overvoltages in a broad spectrum of frequencies. Transformer insulation failure due to high frequency overvoltages can be produced by re-strikes and pre-strikes during the opening or closing of a circuit breaker [69]. This phenomenon is inherent to all circuit breakers, although the vacuum circuit breaker (VCB) is especially well known for it due to its high ability to cause and interrupt high frequency currents of several hundreds of kHz, as explained in section 3.2.1. The nature and occurrence of re-strikes and pre-strikes in a circuit breaker depends on the network it is connected to, and the response of each transformer to high frequency transient voltage will be different.

3.2.   THEORY

Some fundamental concepts which have relevance to switching transients in offshore wind farms are presented here.

3.2.1. MULTIPLE RE-STRIKES AND PRE-STRIKES

An example circuit to illustrate multiple re-strikes and pre-strikes in circuit breakers is shown in Fig. 3-1. This might represent the switching of an unloaded transformer which is connected by a cable to the circuit breaker. The inductance of the unloaded transformer is represented by L_2 and is several orders of magnitude larger than the source inductance L_1. The capacitance of the load, C, is determined by the length and type of cable. When the circuit breaker opens, the power factor is low and the voltage is near to its peak when the current is interrupted at current zero.
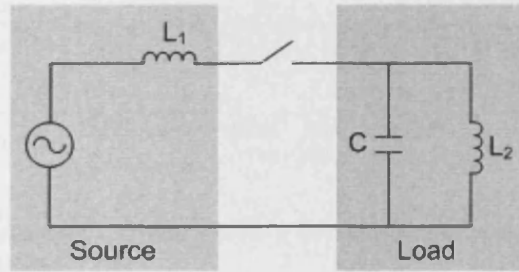
Fig. 3-1. Circuit to illustrate multiple restriking transients

The capacitance, C, then discharges through L_2 and oscillates about its final ground potential at a frequency:

$$f_1 = \frac{\omega_1}{2\pi} = \frac{1}{2\pi(L_2 C)^{1/2}}$$

(3-1)

The value of f_1 is usually in the range of hundreds of Hz to tens of kHz [68]. If the voltage across the opening contacts is higher than the voltage withstand capability of the contacts, a re-strike will occur, as shown in Fig. 3-2. The capacitance is then reconnected to the supply and will oscillate about the instantaneous supply voltage at a frequency:

$$f_2 = \frac{\omega_2}{2\pi} = \frac{1}{2\pi[L_1 L_2 C/(L_1 + L_2)]^{1/2}}$$

(3-2)

If this high frequency current, which is superimposed on the power frequency current, results in a zero current crossing, there is a possibility that the circuit breaker will clear the arc. In this case, C can be left charged to a high voltage and will again

discharge through L_1. As the contacts of the circuit breaker separate further, any further breakdowns will take place at a higher voltage, with the subsequent oscillation at frequency f_2 leading to a correspondingly higher peak.
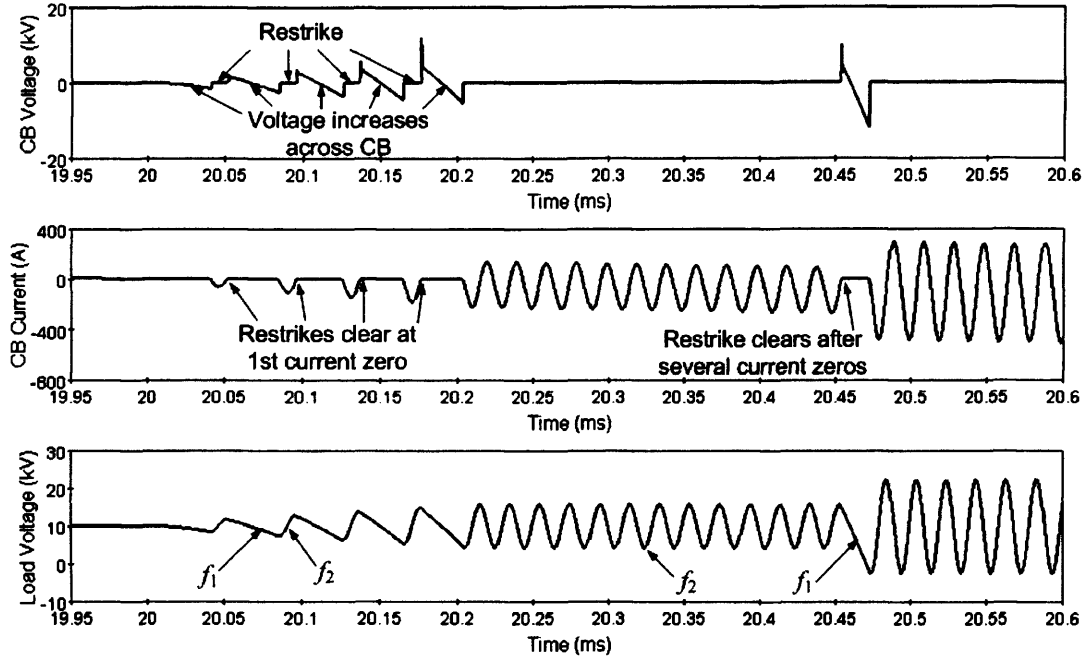
Fig. 3-2 Simulated Voltage and Current across a circuit breaker and the corresponding voltage across the load during restrikes

Multiple pre-strikes may occur during the closing of a circuit breaker, in a similar way to that described for multiple re-strikes. The main difference between the two is that during closing of the circuit breaker, the withstand voltage is decreasing so there should not be an escalation in voltage.

3.2.2. TRAVELING WAVES AND SURGE IMPEDANCE

The phenomenon of traveling waves in long transmission lines and cables has been known for many years. In order to study traveling waves, the parameters of the line or cable should not be considered as lumped parameters, but rather distributed uniformly throughout the length [70]. The representation of a long transmission line is given in Appendix 4B, where the characteristic impedance and the propagation constant are derived.

When dealing with high frequencies, losses are often neglected and the propagation velocity and characteristic impedance reduces to:

$$v = \sqrt{\frac{1}{LC}}$$

(3-3)

$$Z_0 = \sqrt{\frac{L}{C}} \qquad\qquad (3\text{-}4)$$

Where v is the propagation velocity in m/s, Z_0 is the surge impedance in ohms, L is the series inductance in henrys and C is the shunt capacitance in farads of the cable or transmission line. The propagation velocity is close to the speed of light (3×10^8 m/s) for overhead lines and between a half to two thirds this value for underground cables. The characteristic of a transient is mainly determined by the surge impedance of the transmission line or cable. It has a direct impact on the time derivative of the transient overvoltage: the lower the surge impedance, the higher the time derivative of the transient overvoltage. An example is shown in Fig. 3-3, which consists of a transmission line or cable with surge impedance, Z_0, connected to a transformer with stray capacitance, C.
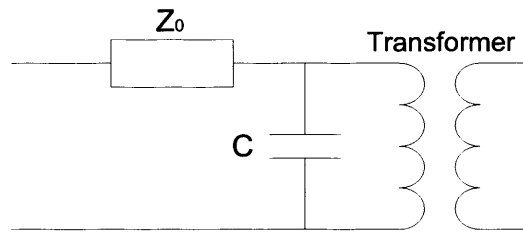
Fig. 3-3 A simple system consisting of a transmission line or cable connected to a transformer.

For high frequency transient analysis, the inductance of the transformer can be neglected since its value is large and results in a time constant several orders of magnitude slower than the time constant involving the stray capacitance. The time constant, τ, for the voltage across the transformer when subjected to a transient propagating along a cable or an overhead line depends on the surge impedance, Z_0, and the stray capacitance of the transformer, C:

$$\tau = Z_0 \cdot C \qquad\qquad (3\text{-}5)$$

Whilst the surge impedance of overhead lines is typically 300-400Ω, it is only around 40Ω for cables [68]. This means that the same transformer will experience transient overvoltages with time derivatives at least 10 times higher if it were connected to a cable instead of an overhead line.

3.2.3. REFLECTIONS AND REFRACTIONS

The proportionality between voltage and current is determined by the characteristic impedance of the line or cable. When a wave arrives at a point of discontinuity,

where the characteristic impedance changes, an adjustment must occur to keep this proportionality, taking the form of two new wave pairs. The reflected voltage wave and associated current wave travel back down the line superimposed on the incident wave whilst the refracted wave penetrates beyond the discontinuity.

The incident, reflected and refracted current waves will have the same shape as their respective voltage waves and the following amplitudes:

$$I_1 = \frac{V_1}{Z_a} \qquad\qquad (3\text{-}6)$$

$$I_2 = \frac{V_2}{Z_a} \qquad\qquad (3\text{-}7)$$

$$I_3 = \frac{V_3}{Z_b} \qquad\qquad (3\text{-}8)$$

Where I_1 and V_1 are the incident current and voltage waves, I_2 and V_2 are the reflected waves and I_3 and V_3 are the refracted waves. Z_a and Z_b are the characteristic impedances on the incident and refractive side respectively.

The expressions for the reflected and refracted voltage waves in terms of the incident wave are:

$$V_2 = \left[\frac{Z_b - Z_a}{Z_a + Z_b} \right] V_1 \qquad\qquad (3\text{-}9)$$

$$V_3 = \left[\frac{2Z_b}{Z_b + Z_a} \right] V_1 \qquad\qquad (3\text{-}10)$$

Where $\dfrac{Z_b - Z_a}{Z_a + Z_b}$ is the reflection coefficient and $\dfrac{2Z_b}{Z_b + Z_a}$ is the refraction coefficient.

3.3. REVIEW OF SWITCHING TRANSIENTS AND OVERVOLTAGES

Overvoltages can be classified into five groups according to the IEC 60071-1. These are Continuous Operating Voltage, Temporary Overvoltages, Slow Front (switching), Fast Front (lightning) and Very Fast Front. The classification of frequency ranges involved in the latter four groups is given in Table 3-1.

Table 3-1 Classification of Frequency Ranges [71]

Shape designation	Frequency range for representation	Representation mainly for
Low-frequency oscillations	0.1Hz – 3kHz	Temporary overvoltage
Slow front surge	50/60Hz – 20kHz	Switching overvoltages
Fast front surge	10kHz – 3MHz	Lightning overvoltage
Very fast front surge	100kHz – 50MHz	Restrike overvoltages, GIS

3.3.1. TEMPORARY OVERVOLTAGES

Temporary overvoltages can last for over a hundred cycles and have a slowly decaying amplitude. They can originate from transformer energisation, fault overvoltages, overvoltages due to load rejection and resonance. Temporary overvoltages could occur if the harmonic content of the transformer inrush current excites the power system resonant frequency (known as resonant overvoltages). This has been identified as an issue in systems with transformers and significant lengths of HV cables [72] and also in industrial distribution systems where power factor correction capacitors have been applied [73]. In all cases involving transformer inrush current, the power system has a relatively low resonant frequency. Resonant overvoltages can have magnitudes greater than 3.0 per unit [74].

3.3.2. SLOW FRONT TRANSIENTS

Slow front transients are mainly due to switching operations, including cable discharge, reactive compensation operation and transformer energisation. They could occur during energisation and disconnection in normal operation or during a fault. Ground faults also produce slow front transients.

3.3.3. VERY FAST TRANSIENTS

Transients in the frequency range of 100kHz to 50MHz are termed very fast transients. According to IEC 60071-1 the time to peak is less than 0.1us, with a total duration of less than 3ms. Very fast transients can occur in a number of situations, however they are not covered by standards at present. They have been extensively studied in Gas Insulated Switchgear (GIS) systems, where the geometry of the system supports the generation and propagation of very fast transients [75, 76]. In the case of dielectric breakdown across the contacts of a switch or to ground, the voltage collapse can occur in 3 to 5ns which can excite resonances within the GIS at frequencies up to 100MHz [77]. Studies have also been carried out on very fast

transients in distribution networks, particularly on their impact on transformer and motor insulation [78]. The majority of very fast transient studies in medium voltage networks have focused on issues in mining and other industrial systems, where the economic impact of failure is high [79].

VCBs are widely used in medium voltage networks because they have outstanding breaking properties along with low maintenance requirements [80, 81]. It has long been recognised that the combination of VCBs and cable networks in industrial systems can cause problems with very fast front transients if the system is not designed properly [82-85]. Multiple restrikes in VCBs generally have frequencies in the range of 10kHz to 1MHz [77].

The effect of four types of distribution cables on very fast transients was studied in [86]. It was shown that a cable with large high frequency loss does not generally decrease the amplitude of a surge appreciably but it does lengthen the rise time of the surge substantially by absorbing high frequency energy from the surge.

3.3.4. IMPACT OF SWITCHING TRANSIENTS ON TRANSFORMERS

Every transformer has particular internal natural frequencies which may be excited by a transient applied at its terminal, causing dielectric stresses [87, 88]. Two distinct types of excitation are described in [88]; a once-only surge and regularly repeated surge voltages. The once-only surge has a damped oscillatory response with a frequency which is mainly dependent on the configuration of the system. The second type of excitation could be generated by multiple restriking of a circuit breaker. In [89] it was suggested that the internal transformer insulation may be overstressed when certain wave shapes such as a fast front long tail switching surge and in particular oscillating overvoltages are applied at the terminals of the transformer, even if the voltage magnitude is below the surge arrester protective level.

There have been many transformer insulation failures attributed to switching transients, even though these transformers had passed all standard tests and complied to requirements [69, 90-92]. In [93], transformer failures due to primary circuit breaker switching transients were reviewed. The common contributing factors to potentially damaging switching transient voltages were inductive load switching, circuit breaker characteristics, short cable lengths between the circuit breaker and

transformer (200 feet or less) and dry type transformers (although oil filled were not immune).

Studies on a 11kV/230V distribution transformer that was connected to a cable on the high voltage side showed that the application of a step voltage to the cable results in a resonant overvoltage on the open low voltage side of the transformer [94]. It was shown that the highest overvoltages occur if the dominating frequency component of the cable voltage matches one of the dominating frequency components of the voltage transfer from the high to low voltage side of the transformer. For a particular transformer, the voltage ratio was particularly high at 50kHz, which would require a cable length of 800m to produce the highest overvoltage.

The subject of the performance of transformers in the presence of oscillatory transients is being addressed by an IEEE Transformer Committee Working Group on "Switching transients induced by Transformer/Breaker Interaction". This Working Group is producing an IEEE Guide which describes the conditions that may produce oscillatory switching transient voltages and discusses several mitigation methods [95]. A CIGRE Joint Working Group (JWG A2/A3/B3.21 "Electrical environment of transformers") studied the potential effects of fast transients and fast front surges on transformers. This Joint Working Group developed a methodology of risk identification and mitigation allowing individual case-by-case decisions to be made as to what risk factors may exist in a specific application [96]. The increasing number of transformer dielectric failures has motivated CIGRE to initiate a new Working Group (WG A2/C4.39 "Electrical transient interaction between transformers and the power system"), which started in 2008. The scope and aim of this working group includes a survey of utility experiences regarding transformer failures involving transients, a discussion on the possibility of pinpointing risk factors that may cause failures and the development of a methodology for transient system studies aimed at evaluating a range of frequencies appearing during switching.

3.4. IMPORTANCE OF SWITCHING TRANSIENTS IN OFFSHORE WIND FARMS

3.4.1. DIFFERENCE TO ONSHORE NETWORKS

The collection grid topology of large offshore wind farms varies significantly from other transmission and distribution networks. Due to economies of scale, the wind turbines are large – typically with ratings between 2 to 5MW – with a rotor diameter of around 100m. In order to reduce turbulence the turbines are separated by a distance of at least 5 rotor diameters. The turbines are connected via submarine cables to radial array feeders which are then connected to an offshore substation. The large area required for an offshore wind farm results in large cable systems with a high number of radial array feeders and step-up transformers, as shown in Fig. 3-4.
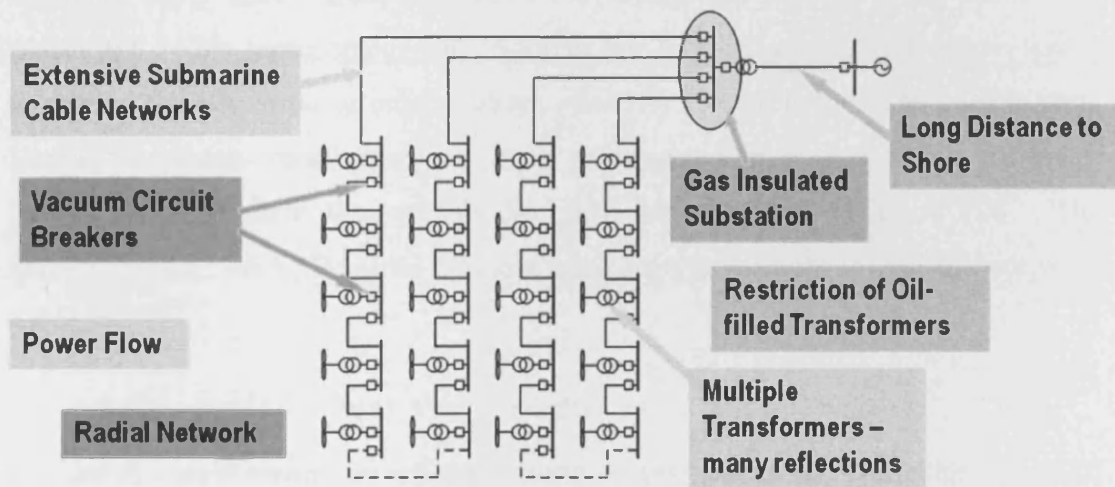
Fig. 3-4 Some features of an offshore wind farm transmission system.

The power collection and transmission systems of existing offshore wind farms are designed in a similar way to medium voltage underground cable systems for urban distribution [81]. There are however a number of differences between the two systems. One difference is the direction of power flow in the offshore grid, which flows from lower to higher voltage levels. The 'loads' in the offshore grid are almost exclusively rotating machines mostly with power electronics, with large variations in both active and reactive power. Another specific characteristic of offshore wind farms is the limited access for maintenance and repair due to adverse weather conditions at certain times of the year. In some respects, there are similarities between offshore transmission systems and industrial distribution systems, where there are large load fluctuations, rotating machines, high reliability and low maintenance requirements are required. There is a significant difference between

these two systems due to the size of the network, which will be very large for a wind farm because a separation of more than 500m is required between each adjacent wind turbine.

In addition to the primary equipment, there may also be reactive compensation equipment at one or both ends of the high voltage cable and harmonic compensation at the onshore end of the high voltage cable. The UK regulatory regime for offshore transmission at 132kV and above, which was implemented in July 2010, requires Settlement Metering Equipment to be located on the offshore installations [97]. The associated current and voltage measurement transformers may be required to be installed on each array. Offshore wind farms in the UK have to comply with the ENA P28 recommendation. ENA P28 was intended to protect customers close to industries using heavy loads and limits the voltage dip allowed when connecting loads [98]. This requirement can result in the installation of timer relays which switch out the MV wind turbine breakers when the voltage in the array goes to zero. The wind turbine transformers are then reconnected in groups which are small enough not to violate the voltage dip restriction imposed by ENA P28. The interpretation of ENA P28 costs offshore wind farm developers around £5k per wind turbine [99].

3.4.2. THE OFFSHORE ENVIRONMENT

The harsh environment at offshore wind farms results in particular types of equipment being specified. Particular care has to be taken with mineral-oil-filled transformers and all liquid filled transformers must have a bund to prevent leaks [100]. Offshore wind turbines built to date use either liquid or dry-type cast resin transformers. The majority of wind turbines at present have silicon oil transformers, as they are used by Siemens Wind Power which dominates the market. This situation could change if Vestas and other manufacturers who use dry-type transformers get back into the offshore market. High reliability of equipment is a major requirement for offshore wind farms, meaning that VCBs are often specified as they require little maintenance. Submarine cables generally have one or more longitudinal water barrier consisting of semi-conducting water swelling tapes, at least one anti-corrosion sheath and a steel armour to provide mechanical strength. The offshore substation employs gas insulated HV switchgear, as this is compact and provides environmental protection.

3.4.3. IMPACT ON OFFSHORE TRANSFORMERS

It is likely that the issues of potentially damaging transient overvoltages due to VCB and transformer interaction will arise in the design of offshore wind farms. Whilst Very Fast Front transients are usually associated with the switching of disconnectors in GIS, they could occur in offshore wind farms due to the reflections within the network. A fault in an offshore transformer would be more severe in terms of both repair costs and lost revenue than for an onshore transformer due to its location.

There are relatively few large offshore wind farms in operation at present; however there has been a high rate of failures of transformers. In one particular offshore wind farm all 80 of its' wind turbine nacelles were brought ashore to correct a number of issues, one of which being the replacement of the transformers, since within only a few months operation 20 – 30% of them had failed [101]. Eighty percent of the transformers at Middelgrunden offshore wind farm have also been replaced, with the first transformers breaking down shortly after production started in 2001. In [102] methods to optimize the cost spent on the replacement of defective transformers at Middelgrunden are described. The average value of the energy production loss was calculated to be 40,000 Euros per turbine, which is close to the total cost of installation for the replacement transformer, showing that the length of the exchange process is important. The overall cost of an optimized exchange of transformer (in 2007) was 115,000 Euros. In another offshore wind farm, a failure of the main offshore transformer led to a 4.5 month outage of the entire 166MW wind farm [103]. Although the various manufacturers and designers involved argued over the causes of these problems, such as adverse weather conditions, the root cause was the breakdown of insulation which eventually caused electrical short circuits. It is possible that high frequency, high voltage switching transients made a major contribution to the insulation failure. All the examples mentioned here relate to transformer failures which originate in the early years (2000 – 2003) of offshore wind farm development and therefore represent the early stages on the learning curve. This clearly illustrates to the offshore wind industry that care has to be taken when designing the MV systems for offshore wind farms.

3.4.4. OTHER ISSUES RELATED TO TRANSIENTS IN OFFSHORE WIND FARMS

With respect to the Continuous Operating Voltage, the remote ends of arrays may operate at a high voltage when the grid voltage is high and the wind power output is

high. The selection of the surge arrester Continuous Operating Voltage (COV) may be affected by this high operating voltage and also by harmonics which could increase the system peak voltage.

The energy capability of surge arresters is determined by IEC line discharge classes, which assumes that switching surges occur in a system with surge impedances of several hundred ohms (i.e. overhead transmission circuits). In offshore wind farms, where there is a low surge impedance due to the extensive cable networks, the energy capability of metal oxide surge arresters may be reduced if the currents are significantly higher than the values stated for typical line discharge currents.

Often the Lightning Impulse Withstand Voltage (LIWV, also known as BIL) and Switching Impulse Withstand Voltage (SIWV, also known as SIL or BSL) are already given for equipment, and verification of the standard insulation levels is required rather than the selection of them. This is usually the case for offshore wind farms, where the equipment may have been ordered well in advance. In this situation, an inverse approach to the insulation coordination procedure given by the IEC may be required. The usual insulation coordination process for wind farms is to select the insulation level of the transformers, select the surge arresters required to protect that insulation level, and then determine the amount of transient over voltage which can be withstood [104].

The zero-missing phenomenon is defined as the ac current not passing through zero for several power frequency cycles. If there is no current zero, it is not possible for the circuit breaker to interrupt the current without the risk of damage, except if the circuit breaker is designed to interrupt dc current. The zero-missing phenomenon has been identified as a potential issue when energizing a long HVAC cable which is connected to reactive compensation [105]. In an unloaded cable system, the shunt reactor current is almost in phase opposition to the current in the cable which reduces the amplitude of the ac component through the circuit breaker. The shunt reactor current will have a transient dc component. This may result in the current through the circuit breaker having a dc component which is larger than the ac component, resulting in the zero-missing phenomenon.

Circuit breakers may be required to switch capacitive currents due to the extensive cable networks, which can impact both their opening and closing capability. During opening, the capacitive current is small (up to several hundreds of Amps) compared

to the rated short-circuit current for which the circuit breaker is designed. This means that the capacitive current can be interrupted very shortly after the circuit breaker contacts have opened. The voltage lags the load by 90 degrees, so interruption of the power frequency current occurs when the system voltage is at its peak. This can produce multiple re-strikes in a similar manner to those described in section 3.2.1. During closing of the circuit breaker (energisation), large inrush currents can flow associated with the charging of the cable over the inductance of the system. This inrush current is limited by the surge impedance of the cable so is usually smaller than that associated with capacitor banks [70]. High overvoltages could occur if the cable is energized with trapped charge [77] (the cable was pre-charged as a result of a preceeding breaker operation); this could occur if there is no discharge path (i.e. the cable is not connected to the offshore transformer) or if the cable is re-closed after only a short interval.

3.5. REVIEW OF SWITCHING TRANSIENT STUDIES IN OFFSHORE WIND FARMS

3.5.1. TEMPORARY OVERVOLTAGES

Temporary overvoltages may arise when a large offshore wind farm with a long high voltage cable to shore goes into islanded operation due to the operation of the on-shore main circuit breaker [106, 107]. An overvoltage due to this was experienced by the Danish Transmission System Operator at Horns Rev A 160MW offshore wind farm in 2005. The wind farm is connected by 55km of undersea/ground 150kV cable to a 150kV substation. When the main circuit breaker at the substation disconnected the wind farm and cable from the grid, the measured voltage magnitude was so high that it exceeded the measuring equipment range. The voltage magnitude was estimated to be in the range of 2p.u. Immediately after the disconnection, and while the wind turbines were still operating, not only the voltage magnitude but also the operating frequency increased rapidly from the normal 50Hz. By the time the wind turbines were disconnected the frequency had reached 60Hz, the voltage magnitude then decayed and the frequency settled to the natural frequency of the network. It was found that the compensation reactor absorbed some reactive power from the isolated grid and helped to reduce the voltage increase rate. This situation at Horns Rev A was analyzed in [106] along with a planned large offshore wind farm in Denmark. It was shown that the active power supply from the wind turbines to the

isolated wind farm network must be interrupted as fast as possible because the active current magnitude is proportional to the voltage increase rate. In a further study, it was shown that converter-controlled wind turbines cannot be represented by a synchronous generator model when in isolated operation with long HVAC cables [108]. The temporary overvoltages initiated by the synchronous generator model were not as severe as those initiated by the converter-controlled wind turbines.

In [109] it was highlighted that the combination of a long HVAC cable and offshore transformer can result in a low system resonant frequency which could coincide with one of the harmonic components present in transformer inrush current. This may result in a sustained overvoltage and caused operational problems on a number of offshore installations during commissioning.

3.5.2. VERY FAST FRONT OVERVOLTAGES

Switching transients in a 160MW offshore wind farm were studied in PSCAD/EMTDC in [81]. It was shown that the electrical stress on transformers during transients depended on the wave propagation in the cable system and on their location in the system. In order to analyse this fast phenomenon a cable model which included both wave propagation and frequency dependence was used.

Two cases of energizing a wind farm are shown in [81], the first when a feeder is first to connect and the second when the feeder is the last to connect. The cables are energized with the transformer during no load and saturation is included in the transformer model. The rate of rise of voltage at the first transformer with no other feeders connected was around 2kV/μs whereas the rate of rise of voltage for the same transformer but when all other feeders were connected was around 25kV/μs. The rise time was increased by over two orders of magnitude when all feeders were connected.

A single line to ground fault (SLGF) was simulated in [81] along with the clearing of the fault by the feeder VCB. The SLGF was placed at the base of the first wind turbine (at the end of an 80m cable which connects to the transformer located in the nacelle) at one of the feeders. Although the fault caused a step voltage in the system with travelling waves similar to feeder energizing, an expanded timescale showed that the faulted phase was exposed to very high frequency reflecting voltage waves (625kHz) with very fast fronts. The reason for the high repetition frequency is the short distance (80m) between the fault and the transformer causing very short

travelling times for the propagating waves. The short cable also had negligible damping effects which cause the very fast front. When the fault was cleared by the feeder VCB, three reignitions occurred. The voltages at the transformers were similar to those during energisation except that the reignitions caused much higher voltages. During energisation, voltage steps reached 20kV and 40kV in the last transformer, whereas the voltage steps during disconnection caused voltage steps of 60kV and 100kV for the last transformer.

3.5.3. COMPARISONS WITH MEASUREMENTS

The correct modeling of offshore wind farm equipment is important for switching transient studies. The vacuum circuit breaker model must include both transient voltage withstand capability and its ability to interrupt high-frequency current. The accuracy of simulations of an offshore wind farm using Power Factory was compared with energisation measurements in [110], with the measurement system being described in more detail in [111]. It was shown that a distributed parameter cable model was essential. The Power Factory simulations were carried out with a 0.2μs integration step size and an output step size of 0.4μs, which corresponds to the 2.5MHz sampling time of the measurements. A travel speed for the wave propagation was calculated from the measurements to be $0.51 \cdot c$ (152.9m/μs), where c is the speed of light. Spikes with maximum amplitude of 0.5p.u occur in the measured current at the turbines which correspond to the arrival of the voltage wave. The wave propagation found in the simulations was about ¾ of the speed calculated from the measurements. A small capacitor (0.5nF) was required to represent the capacitance between the transformer HV terminal and ground in order for the current spikes to be simulated. The current spikes were shown to be very sensitive to this parameter.

Further simulations and comparisons with the measurements made at Nysted were made in both Power Factory and PSCAD/EMTDC in [112, 113]. The simulations in both programs had a similar magnitude to the measured steep fronted first wave, however could not accurately emulate the measured overvoltage caused by the voltage wave reflections. This difference is most likely due to insufficient details in the circuit breaker model, which did not include the interruption of high-frequency current. The cable models used in both programs also overestimated the damping in the system.

Simulations of a wind farm in PSCAD/EMTDC were compared to measurements made in the cable laboratory of ABB Corporate Research in [114-117]. The cable system laboratory was set up to be a scaled representation of a wind farm, with a total of 600m of submarine cable (24kV). The propagation speed of the surge was quicker in the simulations when compared to measurements. For frequencies up to a couple of kHz it was shown that an accurate transformer model required the frequency dependency of transformer resistances to be accounted. For higher frequencies the stray capacitances dominate the transformer response. The magnitudes and rise times of the critical surges were accurately simulated, however there was poor damping of the high frequency oscillations.

3.5.4. TECHNIQUES TO REDUCE SWITCHING TRANSIENTS

In [114-117], surges which exceeded the Basic Impulse Level (or Lightning Impulse Withstand Voltage) of dry-type transformers were recorded during both the simulations and measurements, even when surge arresters were used. A number of mitigation methods were tested in [116], with the combination of surge capacitor protection with surge arresters performing best.

Pre-insertion resistors can be used to reduce the overvoltage and frequency of transient recovery voltages. This technique requires two circuit breakers in parallel, one of which is in series with a resistor. The circuit breaker in series with the resistor is closed first (the inrush current is then limited by the resistor), then the second circuit breaker is closed after a few power frequency cycles. The transients in an offshore wind farm could be reduced significantly by using pre-insertion resistors [118].

Point-on-wave switching is a way to reduce transients by controlling each of the three poles in the circuit breaker individually, closing each pole with a certain time delay. Different time delays are used depending on whether the load is capacitive or inductive. In [118] it was shown that it is difficult to derive suitable synchronization parameters in cases where there is both capacitive (the HV cable) and inductive (the offshore transformer) loads.

4. MODELLING OF OFFSHORE WIND FARMS FOR SWITCHING TRANSIENT STUDIES

4.1. INTRODUCTION

The modelling of switching transients is important in order to identify the overvoltages which may occur at various points within the offshore wind farm. Models for circuit breakers, cables, transformers and wind turbines for switching transient studies are reviewed. The modelling approach used for each main component in the offshore wind farms studied in this thesis is presented. Some simple applications of the models are included to describe their behavior.

4.2. CIRCUIT BREAKERS

A circuit breaker can be considered as one fixed and one moving contact. The contacts are placed inside a container which holds the extinguishing medium, such as oil or SF6 or they could alternatively be inside a vacuum bottle. Under normal operation the contacts are closed and current flows through the circuit breaker without any significant losses.

When the circuit breaker is signalled to open, an external mechanism separates the contacts. As the contacts start to separate, current continues to flow as an electric arc between the contacts. This arc will continue until the energy being supplied to it is removed by external means. In an AC network, the current goes temporarily through zero twice every cycle. It is at these points (called current zero) that the circuit breaker has the opportunity to extinguish the arc as this is when the energy input briefly goes to zero.

4.2.1. CIRCUIT BREAKER MODELS

The simplest model of a circuit breaker has zero impedance when the circuit breaker is closed and infinite impedance when the circuit breaker is open and opens at the first current zero crossing after the tripping signal is given. This model is used to obtain the Transient Recovery Voltage (TRV) of a circuit breaker [151].

More elaborate models consider the arc as a time-varying resistance or conductance. However this requires arc parameters which are not always easy to obtain [119]. The most advanced model represents the circuit breaker as a dynamically varying

resistance or conductance, which is determined by the past values of voltage and currents in the arc itself [119].

4.2.2. REVIEW OF VCB MODELS

A single phase VCB model is described in [83], along with the factors which can influence the overvoltage generated when reignitions occur during opening. These factors include circuit parameters and switch characteristics such as rate of change of dielectric strength and interrupting capability, and random events such as the time between contact seperation and the power frequency current zero (called arcing time). The electrical strength of the contact gap was assumed to increase linearly with time. Analysis of these factors was carried out using this model and verified by measuring voltage and current across a number of VCBs in a test circuit.

A three-phase VCB model in PSCAD which incorporated the dielectric strength, arcing time, current quenching capability and the statistical nature of current chopping was developed in [80]. The dielectric strength of the VCB increased linearly with time and was calculated using a Gaussian distribution with a standard deviation of 15%.

The modeling and simulation of escalation in voltages and reignition behaviour in VCBs when used as generator circuit breakers is described in [120]. Nine representative medium voltage VCB models were analysed. An RC branch parallel to the VCB was included to represent the open contact gap stray capacitance. The VCB characteristics were modelled by linear equations for both the breakdown voltage strength and the high frequency derivative of the current clearing capability. It was shown that multiple re-strikes may produce an escalation in voltage for short arcing times (between $0 - 100\mu s$).

4.2.3. VCB MODEL USED IN THIS RESEARCH

Re-ignitions and pre-strikes were incorporated into the vacuum circuit breaker model using logic as shown in Fig. 4-1, for the opening and closing operations respectively. There were only two states that characterise the breaker; it was either open or closed. The state of the breaker was determined by the current flow through the circuit breaker, the voltage across the breaker and its previous state. The controls for a single phase of the VCB model are shown in Fig. 4-2.
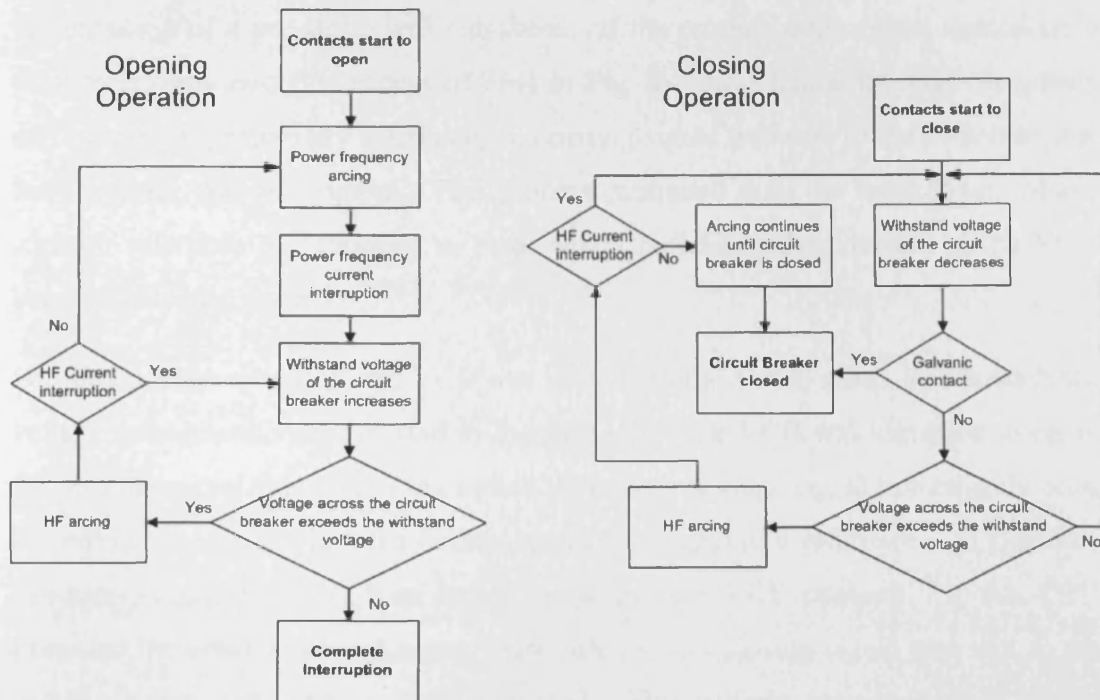
Fig. 4-1. Logic for VCB closing and opening operations.
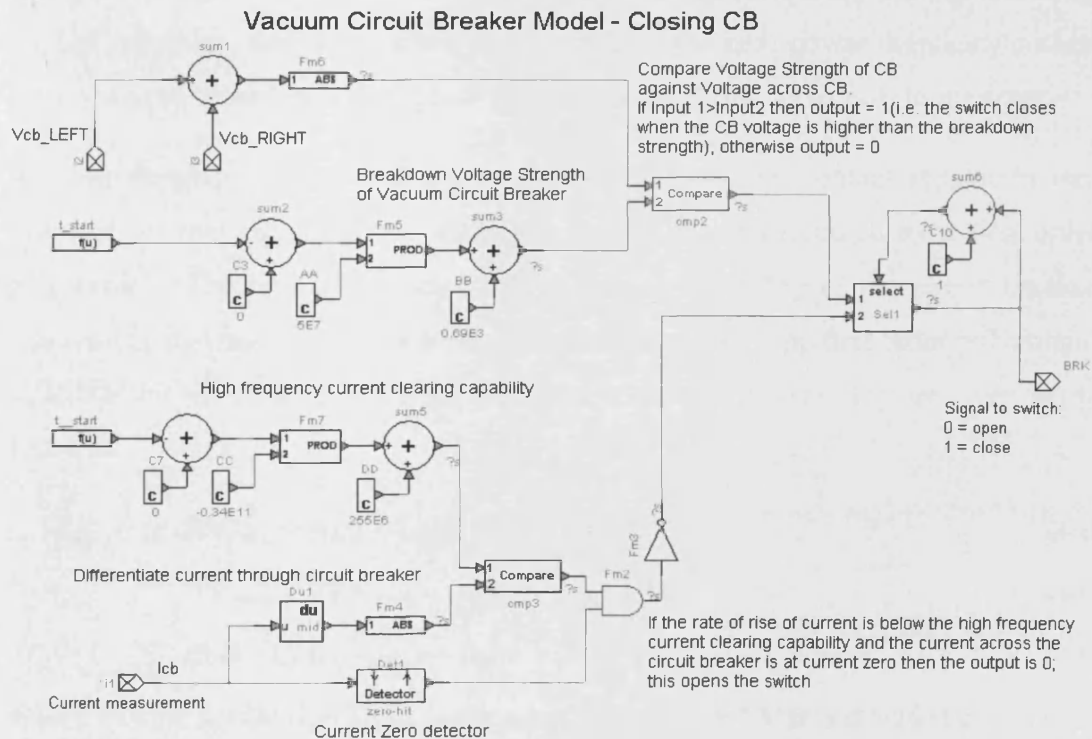
Fig. 4-2. Controls for a single phase of the VCB model

When the VCB model was signalled to close, the breakdown voltage strength reference started to decrease. When the voltage across the VCB exceeded this breakdown voltage strength reference, a closing signal was sent to the switch so that

77

the initiation of a pre-strike was simulated. If the current slope signal immediately prior to current zero (the output of Fm4 in Fig. 4-2) was below the high frequency current clearing capability reference, an opening signal was sent to the switch so that the pre-strike was interrupted. This process continued until the breakdown voltage strength reference had reduced to zero, which represents the contacts of the VCB being in galvanic contact.

For the opening operation, the VCB was initially in the closed state. The breakdown voltage strength reference started to increase when the VCB was signalled to open. An opening signal was sent to the switch if the current slope signal immediately prior to current zero was below the current quenching capability reference. A Transient Recovery Voltage (TRV) then builds up across the VCB contacts. If this TRV exceeded the breakdown voltage strength reference, a closing signal was sent to the switch so that a re-ignition was simulated. This process continued until it was terminated in one of three ways [120]: 1) the VCB successfully interrupts the current when the TRV after the last current clearing does not exceed the breakdown voltage strength reference; 2) the VCB fails to interrupt the high frequency current following the last reignition, and interruption is successful at the next power frequency current zero when the breakdown voltage strength is higher; 3) the VCB fails to interrupt.

A linear dependency between the breakdown voltage and contact separation was assumed, so that the dielectric withstand voltage was represented by a first order polynomial. The high frequency current clearing capability of the circuit breaker was represented using a first order polynomial [80, 120]. The first order polynomial equations for the dielectric strength and current quenching capability are given in (4-1 to 4-3).

$$BV_{open} = A_A(t - t_{open}) + B_B \qquad (4\text{-}1)$$

$$BV_{close} = TRV_{limit} - (A_A(t - t_{close}) + B_B) \qquad (4\text{-}2)$$

$$dI/dt = C_C(t - t_{open}) + D_D \qquad (4\text{-}3)$$

Where t is the actual time, t_{open} is the time at which the VCB contacts start to open, t_{close} is the time at which the VCB contacts are first in galvanic contact. BV_{open} and BV_{close} are the dielectric withstand voltage (V) during opening and closing respectively, dI/dt (A/μs) is the high frequency current clearing capability and TRV_{limit} is the maximum dielectric strength that the VCB can withstand. The parameters A_A, (V/s) and C_C (A/s²) represent the slope, and B_B (V) and D_D (A/s)

represent the intercepts. The values of A_A and B_B vary depending on the vacuum circuit breaker and values during opening have been observed to range between 1.5 to 50V/µs for A_A [83] and 0 to 1kV for B_B [80, 120]. During closing the contacts travel substantially faster, so the value of A_A is higher than its value during opening, with values of up to 100V/µs cited in [114, 121]. The value of C_C are between -34kA/µs^2 and 310kA/µs^2 [122], although in the majority of models [80, 82, 123-126] it has been set to equal 0. The value of D_D can range between 30 to 600A/µs. Appendix 4A includes a list of typical values for these constants.

Current chopping was not included in the model as it was assumed that the more serious overvoltages will be caused by multiple pre-strikes and re-strikes. The contacts of modern vacuum circuit breakers have also been developed so that the risk and level of current chopping is relatively low.

Although a low value of resistance could be used to represent the VCB during arcing, the resulting voltage across the VCB was considered to be too low (it is around 20V [127]) to have any significant impact on the study of transients in offshore wind farms, so was not included in the model developed for this research. This assumption had been found to be adequate in [83].

4.2.4. TESTING OF THE MODEL

A circuit which represents a medium voltage network was used to test the model of the VCB and is shown in Fig. 4-3. This test circuit was used by J. Helmer [128] and later in [80, 115, 122]. This enabled the characteristics of the VCB to be shown.
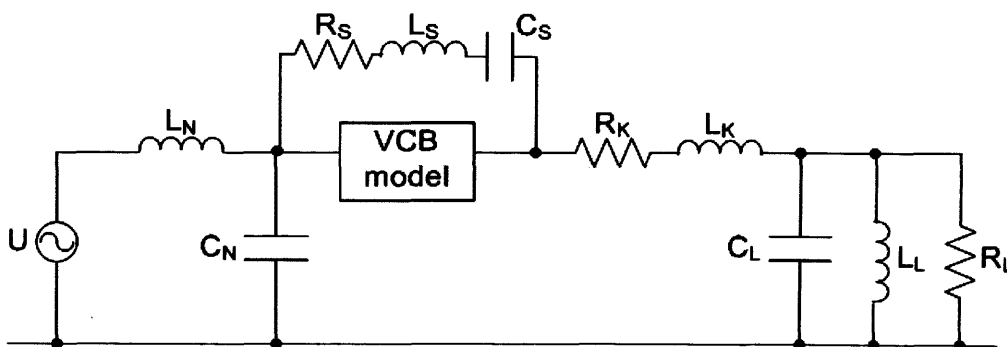
Fig. 4-3. Test circuit for the vacuum circuit breaker model [128].

The values used in the test circuit are given in Table 4-1.

Table 4-1. Values used in the test circuit

Source Voltage	U (kV)	33
Source Impedance	L_N (mH)	5
	C_N (μF)	0.1
Cable connecting VCB to load	R_K (Ω)	2
	L_K (μH)	40
Load, where C_L includes the capacitance of the cable as well as the load	R_L (kΩ)	10
	L_L (mH)	120
	C_L (nF)	10
Parasitic parameters of the VCB	C_S (pF)	200
	L_S (nH)	50
	R_S (Ω)	50
VCB paramters	A_A (V/μs)	20
	B_B (V)	0
	C_C (A/μs^2)	0
	D_D (A/μs)	100

VCB WITHSTAND VOLTAGE

The rate of rise or fall of the circuit breaker withstand voltage depends on the speed of the breaker contacts during opening or closing. The effect of A_A on the voltage developed across the VCB during opening is shown in Fig. 4-4. In this figure, the top graph shows the voltage across the VCB for A_A equal to 20V/μs whereas the bottom graph shows the voltage across the VCB for A_A equal to 50V/μs. All other parameters remain unchanged.
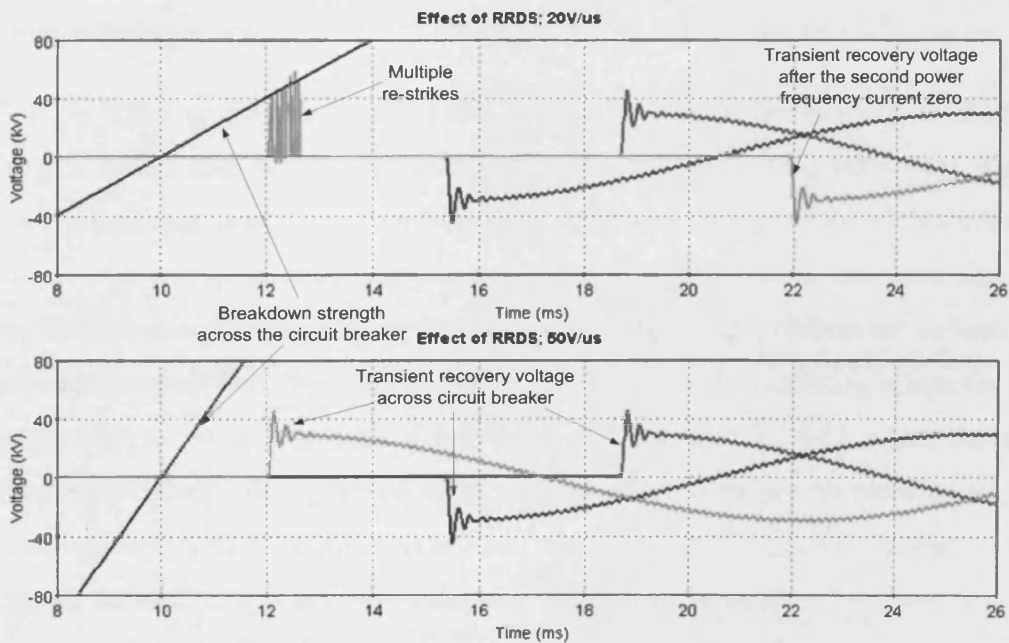
Fig. 4-4. The effect of A_A (the rate of rise of breakdown strength) on the voltage across the VCB during opening.

When A_A equalled 20V/μs multiple re-strikes occurred in phase c (the green curve in Fig. 4-4), the arc was not successfully interrupted until the second power frequency current zero. When A_A was equal to 50V/μs, all three phases were successfully interrupted at the first power frequency current zero. The probability that the circuit breaker extinguishes the arc at the first power frequency current zero increases with an increasing rate of rise of breakdown strength.

HIGH FREQUENCY CURRENT CLEARING CAPABILITY

The high frequency current clearing capability of the VCB was determined by D_D as the value of C_C was set to 0. This meant that the value of D_D represented the maximum rate of change of current which the VCB was able to clear. The value of D_D was increased from 100A/μs to 200A/μs whilst keeping all other parameters unchanged. As shown in Fig. 4-5, there were a greater number of re-ignitions when D_D was 200A/μs than when it was 100A/μs.

This is explained by observing the current waveforms in Fig. 4-5. When D_D is low (100A/μs in this case), the conduction period of the high frequency component is increased as it took longer for the high frequency current to reduce to a value of 100A/μs or lower. Since the high frequency current is superimposed on the power frequency current there will come a point (at 12ms in Fig. 4-5) when there are no more high frequency current zero crossings, so the arc will not be extinguished.

For D_D equal to 200A/μs, the circuit breaker is able to break the high frequency current earlier than for a value of D_D equal to 100A/μs. This allows the transient recovery voltage to occur earlier (when the withstand voltage of the circuit breaker is lower, as it increases over time during opening) so there is an increased chance of another re-ignition. The reignited arc is once again extinguished earlier so there is an increased chance that there is a high frequency current zero crossing where the arc is extinguished. It is not until much later (13.8ms in Fig. 4-5) when the power frequency current has increased to an amount where there are no more current zero crossings with a di/dt of 200A/μs or less. The arc then continues to conduct until the second current zero, when the withstand voltage of the breaker has increased to an amount where no re-ignitions are able to occur.
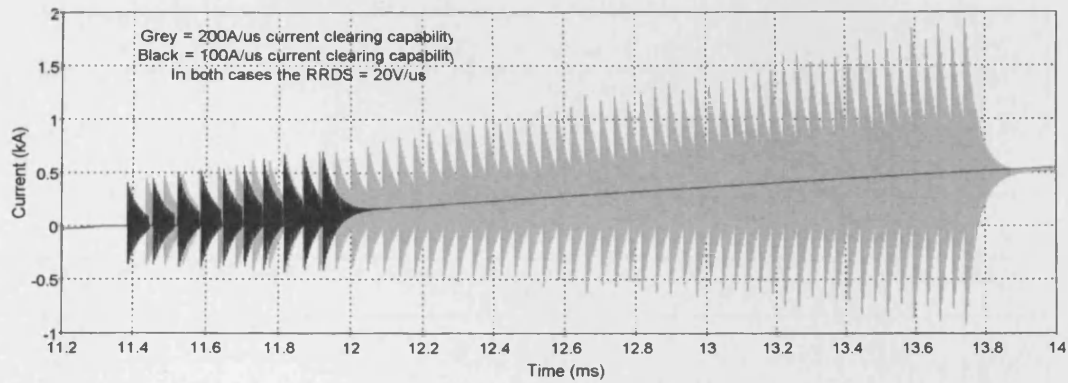
Fig. 4-5. The effect of D$_D$ (the high frequency current clearing capability) on the current across a VCB during opening.

ARCING TIME

The arcing time of a circuit breaker is defined as the time between the initiation of contact separation to the next power frequency current zero. A longer arcing time allows the VCB to develop a higher dielectric strength so is more likely to lead to a successful interruption of the arc.

The voltage and current across the circuit breaker are shown in Fig. 4-6 for two different arcing times of 0.65ms and 1.76ms (these arcing times are chosen for clarity in the figure). When the arcing time was 1.76ms, the circuit breaker had developed a higher withstand voltage before the first current zero and so the number of re-strikes was lower than when compared to a shorter arcing time of 0.65ms.

In both of these cases, the circuit breaker was unable to successfully clear the arc until the second power frequency current zero. If the RRDS of the circuit breaker is higher than the 20V/μs used in this example, there is a greater probability a longer arcing time will result in a successful clearing at the first power frequency current zero.
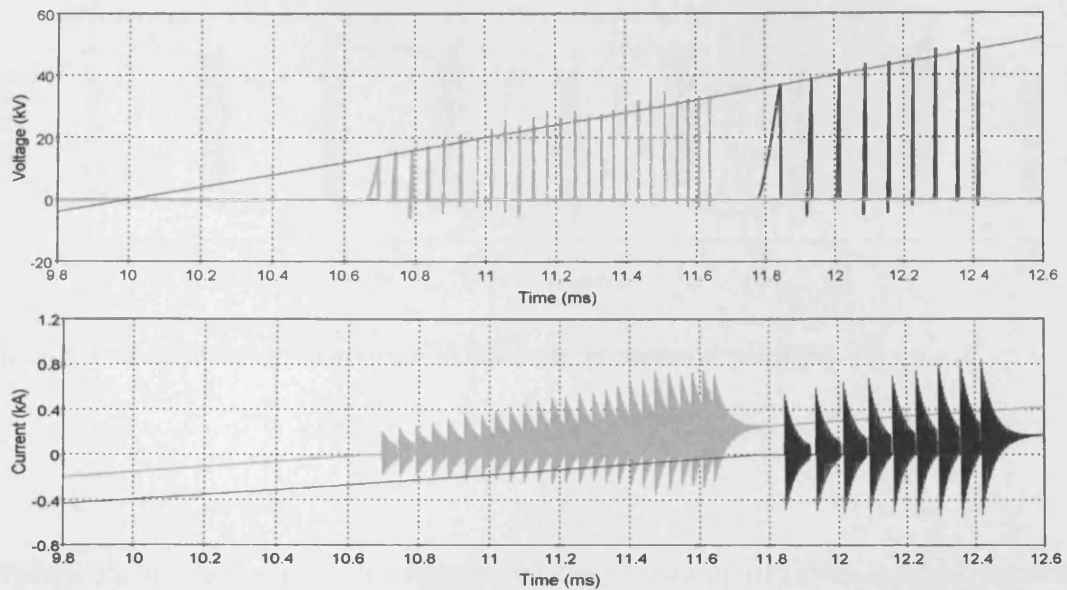
Fig. 4-6. The effect of arcing time, 0.65ms (grey) and 1.76ms (black) on the voltage and current across a VCB.

UNSUCCESSFUL CLEARING

When a circuit breaker reignites during opening, voltage escalation occurs and the interruption process terminates in one of three ways [68]. The first possibility is that the breaker successfully interrupts at the first power frequency current zero. The second possibility is that the breaker fails to interrupt the high frequency current and interruption is accomplished in one of the next power frequency current zeros. The third possibility is when the breaker fails to interrupt. This may cause damage to itself and to the equipment it is connected to.

The unsuccessful operation of a circuit breaker is shown in Fig. 4-7. Here the breakdown voltage of the breaker when it was fully open was set to 42kV. The breaker was unsuccessful at clearing the arc because the transient recovery voltage exceeded the withstand voltage. At every current zero there were multiple re-ignitions. This process will continue either until a different circuit breaker is operated, or until equipment failure occurs.
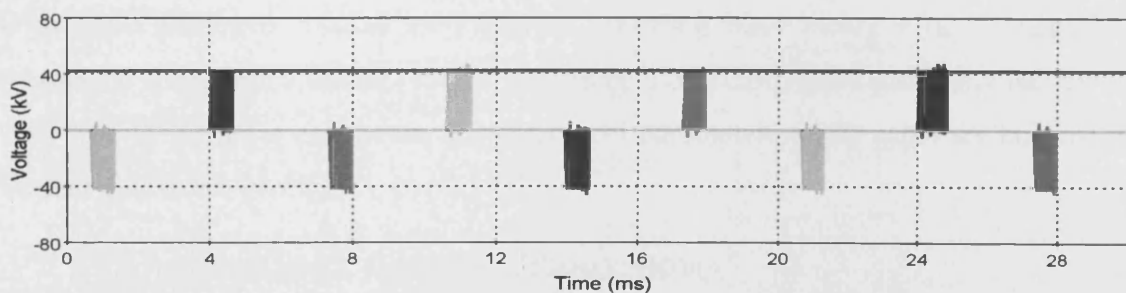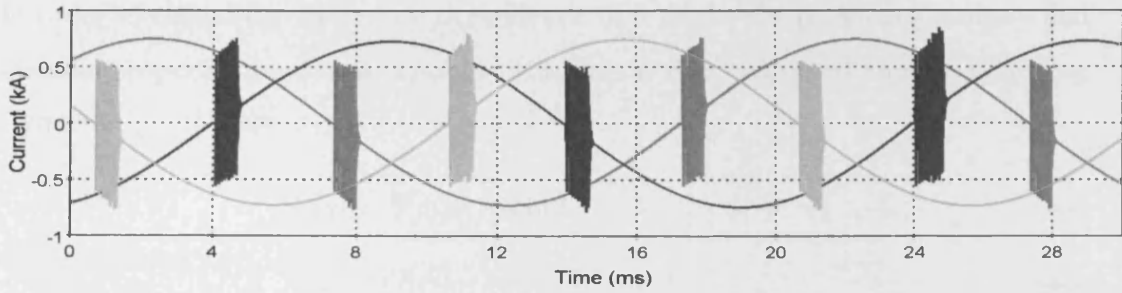
Fig. 4-7. Voltage and current across a VCB during unsuccessful operation.

4.3.   CABLES

There are a number of models available for the simulation of cables during transients in power systems.

4.3.1. LUMPED PARAMETER MODEL

High Voltage cables can be represented by an equivalent π network using lumped constants as shown in Fig. 4-8.   A model such as this is generally used for steady state calculations.   It is also sufficient for transient studies when the length of the cable is short, i.e. the travel time is less than the solution time-step [129].
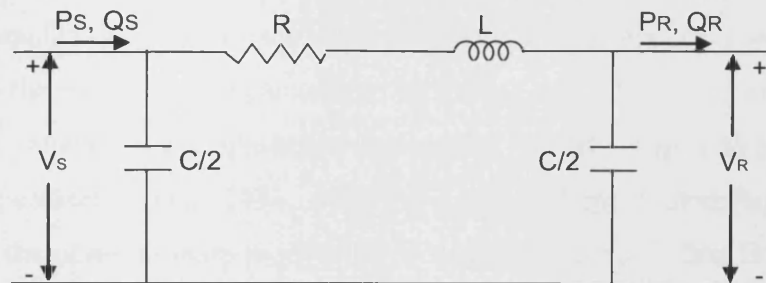
Fig. 4-8. Single phase equivalent π network of a High Voltage cable.

4.3.2. DISTRIBUTED PARAMETER MODEL

Distributed parameter models are based on travelling wave theory with a constant frequency.   Bergeron's model [130] is an example of a distributed parameter model. This type of model is used when only electrical parameters of the cable are known. Further details are given in Appendix 4B.

4.3.3. FREQUENCY DEPENDENT CABLE MODEL

In order to model the frequency dependence of a cable, the physical geometry and material properties have to be known. This data is then converted into the following form:

$$Z_s(\omega) = R(\omega) + j\omega L(\omega)$$ (4-4)

$$Y_s(\omega) = G(\omega) + j\omega C(\omega)$$ (4-5)

where R, L, G, and C are the series resistance, series inductance, shunt conductance and shunt capacitance per unit length of the cable system. These quantities are calculated as a function of frequency and are represented in n by n matrices where n is the number of parallel conductors in the system.

The series impedance matrix, $\mathbf{Z_s}$ and the shunt admittance matrix, $\mathbf{Y_s}$ described above are calculated in the frequency domain. They are used to calculate the propagation and characteristic admittance matrices ($\mathbf{H}$ and $\mathbf{Y_c}$ respectively):

$$\mathbf{H} = e^{\left(-\sqrt{\mathbf{Y_s Z_s}} \, l\right)}$$ (4-6)

$$\mathbf{Y_c} = \sqrt{\mathbf{Y_s Z_s^{-1}}}$$ (4-7)

where l is the length of the transmission line. The technique of using the $\mathbf{H}$ and $\mathbf{Y_c}$ matrices to simulate a transmission line is called the method of characteristics. Models within the method of characteristics technique are either based on a constant transformation matrix with frequency-dependent modal propagation constants (frequency dependent model) [131, 132], or a phase-domain modeling approach [133-135]. In the phase domain model, the propagation matrix is first fitted into the modal domain and the resulting poles and time delays are determined. High efficiency is achieved by grouping modes with similar time delays and by columnwise realisation of the propagation and characteristic admittance matrices[134]. The phase-domain model has been shown to increase the efficiency of the time domain solution and also eliminates stability problems which are occasionally encountered in modal domain models [136] and forms the basis of the Wideband cable model in EMTP-RV which was used in this thesis.

4.3.4. COMPARISON OF CABLE MODELS

The unit step voltage response of a cable using three different models is shown in Fig. 4-9.

Comparison of the Unit Step Voltage response of a 16PI, CP and WB model for a 5km Cable
— 16PI@vn [EMTP1] — Constant_Parameter@vn [EMTP1] — Wideband@vn [EMTP1]
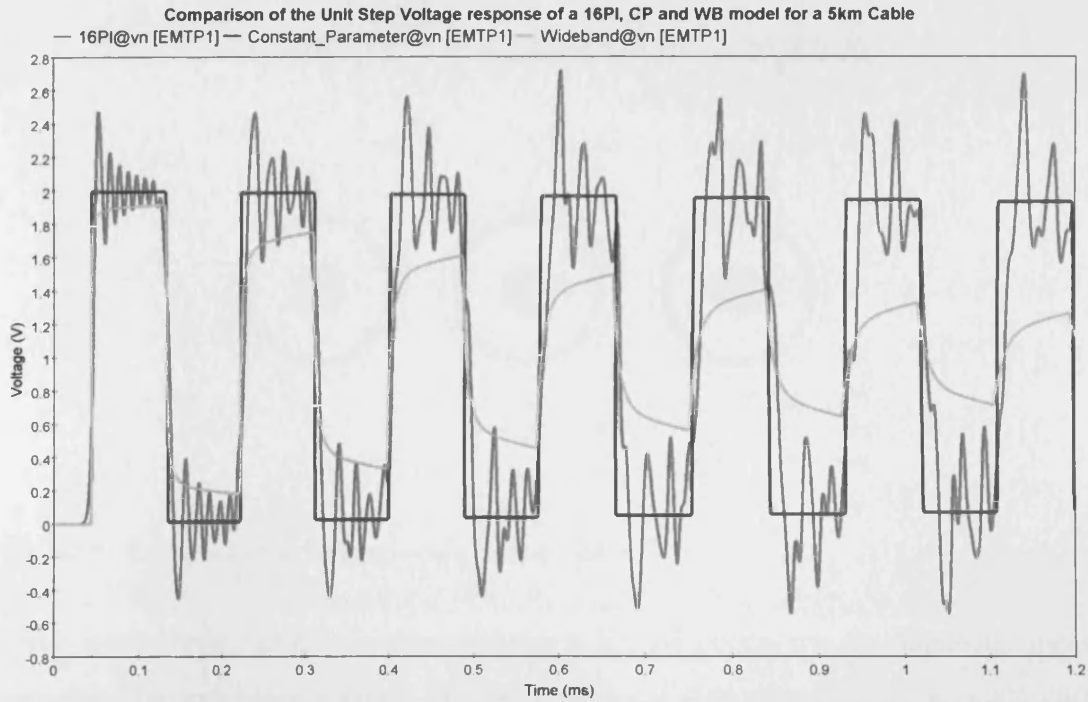
Fig. 4-9. Comparison of the Unit step voltage response of a 16PI (red line), Distributed (Constant) Parameter (blue line) and Frequency Dependent (Wideband) model (green line) for a 5km cable.

Even when a relatively short cable of 5km was modeled as 16 PI networks in series it did not produce an accurate response, as shown in Fig. 4-9. The distributed parameter model produced square voltage waves. The frequency dependent model takes into account that the speed of travel (or propagation) of a signal is determined by its frequency. High frequency components propagate faster than low frequency components. This effect is noticeable in the rounding of square pulses and the reduction in the amplitude of impulses, as seen in the green curve of Fig. 4-9.

4.3.5. SINGLE CORE COAXIAL CABLES

An example layout for single-core coaxial cables is shown in Fig. 4-10. The values for soil resistivity (ρ_g) and relative permeability (μ_g) must be specified. The soil resistivity ranges from about 1Ωm (wet soil) to about 10kΩm (rock), whilst the resistivity of sea water ranges from 0.1 to 1Ωm [137].
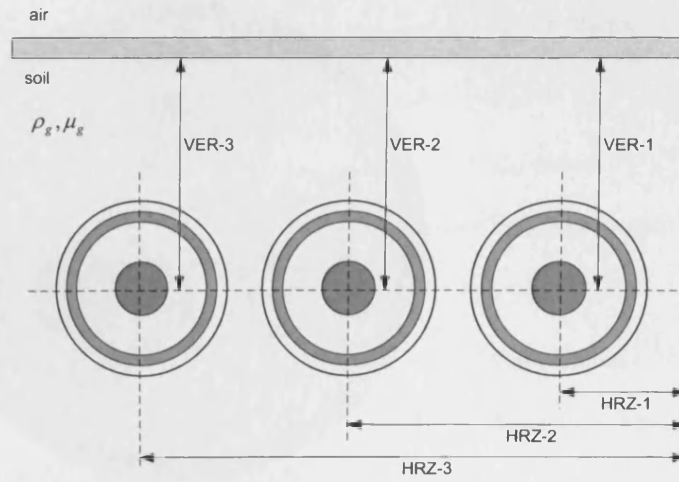
Fig. 4-10. Example layout for single-core coaxial cables.

Each single-core cable is represented by a set of concentric homogenous pipes separated by insulating layers. Fig. 4-11 shows a representation for a single core cable without armour.
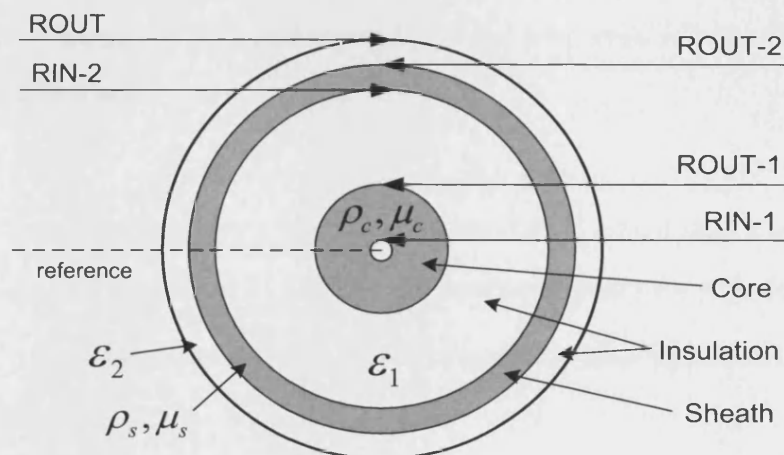
Fig. 4-11. A single-core cable with 2 conductors.

4.3.6. PIPE-TYPE CABLES

The general structure of a pipe-type cable is shown in Fig. 4-12. The individual single phase cables are enclosed inside the pipe. The geometry of the pipe is specified in a similar manner to the single-core cable.
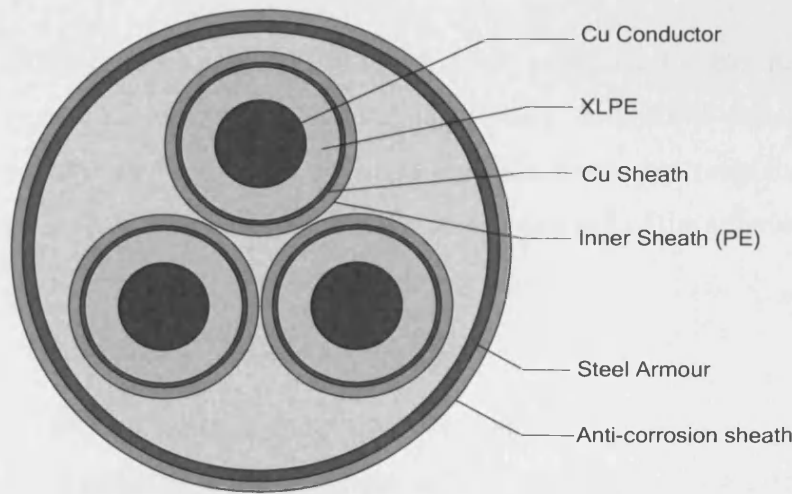
Fig. 4-12. An example pipe-type cable

4.3.7. CONVERTING CABLE DATA FOR INPUT INTO EMTP-RV.

In practice the cable design is different from the simple configurations assumed in Fig. 4-11 and Fig. 4-12. In particular, the core may be of a stranded design, there are inner- and outer- semiconducting screens and the sheath may be composed of a wire screen. It was not possible to specify these configurations directly into EMTP-RV, however, conversions to the geometry and material properties were performed so that they were represented.

CORE

The core was represented by a homogenous conductor which was specified by the resistivity ρ_c and the radius r_1. If the core conductor was of a stranded design, the resistivity ρ_c' of the core material was increased to take into account the space between the strands [137]:

$$\rho_c = \rho_c' \frac{\pi \cdot r_1^2}{A_c} \tag{4-8}$$

where A_c is the nominal cross sectional area of the core. The following table gives values for resistivity ρ_c' of annealed copper and hard drawn aluminium at 20°C [138, 139]:

Table 4-2 Resistivity of annealed copper and hard drawn aluminium

Material	Resistivity ρ_c' (Ωm)
Copper	1.7241E-8
Aluminium	2.8264E-8

88

If the DC resistance, R_{DC}, of the core was specified by the manufacturer, the resistivity was alternatively calculated using (4-9). In [140] it was shown that either (4-8) or (4-9) can be used to calculate the core conductor resistance, as the small difference between the two does not affect the accuracy of the simulation results.

$$\rho_c = R_{DC} \frac{\pi \cdot r_1^2}{l} \tag{4-9}$$

INSULATION AND SEMICONDUCTING SCREENS

The main insulation of high voltage cables is always sandwiched between two semiconductive layers. The electric properties of these semiconductive screens affect the propagation characteristics of a cable. Their relative permittivity is of the order of 1000 due to their high carbon content. This causes the capacitance of the screens to be much higher than that of the insulation. Since the resistivity of the semiconducting screens is much higher than the core and sheath (it is required by IEC 60840 to be below $1000\Omega m$ and $500\Omega m$ for the inner and outer semiconductive layers respectively), the screens do not contribute to the longitudinal current conduction.

It was not possible to specify the semiconductive layers directly in EMTP-RV (and other EMTP type programs). According to [137, 141], the semiconducting layers was taken into account by replacing the semiconductors with the main insulating material and increasing the permittivity of the total insulation so that the electric capacitance between the core and sheath remained the same.

The conversion of the permittivity was done as follows [137]:

$$\varepsilon_r = \varepsilon_{r\,ins} \frac{\ln(r_2 / r_1)}{\ln(b / a)} \tag{4-10}$$

where r_1 and r_2 are the core radius and the sheath inner radius respectively, a and b are the inner and outer insulation radii respectively, and $\varepsilon_{r\,ins}$ is the permittivity of the insulating material (for XLPE, $\varepsilon_{r\,ins}$ = 2.3). This neglects the possible attenuation caused by semiconducting screens which impacts the results for very high frequency transient simulations.

If the cable capacitance C is stated by the manufacturer, the relative permittivity can be calculated as [141]:

$$\varepsilon_r = \frac{C \ln(r_2 / r_1)}{2\pi\varepsilon_0} \tag{4-11}$$

where ε_0 = 8.854E-12.

INNER SHEATH

In some cases, the inner sheath conductor of the cable consisted of a wire screen. It was not possible to specify a wire screen in EMTP-RV, so the wire screen was replaced with a tubular conductor. The tubular conductor had a cross sectional area equal to the total wire area A_s. With an inner sheath radius of r_2, the outer radius r_3 then becomes [137]:

$$r_3 = \sqrt{\frac{A_s}{\pi} + r_2{}^2} \tag{4-12}$$

There was an option to ground the inner sheath in EMTP-RV. When this option is selected, the sheath is assumed to be at ground potential along the length of the cable and it is eliminated from the Z and Y matrices. Since sheath conductors are usually grounded at both ends of the cable, this option was applied since the induced transient sheath voltages along the cable will generally be negligible compared to voltages on core conductors. However, in situations such as lightning or a ground fault when the ground potential can rise, or in cross-bonded cable systems, the sheath was included.

ARMOUR

Submarine cables normally have a magnetic steel armour which provides additional mechanical strength. The permeability of the armour depends on whether wires or tapes are used. If wires are used, then the wire diameter and laying angle of the round, square or flat wires being used will influence the permeability.

This armour is generally very thick, which prevents high frequency flux penetrating it and so a voltage drop does not occur along it. Many submarine cables also have a wet-type construction which means the conductive sea water can penetrate the armour. Therefore, the armour was assumed to be at ground potential in the simulation, which had the advantage of a shorter simulation time.

PIPE-TYPE CABLES

Three-phase cables essentially consist of three single-core cables which are contained within a common shell. For most submarine cables, this common shell consists of a metallic armour and a protective layer (polypropylene and bitumen for example). This type of cable was directly modelled using the pipe-type representation in EMTP-RV.

Generally, the space between the single-core cables and the enclosing pipe is filled with a composition of insulating materials (and a fibre optic cable), but in EMTP-RV it was only possible to specify a homogenous material. However, the representation of this medium is not very important [137]. This is because the sheath conductors are normally grounded at both ends, so the potential along the sheath is low compared to that of the core conductor. As a result, simulated transients on phase conductors are insensitive to the properties of the insulator external to the sheath.

4.3.8. EFFECT OF CHANGING CABLE INPUT PARAMETERS

Generally, input parameters for cable systems are more difficult to obtain than for overhead lines due to the small geometrical distances involved. The cable parameters are also highly sensitive to errors in the specified geometry. As shown earlier, it is not straightforward to represent certain features of the cable such as wire screens, semiconductive screens and armours. There may also be uncertainties in the geometrical data since cable standards [142, 143] only put limitations on the minimum thickness of each cable layer in relation to the nominal thickness. This means that the insulation and semiconducting screens may be thicker than stated in the manufacturer's data sheets. The insulation and semi-conducting screens were shown to be thicker than stated in manufacturers data sheets in [140, 141]. In [141] the measured thickness of the inner semi-conducting screen, insulation and outer semi-conducting screen were each 0.7mm thicker than that specified by the manufacturer. This had the effect of decreasing the propagation velocity by 10% and increasing the characteristic impedance by 10%, when compared to simulations which neglected the semi-conducting screens.

In this section, a step voltage was applied at the sending end of a single-core test cable, and the voltage caused at the receiving end was measured. All sheaths were treated as being continuously grounded. The effects of the sheath design,

91

semiconductor layers and armour are investigated in [137], which is the basis for the following simulations which were carried out in EMTP-RV.

SHEATH DESIGN

Fig. 4-13 shows the step response of a 5km cable with the following cable sheaths; 1, 2, and 3mm Pb, and 0.2mm Cu.
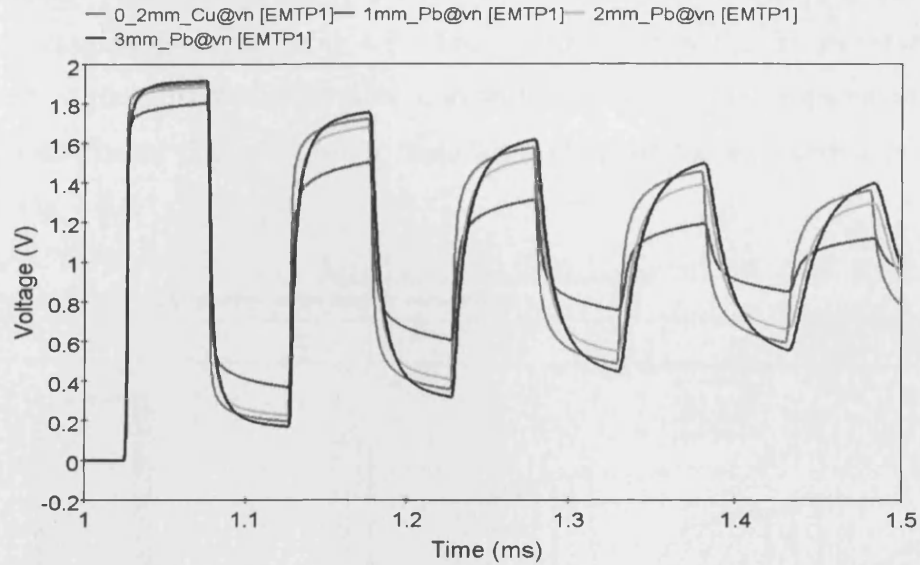
Fig. 4-13. The effect of sheath design on overvoltage at the receiving end of a single-core cable after a step voltage (1V) is applied at the sending end.

A reduction in thickness of the lead sheath from 3mm to 2mm had a negligible effect on the attenuation. However, when the lead sheath thickness was reduced from 2mm to 1mm, the attenuation of the cable increased significantly. This is explained by considering (4-13):

$$\delta = \sqrt{\frac{2}{\omega\mu\sigma}} \tag{4-13}$$

where δ is the penetration depth, which is the depth at which the strength of the electromagnetic field has decreased to $1/e$, or about 37% of the surface density. As the frequency increases, the penetration depth decreases. When the penetration depth δ is smaller than the thickness of the sheath, the magnetic flux external to the sheath is small. This shielding effect increases with decreasing resistance of the sheath.

The dominant frequency component of the 5km cable was about 10kHz. At this frequency, the penetration depth in lead was found to be 2.4mm, so an increase of sheath thickness beyond this value will not cause a significant change in response.

92

Due to the lower resistivity of the copper sheath, the penetration depth at this frequency was reduced to 0.66mm, so it did not need to be as thick as the lead sheath to provide a similar response.

SEMICONDUCTOR THICKNESS

Fig. 4-14 shows the step response of a cable with the following semiconductor thicknesses; 0, 1, 2, and 3mm. The relative permittivity and the propagation speed for each case are given in Table 4-3. The responses show that an increase in the thickness of the semiconductor layer lead to a decrease in the propagation speed. The semiconductor thickness had no significant effect on the attenuation, as can be seen in Fig. 4-14.
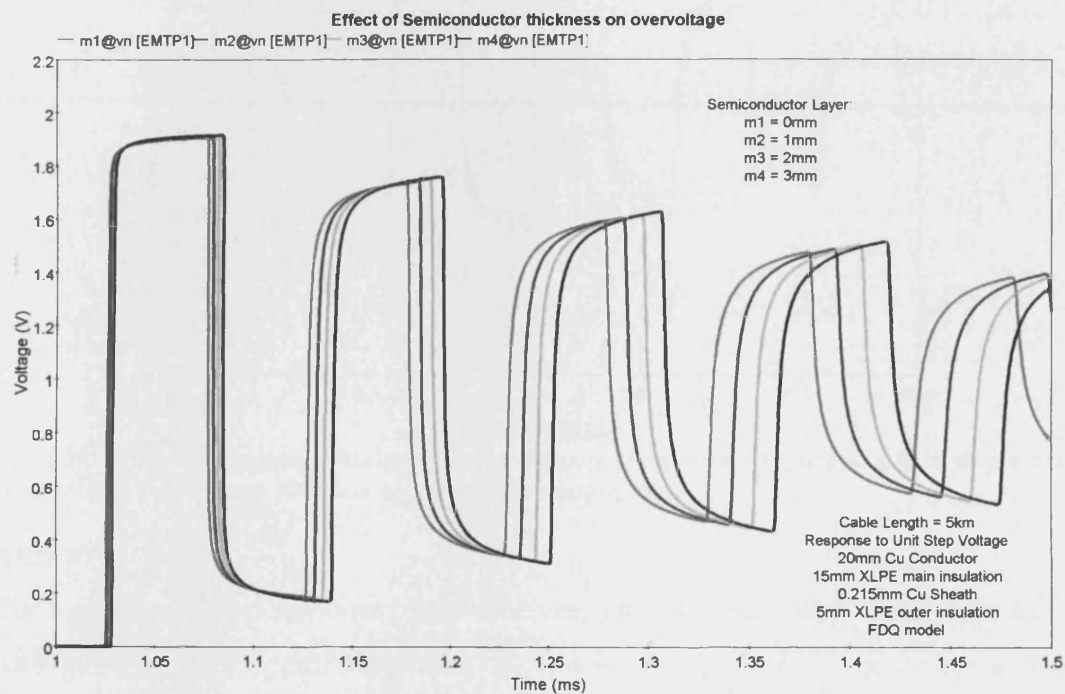
Fig. 4-14. Effect of semiconductor thickness on overvoltage at the receiving end of a 5km single-core cable after a step voltage (1V) is applied at the sending end.

Table 4-3. Values of corrected relative permittivity and propagation speed for cables with different semiconductor thicknesses

Semiconductor thickness (mm)	Corrected Relative permittivity (ε_r)	Propagation speed (m/µs)
0	2.3	198.0
1	2.462	191.6
2	2.625	185.5
3	2.789	179.9

INSULATION THICKNESS

Cable standards specify the minimum thickness of each cable layer in relation to the nominal thickness. In many cases, the actual thickness of these layers exceeds the values specified. Fig. 4-15 shows the open circuit step response of the receiving end of a 5km cable with different insulation thicknesses. It can be seen that an increase in insulation thickness caused a reduction in the attenuation, whilst the propagation speed was unaffected.
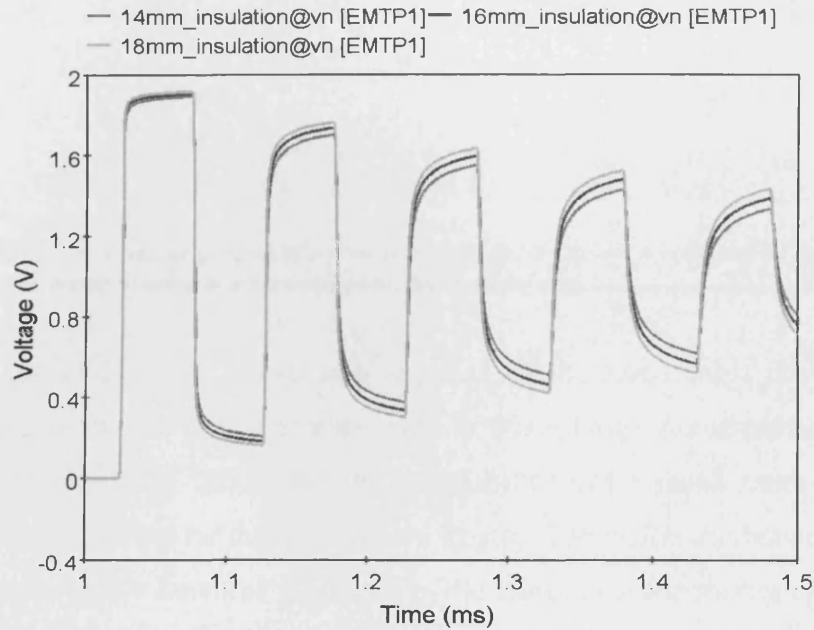
Fig. 4-15. Effect of insulation thickness on overvoltage at the recieving end of a 5km single-core cable after a step voltage (1V) was applied at the sending end.

ARMOUR

The open circuit step response of the receiving end of a 5km long single core cable with an armour of 5mm steel wires is shown in Fig. 4-16. The response was simulated for an armour permeability, μ_r, of 0, 10 and 100. The three waveforms for the different permeability values were very similar, with only a slight increase in the attenuation for higher values of permeability.
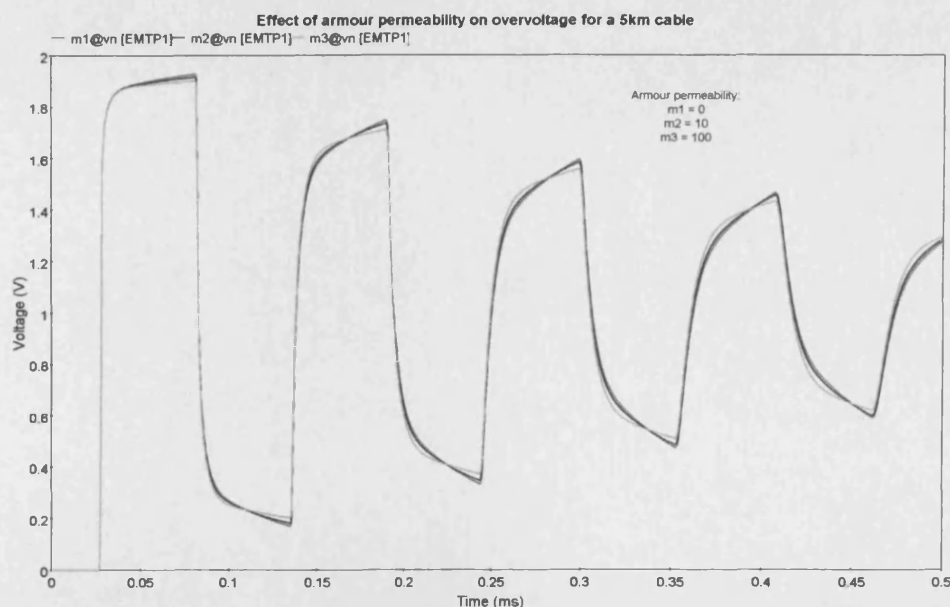
Fig. 4-16. Effect of armour permeability on overvoltage at the receiving end of a 5km single-core cable after a step voltage (1V) is applied at the sending end.

Fig. 4-17 shows the open circuit step response of the same cable design as that shown in Fig. 4-16, except that here the cable is 50km long. A comparison between Fig. 4-17 and Fig. 4-16 shows that the permeability had a much more significant effect on the attenuation for the longer cable length. The difference between the two figures was due to the increased frequency of the transient at the shorter cable length. The increased frequency means that the magnetic field is not able to appreciably penetrate the sheath conductor. This indicates that the correct representation of the armour is important for switching transients involving the long high voltage cables connecting offshore wind farms to shore. The armour permeability is less likely to have a significant effect on the transients experienced in the shorter array cables.
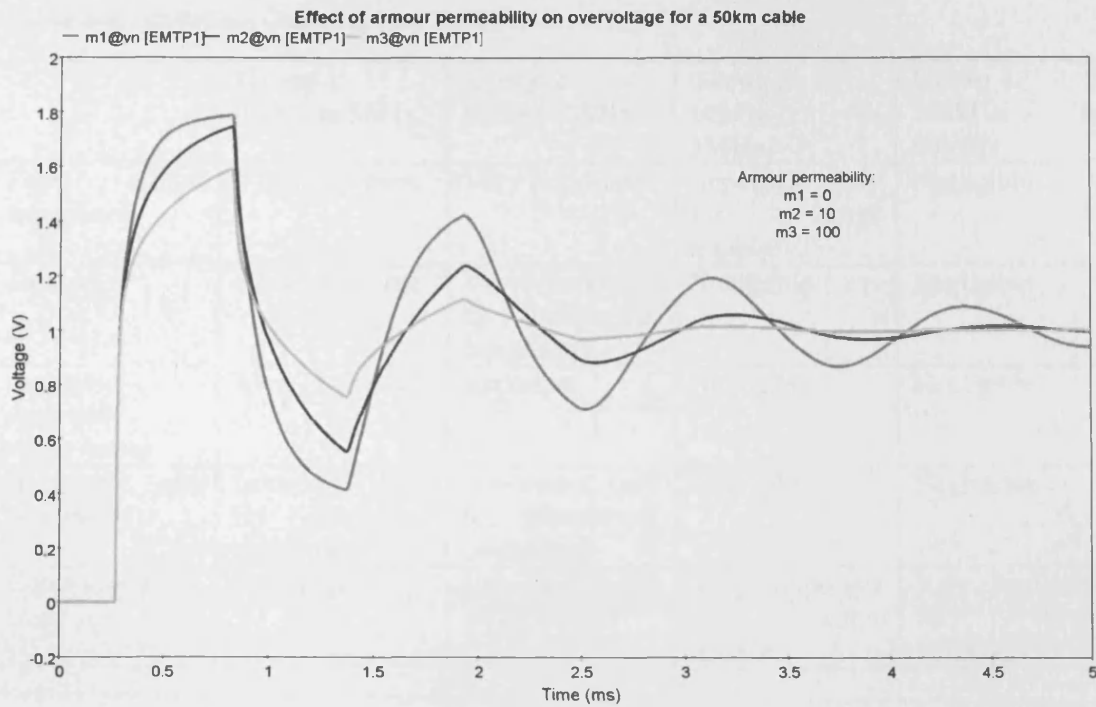
Fig. 4-17. Effect of armour permeability on overvoltage at the receiving end of a 50km single-core cable after a step voltage (1V) is applied at the sending end.

4.4. TRANSFORMERS

A complete model for a transformer would require every turn to be represented and all mutual couplings with every other turn to be included. In practice however, such a model would be impractical – it would be very difficult to obtain such data and the inclusion of such a model for each transformer within the system would require a very significant run-time for the simulation.

Simplified models of transformers are usually sufficient, with the model chosen depending on the purpose of the simulation [77]. Table 4-4, which is taken from CIGRE modelling guidelines [71] shows the importance of modelling various transformer parameters for the four main frequency ranges.

Table 4-4. Modelling Guidelines for Transformers [71]

	Group 1 0.1Hz to 3kHz	Group 2 60Hz to 3kHz	Group 3 10kHz to 3MHz	Group 4 100kHz to 50MHz
Short circuit impedance	Very Important	Very Important	Important only for surge transfer	Negligible
Saturation	Very Important	Very important for transformer energising	Negligible	Negligible
Frequency-dependent series losses	Very Important	Important	Negligible	Negligible
Hysteresis and iron losses	Important only for resonance phenomena	Important only for transformer energising	Negligible	Negligible
Capacitance coupling	Negligible	Important for surge transfer	Very Important for surge transfer	Very Important for surge transfer

4.4.1. TRANSFORMER MODELLING FOR LOW FREQUENCY TRANSIENTS

Models used to represent transformers in system studies are usually reduced order models where the main focus is the transformer's terminal behaviour [144]. For frequencies up to 3kHz, core nonlinearities are important and need to be implemented in the transformer model [145].

In EMTP-RV the three-phase transformer model consists of three identical single phase units as shown in Fig. 4-18, with the value of the initial flux values set independently for each single phase unit.
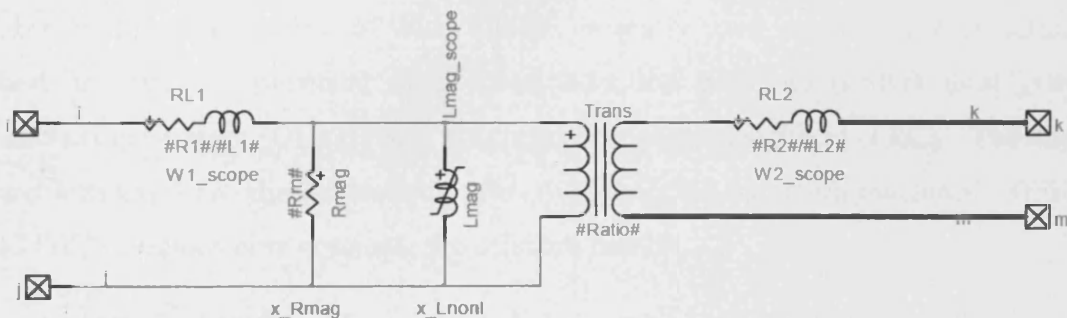
Fig. 4-18. The basic building block used in EMTP-RV for a single phase unit of a transformer.

4.4.2. TRANSFORMER MODELLING FOR HIGH FREQUENCY TRANSIENTS

The capacitance of transformers can usually be ignored at low frequencies. However, at high frequencies the inter-turn capacitance together with the inter-winding and winding to ground capacitances becomes significant as they determine

the voltage distribution across the internal windings when a transformer is subjected to an impulse.

4.4.3. MODELS USED IN THIS THESIS

The three phase transformer models available in EMTP-RV were used in this report. The saturation characteristics and the hysteresis and iron losses were included in this model.

The transformer capacitance was assumed to be distributed uniformly over the length of a winding so was represented by a total capacitance referred to a transformer terminal in a model [68], as shown in Fig. 4-19. This was considered acceptable for the studies made in this thesis as the internal voltage distribution in the transformer was not relevant for the results. Typical values for this capacitance are given in [68].
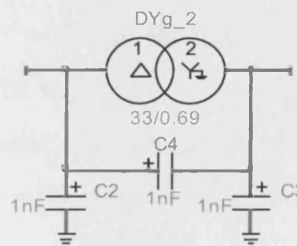
Fig. 4-19. Model of transformer with capacitances between primary winding to ground, secondary winding to ground and primary to secondary windings included.

4.5. WIND TURBINES

There are three main types of wind turbine presently used in offshore wind farms. These are directly connected fixed speed induction machines (FSIG), doubly-fed induction generators (DFIGs) and fully rated converter machines (FRC). The first wind turbines located offshore were directly connected induction machines. DFIG and FRC machines now dominate the offshore market.

For the DFIG and FRC machines, a detailed simulation would require each switching device within the converter to be modelled.

4.5.1. THE DEVELOPMENT OF SUITABLE STANDARD MODELS

There is a need for wind turbine models that are standard, publicly available and not specific to any particular design. The IEEE, IEC, the North American Electric Reliability Corporation, the Western Electricity Coordinating Council and the Utility

Wind Integration Group, have all initiated working groups to develop and validate suitable models.

The majority of the models being developed by these groups are for power flow and stability (positive-sequence) studies so that high levels of wind power generation can be simulated. These models are not likely to be suitable for switching transient studies which involve a shorter time-scale.

4.5.2. REVIEW OF WIND TURBINE MODELS FOR SWITCHING TRANSIENT STUDIES

ISLANDED OPERATION

The disconnection of an offshore wind farm can cause high temporary overvoltages and was discussed in more detail in Section 3.2.1. There is limited information on the control of WTs during temporary overvoltages due to islanding, except that the WT should "immediately" trip when its terminal voltage exceeds 1.20pu [108]. In the event described in [106], the tripping occurred about 50ms after the moment the offshore wind farm was disconnected from the grid. Models for converter-controlled wind turbines during islanded operation were discussed in [108]. The converter-controlled wind turbines were modelled as a lumped, three phase current source with independent control of the active and reactive current components. The converter switching dynamics and any injection of higher-order harmonics were not included. It was shown that converter-controlled wind turbines (both DFIG and FRC) cannot be represented by a synchronous generator model when in isolated operation as the overvoltages caused by the synchronous generator model were not as severe as when the wind turbines were represented by a controlled current source.

FAULT CURRENT CONTRIBUTION

For simulations involving faults (such as TRV studies), the model used for the wind turbine should represent its fault current contribution. The fault current contribution from a wind turbine will depend on whether it is a FSIG, a DFIG or a FRC machine. Standards which provide short circuit calculation guidelines do not presently specifically refer to wind turbine generators. The calculation of a wind farm's short circuit current contribution is not only important for the rating of switchgear but also for the coordination of network protection.

According to IEC 60909 [146], induction generators for the purpose of short-circuit calculations can be represented as a 1pu voltage source in series with the direct axis sub-transient inductance. In [147], an equivalent circuit is used to represent a 50MW wind farm consisting of FSIG for short circuit calculations.

The DFIG requires a provision to protect the generator-side converter during short circuits, as large currents will flow in the rotor circuit and through the generator-side converter during system faults. The response of a DFIG can be divided into two phases [148]. During the first phase, which lasts approximately 2 to 3 cycles, it can be considered to operate as an FSIG. In the second phase, the current on the rotor-side of the converter is limited by a control function or crowbar protection and is typically under 3pu.

The short circuit current of FRC machines is determined by the converter and does not significantly exceed the nominal rated current of the converter. After a fault in the system is detected by the fully rated generator, the grid-side converter rapidly limits the output to its nominal value. The FRC can therefore be approximated as a constant current source [148]. It should be noted that due to the fact that FRCs are only capable of supplying short circuit current which is three times the nominal rated current or less, traditional over-current protection may not be effective. Alternate means for detecting the fault will then be required.

4.5.3. EQUIVALENT WIND FARM MODELS

For large scale system studies, there is a further requirement for modeling wind farms as an equivalent model. The development of an equivalent model for each array in a wind farm would also be useful for switching transient studies as it would decrease simulation time.

In [149, 150] a technique for representing a DFIG wind farm as an equivalent unit in power system studies is described. The wind farm collector system was represented by an equivalent wind turbine generator, an equivalent wind turbine transformer and equivalent array cable system. The main wind farm transformers and reactive compensation were modelled separately.

In [106] a 160MW wind farm was represented by a single machine equivalent at the rated terminal voltage of the wind turbines. This was then connected through a 36/0.7kV transformer. The medium voltage (36kV) array cables were represented by

a capacitor which had a reactive power rating of 4MVAr, corresponding to the reactive power generation of the array cables. The wind farm was then connected to the offshore 150/36kV transformer and the 150kV cable to shore.

4.5.4. MODELS USED IN THIS RESEARCH

For the studies in this thesis, all three wind turbine generator types were represented by a voltage source behind a reactance. The value of reactance was calculated based on the fault level contribution of the wind turbine. These fault levels were 6pu, 3pu and 1pu for the FSIG, DFIG and FRC respectively, based on a base (rated output) of 3MVA (the calculations for the DFIG is given in Appendix 4C).

More detailed models using a controlled current source were not used, as it was not clear how the control system responds shortly (the first few milliseconds) after a fault or after going into islanded operation. Changes to grid code requirements, such as High Voltage Ride Through may mean that the way in which wind turbines are controlled during a fault or after going into islanded operation will be altered in the future.

4.6. SUMMARY

Suitable models for switching transient studies in offshore wind farms have been identified, taking into account that equipment data and specifications may contain limited information concerning high frequency characteristics.

A model for a vacuum circuit breaker which includes the withstand voltage and the ability of the circuit breaker to clear high frequency currents was developed in EMTP-RV. The model was then integrated into a test system so that the effect of withstand voltage, high frequency current clearing capability and arcing time could be investigated.

For transient studies, the way in which the various components of a cable are represented can have a significant effect on the simulation results. Since electromagnetic transient programs only allow homogenous tubes to be specified, it was necessary to convert the manufacturer's data into a different format. However, manufacturers are only required to specify the minimum thickness of the various layers in the cable, so the data may not provide the correct representation of the cable being modelled.

For switching transient studies in the offshore wind farm system, the terminal behaviour of transformers is required. The transformer models included the magnetizing characteristic, which is important for energization studies and the winding capacitance which is important for surge transfer.

For switching transient studies involving the medium voltage arrays, the voltage magnitude and waveshape seen at each wind turbine transformer is different. This means that the wind turbines in the particular array being studied cannot be grouped together into an equivalent model. A simple 'voltage source behind an impedance' model was chosen to represent the three main types of wind turbines, with the impedance chosen depending on the fault current contribution of the wind turbine.

5. COMPARISON OF SIMULATIONS WITH SWITCHING TRANSIENT MEASUREMENTS AT NYSTED OFFSHORE WIND FARM

With the expected increase in size and cost of offshore wind farms, the accurate prediction of transient overvoltages becomes more important. Validation of the modelling of offshore wind farm equipment is essential for switching transient studies. A measurement campaign had been conducted at Nysted Offshore Wind Farm, where three GPS synchronized measuring systems were installed and used for simultaneous measurement at three locations within the wind farm [111]. Transient simulations in EMTP-RV were compared with these measurement results (which were provided by DONG Energy) in order to validate the models used in switching transient studies.

The work described in this chapter has involved collaboration with DONG Energy and DTU, Denmark. DONG Energy kindly allowed the use of their measurement results at Nysted offshore wind farm. Simulations of Nysted offshore wind farm (by DONG Energy and DTU) had previously been compared with these measurements in [110-113]. Simulations were carried out in PowerFactory in [110-113] and in PSCAD in [112, 113]. These simulations showed that a distributed parameter cable model was essential, however the wave propagation calculated from the measurements was ¾ of the speed in the simulations. An ideal circuit breaker model was used. The simulation results in [110-113] did not accurately emulate the measured overvoltage caused by the voltage wave reflections.

The results in [110-113] highlighted that further work was required on the circuit breaker and cable models. The work carried out in this Chapter focused on validating the Vacuum Circuit Breaker model which represents pre-strikes (developed in Chapter 4) for the closing operation and on assessing the influence of input parameters for the cable model on the propagation characteristics.

5.1. NYSTED OFFSHORE WIND FARM

Nysted offshore wind farm was installed in 2003 and is operated by DONG Energy. It consists of 72 wind turbines with a rated power of 2.3 MW each. Four radial arrays connect to each 33kV winding of the main 132/33/33kV offshore transformer.

Each of the eight arrays has nine wind turbines, as shown in Fig. 5-1. The wind turbines were manufactured by former Bonus, now Siemens Wind Power.

Switching transient measurements had been carried out at Nysted offshore wind farm as part of a project titled "Voltage conditions and transient phenomena in medium voltage grids of modern wind farms", which was funded by Energienet.dk. This project was a collaboration between DELTA, DONG Energy, Vattenfall and Riso National Laboratory [111].

Measurements of both voltage and current were made at three locations within Nysted offshore wind farm, and were located at the positions shown in Fig. 5-1. The line-to-ground voltages were measured with capacitive voltage dividers connected to a data logger through a high bandwidth amplifier developed by DELTA. The bandwidth (3dB) of the voltage measurements was 1Hz to 10MHz. The line currents were measured with flexible current clamps with a bandwidth (3 dB) of 0.55Hz to 3MHz. Switching transient measurements were recorded with a sampling frequency of 2.5MHz for up to 5 minutes since the GPS synchronisation had to be coordinated with the manual switching of the circuit breakers by phone. The configuration of Nysted and the measurements made are described in more detail in [111, 112, 151].
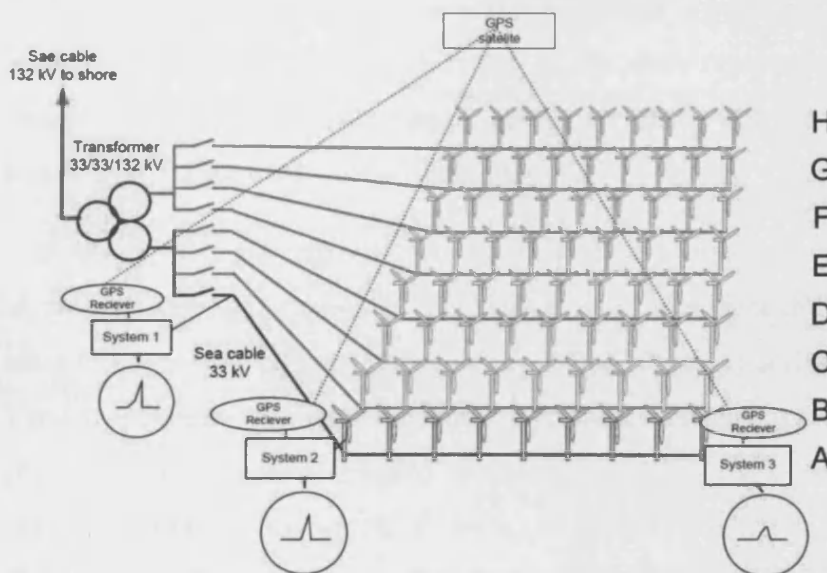
Fig. 5-1. The position of measurement equipment located at the platform, turbine A1 and turbine A9. Reproduced from [113].

5.2.   THE SIMULATION OF NYSTED OFFSHORE WIND FARM

In this study, the medium voltage (33 kV) array cables were represented by frequency dependent phase domain models [134]. The geometry of these cables was taken from the manufacturer's data sheets (provided by DONG Energy). Conversions of the geometry and material properties were carried out following IEEE guidelines [152] in order to model the cables. This was necessary as EMTP-RV only provided options to model solid conductors, and did not provide an option to include semi-conducting screens. All high voltage (132 kV) cables in this study were modelled as PI equivalents using data provided by the manufacturer. This was due to the fact that the transients of interest were in the medium voltage network.

The capacitances between primary winding to ground, secondary winding to ground and primary to secondary windings were included for both the main 132/33/33kV transformer and the wind turbine transformers. These values were based on manufacturers' information provided by DONG Energy. The saturation characteristics of the transformer core were included, however this was estimated since no information was available.

The switching took place with no generation, so the WTs were excluded from the model. The nine wind turbine transformers of the array being energized were included in the simulations. The other arrays were represented by their total cable length only, which were frequency dependent phase domain models. These other arrays were terminated with a 1MΩ resistor.

The simulation time step was set to 0.4μs in the simulations so that it was the same as the measurement time-step. The data used to represent the models was based on manufacturer's data sheets (provided by DONG Energy) and the state of the system. The exceptions to this were the cable relative permittivity and the values of the VCB parameters. The cable relative permittivity was initially corrected to match the measured propagation speed, v, using $\varepsilon_r = (c/v)^2$, where c is the speed of light (300km/ms). Previous work [112] had corrected this value following the guidelines in [137], however this had produced a simulated propagation speed which was too fast. The VCB parameters were estimated based on the measurements and values cited in literature. The surge arresters and CT/VTs were not included in the simulations.

5.3.   VALIDATION OF THE OFFSHORE WIND FARM MODEL

5.3.1. VACUUM CIRCUIT BREAKER MODEL

Although direct measurements of voltage and current in the VCB were not made, it was possible to determine the timing and number of pre-strikes for each phase from the current and voltage measured at the platform, as shown in Fig. 5-2. This then enabled the validation of the VCB model.

The measured current at the platform was the same as the current flowing through the VCB, so was compared with the simulated current through the VCB. The pole span (the time between the first pre-strike of one phase and the first pre-strike in another phase) was found from both the measured current and voltage at the platform and was 110μs between phase a and b and 450μs between phase b and c.
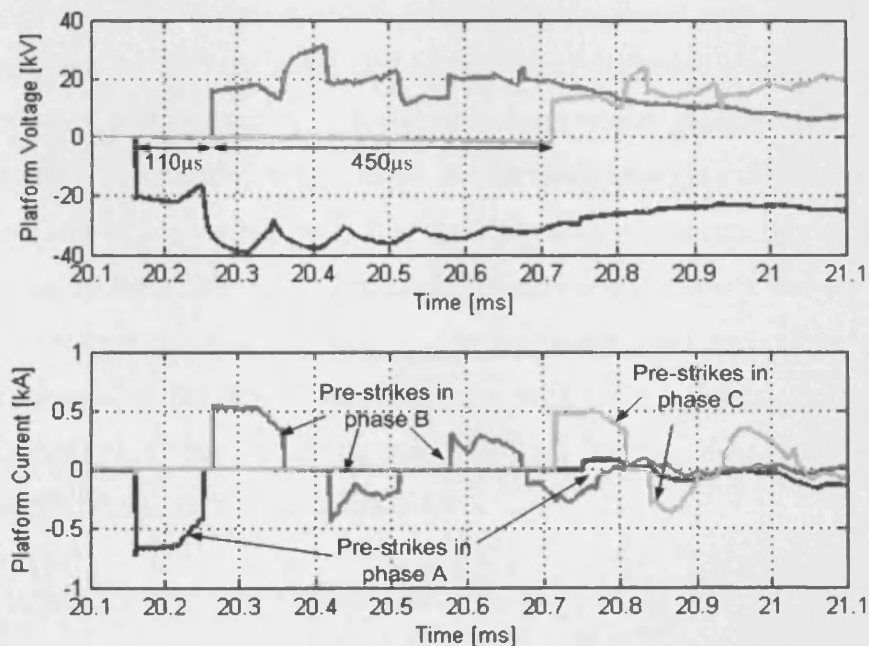
Fig. 5-2. Three phase voltage and current measured at the platform during energisation.

In Fig. 5-3 to Fig. 5-5, results from a number of different VCB models are compared.

The first case is for an ideal circuit breaker, shown in Fig. 5-3. All three phases closed at the same instant (i.e. there is no pole span between phases). The current waveforms were quite different, with the exception of the first 100μs of the phase A current. This was due to the simplicity of the model which did not include the ability to simulate pre-strikes.
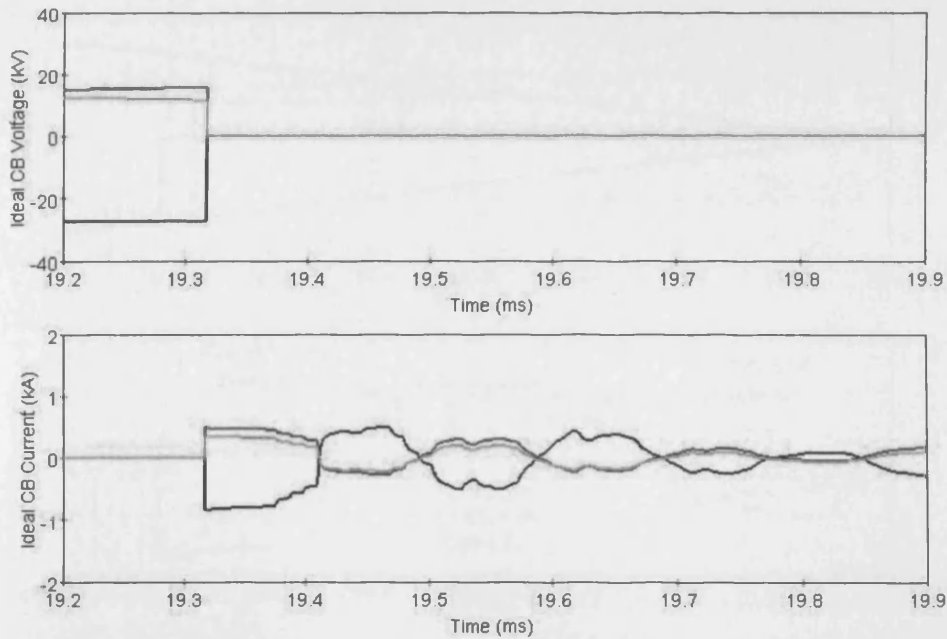
Fig. 5-3. Current and voltage across an ideal circuit breaker during energisation.

Fig. 5-4 shows simulation results when all three phases were signalled to close at the same time and had the same rate of change of dielectric strength, A_A, of 100kV/µs. The simulated current waveform now bears more resemblance to the measured waveform, as the half-wave shapes of the cable charging current are now apparent. The main difference here was that the pole span was much shorter in the simulation (100µs between phase a and b, and 140µs between phase a and c). The pre-strikes also occurred in a much quicker succession (there was a second pre-strike in phase A very soon after the first in the simulation, which did not occur in the measurements). This indicated that 100kV/µs was too high for the rate of change of dielectric strength for this switching operation.
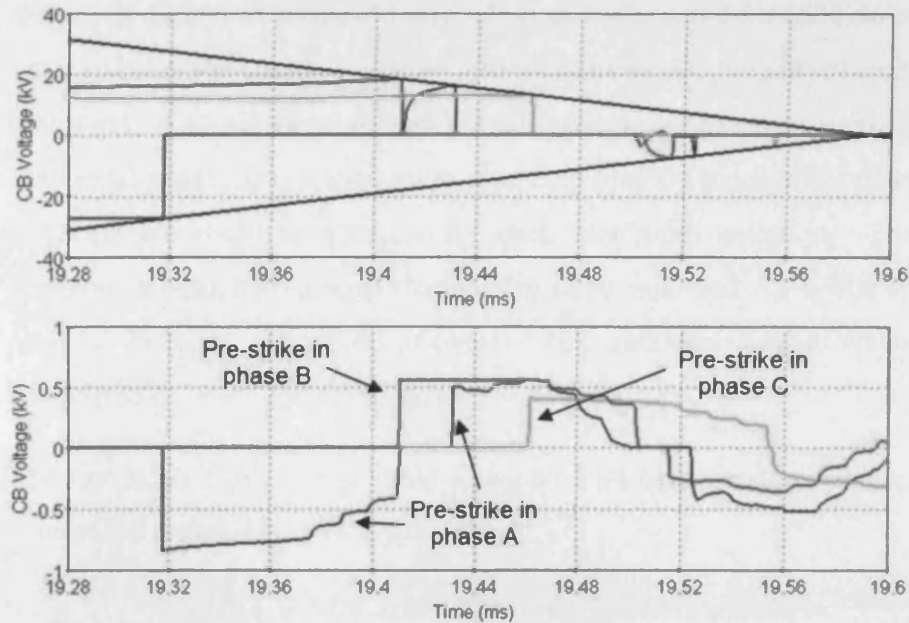
Fig. 5-4. Three phase voltage and current across the VCB when each pole of the VCB is assumed to close at the same time, with a rate of change of dielectric strength (black lines) of 100kV/µs.

In Fig. 5-5 the rate of change of dielectric withstand voltage, A_A, was reduced to 40kV/µs, with the three poles of the circuit breaker signalled to close simultaneously. The current waveforms were more similar to the measurements, with the pole span and the occurrence of pre-strikes in each phase being close.
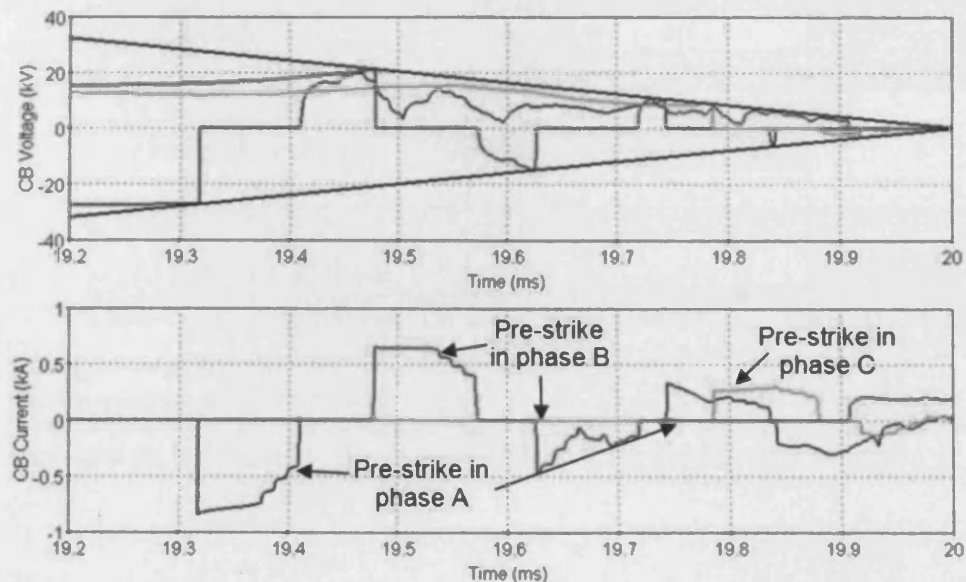
Fig. 5-5. Three phase voltage and current across the VCB when each pole of the VCB is assumed to close at the same time, with a rate of change of dielectric strength (black lines) of 40kV/µs.

In reality, there was a scatter in the mechanical pole closure times of the three poles due to tolerances in the VCB drive mechanism. It was also likely that the rate of

change of dielectric withstand was not exactly the same for each pole. Therefore, in order to bring the simulations closer to measurements, the rate of change of dielectric withstand, A_A, and time at which each pole starts to close were altered for each individual phase. It is important to note here that the mechanical pole closure time is statistical so would be different for each switching operation. The previous case however, in which all phases close at the same time and A_A is 40kV/µs, was able to produce the same magnitude of overvoltages and very similar wave-shapes so was considered to be a good compromise.

The results in Table 5-1 provide a comparison between the different VCB models against the measured waveforms.

Table 5-1. Comparison of VCB models against the measured waveforms

VCB model	Location	Max. transient overvoltage (kV)	Total No. of pre-strikes in all phases
Ideal Circuit Breaker	Platform	30.0	0
	WT_A1	37.6	
	WT_A9	39.7	
VCB with 100kV/µs	Platform	34.9	4
	WT_A1	36.1	
	WT_A9	38.7	
VCB with 40kV/µs	Platform	37.4	5
	WT_A1	36.1	
	WT_A9	38.8	
VCB with pole span changed to match measurements	Platform	37.1	6
	WT_A1	35.9	
	WT_A9	38.5	
Measured	Platform	39.4	7
	WT_A1	36.5	
	WT_A9	40.3	

A comparison of the phase a voltage at the platform, WT_A1 and WT_A9 for the ideal circuit breaker model and the VCB model with 40kV/µs is shown in Fig. 5-6.
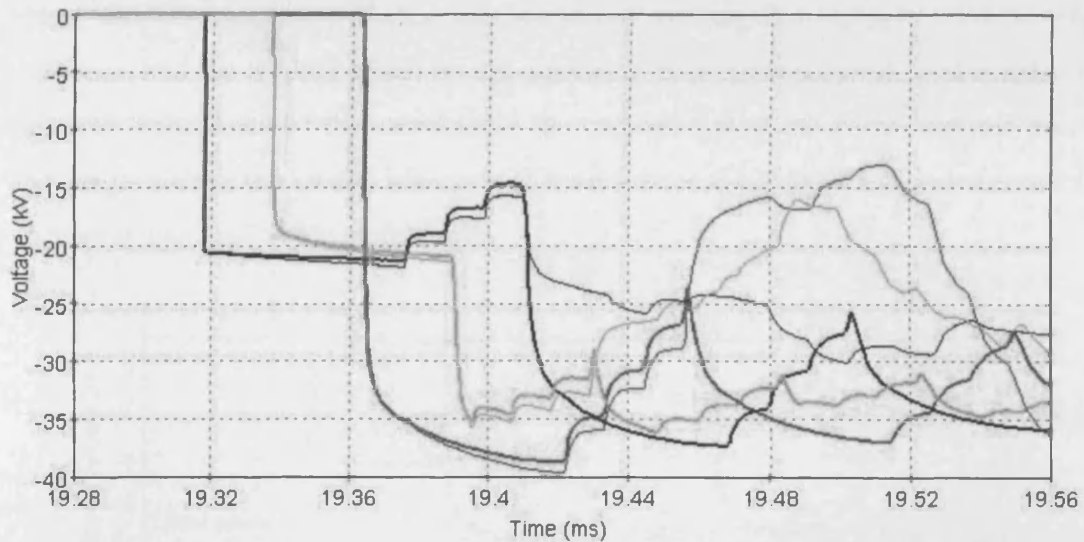
Fig. 5-6. Comparison of phase A voltages at the platform (blue), WT_A1 (green) and WT_A9 (red) for an ideal circuit breaker (thin lines) and the VCB with 40kV/μs (thick lines)

The results in Fig. 5-6 show that although the initial rate of change of voltage was the same for both cases, the voltage magnitude of the first peaks was higher for the ideal circuit breaker than for the VCB model with 40kV/μs. The initial waveform (the first 0.1ms) for the ideal circuit breaker model was closer to the measured waveform than for the VCB model with 40kV/μs. The slight difference between the two simulations in the first 0.1ms after the first phase connects was that all phases were connected at the same time for the ideal circuit breaker whilst in the VCB model the other phases had not yet connected. This suggests that the voltage (in the cable model) of the first phase to connect was only slightly affected by the other two phases. The difference between the two circuit breaker models became more significant after 19.4ms, 19.43ms and 19.45ms at the platform, WT_A1 and WT_A9 respectively; this was due to the ability of the VCB model to simulate pre-strikes.

5.3.2. CABLE MODEL

Measured and simulated phase A voltages at the three measurement locations and phase A current at the platform for the first 300μs are shown in Fig. 5-7. The time taken for the wave to travel from the platform to the last wind turbine was 45μs, which was the same in both measurement and simulation.

The most noticeable difference between the measurements and simulations in Fig. 5-7 is the magnitude of the cable charging current at the platform, which was around 20% larger in the simulations. This difference is most likely due to the value of relative permittivity chosen for the main insulation of the cables in the simulations,

110

which was corrected to match the measured propagation speed. Whilst this correction had the desired effect on the simulated propagation speed, it also affected the surge impedance of the cable since the capacitance of the cable was increased. The surge impedance of the cables was found to be 23Ω from the measurements, whereas it was 19Ω in the simulations.
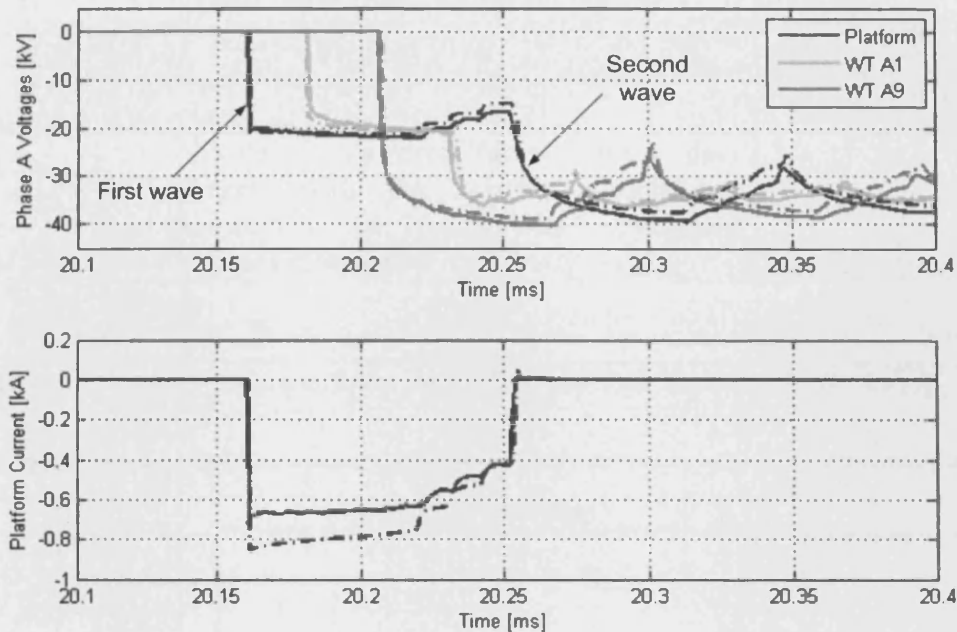
Fig. 5-7. Measured and simulated phase A voltages and currents at Nysted during energisation. The top figure shows the voltages at the three measurement locations, whilst the bottom figure shows the current at the platform. Solid lines show the measurements and the dashed lines show the simulation results.

The input data for the 33kV cable models was based on the specified dimensions of the cable given by the manufacturer. In reality however, these dimensions may differ due to the small geometries involved and the fact that standards (IEC 60502, for example) only place limits on minimum thickness of each cable layer.

Four cases were studied to determine the effect that different insulation and semiconductor screen thicknesses had on the charging current as described in Table 5-2. The relative permittivity in cases 1 to 3 in Table 5-2 were calculated following IEEE guidelines as described in Chapter 4, which modifies the value to take into account the semiconductive layers in the cable [137]. Case 4 had the same dimensions as case 1; however the relative permittivity was corrected to match the measured propagation speed, with a value of 3.8.

111

Table 5-2. Four study cases to determine the effect of cable dimensions and relative permittivity on cable charging current.

Case No.	Data	Corrected value of Relative Permittivity
1	Cable dimensions taken directly from the data sheet	2.8
2	1mm added to the insulation thickness	3.0
3	1mm added to both the semi-conducting screens and 1mm added to the insulation thickness	3.38
4	Cable dimensions directly from data sheet, with the relative permittivity corrected to match the measured propagation speed	3.8

The phase A current at the platform for each of the four cases is shown in Fig. 5-8.
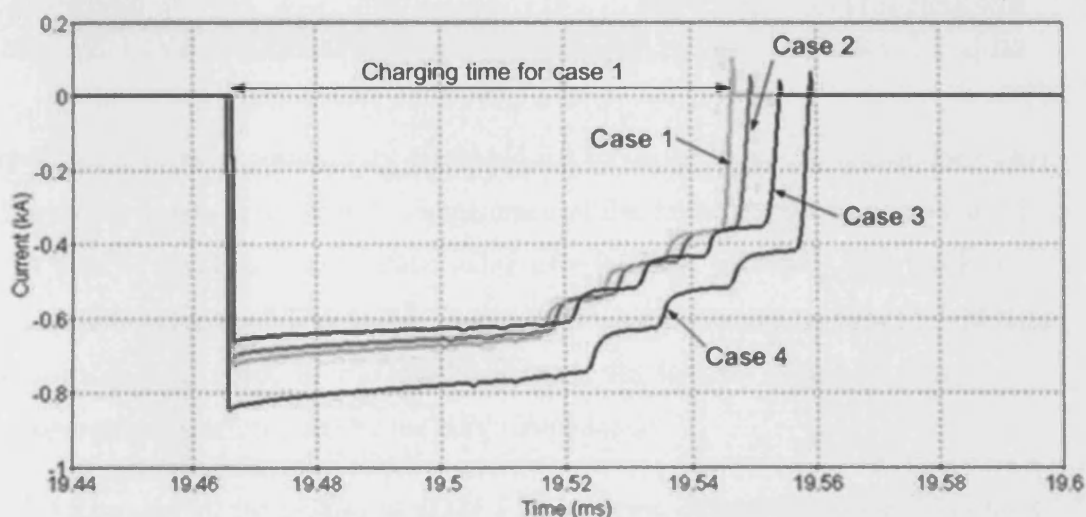
Fig. 5-8. Simulated cable charging current at the platform for the four cases. The cable lengths are the same for all cases.

Table 5-3 provides a comparison of the maximum transient overvoltage, rate of change of voltage for the first voltage step, travel time and maximum charging current for each of the 4 cases.

112

Table 5-3. Comparison for the four study cases and the measured waveforms.

Case no.	Location	Max. transient overvoltage (kV)	dV/dt of first voltage step (kV/µs)	Time to travel from the platform to WT_A9 (µs)	Max. Charging current (A)
1	Platform	37.7	102	38	725
	WT_A1	36.5	22		
	WT_A9	38.9	30		
2	Platform	38.1	102	40	701
	WT_A1	36.8	24		
	WT_A9	39.3	19		
3	Platform	38.6	102	43	661
	WT_A1	37.3	22		
	WT_A9	39.7	19		
4	Platform	37.1	102	45.6	847
	WT_A1	35.9	25		
	WT_A9	38.5	27		
Measured	Platform	39.4	26	45.6	687
	WT_A1	36.5	18		
	WT_A9	40.3	23		

Increasing the relative permittivity increased the cable capacitance, which decreased the propagation speed and the surge impedance of the cable. This can be seen in Fig. 5-8, as case 4, which had the highest value of relative permittivity, had the longest charging time (corresponding to the time it takes for the wave to travel to the last wind turbine and return to the platform) and the largest charging current (the charging current is determined by the surge impedance).

The charging current magnitude in cases 2 and 3 were closest to the measurements. The simulated peak overvoltages at the platform were 95.7%, 97.5%, 98% and 94% of the measured peak overvoltage for cases 1, 2, 3, and 4 respectively. It is therefore likely that the insulation and semiconducting screens were thicker than the values specified, being closest to case 3.

Although the increased insulation and semiconducting screen thicknesses resulted in a slower propagation speed, it was still not as slow as the measured speeds. This could be due to the cable lengths used in the simulation, which did not include vertical and additional slack lengths as these values were not available.

5.3.3. REPRESENTATION OF HIGH VOLTAGE CABLES

A frequency dependent model of the high voltage (132kV) export cable was included in a simulation to compare it against the simulation using the PI model. There was no difference between the two simulations. This suggests that for studies of energisation within the collection grid of an offshore wind farm, the high voltage export cable can be modelled as a PI model which enables the computation time to be reduced.

5.3.4. RATE OF CHANGE OF VOLTAGE

The rate of change of voltage at the platform, WT_A1 and WT_A9 are given in Table 5-3. The rate of change of voltage at the platform of the initial phase to connect was 102kV/μs and 26kV/μs for the simulations and measurements respectively. The voltage wave was doubled at WT_A9 and was more rounded, with initial rate of change of the simulated voltage step being between 83% and 130% of that measured, depending on the cable model.

Although the magnitude of the voltage step was the same at the platform, it occurred over 2 measurement steps (0.8μs) whereas it occurred over ½ a simulation time step (0.2μs), which explains why the rate of change of voltage was much higher in the simulations compared to the measurements. The voltage step occurred across ½ a time step in the simulations due to the use of the Trapezoidal and Backward Euler integration in EMTP-RV, as described in Appendix 5A. At the first voltage step at the platform, a discontinuity occurred which caused the usual trapezoidal method of integration (which was carried out over one time step of Δt) to be switched to the Backward Euler method (which was carried out in two time-steps of Δt/2). The simulation then resumed with the standard Trapezoidal method of integration.

In order to compare the rate of change of voltage (and current) in more detail, the inductance of the busbars should be included in the model [153]. Further details of this are given in Chapter 7. However, the time-step was too large compared to these rise-times and the measurement equipment will also have some time-constants, so it was not possible to compare these in more detail.

5.3.5. CURRENT SPIKES AT THE TRANSFORMERS

The measured and simulated phase A currents at WT_A1 and WT_A9 are shown in Fig. 5-9. The current spikes occurred when the voltage wave arrived at the transformer and were due to the capacitance between the HV windings and ground.

The magnitudes of the peaks at the first wind turbine were similar. The spikes were more rounded at the last wind turbine in the array, however the magnitude of the spikes in the simulation were roughly half that in the measurement.
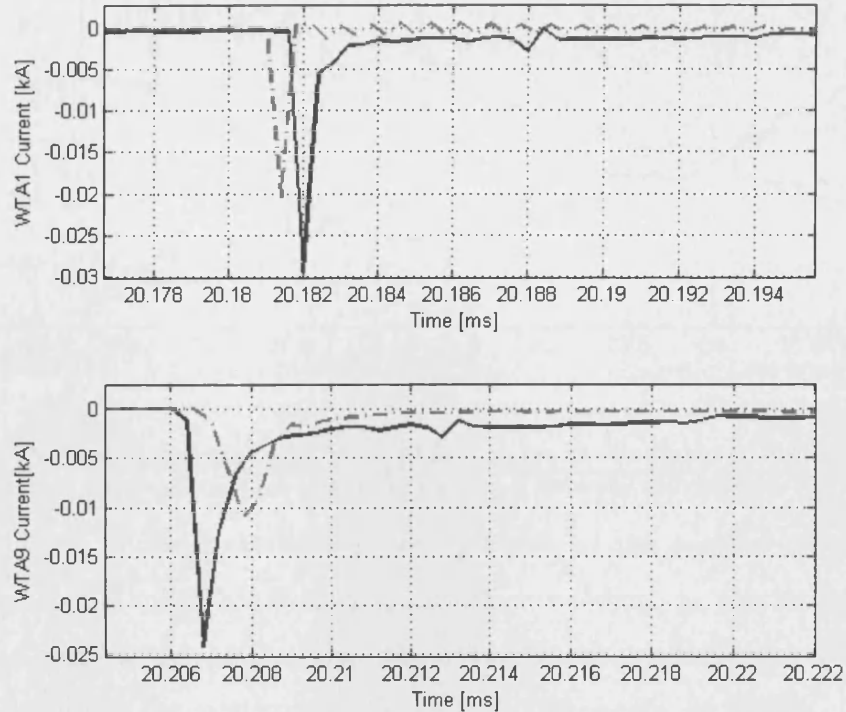
Fig. 5-9. Measured (solid blue) and simulated (dashed red) phase A currents at WT_A1 and WT_A9.

The simulation time-step (0.4μs) was too large compared to the time constants involved, so the results were not reliable. However, when the simulation time-step was decreased to 0.02μs the magnitude of the current at WT_A1 and WTA9 was 34A and 21A respectively, which was closer to the measurements.

5.3.6. OSCILLATIONS

There were some oscillations present in both the simulations and measurements during the first half cycle after connection. These oscillations had a frequency of 2.1kHz in the simulation, whereas they were 1.2kHz in the measurements and can be seen in Fig. 5-10.
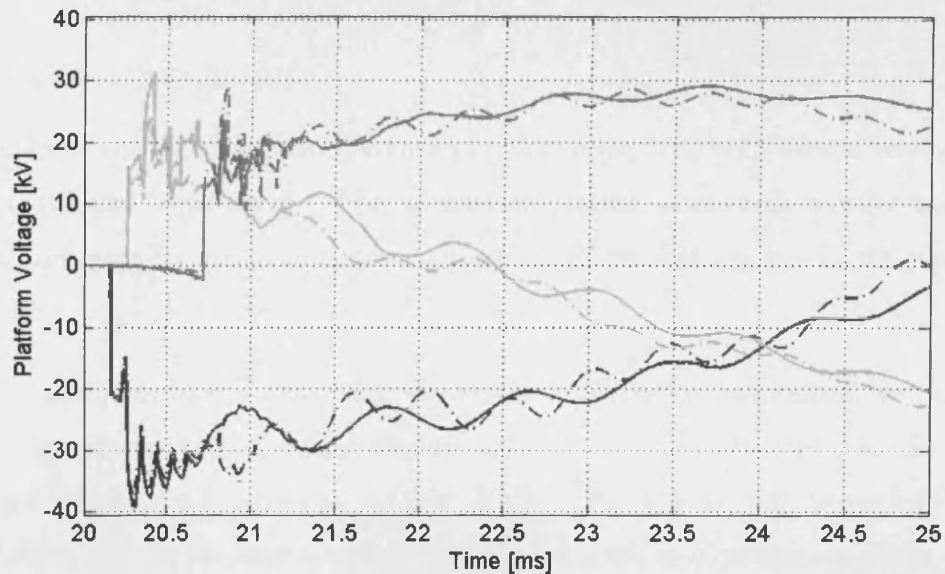
Fig. 5-10. Measured and simulated three phase voltage at the platform during energisation. Solid lines show the measurements and the dashed lines show the simulations.

The frequency of these oscillations was affected by the number of radial arrays connected to the other 33kV main transformer winding, as shown in Fig. 5-11. When the radial arrays on the other 33kV transformer winding were not connected the oscillations in the system were decreased in frequency to 880Hz. These were resonant frequencies of the wind farm collection grid system.
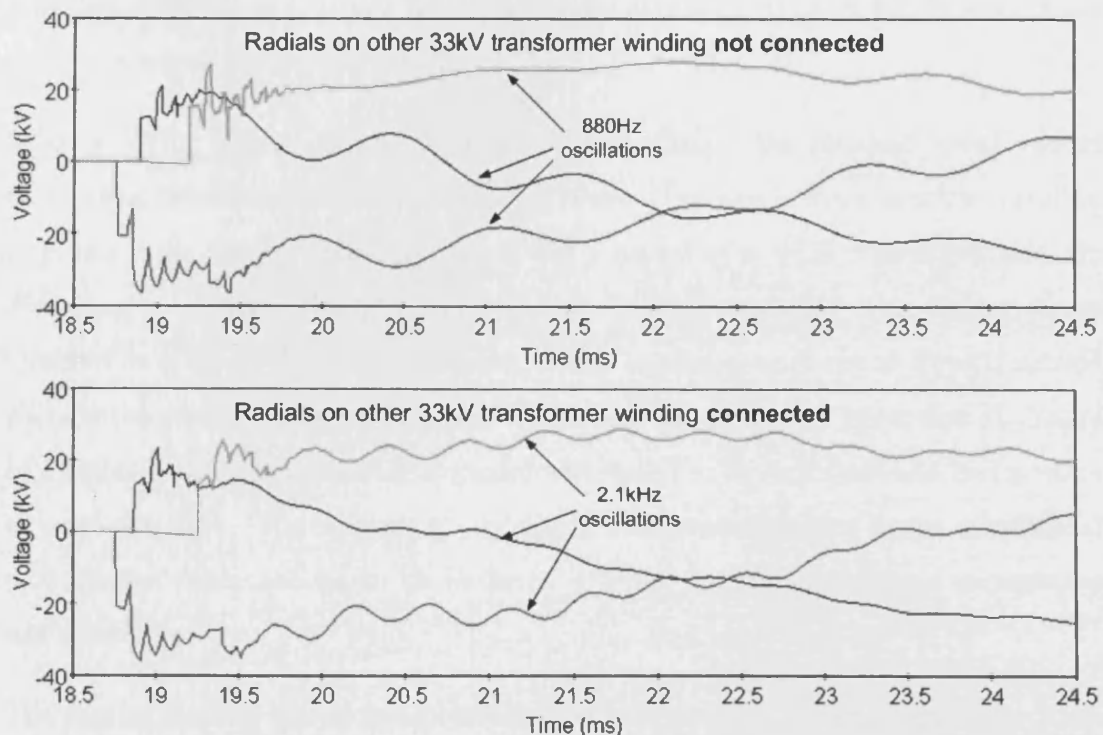
Fig. 5-11. The effect on the simulated thee phase voltages at the platform due to the radial arrays E to H being already connected to the other 33kV main transformer winding.

5.4. SUMMARY

Simulations during energisation of a array were compared with measurements made at an offshore wind farm. The simulation results were very similar and good agreement with the measurements has been achieved with regards to the magnitude and rise-times of the voltage waves.

All components were modelled based on information contained in technical specifications provided by manufacturers. The exception to this was the rate of change of dielectric strength of the VCB, which was not provided by the manufacturers and selected to match the measurements as closely as possible.

The study highlighted the difficulties in modelling cables accurately, which was found to be due to the small geometries involved, where only a small change in semi-conductor sheath or insulation thickness had a relatively significant effect on the propagation speed, attenuation and surge impedance. The simulation results indicated that the insulation and semiconductor screens were each around 1mm thicker than that specified in the data sheets, which is consistent with [141],[140]. This had the effect of decreasing the propagation speed and increasing the surge impedance of the cable, which was shown to be necessary in order for the simulation models to match the measurements.

When studying the magnitudes of transient overvoltages, the standard 'ideal' model of a circuit breaker was shown to be insufficient. The ideal circuit breaker was able to produce the steep fronted first wave, but a model of a VCB which included the dielectric breakdown strength and current clearing capability was shown to be required in order to simulate pre-strikes, which caused a more round fronted second wave at the platform and increased the transient overvoltage. A linear rate of change of dielectric strength for the VCB model was found to be sufficient and had a value close to $40kV/\mu s$. Furthermore it was found that the differences in the mechanical pole closure times needed to be included in order for the simulations to replicate measurements.

The results showed that it was possible to obtain accurate results even when some parts of the network were simplified. When simulating energisation transients in the MV network of the wind farm, the HV cables were represented as PI networks. The

other rows in the wind farm were represented by a frequency dependent model of the total row cable length, terminated by a $1\text{M}\Omega$ resistor.

6. TRANSIENT RECOVERY VOLTAGES

6.1. INTRODUCTION

A Transient Recovery Voltage (TRV) is the voltage that appears across the contacts of a circuit breaker immediately after the arc is extinguished. The shape of this transient is determined by the configuration of the system and can be oscillatory, triangular, exponential or any combination of these. The main stresses which a circuit breaker must withstand in order to successfully perform a switching operation are the amplitude of the TRV, the Rate of Rise of the transient Recovery Voltage (RRRV) and the short circuit current [70].

The TRV capability of a circuit breaker is defined by a two-parameter (U_C, t_3) or four-parameter (U_1, t_1, U_C, t_2) envelope of required withstand capability. The IEC two-parameter and four-parameter envelopes are shown in Fig. 6-1.
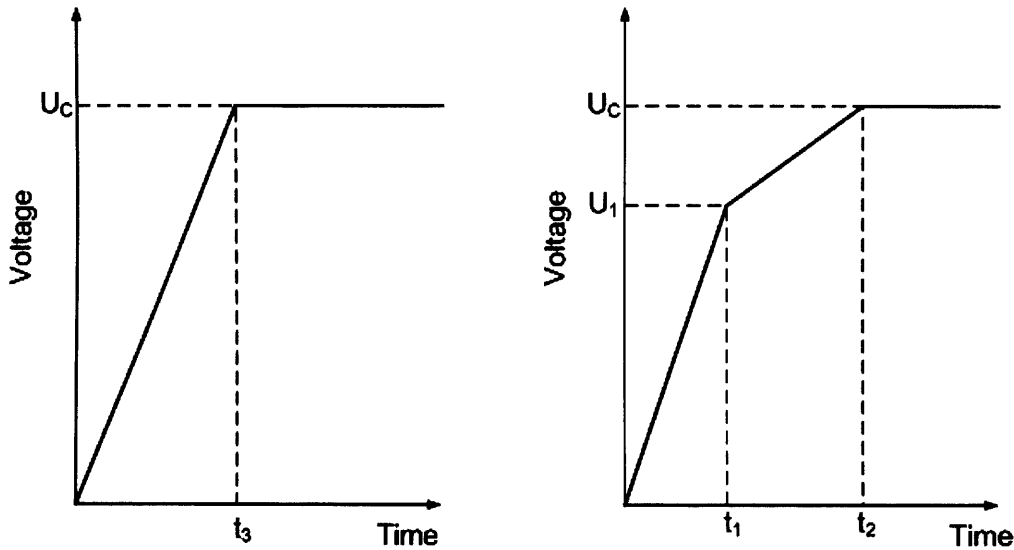
Fig. 6-1. Two- and Four-parameter envelopes in IEC 62271-100

The TRV capability of a circuit breaker is considered to be sufficient if this envelope is higher than the two- or four-parameter envelope of the system TRV. This comparison between the TRV capability and system envelopes enables the assessment of the two regions where reignitions are likely to occur, i.e. during the initial part of the TRV where the RRRV is at a maximum and the maximum peak voltage of the TRV. The system TRVs in this study were compared with the corresponding two-parameter TRV capability envelopes given in Table 6-1 [151]. The TRVs in the offshore wind farm should be below these values.

Table 6-1. TRV as specified in IEC 62271-100:2001 for 36kV and 145kV circuit breakers [151]

Voltage (kV)	Test duty	TRV peak (kV)	Time to peak (μs)	Rate of Rise (kV/μs)
36	T10	66	23	2.88
	T30	66	23	2.88
	T60	66	46	1.44
	Out-of-phase	92	214	0.43
145	T10	235	34	7
	T30	237	47	5
	T60	231	228	3
	OP1-OP2	296	232-464	1.54

The parameters which define the TRV capability envelopes vary as a function of the fault current magnitude. The T10, T30 and T60 test duties are the ratio of the symmetrical component of the current to the related required symmetrical interrupting capability of the circuit breaker, corresponding to 10, 30 and 60% respectively.

TRV values defined in IEC 62271-100 are based on values that would be obtained during interruption by an ideal circuit breaker. In reality, the TRV is modified by the circuit breaker arc [154], meaning that the TRV measured across the terminals of two different types of circuit breaker under identical conditions could be different. It would be a huge task to include these different arc models for the calculation of a TRV, so the TRV which results when an ideal circuit breaker interrupts is used as a reference.

TRV assessments are required not only on the circuit breakers within an offshore wind farm but also on the existing circuit breakers to which the offshore wind farm is connecting to. The networks of large offshore wind farms vary significantly from other transmission and distribution systems and the TRVs which are produced may have different characteristics. The larger amount of inherent capacitance in the offshore cable systems means that the RRRVs of these systems are slower than for overhead line connected systems.

A TRV assessment for 138kV circuit breakers with the addition of an onshore wind farm was made in [155]. It was shown that the TRVs with the addition of the new wind farm did not exceed the existing breaker capabilities. The fault current level at the substation increased by 1%, due to the 43km transmission line from the wind

farm to the substation, which limited the fault current. TRV investigations to assess the suitability of 132kV circuit breakers for an offshore wind farm connection were made in [156]. The results indicated that three phase ungrounded faults produced the worst case TRVs and that the TRVs marginally exceeded limits in some cases. The TRVs for the 33kV offshore circuit breakers were shown to be within the RRRV limits specified in [151], however the TRV amplitude exceeded 66kV for the T30 duty.

6.2. TRV AND RRRV IN AN EXAMPLE WIND FARM

In order to study the type of TRVs which may be experienced within an offshore wind farm, an example network was modelled in EMTP-RV, as shown in Fig. 6-2.
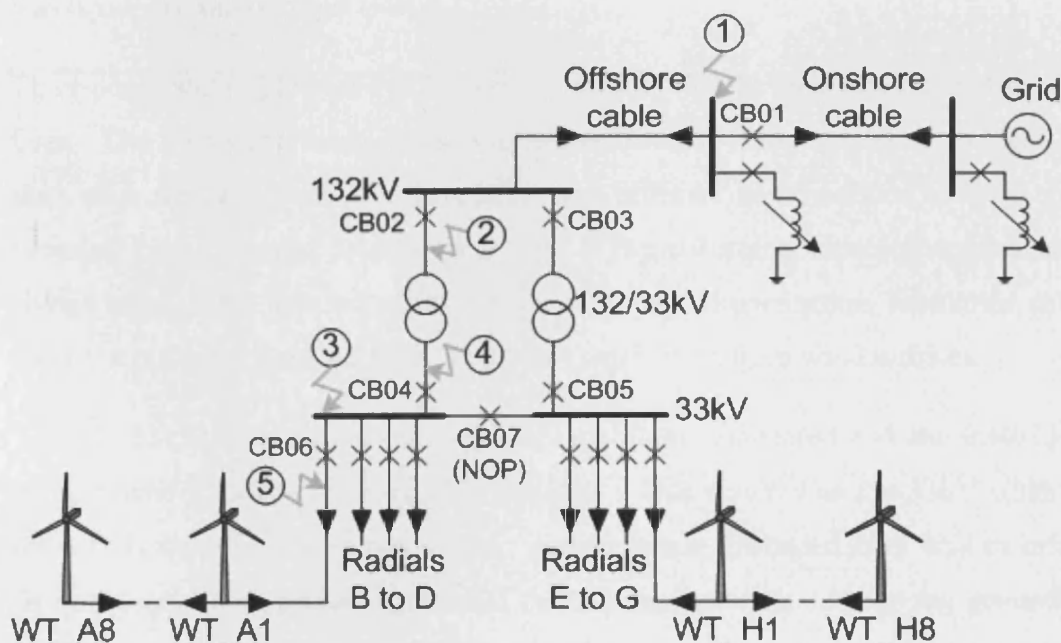
Fig. 6-2. Example offshore wind farm network

There were 8 arrays from A to H, each connecting 8 3MW wind turbines to an offshore substation. Under normal conditions, four of the radial arrays each connect to one of the two 33/132kV step-up transformers on the offshore substation which then connect to a three phase submarine cable. The submarine cable was connected to a land cable at the shore. Reactive compensation was located at the shore connection point and also at the onshore substation which connects to the grid. If one of the offshore transformers was taken out of service for some reason, the circuit breaker connecting the two 33kV busbars was closed, so that all 8 arrays connected to one transformer. In this case, the wind turbines were required to operate at a reduced output.

The wind turbine generators and grid were represented by a 'voltage behind a reactance' model. The fault level of the grid was set to 1500MVA, with an X/R ratio of 10. The wind turbine transformer and 33/132kV transformer models included the magnetizing characteristic and winding capacitances. All cables were modeled using a frequency dependent distributed parameter model. There was a 10m length of connection between the 33/132kV step-up transformers and the 132kV circuit breakers which was represented by a PI equivalent. Stray capacitances were included to represent busbars and other equipment such as CVTs and were chosen following [153]. The capacitance of equipment between CB04 and the transformer terminals was 1nF, the stray capacitance of each 33kV busbar was 1.8nF (assuming 60pF/m x 30m busbar). The capacitance of a closed 33kV and 132kV circuit breaker was 0.1nF and 0.3nF respectively.

Three phase and single phase faults were applied at various locations within the wind farm. The TRVs appearing across the circuit breakers which operated to clear the fault were then assessed. As there are many different combinations of fault type, location, circuit breaker location and type of wind turbine, selected studies were shown here. These focused on the effect of reactive compensation, submarine cable length, array cable lengths and fault current contribution from wind turbines.

The 132/33kV offshore transformers were star/delta connected and the 0.69/33kV wind turbine transformers were also star/delta. This resulted in the 33kV offshore network being effectively ungrounded. A three phase grounded fault was therefore the same as a three phase ungrounded fault in this network. A zig-zag grounding transformer was applied on the 33kV network in the latter part of section E to show the effect on a single-phase fault.

Five fault locations were considered, as shown in Fig. 6-2:

1) Terminals of the CB at the connection between the onshore and offshore cable.

2) HV terminals of the offshore transformer.

3) The 33kV busbar connecting radial arrays A to D.

4) The 33kV terminals of the offshore transformer.

5) The terminals of the CB connecting radial array A.

Initial studies were made without the inclusion of reactive compensation and were shown in Table 6-2. The onshore and offshore 132kV export cable lengths were 10km and 30km respectively. The corresponding test duty for each of the cases was determined from the simulated fault current through the circuit breaker before it opened. The TRV values which exceeded the reference values in Table 6-2 are shown in bold.

Table 6-2. TRV results for a three phase fault at the 5 locations

Fault No.	CB which operates	Fault current (kA)	Test duty	Initial Peak V (kV)	Max peak (kV)	Initial RRRV (kV/μs)
1	CB01 (80ms)	7.99	T30	157.15	203.86	0.22
	CB04 (100ms)	2.89	T10	7.09	**73.63**	0.65
1	CB01 (80ms)	7.99	T30	157.15	203.86	0.22
	CB02 (100ms)	0.95	T10	127.57	**280.05**	0.035
2	CB01 (80ms)	6.34	T30	146.29	163.24	0.2
	CB04 (100ms)	3.07	T10	7.14	**69.01**	0.52
2	CB04 (100ms)	2.98	T10	7.07	60.4	0.501
	CB02 (80ms)	6.75	T30	139.95	186.33	0.079
3	CB04 (80ms)	14.15	T60	33.41	33.41	**2.16**
	CB06 (100ms)	0.66	T10	57.11	66.40	0.047
3	CB02 (80ms)	3.71	T10	107.38	180.83	0.173
	CB06 (100ms)	0.232	T10	22.95	22.95	0.038
4	CB04 (80ms)	3.27	T10	58.08	**68.96**	0.054
	CB02 (100ms)	3.74	T10	115.94	178.86	0.19
5	CB06 (80ms)	15.72	T60	21.7	28.96	0.054

From these results, the worst situation in terms of RRRV was fault no. 3, when CB04 opened first to clear the fault. This was the only case in which the RRRV exceeded the values given in Table 6-1. The voltage and current through CB04 when clearing the fault were shown in Fig. 6-3 and a comparison with the TRV envelope was shown in Fig. 6-4. Some of the TRVs contained more than one frequency, resulting in an initial peak voltage at one frequency and later a maximum peak voltage at a lower frequency. The initial peak overvoltage was not exceeded in any of the

situations; however the maximum peak overvoltage did exceed the TRV peak specified in IEC 62271-100 for faults 1, 2 and 4.
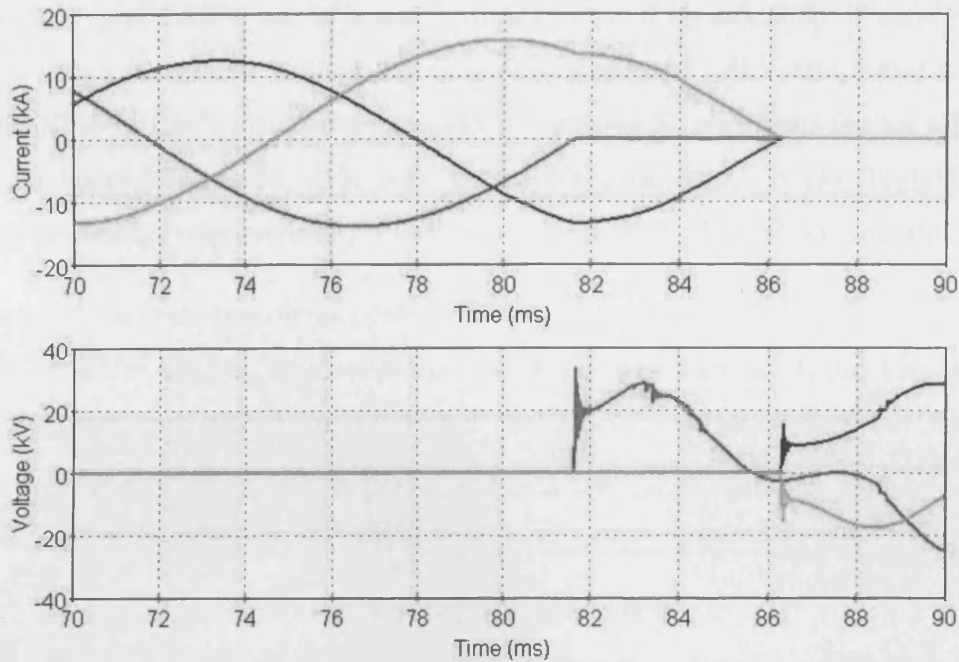
Fig. 6-3. Three phase voltage and current across CB04 when clearing Fault no. 3.
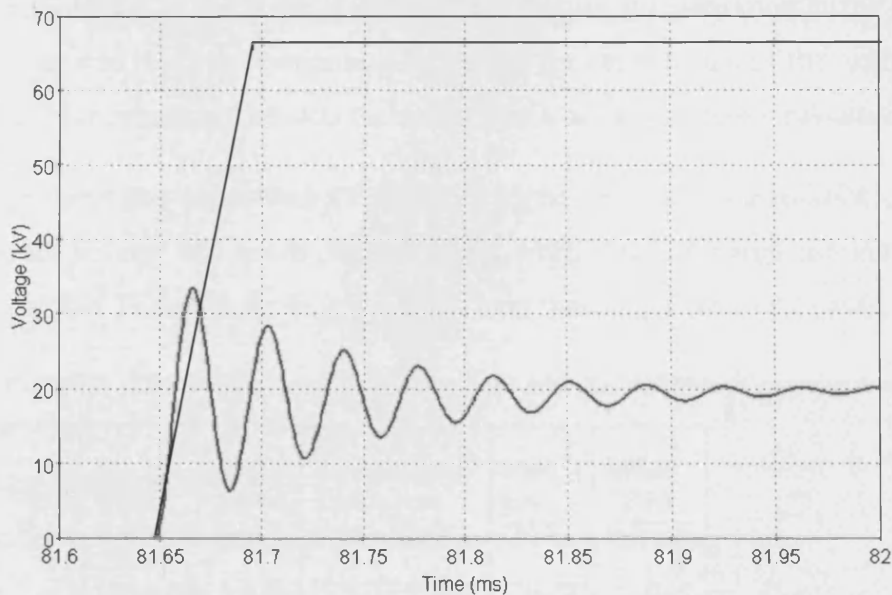
Fig. 6-4. Time expansion showing the first pole to clear TRV for CB04, which exceeds the T60 test duty, the black two parameter TRV curve.

These faults were studied with all wind turbines connected and generating at full output, using the FRC model which had a fault current output of 1pu. It is assumed that the wind turbine generators will trip 100ms after the fault. By this time, the circuit breakers have operated to clear the fault, so during these studies, the wind turbines were still connected during the switching operations. In reality, it may take

longer for the circuit breakers to operate (and for the wind turbines to trip); however, in order to limit computational time, the simulations were run for 140ms.

The TRV and RRRV for fault no. 5 were increased significantly if there were no other arrays connected, with an initial peak voltage of 31.8kV and initial RRRV of 1.97kV/μs for CB06. This was expected as the damping on the un-faulted side of the circuit breaker increased with increased cables connected. It also highlights that TRV studies are required under a number of different configuration scenarios.

If one of the main transformers was taken out of service, all the 33kV arrays were connected through only one transformer to shore. For fault no. 1, this had the effect of doubling the fault current through the CB02 and increasing the maximum overvoltage to 351kV, with an RRRV of 0.11kV/μs. The fault current and TRV was not significantly affected for CB01.

6.2.1. ADDITION OF REACTIVE COMPENSATION

The reactive compensation between the onshore and offshore cables was rated to compensate for all of the capacitance of the offshore cable and half of the capacitance of the onshore cable. The reactive compensation at the grid connection point was rated to compensate for half of the capacitance of the onshore cable. The reactive compensation was represented by a delta connected inductance.

The previous cases were all studied with no reactive compensation connected. The peak voltage and initial RRRV values when reactive compensation was added are given in Table 6-3 for faults 1, 2 and 3, as these were the worst cases.

Table 6-3. TRV results for a three phase fault with the addition of reactive compensation

Fault No.	CB which operates	Fault current (kA)	Test duty	Initial Peak V (kV)	Max peak (kV)	Initial RRRV (kV/μs)
1	CB01 (80ms)	8.36	T30	162.78	225.55	0.22
	CB02 (100ms)	0.82	T10	119.72	**285.25**	0.06
2	CB01 (80ms)	6.56	T30	151.61	168.73	0.21
	CB04 (100ms)	3.07	T10	7.31	**71.13**	0.66
3	CB04 (80ms)	15.82	T60	33.33	33.33	**2.11**
	CB06 (100ms)	0.81	T10	57.48	66.29	0.04

From Table 6-3, it can be seen that the addition of reactive compensation had the effect of increasing the peak voltages slightly. It did not have a significant effect on the RRRV.

6.2.2. EFFECT OF MAIN SUBMARINE CABLE LENGTH

Large offshore wind farms with AC connections generally have HV transmission submarine cable lengths to shore of up to 60km. This cable length will effect the expected TRVs within the offshore wind farm, so was studied here. The effect of the main submarine HV cable length on the TRVs for faults 1 and 3 are shown in Fig. 6-5 and Fig. 6-6 respectively.
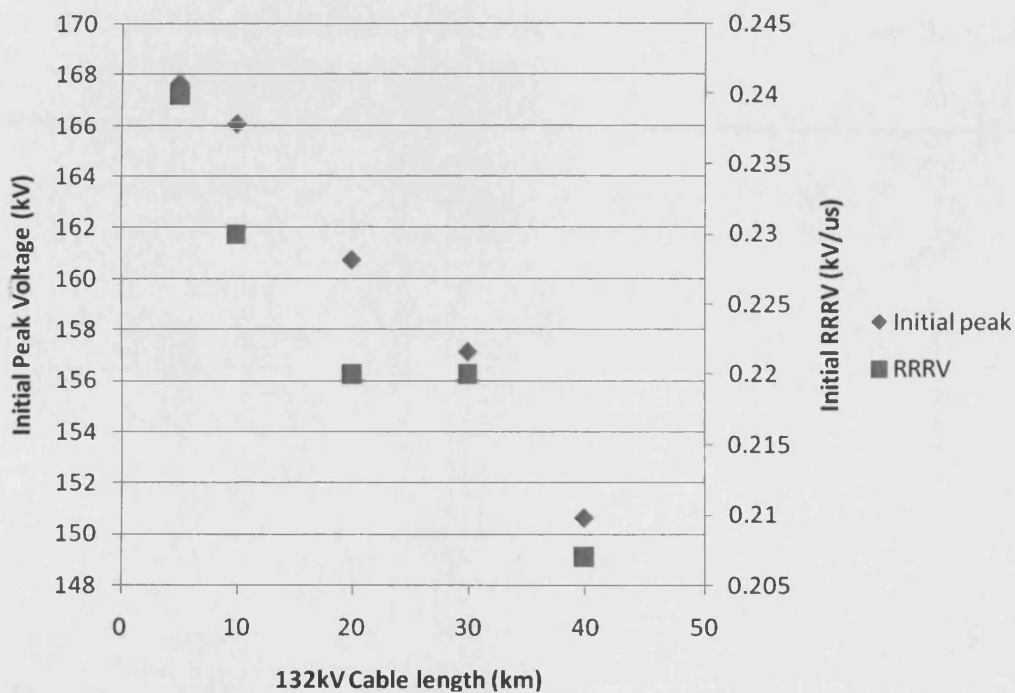
Fig. 6-5. Initial peak voltage and RRRV for CB01 when clearing fault no. 1 for 132kV submarine cable lengths between 5 and 40km.
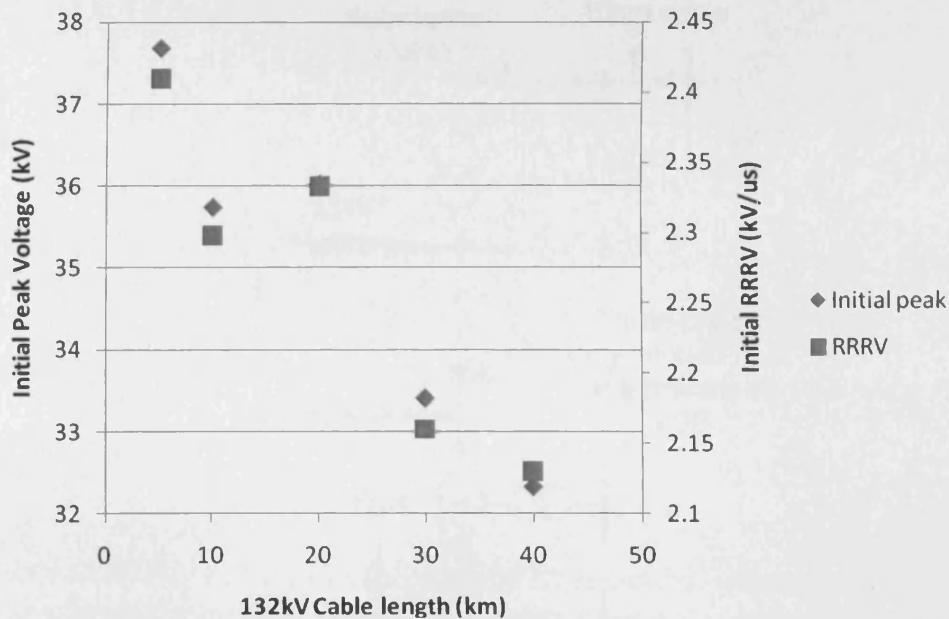
Fig. 6-6. Initial peak voltage and RRRV for CB04 when clearing fault no. 3 for 132kV submarine cable lengths between 5 and 40km.

Overall, the effect of increasing the submarine cable length was to decrease the RRRV and peak TRV. This was due to the additional damping of the cable.

6.2.3. EFFECT OF THE 33KV ARRAY CABLE LENGTHS

The 33kV cable length between the platform and first wind turbine in an array can vary from a few hundred meters to a few kilometres. The effect of this cable length on TRVs is most likely to be noticeable on the 33kV radial array circuit breaker. In order to study this, fault no.5 was applied for 33kV cable lengths from 800m to 12km, as shown in Fig. 6-7. The results are shown in Fig. 6-8.

127
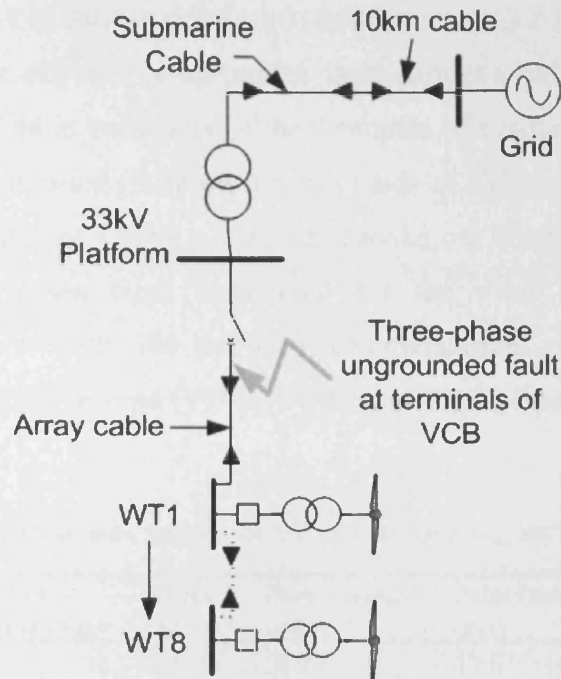
Fig. 6-7. Location of fault for study on 33kV array cable length.
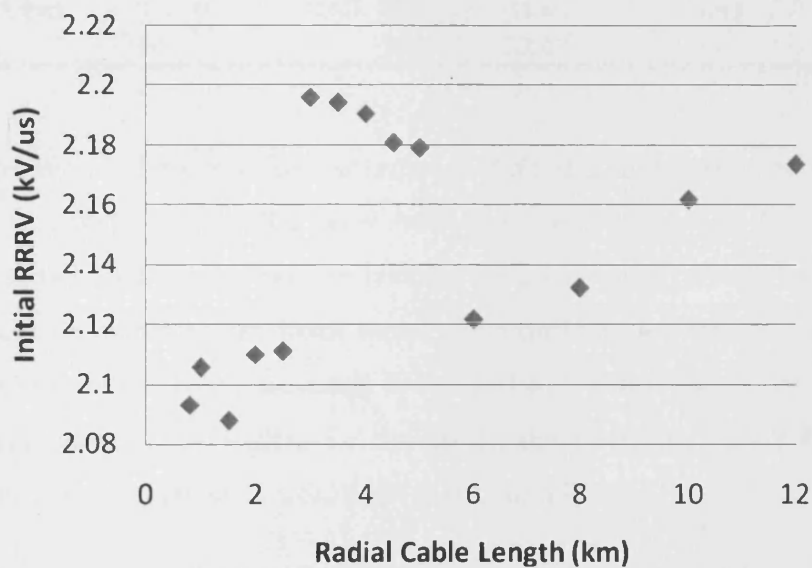
Fig. 6-8. Effect of radial array cable length on the RRRV of CB06.

The RRRV across CB06 did not vary significantly as the radial array cable length increased. The highest value of RRRV was with a radial array cable length of 3km. The peak in RRRV values around this cable length may be due to some interaction of resonances in the system; however it was only a few percent higher than the values for other cable lengths.

6.2.4. FAULT CURRENT CONTRIBUTION FROM WIND TURBINES

In order to study the effect of wind turbine fault current contribution on TRVs, a 3 phase fault was applied at both sides of the terminals of a radial array circuit breaker to create either a source-fed (fault on the array side of CB06) or a wind-turbine-fed fault (fault on grid side of CB06). This was carried out when no other arrays were connected. Three cases were considered for the wind turbine fault current contribution, these were 100, 300 and 600% of rated current, which corresponded to the three types of wind turbine (FSIG, DFIG and FRC respectively). Results are shown in Table 6-4.

Table 6-4. RRRV and Initial peak voltage for CB06 when clearing fault no. 5.

	Fault Current Contribution (pu)	RRRV (kV/µs)	Peak Voltage (kV)	Fault Current (kA)
	1	2.2176	38.27	13.83
Source Fed	3	2.2258	38.27	13.83
	6	2.1584	38.23	13.83
	1	0.04361	50.73	0.8
WT Fed	3	0.06211	53.86	1.62
	6	0.0755	53.07	2.6

The results show that for a source-fed fault, the fault current was not affected and the peak voltage and RRRV were not significantly affected. For the wind turbine fed fault the fault current was highest for the FSIG wind turbines, which was expected as the fault contribution from these wind turbines is highest. The RRRV was also highest for the FSIG, although it was still well below the values set in standards. The peak voltage was higher for the DFIG and FSIG than the FRC but was still well within the values set in IEC 62271-100 for TRVs.

6.2.5. SINGLE PHASE FAULT AT THE BASE OF WTA1

High overvoltages occur if a single phase fault occurs at the base of a wind turbine and the circuit breaker connecting that radial array then opens to clear the fault, but the wind turbines continue to generate [104]. An example is shown here, where a single phase fault was applied to the base (33kV side) of WT_A1. The fault was then cleared by CB06.

The voltage at the array side of CB06 and the voltage and current across CB06 are shown in Fig. 6-9 and Fig. 6-10 respectively.
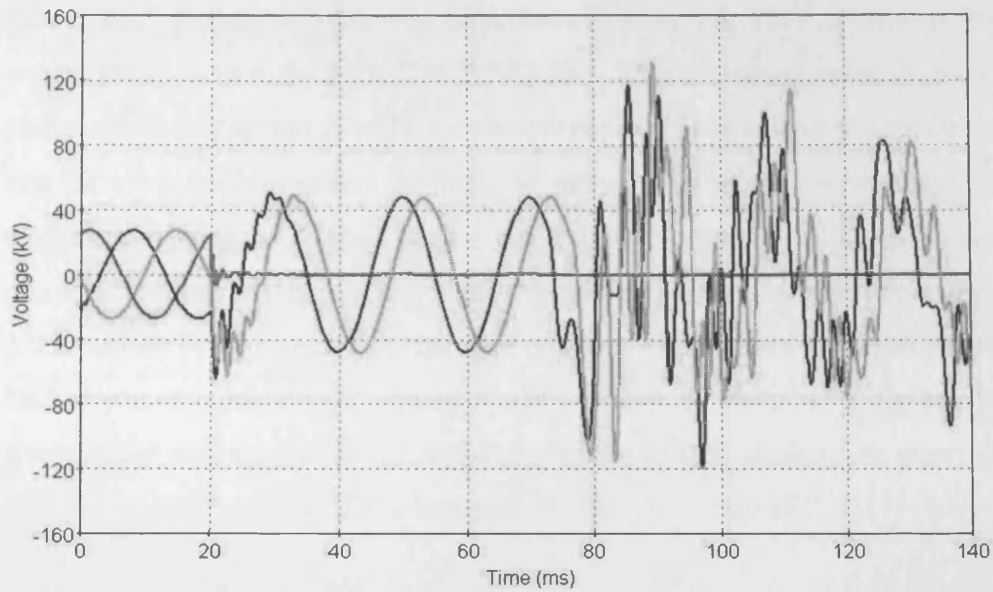
Fig. 6-9. Three phase voltage at the array side of CB06 when a single phase fault is applied to the base of WT_A1 at 20ms. CB06 opens at 70ms.
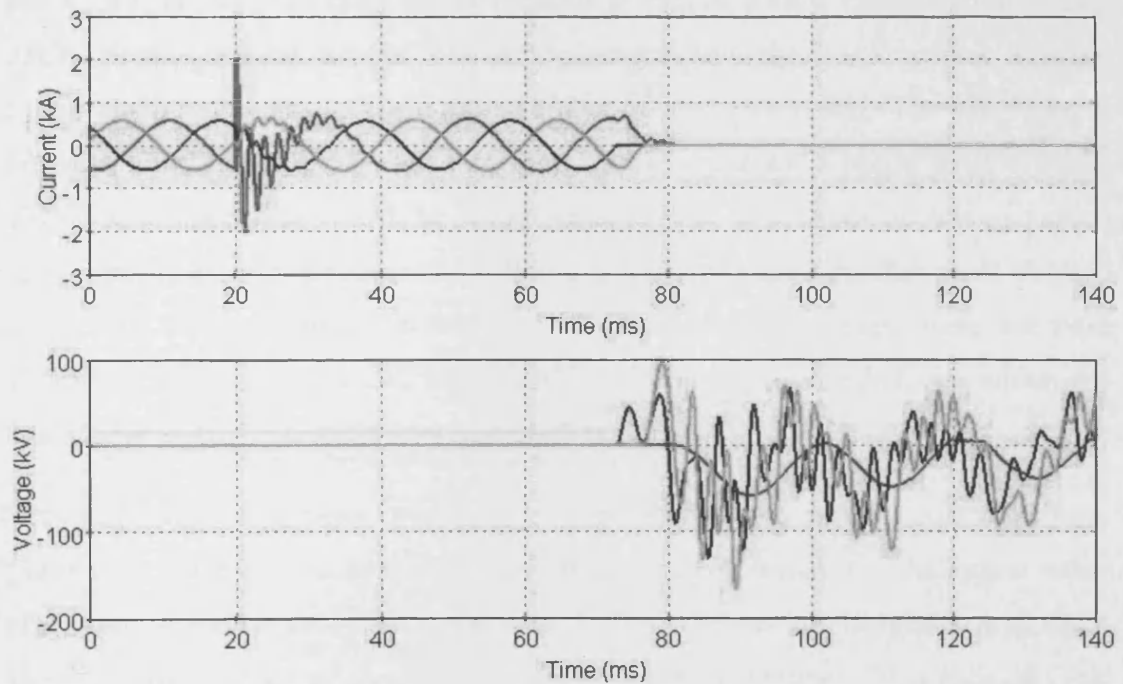
Fig. 6-10. Three phase current and voltage across CB06 when clearing a single phase fault at the base of WT_A1.

The overvoltages following interruption by CB06 were significant, reaching 168kV, which was well above the maximum TRV peak for 33kV circuit breakers in IEC 62271-100. If some of the wind turbines stopped generating at 50ms due to the fault, the maximum TRV peak was reduced to 80kV. If the fault occurred at WT_A9 instead of WT_A1 there was very little difference to the TRV that occurs in CB06.

CB02 was operated to clear the fault and the resulting TRV at this circuit breaker was within the limits in IEC 62271-100. This however resulted in temporary disconnection of arrays A to D and the overvoltage was still very high on the faulted side of the circuit breaker. In order to avoid these high overvoltages, grounding transformers may be applied at each array [104], or at the 33kV busbar, depending on the switching regime. When a zig-zag grounding transformer was included on the 33kV busbar it didn't reduce the overvoltages experienced by CB06, however the faulted phase current was increased, with a peak of 9kA. If a zig-zag grounding transformer was applied at the array side of the circuit breaker, the overvoltage was reduced to 88kV across CB06, however this still exceeded IEC 62271-100.

6.3. SUMMARY

The studies showed that the majority of TRVs were within the specified peak voltage and RRRV values. The only circuit breakers to exceed RRRV values were the main 33kV circuit breaker at the offshore platform and the 33kV circuit breaker connecting a radial array. There are a number of solutions to this. The 33kV circuit breakers could be upgraded so that they are able to withstand a higher RRRV, or the 33kV circuit breakers could be fitted with grading capacitors or line-to-ground capacitors which would reduce the RRRV. A different circuit breaker could be used to clear the fault, sacrificing faulted zone discrimination, for example using the main 132kV circuit breaker instead, as the TRV with this circuit breaker was within the limits.

Very high maximum peak overvoltages were shown to occur in some situations. These were shown to occur at all of the offshore circuit breakers. The largest value of maximum peak overvoltage in the main 132kV offshore circuit breaker was when all arrays were connected through only one offshore transformer. This indicated that TRV studies should be carried out for all operating conditions. Very high maximum peak overvoltages were also shown to occur in the 33kV radial array circuit breakers. These overvoltages were reduced by grounding transformers. The studies of a single phase fault on an array indicated that in order to reduce overvoltages to acceptable levels, grounding transformers were required at each array or the wind turbines should stop generating prior to the circuit breaker interrupting. Surge protection may also be required and it would be necessary to check that the temporary overvoltage capability of surge arresters is not exceeded.

Simple voltage source behind a reactance models were used to represent the wind turbines, with the reactance set so that the fault current rating was 6pu, 3pu or 1pu for the FSIG, DFIG and FRC respectively. There were no significant differences between the TRVs experienced for the three different wind turbine types. The disconnection of an array following a single-phase fault should be considered when High Voltage Ride Through requirements for wind turbines are being determined. It is expected that the control systems of the DFIG and FRC wind turbines will have an impact on the fault current contribution.

7. ENERGISATION AND DISCONNECTION TRANSIENTS

7.1. DESCRIPTION OF WIND FARM MODEL

A typical offshore wind farm was modelled in EMTP-RV in order to study the type of switching transients which may be experienced. The configuration of the wind farm was the same as that described in Chapter 6 and is shown in Fig. 7-1.
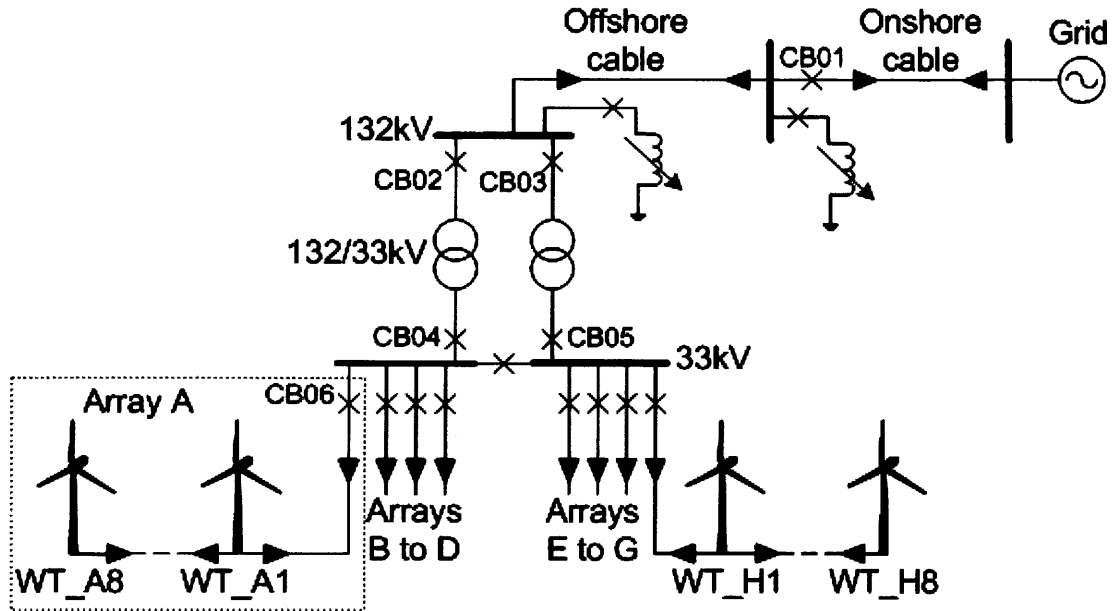
Fig. 7-1. Example offshore wind farm network

7.2. ENERGISATION OF THE EXPORT CABLE

There are a number of possible switching strategies for energising an offshore wind farm. These include energisation of the cable on its own, with reactive compensation connected and with the main offshore transformers connected, as shown in Fig. 7-2. These four connection strategies were simulated in EMTP-RV by closing circuit breaker CB01 in Fig. 7-1.
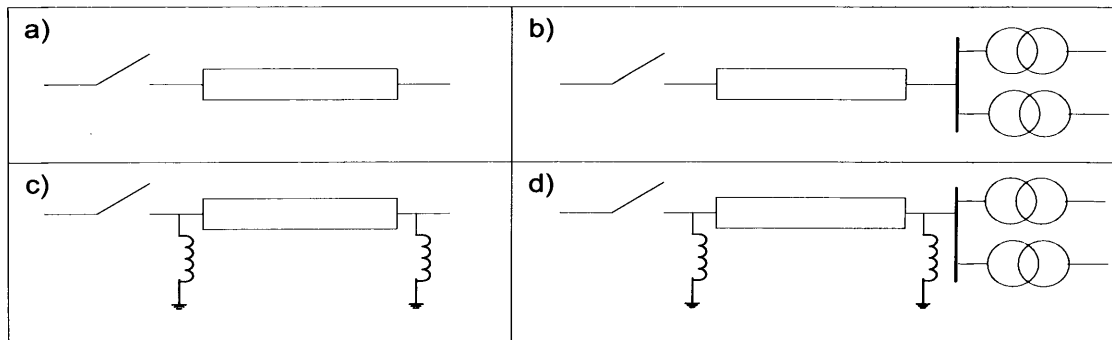
Fig. 7-2. Energisation options for the export cable. a) cable only, b) cable and offshore transformers, c) cable with reactive compensation and d) cable, offshore transformers and reactive compensation.

133

The energisation of a 90km 132kV cable for each of the four energisation strategies in Fig. 7-2 was simulated. All these simulations involved the energisation through a 30km land cable. The closing instant of the circuit breaker was selected to occur at a switching instant which produces the maximum transient overvoltage so that each switching strategy could be compared. This switching instant was determined by carrying out a systematic switching study, where the switching time was varied from 20ms to 26.65ms in 0.05ms steps (133 simulations in total). The pole-span between closing of the circuit breaker was selected to be zero and an ideal circuit breaker model was used. The results are given in Table 7-1.

Table 7-1. Maximum voltages and currents during energisation of a 90km 132kV cable.

	a) Cable only	b) Cable + both transformers	c) Reactive compensation connected	d) Both transformers and reactive compensation connected
Max. Platform ph-grnd voltage (kVpeak)	199	199	185	185
Max. Platform ph-grnd voltage (pu)	1.84	1.85	1.72	1.72
Max. Shore ph-grnd voltage (kVpeak)	170	169	162	160
Max. Shore ph-grnd voltage (pu)	1.58	1.57	1.50	1.48
Max. Platform ph-ph voltage (kVpeak)	309	319	288	286
Max. Platform ph-ph voltage (pu)	2.87	2.96	2.67	2.65
Max. current through CB01 (kApeak)	2.4	2.7	2.4	2.8
Current through CB01 1s after energisation (kApeak)	0.67	0.75	0.05	0.02

The highest overvoltages occurred when the cable is energized without any reactive compensation (the first two columns in Table 7-1). The maximum overvoltage at the platform and shore were very similar at both locations when the cable only was energized and for when the cable and transformers were energised.

When the reactive compensation was connected the magnitude of the current through CB01 was close to zero after 1s, whereas it was around 0.7kApeak when no reactive compensation was connected. This is because the reactor is fully compensating the

capacitive current of the cable at the onshore connection point. The voltage at the grid settled at 1.09 after the energisation of the cable. When reactive compensation was included, the voltage at the grid settled at 1.0pu following energisation.

The three phase voltage and current during the first 1s at the onshore connection point are shown in Fig. 7-3 and Fig. 7-4. The three phase voltage and current during the first 160ms at the onshore connection point are shown in Fig. 7-5 and Fig. 7-6.

The voltage took 50ms to settle when the cable only was energized, whereas it took 1 second for the transient to settle to a steady-state when the cable and transformer were energized together, as shown in Fig. 7-3. When the transformers were included the duration of the transient was increased due to the transformer inrush currents, which can be seen in Fig. 7-4 and Fig. 7-6.

When the reactive compensation was included there was a low frequency (just over 1Hz) oscillation in the current which was damped out after 1 second. This caused the zero-missing phenomenon (which can be seen in Fig. 7-4c and Fig. 7-6c) and the current did not pass through zero for 300ms. This would cause the circuit breaker to fail if it were to try to open within the first 300ms after closing.
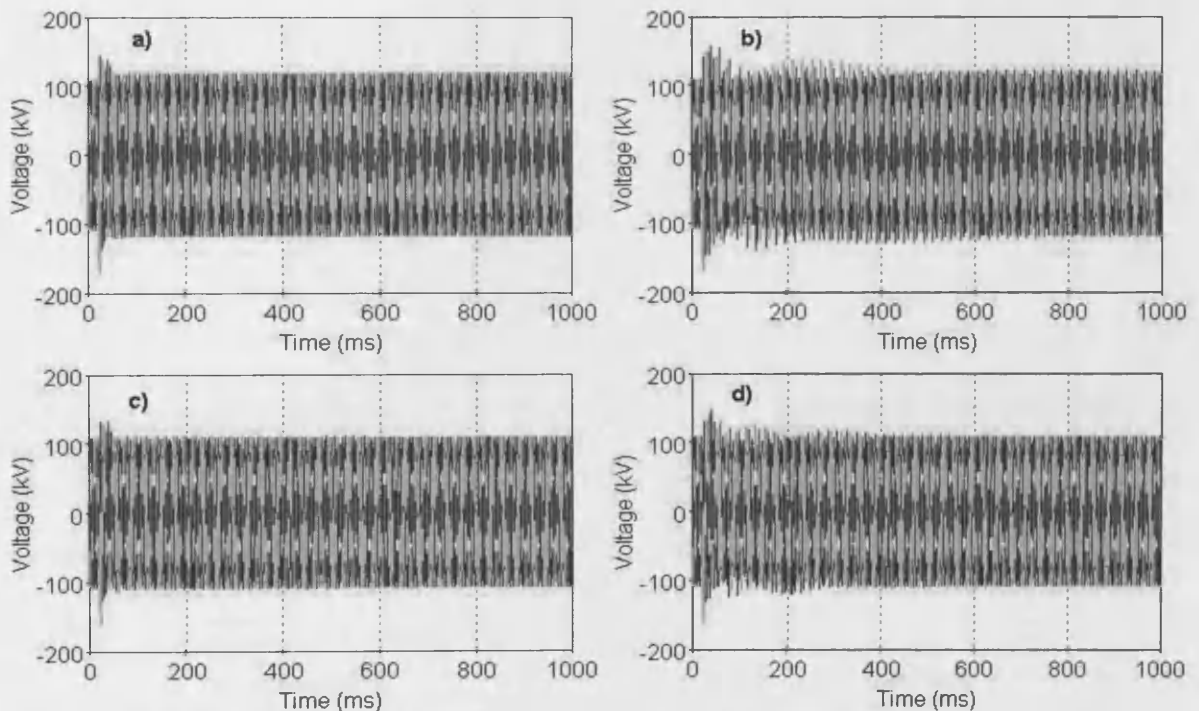
Fig. 7-3. Three phase voltage at the onshore connection point during energisation of a 90km export cable. Energisation of a) cable only, b) cable and transformers, c) cable and reactive compensation, d) cable, transformers and reactive compensation.

135
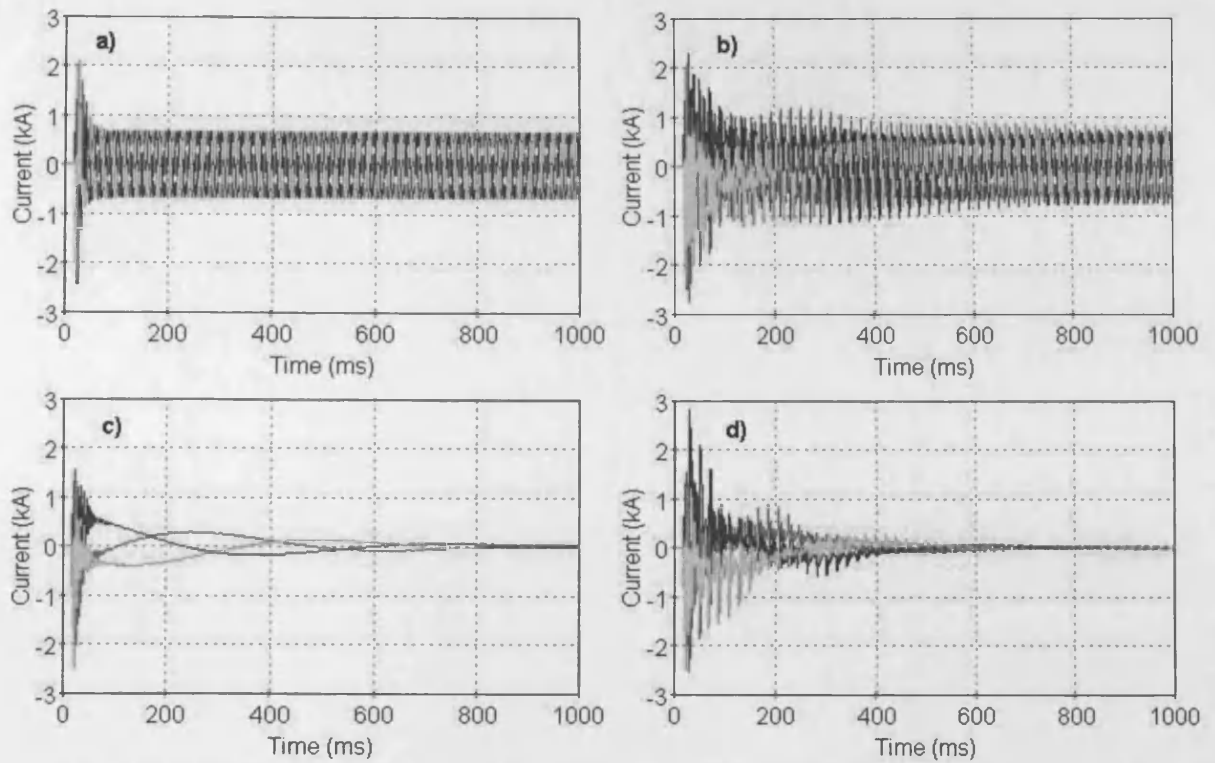
Fig. 7-4. Three phase current at the onshore connection point during energisation of a 90km export cable. Energisation of a) cable only, b) cable and transformers, c) cable and reactive compensation, d) cable, transformers and reactive compensation.
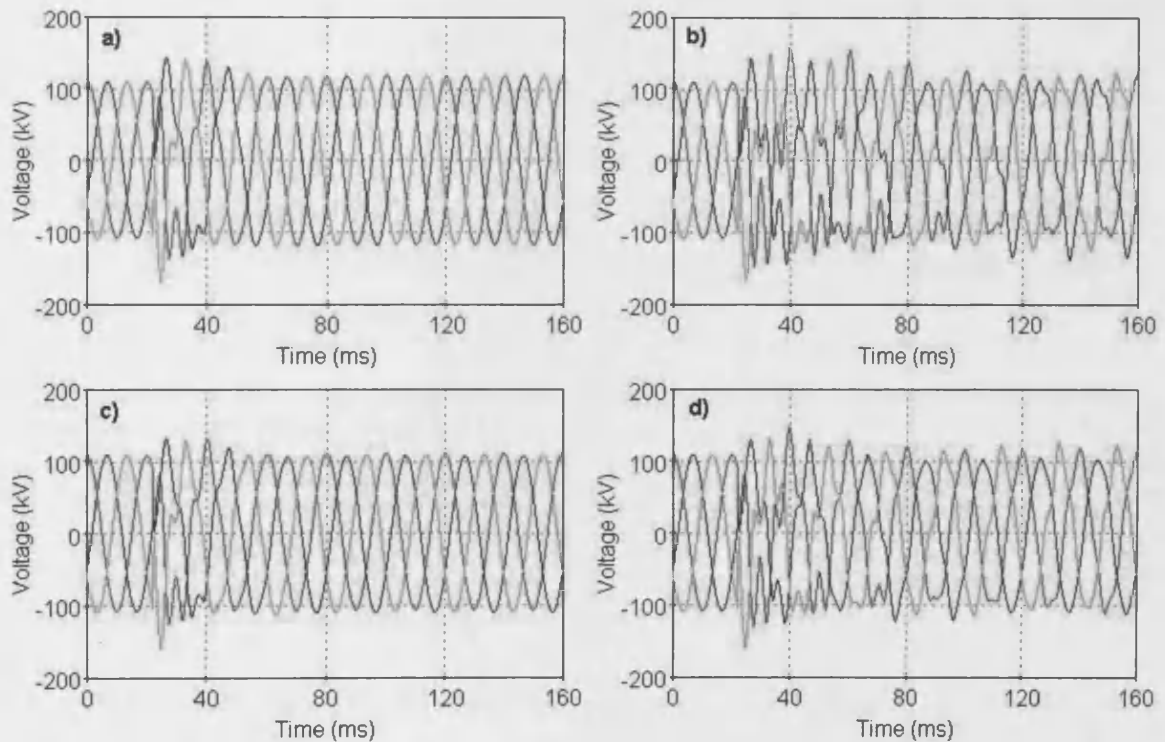
Fig. 7-5. Three phase voltage at the onshore connection point during energisation of a 90km export cable. Energisation of a) cable only, b) cable and transformers, c) cable and reactive compensation, d) cable, transformers and reactive compensation.

136
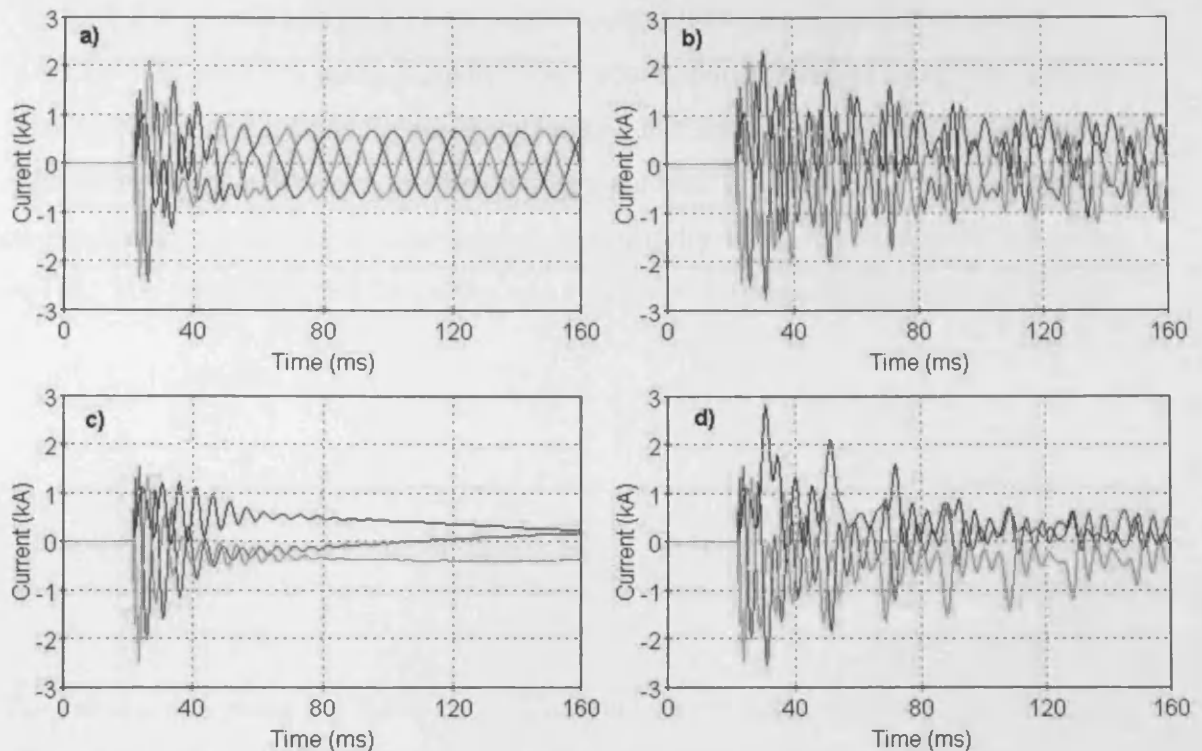
Fig. 7-6. Three phase current at the onshore connection point during energisation of a 90km export cable where a) to d) correspond to the configurations shown in Fig. 7-1.

7.2.1. SENSITIVITY TO ARMOUR PERMEABILITY

In Chapter 4 it was shown that the permeability of the armour had a more significant effect on long cables than on short (under 10km) cables. Therefore, the sensitivity of the overvoltage at the platform to the armour permeability for a cable length of 90km was simulated. The maximum overvoltage was found for armour relative permeabilities of 1, 10 and 100, as shown in Table 7-2.

Table 7-2. Effect of relative permeability on the maximum phase to ground voltage at the platform during energisation of a 90km cable.

	Relative Permeability		
	1	10	100
Max Voltage (kV)	200.1	199	198.1
Max Voltage (pu)	1.86	1.85	1.84

The results show that the relative permeability of the armour does not have a significant effect on the overvoltage at the platform. There was only a 1% increase in the overvoltage when the relative permeability was decreased from 100 to 1.

137

7.2.2. SENSITIVITY TO INSULATION AND SEMI-CONDUCTOR THICKNESS

In Chapter 5, both the main insulation and semiconductor layers were found to be 1mm thicker than that specified in data sheets. The sensitivity to different insulation and semiconductor thicknesses was therefore studied, to determine what effect it has on the energisation results. The relative permittivity was calculated using equation (4-10). The capacitance of the cables was calculated by rearranging equation (4-11):

$$C = \frac{2\pi\varepsilon_0\varepsilon_r}{\ln(r_2/r_1)}$$

(7-1)

The surge impedance was calculated as:

$$Z_C = \frac{1}{2\pi}\sqrt{\frac{\mu_0}{\varepsilon_0\varepsilon_r}}\,\ln(r_2/r_1)$$

(7-2)

The results are given in Table 7-3. The maximum voltage was not significantly affected by a change in either semiconductor or insulation thickness.

Table 7-3. Effect of semiconductor and insulation thickness on the platform voltage and current at the shore during energisation of a 90km export cable. The per unit value of current is calculated with Sbase = 200MVA.

	Semiconductor thickness (mm)			Extra insulation thickness (mm)		Semiconductor and extra insulation thickness (mm)
	0	1	2	1	2	1
Relative Permittivity, ε_r	2.3	2.40	2.74	2.3	2.3	3.12
Cable capacitance (uF/km)	0.201	0.191	0.202	0.192	0.183	0.239
Surge Impedance, Z_C (Ohm)	25.16	26.98	27.33	26.38	27.57	24.63
Maximum Platform Voltage (kV)	199	199.6	189.5	199.37	199.6	199.8
Maximum Platform Voltage (pu)	1.85	1.85	1.76	1.85	1.85	1.85
Peak Charging Current at the shore (kA)	2.4	2.51	2.67	2.35	2.27	2.7
Peak Charging Current at the shore (pu)	1.94	2.03	2.16	1.90	1.83	2.18
Peak (steady-state) Current at the shore (kA)	0.67	0.7084	0.747	0.64	0.61	0.786
Current (steady-state) at the shore (pu)	0.54	0.57	0.60	0.52	0.49	0.64

The charging current of the cable was significantly affected by the insulation and semiconductor thickness. In the manufacturer's data sheet [15], the charging current per phase at 50Hz is given as 5.6A/km. This corresponds to 5.6 x 90 = 504A rms

(0.71kA peak) charging current for the 90km export cable, assuming that there are no losses. The simulated steady state current was closest to this value when 1mm semiconductor thickness was added to each side of the main insulation (as shown in the second column of Table 7-3). Depending on the insulation and semiconductor thickness, the charging current varied from being 10% below that stated in the data sheets to 20% above the stated charging current in the data sheet. This should be taken into account when carrying out studies to determine the amount of reactive compensation required.

7.2.3. EFFECT OF POINT-ON-WAVE OF SWITCHING

The closing time (point-on-wave) of the circuit breaker influences the generated overvoltage and may occur anywhere on the power frequency cycle. A systematic switching study, as described earlier, was carried out and the maximum peak phase-to-ground voltage at the platform and peak current at the shore was then determined for each of the 133 simulations. This was carried out for export cable lengths of 30, 50, 70 and 90km and the results are shown in Fig. 7-7. The probability of occurrence shown in Fig. 7-7 is the number of occurrences divided by 133, the total number of simulated switching events.
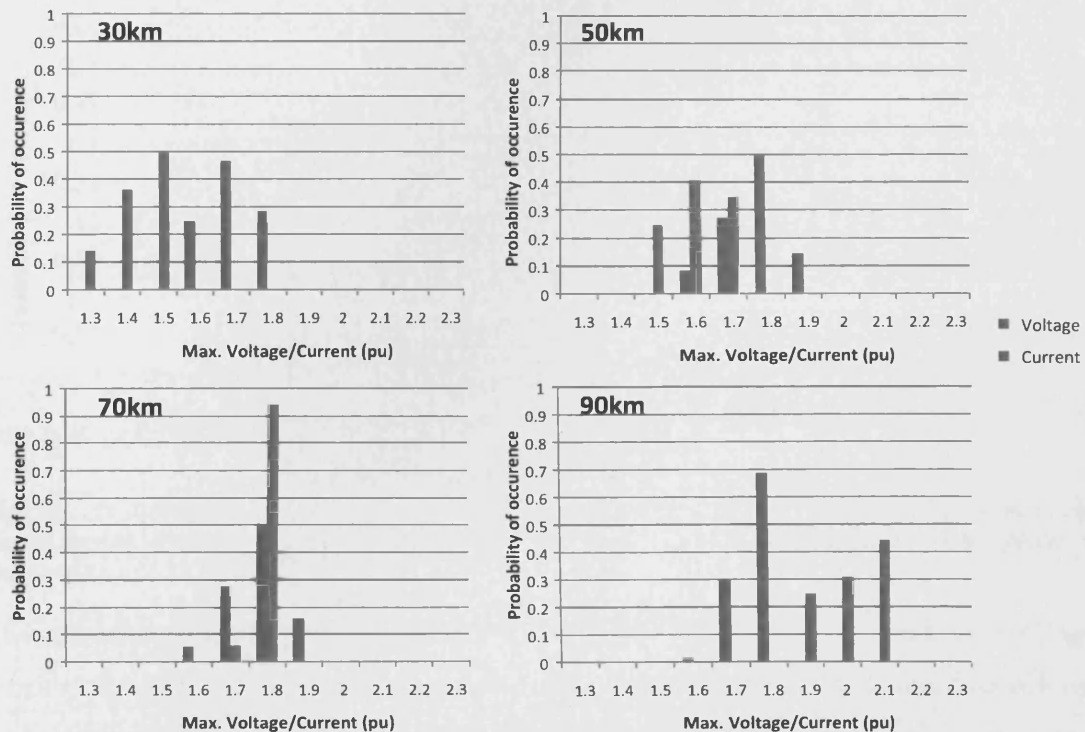
Fig. 7-7. Probability of occurrence for maximum platform voltage and maximum current at the shore during energisation of a 30km, 50km, 70km and 90km export cable. Simulations carried out with no pole-span.

The lowest currents occurred for the 30km cable, with a mean value of 1.43pu. The current increased as the cable length increased, with a mean value of 2.02pu for a cable length of 90km. The mean value of the maximum platform voltage did not vary as significantly when the cable length was increased.

7.2.4. SENSITIVITY TO POLE-SPAN

The three phases of a circuit breaker were previously assumed to close at the same time (i.e. with no pole-span). In reality, the three phases of a circuit breaker will start to allow the flow of current with a random delay, due to mechanical dispersions and the occurrence of pre-strikes. The time difference between phases which current starts to flow is called the pole-span. A systematic switching study was carried out so that the effect of circuit breaker pole-span could be studied on the transients experienced during energisation of the 90km cable only, with the results shown in Fig. 7-8. Phase a of the circuit breaker was set to close from 20ms, with 133 steps of 0.05ms. For each of these steps, the pole-span between phase a and b and between phase a and c was varied from 0 to 1ms in 0.1ms steps (10 steps total). This results in 133 x 10 x 10 = 13,300 simulations.
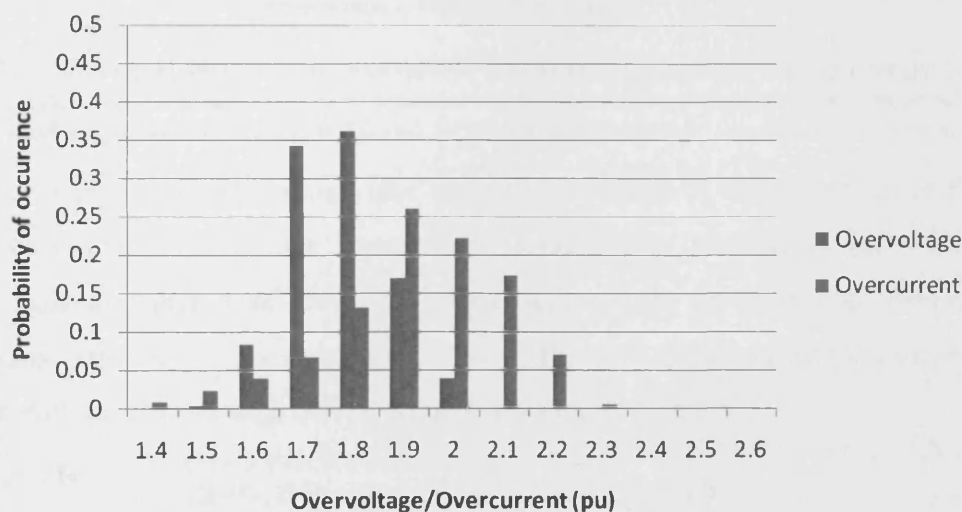
Fig. 7-8. Probability of occurrence for maximum platform voltage and maximum current at the shore during energisation of a 90km export cable. A pole-span of 1ms between phases is included.

The mean overvoltage was 1.77pu, which was 0.6% lower than the mean overvoltage when pole-span was not included. There was a larger deviation of the overvoltage when pole-span was included and the maximum overvoltage which occurs when pole-span was included is 2.02pu compared to 1.84pu when pole-span was not included. The maximum overcurrent which occurs when the pole-span was included was 2.29pu compared to 2.10 when pole-span was not included. The results show

that the inclusion of pole-span increased the maximum currents and voltages by up to 10% compared to when pole-span was not included.

7.2.5. SENSITIVITY TO TRANSFORMER IMPEDANCE

The transformer impedance was originally 15% with an X/R ratio of 40. Energisation of the cable with transformers and reactors connected was simulated for transformer impedance ranging from 20 to 10% with an X/R ratio of each transformer of 40. The results are shown in Fig. 7-9.
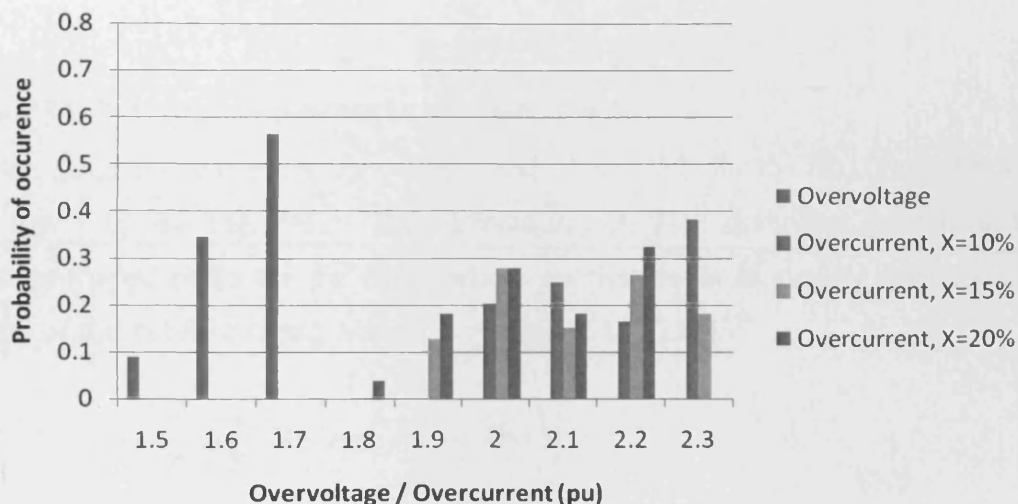
Fig. 7-9. Probability that an Overvoltage and overcurrent occurs during energisation of a 90km export cable with main offshore transformer and reactive compensation connected. Results for transformer impedance of 10, 15 and 20%. Simulations were carried out with no pole-span.

The maximum overvoltage (the maximum voltage at the platform) at the platform was not affected by the transformer impedance. The maximum overcurrent (the maximum current at the shore) that occurs with no pole-span decreases as the transformer impedance increases. When the X/R ratio was varied from 30 to 50, the maximum overvoltage and overcurrent was not affected.

7.2.6. EFFECT OF OTHER CABLES IN THE SYSTEM

The effect of other cables in the system was investigated for the energisation of a 90km export cable. Three cases were considered, the first was the energisation of the cable directly from the grid, the second was the energisation of the cable through a 30km single-core onshore cable and the third was the energisation of the cable when another 90km export cable was already connected. These configurations are shown in Fig. 7-10.
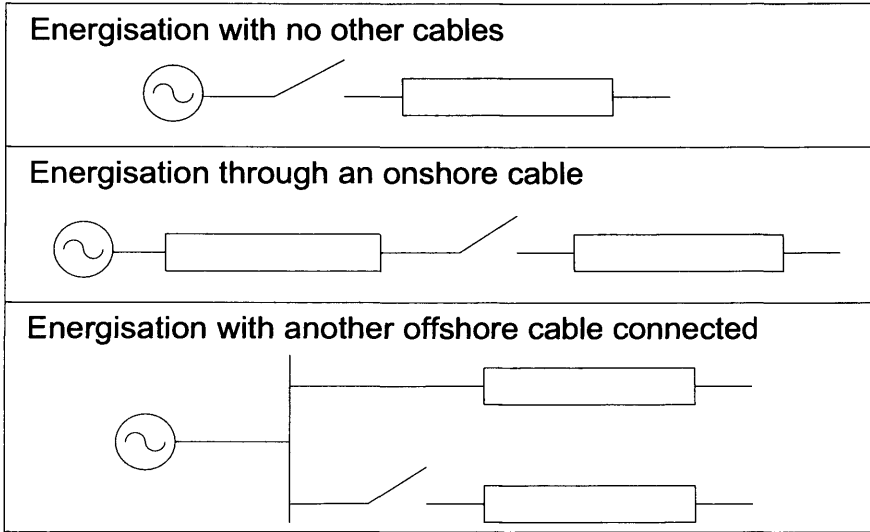
Fig. 7-10. Different configurations for energising a cable.

The voltage and current at the onshore end of the cable for the three cases are shown in Fig. 7-11 and Fig. 7-12. The currents in Fig. 7-12 show that there is an initial square-shaped pulse for the cases where another cable is already energized. The front of this cable charging current is expressed by [153]:

$$i_i(t) = \frac{u_m - u_t}{Z_1 + Z_2}\left[1 - \exp\left(-\frac{Z_1 + Z_2}{L}t\right)\right]$$

(7-3)

Where u_m is the peak of the applied voltage (V), u_t is the trapped voltage on the cable being switched (V), Z_1 and Z_2 are the surge impedance (Ω) of the submarine cable and energised cable respectively and L is the total inductance between the two cables.

Differentiating equation (7-3) at t=0 will give the maximum initial rate of change of this pulse:

$$\left(\frac{di}{dt}\right)_0 = \frac{u_m - u_t}{L}$$

(7-4)

Since L (the inductance between the two cables) was arbitrarily small, the rate of change of inrush current is high. This means that the rate of change of voltage is also high.

The rate of rise of voltage at the onshore end of the cable when there were no other cables energized was 0.12kV/μs. The results in Fig. 7-11 show that the rate of rise of voltage is increased when the cable is energized through the onshore cable and when

142

another offshore cable is connected. In both of these cases, the rate of rise of voltage occurred over half the simulation time-step (1μs).
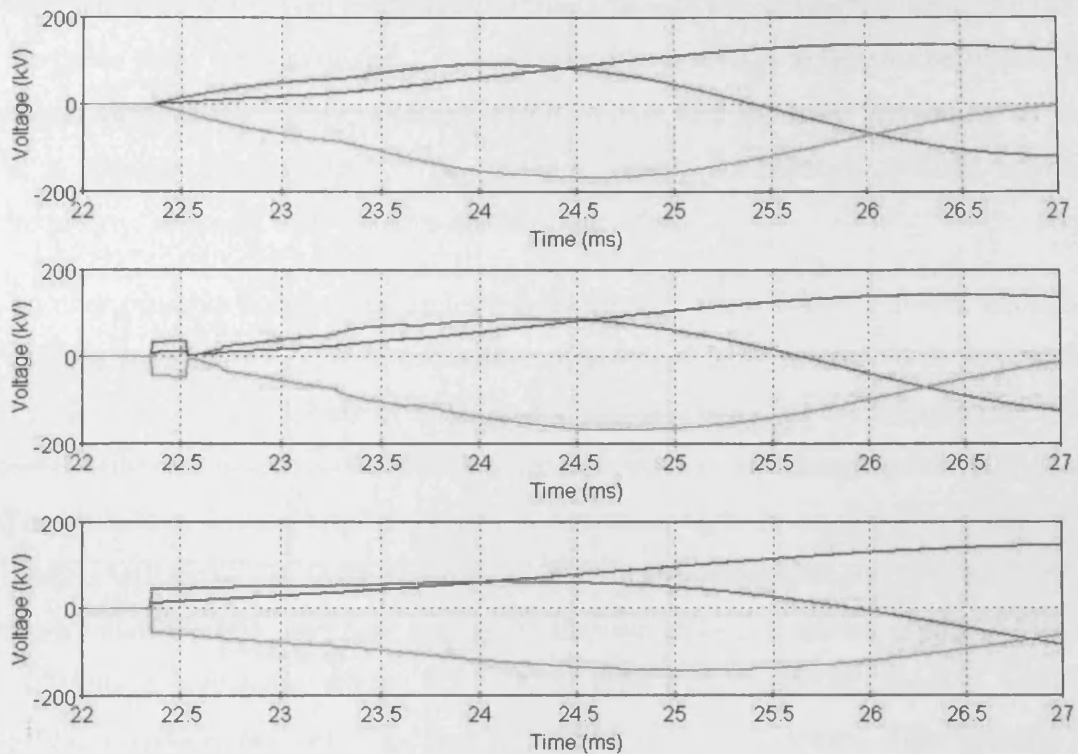
Fig. 7-11. Three phase voltage at the onshore end of a 90km cable during energisation. The top graph shows energisation with no other cables, middle graph shows energisation through a 30km onshore cable and the bottom graph shows energisation when another 90km offshore cable is connected.
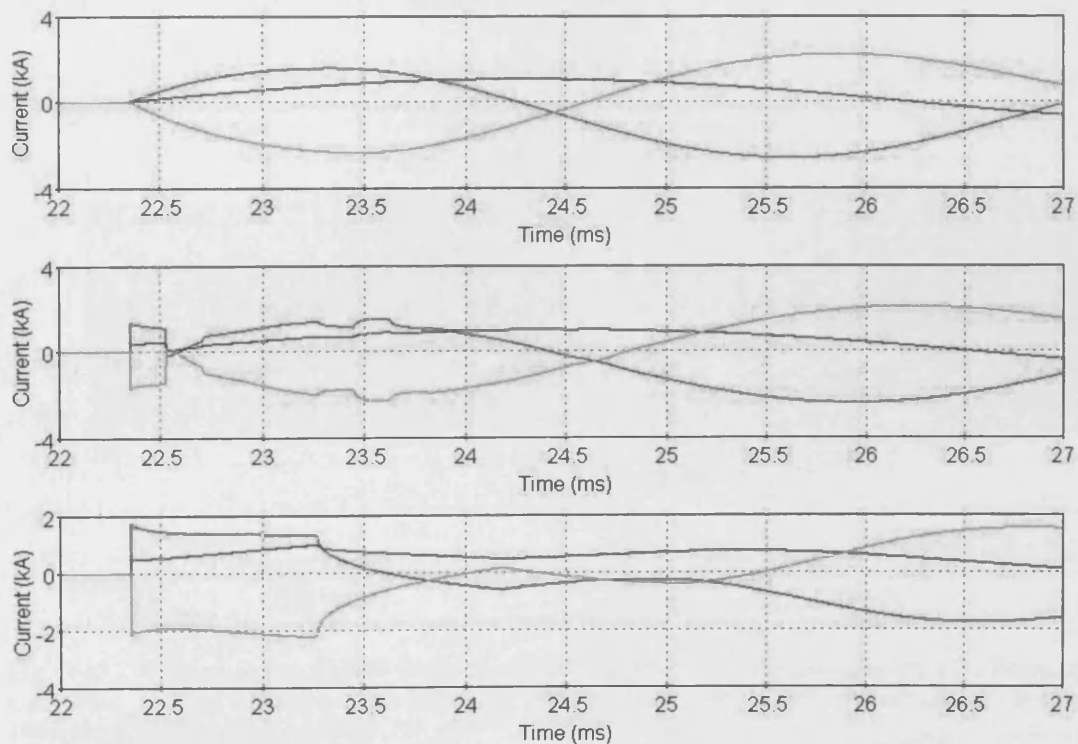
Fig. 7-12. Three phase current at the onshore end of a 90km cable during energisation. The top graph shows energisation with no other cables, middle graph shows energisation through a 30km onshore cable and the bottom graph shows energisation when another 90km offshore cable is connected.

143

7.2.7. TRANSFORMER INRUSH CURRENTS AND RESONANT OVERVOLTAGES

In Fig. 7-3 it was shown that the overvoltages were sustained over a longer period of time when the cable was energized with the offshore transformers compared to when the cable only was energised. This sustained overvoltage is due to the transformer inrush currents during energisation which contain odd and even harmonics. If there is a resonant frequency of the network which corresponds with a harmonic frequency, resonant overvoltages could occur [109].

Another possible connection strategy is to energise the offshore network through an onshore transformer. The energisation of a 90km cable connected to the offshore transformers, as described in Section 7-2 was compared to the energisation of the same network through a 400/132kV onshore network (switching on the 400kV side). The switching instant was chosen to be the same in both cases (at the peak of the phase a voltage). The three phase voltages at the onshore connection point (between the submarine cable and land cable) for the two cases are shown in Fig. 7-13. The overvoltage was more severe in terms of both magnitude and duration when the offshore network was switched through the onshore transformer. This indicates that resonant overvoltages will be more severe if the offshore network is energized on the high voltage side of an onshore transformer than if the offshore network is energized through an already energized onshore transformer.
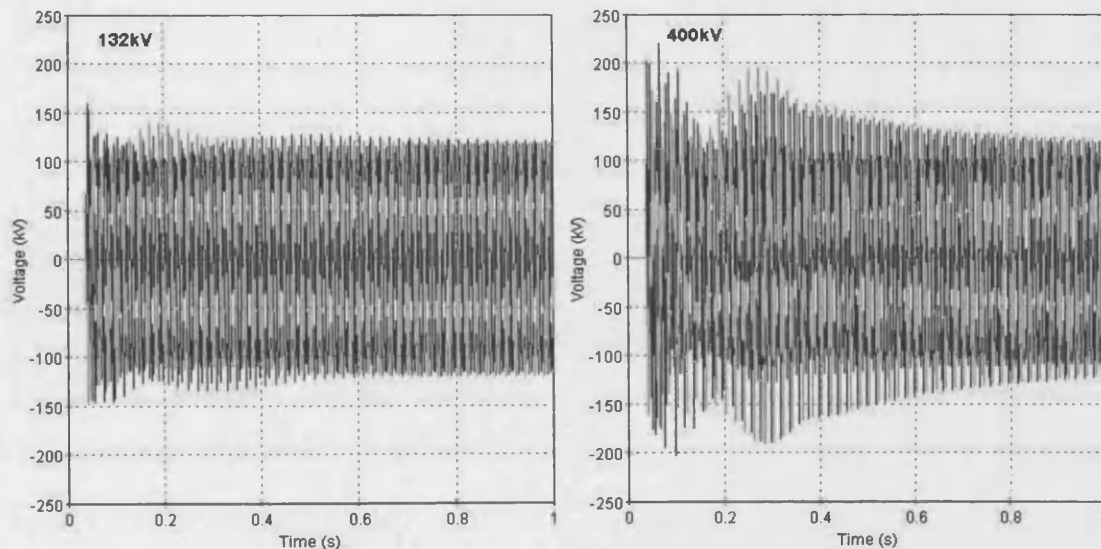
Fig. 7-13. Voltage at the 132kV onshore connection point during energisation of a 90km cable connected to two offshore transformers; directly from the 132kV network and through a 400/132kV onshore transformer.

As the submarine export cable length increases, the resonant frequency of the network will decrease. Since the harmonic content of the transformer inrush current

is higher for lower order harmonics [109], it is likely that harmonic resonances will become more severe as the cable length increases.

7.2.8. RE-CLOSING ON A CABLE WITH TRAPPED CHARGE

When the cable is disconnected, there will be a trapped charge. Fig. 7-14 shows the current across CB01, the voltage at the grid (source) side, at the wind farm (load) side of the circuit breaker and the voltage across CB01 for one of the phases during disconnection of an unloaded 90km cable.
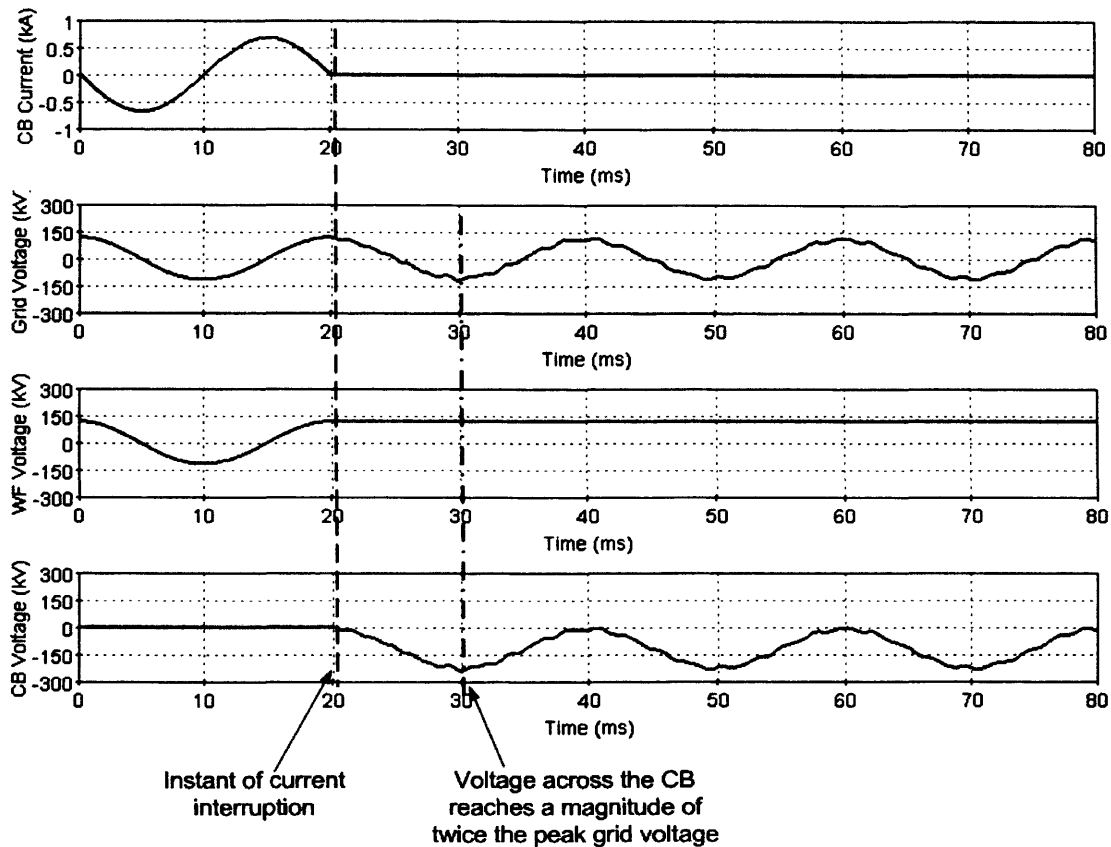
Fig. 7-14. Disconnection of a 90km cable – capacitive current switching.

For an unloaded cable length of 90km, the circuit breaker was required to break 474A rms. This exceeds typical values of rated capacitive breaking duty for 132kV SF6 circuit breakers, which is normally under 200A rms. According to [153], the circuit breaker manufacturer should be consulted if the rated capacitive breaking duty is shown to be exceeded. In section 6.3.1 of [153] the breaking of this type of capacitive current (caused by the unloaded cable) is stated as not posing a problem for circuit breakers of present design, but the possible higher peak recovery voltage present on interruption could be a problem.

As shown in Fig. 7-14 the voltage was at its peak when the current was interrupted. The cable had a trapped charge and the voltage remained constant at the value it had

at current zero (namely, the peak value of the grid voltage as shown on the "WF Voltage" waveform in Fig. 7-14). When the grid voltage had the opposite polarity to the constant voltage on the cable, there was nearly two times the peak value of the grid voltage. In this case, the peak voltage across the circuit breaker CB01 was 239kV, which is below the maximum TRV peak of 296kV specified in Table 6-1 for the OP1-OP2 test duty but above the T10 test duty.

It should be noted that the contacts of the circuit breaker may not be fully open by the time the peak voltage across CB01 occurs, which could result in a dielectric breakdown between the contacts and a further increase in the voltage. These dielectric breakdowns of capacitive current interruption are divided into two categories; reignition (where dielectric breakdown occurs within the first ¼ of the power frequency cycle following interruption) and restrike (where dielectric breakdown occurs after the first ¼ of the power frequency cycle following interruption). Restrikes will lead to further overvoltages (maximum 3pu for a single restrike) whilst reignitions will not produce any overvoltages (maximum 1pu) [153]. The model used for the 132kV circuit breaker was ideal and did not include the ability to represent restrikes or reignitions.

A systematic study was carried out to determine the switching time which causes the worst case in terms of the maximum overvoltage at the platform. This occurs when the circuit breaker re-closes at 112ms. The three phase voltage and current across CB01 during this re-closing operation is shown in Fig. 7-15.

The peak current during re-closing was 5.44kA (4.4pu) in this case, which was over twice the value during energisation with no trapped charge. This was due to the voltage across the circuit breaker being greater during the re-closing operation than during energisation.

The three phase voltages at the onshore and offshore ends of the 90km cable are shown in Fig. 7-16. The peak overvoltage was 256kV (2.38pu) at the onshore end and 327kV (3.03pu) at the offshore end of the cable. These values were over 50% higher than when the cable was energized with no trapped charge. The peak phase to phase voltage at the offshore end of the cable was 542kV (5.03pu).
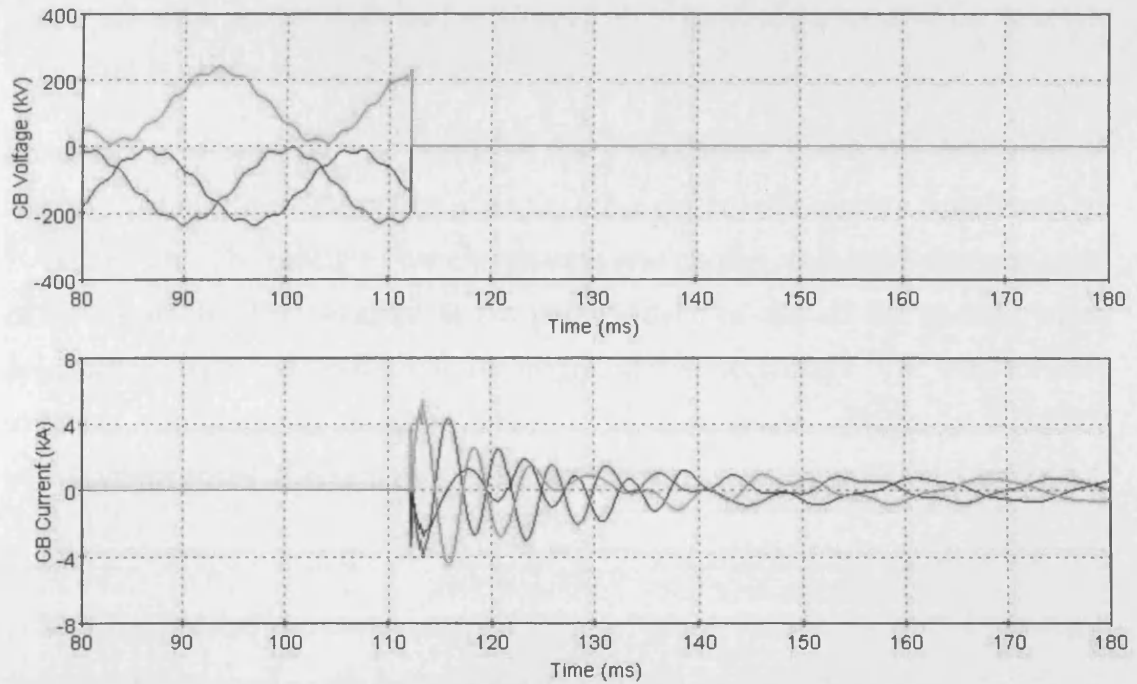
Fig. 7-15. Three phase voltage and current across CB01 during re-closing of a 90km unloaded cable. CB01 is opened at 20ms then re-closed at 112ms.
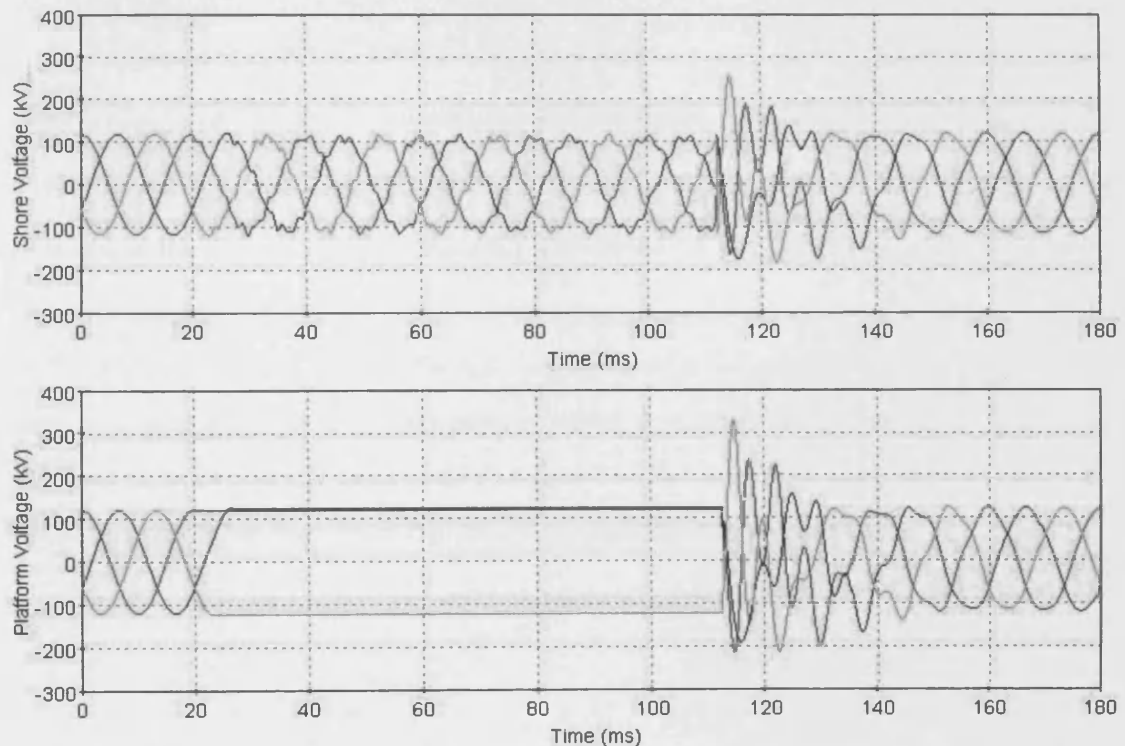
Fig. 7-16. Three phase voltage at the onshore end (top) and offshore end (bottom) of the 90km unloaded cable during a re-closing operation. CB01 opens at 20ms and re-closes at 112ms.

7.3. ENERGISATION OF AN ARRAY

Simulations of the energisation of an array were compared with measurements at an offshore wind farm in Chapter 5. In this section, other configurations for the energisation of an array are considered. The circuit breaker was modelled as a VCB

and is the same as that described in Chapter 4. The configuration of the example wind farm is shown in Fig. 7-1.

Energisation of array A was simulated for a case when it was the first array to energise and for three other cases when the other arrays were already connected (i.e. B, BC, BCD). The timing of the energisation was chosen so that the first pre-strike of the circuit breaker occurred at the peak voltage of one of the phases, which produced the worst case in terms of the magnitude of overvoltage. The wind turbines were not generating during energisation. The three phase voltages at the 33kV busbar which connects arrays A to D and at WT_A1 are shown in Fig. 7-16.

The initial voltage step at the platform, $\Delta V_{platform}$, was largest when the array was first to be energized and decreased as the number of arrays already connected increased, as shown in Fig. 7-17. This is explained by considering Equation (7-5):

$$\Delta V_{platform} = \frac{Z_{platform}}{Z_{platform} + Z_{cable}} V_0 \qquad (7\text{-}5)$$

Where $Z_{platform}$ is the surge impedance at the source side of the VCB, Z_{cable} is the surge impedance of the array cable being energized and V_0 is the voltage at the platform at the instant of energisation. The value of $Z_{platform}$ reduces for each array which is already energized. The lower surge impedance at the source side of the VCB also means that any reflected voltage wave coming from the array being energized sees a lower surge impedance when it reaches the busbar at the platform, resulting in a reflection back into the array. The initial voltage step at the wind turbine increased as the amount of arrays already connected increased.

First radial to connect

Radial B connected

Radials B & C connected

Radials B, C & D connected

Oscillations due to cable-transformer interaction

Oscillations due to pre-strikes
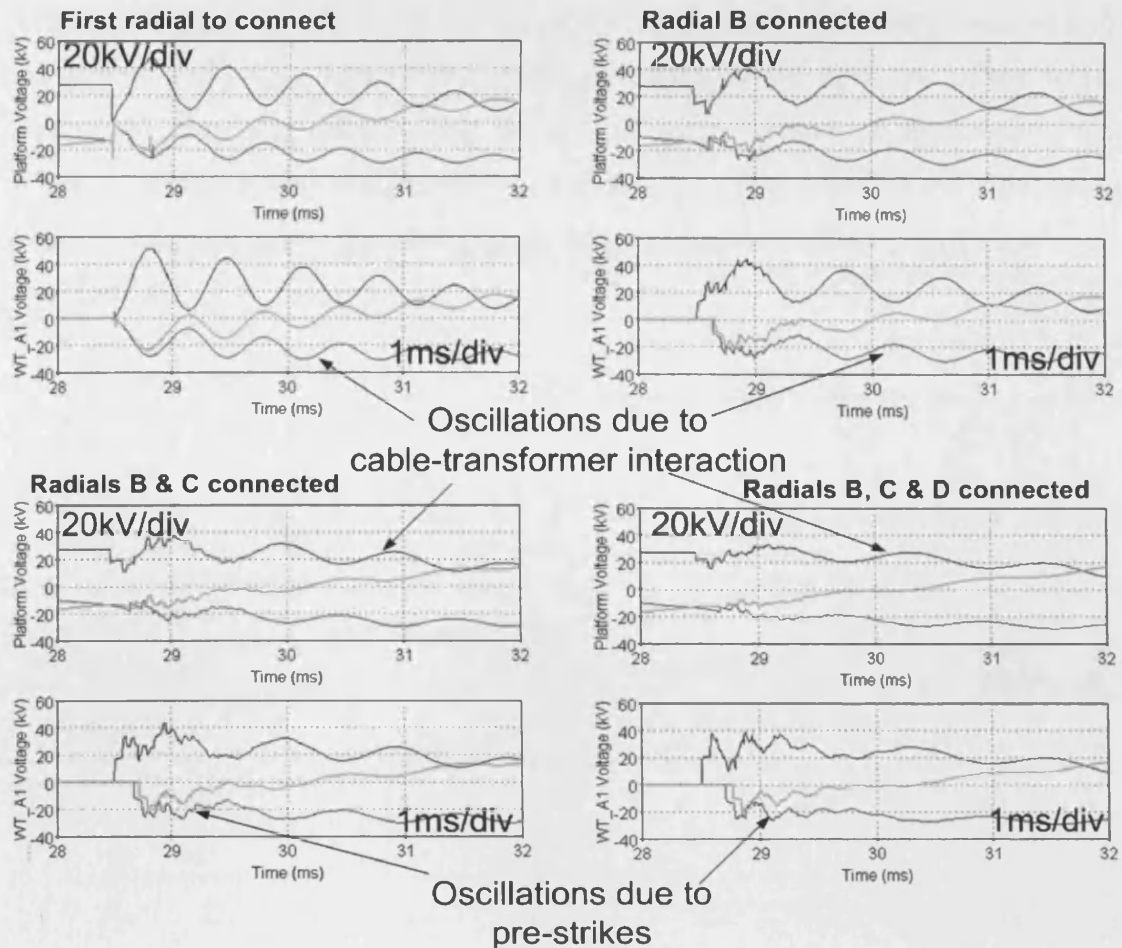
Fig. 7-17. Three phase voltages at the 33kV offshore platform and WT_A1 during energisation of array A.

The results in Fig. 7-17 show that the highest overvoltage (2pu at WT_A1) occurred when array A was first to connect with a corresponding rate of change of voltage is 0.2kV/μs. For the cases when all other arrays were already connected, the overvoltage was lower (1.43pu at WT_A1), however the rate of change of voltage at the wind turbine was significantly increased to 21kV/μs and a number of voltage steps or 'oscillations' occurred due to the pre-strikes. Oscillations due to cable-transformer interaction occurred in all cases and the corresponding frequency was higher when radial array A was first to connect than when other arrays were already connected.

The voltage wave in one phase as it propagates through an array during energisation when array cables B, C and D are already energized is shown in Fig. 7-18. There was a high rate of change of voltage close to the vacuum circuit breaker at the platform. As the wave reached each successive turbine of array A, it became rounded due to the damping in the cable. When the wave reached the last wind

149

turbine in the array (WT8 in the example shown), the wave was visibly rounded and the voltage was nearly doubled due to the wave meeting the open end of the array. Due to this doubling effect within the arrays, surge arresters located within the offshore substation may not provide good overvoltage protection for the equipment located along the array. For this reason, surge arresters should be located at each wind turbine.
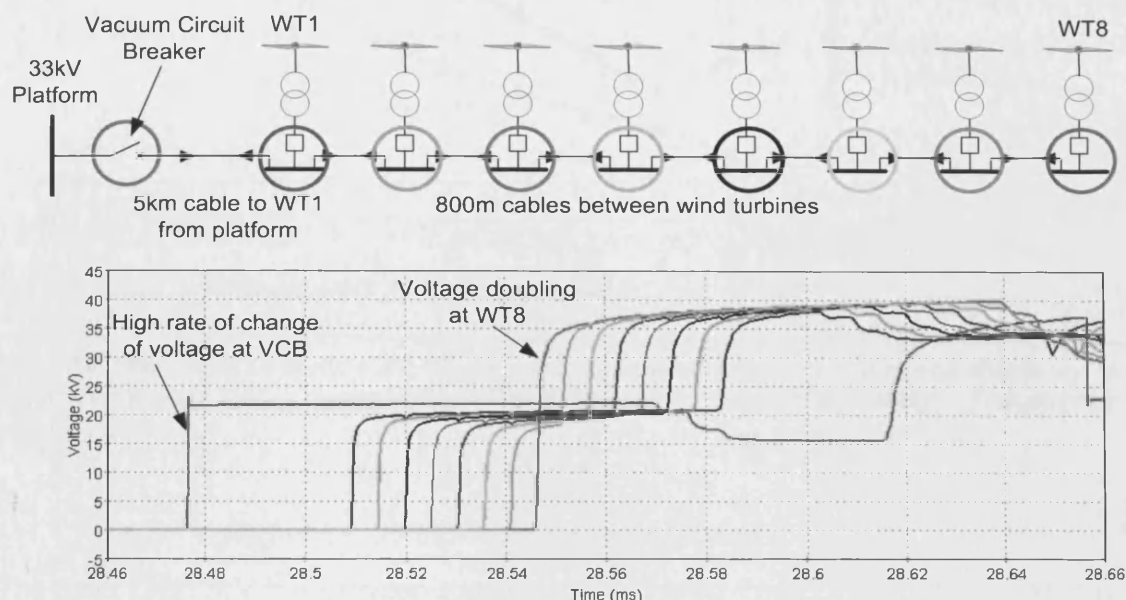
Fig. 7-18. Voltage wave in one phase as it propagates through an array during energisation when all other arrays are already energised. The red waveform represents the voltage at the array side of the circuit breaker. The other waveforms show the voltage seen at the base of each wind turbine. The different coloured circles from wind turbine 1 (WT1) to wind turbine 8 (WT8) correspond to the colours in the graph.

7.3.1. EFFECT OF CABLE LENGTH

The cable length between the platform and WT_A1 was varied for the case when radial array A was the first to connect. The maximum voltage at the platform, WT_A1 and the corresponding frequency of oscillations are shown in Fig. 7-19. The maximum voltage at the platform was highest (2.02pu) when the cable length was 1km and reduced to 1.8pu when the cable length was 10km. The maximum voltage at WT_A1 was higher than the maximum voltage at the platform and had a steady value of around 2.08pu for all cable lengths. The frequency of oscillations was nearly 2kHz when the cable length was 1km and decreased to just under 1.2kHz when the cable length was 10km. The frequency of oscillations decreased as the cable length increased due to the higher capacitance of the longer cables, which reduced the resulting frequency.
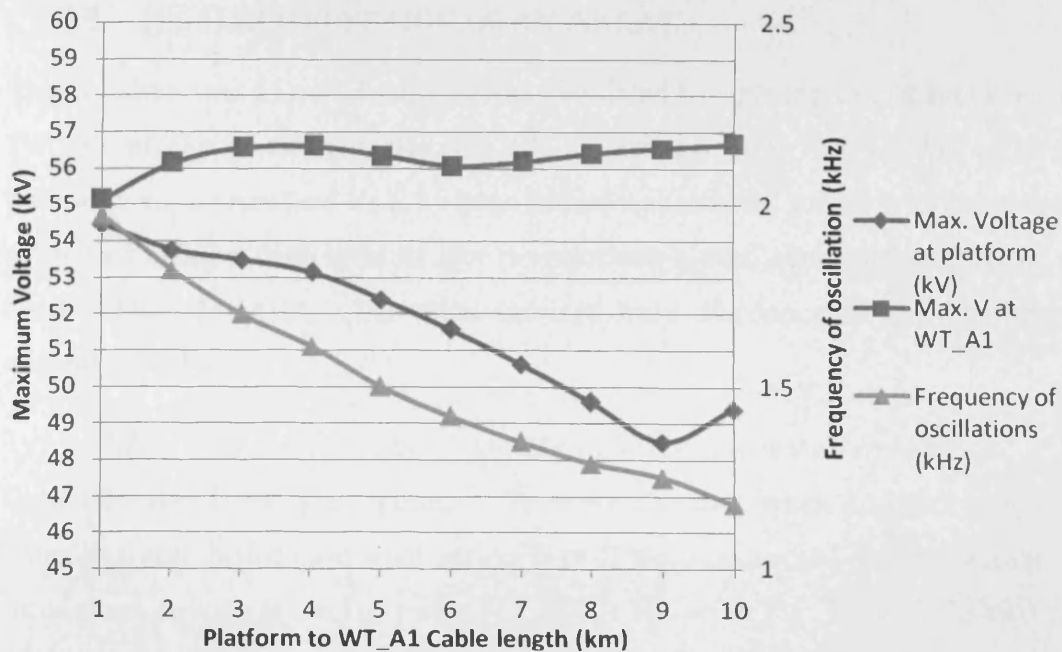
Fig. 7-19. The effect of array cable length on the amplitude of overvoltages and frequency of initial oscillations during energisation of radial array A (closing of CB06). Transformer impedance = 15%.

7.3.2. SENSITIVITY TO TRANSFORMER IMPEDANCE

The main 132/33kV transformer impedance was varied from 15% to 8% for the case when radial array A was first to connect. The maximum voltage at the platform and WT_A1 are given in Table 7-1 along with the frequency of the initial oscillations and maximum current through circuit breaker CB06.

Table 7-4. Effect of transformer impedance during energisation of radial array A.

Transformer impedance (%)	Max Voltage at the platform (kV)	Max Voltage at WT_A1 (kV)	Frequency of initial oscillations (kHz)	Max. current (A)
15	53.47	56.56	1.7	1441
12	52.87	56.17	1.9	1455
10	51.90	55.89	2.0	1475
8	49.62	54.43	2.2	1487

As the transformer impedance decreased from 15% to 8%, the maximum voltage at the platform decreased from 1.98pu to 1.84pu and the maximum voltage at WT_A1 decreased from 2.10pu to 2.02pu. The frequency of initial oscillations increased as the transformer impedance decreased.

7.4.   DISCONNECTION OF AN ARRAY

The disconnection of radial array A was simulated by opening circuit breaker CB06. The rate of change of dielectric strength, A_A, of the VCB was 13V/μs. The wind turbines were represented by a 'voltage behind a reactance' model with the reactance calculated using a fault level of 1pu (to represent a FRC wind turbine), based on a rated output of 3MVA. The wind turbines were disconnected at 50ms after the opening of CB06.

7.4.1. DISCONNECTION OF AN ARRAY DURING NORMAL OPERATION

Circuit breaker CB06 was opened at 70ms for the case when no other arrays were connected and for the case when arrays B to D were connected and generating. The three phase voltage at the array side of CB06 is shown in Fig. 7-20 for the two cases. There were multiple re-strikes in each case which caused voltage escalation.

The overvoltage reached 134kV (5pu) when no other arrays were connected and 95kV (3.53pu) when arrays B to D were connected and generating. Although the overvoltage when no other arrays were connected was below the Lightning Impulse Withstand Voltage (LIWV) specified for 33kV equipment (170kV) by IEC 60071-1, it exceeds Switching Impulse Withstand Voltage (SIWV) values calculated using a test conversion factor given by IEC 60071-1[1].

---

[1] The LIWV of 36kV equipment is 170kV peak according to IEC 60071-1. Although SIWV values at 33kV are not provided in standards, a test conversion factor (given in IEC 60071-1) can be used to convert the LIWV to a SIWV value. The test conversion factor is 1.25 for GIS, 1.1 for liquid-immersed insulation and 1 for solid insulation. The SIWV in the 33kV GIS will be 1/1.25 times 170kV = 136kV (5.05pu). The SIL for the 33kV side of the wind turbine transformers will be 1/1.1 times 170kV = 154.5kV (5.7pu). When the safety factor, Ks, is also included the SIWV is further reduced. For internal insulation, Ks = 1.15. The SIWV in the 33kV GIS is then 1/1.25 x 1/1.15 x 170kV = 118kV (4.4pu). The SIWV for the 33kV side of the wind turbine transformers is: 1/1.1 x 1/1.15 x 170kV = 134kV (5.0pu).
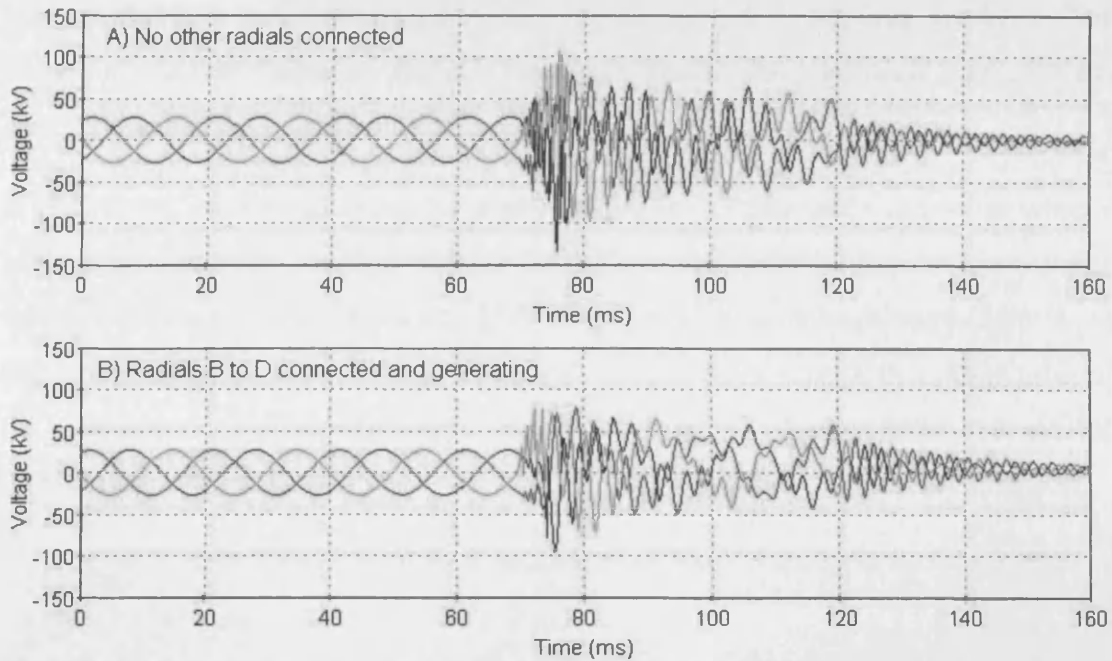
Fig. 7-20. Three phase voltage at the Array side of CB06 when Array A is disconnected at 70ms when the wind turbines were generating. Case A) is when Array A disconnected without any other Arrays connected and case B) is when Array A is disconnected whilst Arrays B to D were connected and generating.

7.4.2. SINGLE LINE TO GROUND FAULT

A single phase fault was applied at the base of WT_A1 which has a 100m cable to the wind turbine transformer. The faulted phase voltage at the WT_A1 and WT_A8 transformer terminals is shown in Fig. 7-21.
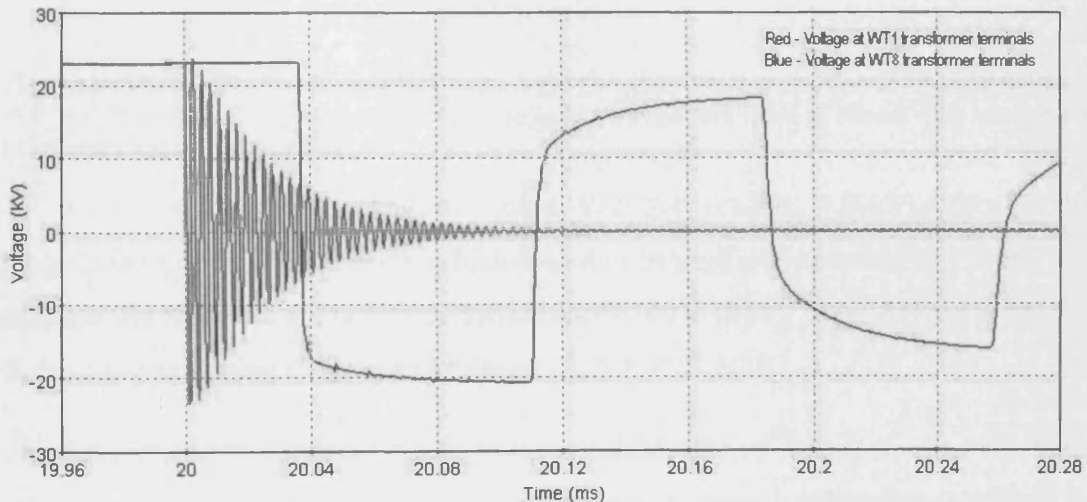
Fig. 7-21. Phase-to-ground voltages at the first wind turbine transformer (red) and last transformer in an array (blue) after a single phase fault has been applied at the base of the first wind turbine.

The fault caused a step voltage and travelling waves similar to the case shown for energization, however there was a much higher repetition frequency due to the shorter cable length to the first reflection point. The frequency of the voltage wave

153

between the fault location and the closest transformer, WT_A1, was 350 kHz. The wave had a lower frequency (6.7kHz) and was heavily damped once it reaches the last transformer (WT_A8) in the array.

In [94] it was shown that excessive overvoltages due to resonance can occur when a cable is connected to the high voltage side of a transformer whilst the low voltage side of the transformer is unloaded. If the frequency of the voltage wave (350kHz in this case) is close to one of the frequencies where there is a peak in voltage ratio of the transformer, high overvoltages could occur on the low voltage side of the transformer.

7.4.3. DISCONNECTION OF SINGLE PHASE FAULT WHEN WIND TURBINE GENERATORS WERE NOT CONNECTED

The single phase fault described in Section 7.4.2 was cleared by opening CB06 at 50ms. The three phase voltage at WT_A1 is shown in Fig. 7-22. The wind turbine generators were not connected.
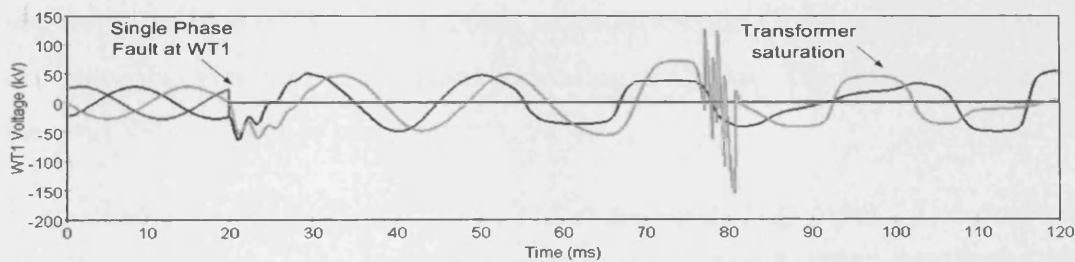
Fig. 7-22. Three phase voltage at WT_A1. A Single phase fault is applied at 20ms to the base of WT_A1. The circuit breaker CB06 starts to open to clear the fault at 50ms. The wind turbine generators are not connected.

As shown in Fig. 7-22, the voltage at WT_A1 reaches 150kV (5.6pu) during disconnection of radial array A which was due to multiple restrikes in CB06. This exceeds the SIWV for 33kV transformers of 134kV (5pu), once the test-conversion factor has been applied to the LIWV specified in IEC 60071-1.

The three phase voltage and current across CB06 when it opens to clear the fault is shown in Fig. 7-23. There were 5 restrikes which caused voltage steps with a very fast front and a high frequency current through CB06.

Following interruption of the current, the voltage has a square wave shape which is caused by the saturation of the wind turbine transformers.

154
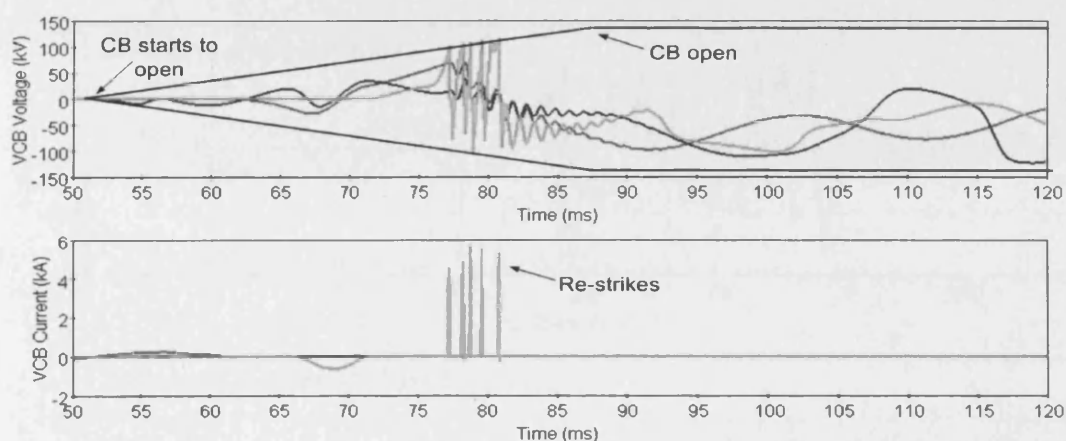
Fig. 7-23. Three phase voltage and current across CB06 when it opens to clear the Single phase fault at WT_A1. The wind turbine generators are not connected.

7.4.4. DISCONNECTION OF A SINGLE PHASE FAULT WITH WIND TURBINES GENERATING

The clearing of a single phase fault (with an ideal circuit breaker) at the base of WT_A1 was shown to cause very high overvoltages in Chapter 6. In this Chapter, a VCB model was used instead of the ideal circuit breaker. A single phase fault was applied at the base of WT_A1 at 20ms. Circuit breaker CB06 then cleared the fault at 70ms. The wind turbines stopped generating at 120ms. The three phase voltage at the array side of CB06 is shown in Fig. 7-24.

The inclusion of the VCB model resulted in multiple re-ignitions. The overvoltage was 185kV (6.87pu) when no other arrays were connected. This exceeds the LIWV for 33kV equipment (the LIWV is 170kV) and far exceeds the SIWV for the wind turbine transformers (the SIWV is 134kV) once the test-conversion factor is applied to convert the LIWV into a SIWV value. When arrays B to D were connected and generating, the overvoltage was lower 167kV (6.20pu), however this overvoltage still exceeds the SIWV for the wind turbine transformers.
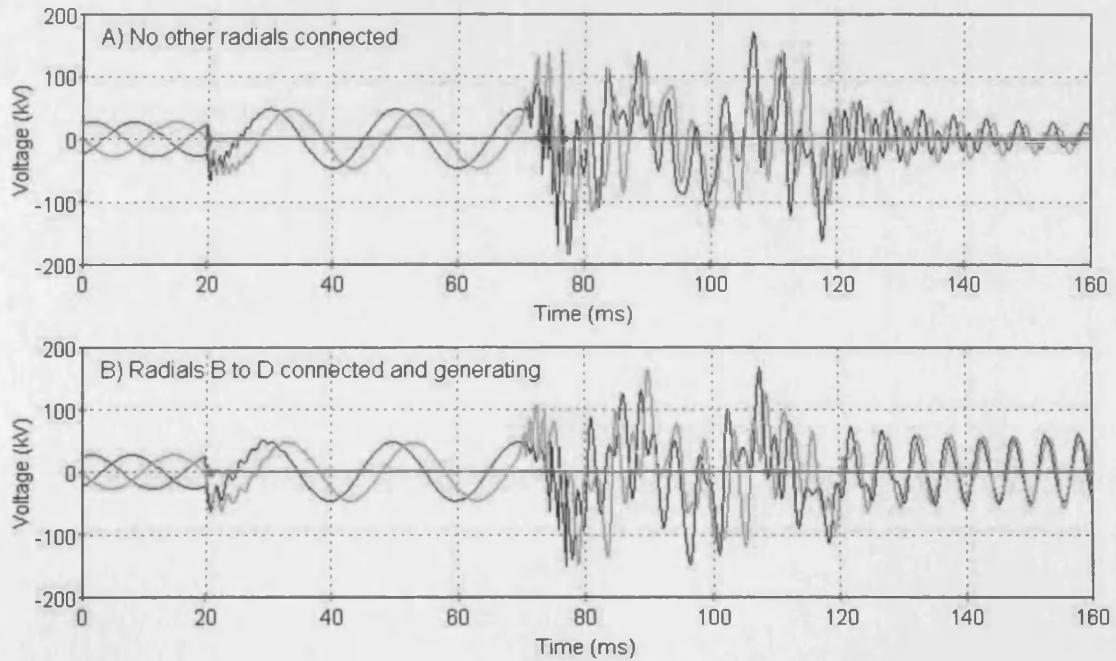
Fig. 7-24. Three phase voltage at the array side of CB06 when radial array A is disconnected at 70ms following a single phase fault at 20ms. The wind turbines are generating until 120ms. Case A) is when array A disconnected without any other arrays connected and case B) is when array A is disconnected whilst arrays B to D are connected and generating.

The waveforms in Fig. 7-24 (where CB06 was represented by the VCB model) can be compared with Fig. 6-8 (where CB06 was represented by an ideal circuit breaker). The overvoltage in Fig. 6-8 reached 130kV (4.8pu), which was lower than when the VCB model was included. It is therefore important to include the VCB model when determining overvoltages within the array when disconnecting a single-phase fault.

When the VCB model was included, there were 'steps' in the voltage due to the multiple reignitions, as shown in Fig. 7-25. The rate of change of voltage during these steps was just under 1kV/µs when no other arrays were connected. When arrays B to D were connected and generating the rate of change of voltage during these steps was significantly higher at 85kV/µs.
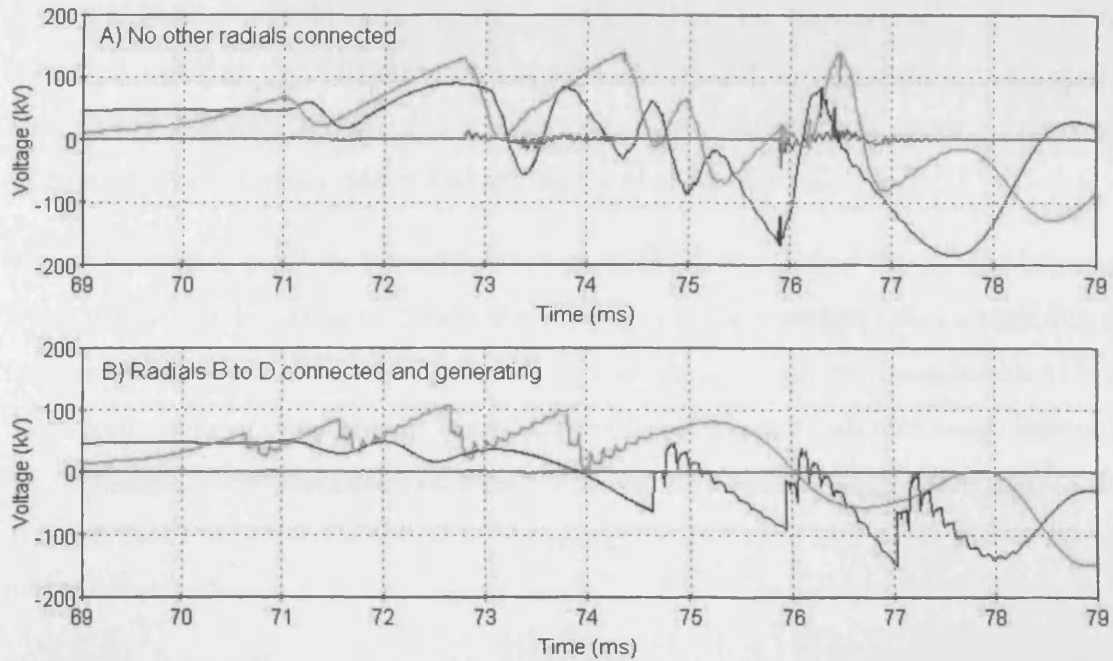
Fig. 7-25. Three phase voltage (during the first 10ms) at the array side of CB06 when array A is disconnected at 70ms following a single phase fault at 20ms. Case A) is when array A disconnected without any other arrays connected and case B) is when array A is disconnected whilst arrays B to D are connected and generating.

7.5. SUMMARY

There are a number of ways in which the offshore wind farm export cable could be energized. The positive and negative points for the four connection strategies are shown in Table 7-5.

Table 7-5. Energisation strategies for the offshore wind farm export cable.

Switching Strategy	Positives	Negatives
Cable only	The duration of overvoltage is less than 50ms.	The re-closing on the cable with trapped charge will cause overvoltages of up to 3pu. Extra circuit breakers are required offshore.
Cable and transformers	Fewer circuit breakers are required offshore.	There is a possibility of resonant overvoltages which are sustained for over a second.
Cable and reactive compensation	Fewer circuit breakers are required. The duration of overvoltage is less than 50ms.	The zero-missing phenomenon occurs, which could cause failure of the circuit breaker if it were to try to open shortly after energisation.
Cable, transformers and reactive compensation	The least amount of circuit breakers are required.	There is a possibility of resonant overvoltages.

A circuit breaker would be required at each end of the export cable when it is energized without the offshore transformer or reactive compensation connected. This would add capital cost and would also mean that there is more equipment offshore (requiring maintenance and adding to reliability issues).

When the export cable and transformer are energized together the overvoltage is lower than when the cable is energized separately but the transient takes a significant time to decay (over a second). The harmonics associated with the energisation of the transformer interacts with the resonant frequencies of the network and cause resonant overvoltages. These resonant overvoltages lasted for a second and were shown to be more severe if the offshore network was energized from the high voltage side of an onshore transformer.

The lowest overvoltages occurred when the export cable was energized with the reactive compensation connected. However, this created a dc offset which caused the zero-missing phenomenon which lasted for several hundreds of milliseconds. This will cause the circuit breaker to fail if the circuit breaker attempts to open whilst the zero-missing phenomenon is occurring.

A variety of overvoltages occured in the example offshore wind farm, ranging from temporary overvoltages to very fast front transients. A summary of the magnitudes of overvoltages investigated in this Chapter is given in Table 7-6. The magnitude of overvoltages was generally more severe in the offshore network than in the onshore network. The rate of rise of voltage was also higher in the offshore network. The highest overvoltage on the onshore network occurred when the export cable was re-closed, due to trapped charge.

Energisation transients within medium voltage array were different depending on how many arrays were already connected and energized. The voltage magnitude at the terminals of the wind turbine transformer was higher when the array was energized with no other arrays connected. The rate of change of voltage at the terminals of the wind turbine was significantly higher when the array was energized with all other arrays already connected.

The disconnection of a array produced the highest overvoltages, which exceeded LIWV and SIWV values given in IEC 60071-1. If a circuit breaker disconnected a array whilst the wind turbines are still generating in normal operation, the

overvoltage was almost 5pu, which was below the LIWV but exceeded the SIWV after a test conversion factor was applied to convert the LIWV to a SIWV value. If the radial array circuit breaker cleared a single phase fault whilst the wind turbines are generating, the overvoltages reached almost 7pu. The rate of change of voltage at WT_A1 was 85kV/μs for the case when other arrays are connected.

Very fast transient voltages with a frequency of 350kHz occurred when a single-line-to-ground fault was applied at the base of a wind turbine, where there was a 100m length of cable connected to the wind turbine transformer.

Table 7-6. Magnitude of overvoltages which occured in the example offshore wind farm studied in EMTP-RV in this Chapter.

Location and type of switching	Overvoltage magnitude (pu, peak)	Comments
Energisation of the export cable	2	The rate of rise of voltage was highest (5.5kV/μs) when another cable is already energized.
Energisation of the export cable and transformers	2	The duration of the overvoltage was over 1 second and the magnitude was higher if the export cable was energised from the high voltage side of an onshore transformer.
Disconnection of the export cable	2.2 (across the circuit breaker)	This exceeded the maximum TRV peak specified in IEC 62271-100.
Re-close of the export cable	3	There was a phase-to-phase overvoltage of 5pu at the offshore end of the cable.
Energisation of an array	2	The rate of change of voltage reached 21kV/μs.
Disconnection of an array during wind turbine generation	5	This exceeds SIWV values for the wind turbine transformers.
Disconnection of an array following a single-line-to-ground fault and whilst the wind turbines are generating	6.8	This exceeds both LIWV and SIWV values specified by IEC 60071-1 for the wind turbine transformers. The rate of change of voltage reached 85kV/μs.

8. CONCLUSIONS AND RECOMMENDATIONS FOR FURTHER WORK

The first part of my work was an assessment of the costs and losses of offshore wind farm transmission systems for BP Alternative Energy. This included a three month placement within BP working with the offshore wind team to produce a technical report on Offshore Wind Farm Design, for which I wrote the chapter on Electrical Design. The work also included studies of potential Round 3 connections.

The second part of my work involved the simulation of switching transients in offshore wind farms. I worked with DONG Energy to validate switching transient simulations by comparing them with measurements at an offshore wind farm. I worked with ALSTOM Grid Research and Technology Centre to study TRVs and switching transients in an example offshore wind farm.

My work has contributed to that of CIGRE Working Group B3.26, of which I was a full member. I was invited to present this work at an International EES-UETP course on 'Transients in Large Offshore Wind Farms' held at DTU, Denmark in June 2010. My work has resulted in 6 papers, 4 of which I was first author.

The main contributions resulting from this research and recorded in this thesis were:

- There was a clear break-even point of DC/AC transmission
- A loss load factor was developed for the estimation of annual losses
- The simulation results of energisation transients in Nysted offshore wind farm were very similar to the measurements made by DONG Energy
- A VCB model was developed and validated against measurements
- The disconnection of an array caused very severe overvoltages, which exceed IEC requirements for both Transient Recovery Voltages of circuit breakers and Lightning Impulse Withstand Voltage of equipment.

The area required for an offshore wind farm leads to extensive cable systems with a large number of radial array feeders and step-up transformers. The location of offshore wind farms means that significant lengths of submarine cable are required to connect the wind farm to the onshore grid.

The choice between AC or DC transmission was mainly determined by the wind farm rating and the cable route lengths connecting the offshore wind farm to the

onshore grid. The capital costs represented the majority of overall costs so were compared for AC and DC solutions in order to find a break-even point.

Over the lifetime of the wind farm, the cost of losses, maintenance and constrained energy became important. A loss-load factor was used to calculate the annual cost of losses.

The combination of extensive cable networks, transformers and vacuum circuit breakers in large offshore wind farms was identified as a potential source of transient overvoltages. With the expected increase in size and cost of offshore wind farms the accurate prediction of transient overvoltages becomes important.

The results from switching transient simulations were used to identify the overvoltages which may occur within an offshore wind farm and to determine Transient Recovery Voltages in circuit breakers. Validation of the modelling of offshore wind farm equipment was essential for effective and reliable switching transient studies.

8.1. CONCLUSIONS

8.1.1. COSTS AND LOSSES OF TRANSMISSION SYSTEMS FOR OFFSHORE WIND FARMS

There was a clear break-even point of DC/AC transmission. There was a certain length of cable, a break-even point, at which DC transmission became more economic than AC transmission. This was due to the lower costs of DC cables than of AC cables and the higher costs of a DC converter station compared to an equivalent AC substation required to transmit the same power. The break-even point for a 300MW offshore wind farm with a 10km onshore cable route was just over 110km, with a capital cost of £700k/MW for the offshore wind farm transmission system. The break-even point was reduced as the capacity of the wind farm increased. The lowest break-even point occurred when the maximum rating of a single HVDC converter platform (1600MW) equalled the wind farm rating. This break-even point was just over 50km for a 1600MW wind farm rating and had a capital cost of slightly under £400k/MW. The break-even point was just above this value for wind farm capacities above 1600MW.

A loss-load factor was developed for the estimation of annual losses. For cable route lengths of over 40km, the HV cable losses accounted for the highest proportion

(67% for a cable length of 40km) of the overall full-load losses in an HVAC connection, whilst the main proportion of losses in an HVDC connection was in the converter stations. In order to calculate the annual losses, a loss-load factor was used. A method for determining the loss-load factor for offshore wind farms was developed and a guideline for the estimation of the annual losses was produced. The loss-load factor was affected by the wind speeds, which were represented by a Weibull curve.

The value of Mean Time To Repair of the offshore converters had a significant effect on the total cost of an offshore wind farm transmission system, changing the most economical transmission connection. The cost of constrained energy was determined by the failure rate and Mean Time To Repair of the offshore converters, transformers and cables. Depending on the design of the transmission system and the value of MTTR, the cost of constrained energy ranged from 2% to 30% of the total cost. An increase in the MTTR of the converters from 1 month to 4 months resulted in the overall cost of a connection with four separate 400MW HVDC converter platforms becoming more economic compared to a connection where there was a single 1600MW HVDC converter platform.

8.1.2. COMPARISON OF SIMULATIONS WITH SWITCHING TRANSIENT MEASUREMENTS AT NYSTED OFFSHORE WIND FARM

Simulations of an offshore wind farm were compared with measurements (made available by DONG Energy) during energisation. This enabled the models to be verified:

- **A VCB model was developed and validated against the measurements. It was required in order to represent pre-strikes which caused successive waves and increased the overvoltage.** Although an ideal circuit breaker model produced the first steep fronted wave, it was unable to represent the pre-strikes. A model for a VCB was developed which included the dielectric breakdown strength and current clearing capability so that pre-strikes and re-strikes were simulated. The simulation results were very similar to the measurements and the rate of change of dielectric strength of the VCB model was found to be 40V/μs. In order to replicate the measurements more closely, the difference in mechanical pole separation times was included; however this did not have a significant effect on the magnitude of the overvoltages.

- **The input data for the cable model was validated by examining the cable charging current and the propagation speed of the transients in the simulations and comparing them with the measurement results.** Energisation transients in Nysted offshore wind farm were simulated in EMTP-RV and compared against measurements made available by DONG Energy. A frequency dependent (phase domain) cable model was used for the medium voltage cables. Through comparison of the simulations with the measurements, it was possible to show that the actual insulation thickness and semiconductor thickness of the cable were each 1mm thicker than that stated in the manufacturer's data sheets. The extra insulation and semiconductor thickness decreased the propagation speed and increased the surge impedance of the cable, which had the effect of decreasing the cable charging current. The increase in insulation and semiconductor thickness was necessary in order for the simulations to match the measurements.

- **Some simplifications to the model were made, which did not affect the simulation result.** It was shown that the high voltage export cable was adequately represented by a PI model (instead of a frequency dependent model) for studies of the switching transients in the medium voltage collection grid of an offshore wind farm. It was not necessary to model the wind turbine transformers and cables individually in each of the arrays, as the results were essentially the same when each array was represented by a cable terminated by a 1MΩ resistor. The length of this cable was the total cable length of the array.

8.1.3. TRANSIENT RECOVERY VOLTAGES

Very high maximum peak TRVs occurred at all of the offshore circuit breakers, which exceeded the TRV requirements in IEC 62271-100:2001. Although the majority of the simulated TRVs were within peak voltage and RRRV values specified by the IEC, very high maximum peak TRVs occurred in some situations. The most severe value of maximum peak TRV at the main 132kV offshore circuit breaker occurred when all arrays were connected through one transformer. The maximum peak TRV in this case was 351kV (3.3pu) which is well above the IEC requirement of 235kV (2.2pu). The maximum peak TRV requirements were exceeded for the 132kV onshore circuit breaker when it disconnected a long unloaded export cable, due to the capacitive charging current. This capacitive

charging current was 474A for a 132kV 90km export cable and exceeds typical capacitive breaking duties of under 200A for 132kV SF6 circuit breakers. The RRRV was exceeded in some cases for the 33kV circuit breakers.

There was no significant difference between the TRVs experienced for the three different wind turbine types. In order to investigate these TRVs, the wind turbines were represented by simple 'voltage source behind a reactance' models, where the reactance was determined by the fault current rating of the wind turbine. Using this model it was shown that the TRVs experienced for the three main wind turbine types were essentially the same in terms of both peak voltage and RRRV. The fault current contribution was highest for the SCIG, which was expected.

8.1.4. SINGLE PHASE FAULT AT THE BASE OF A WIND TURBINE

The simulated disconnection of a single phase fault at the base of a wind turbine resulted in very severe overvoltages which exceeded IEC requirements for TRVs. The maximum peak TRV of the 33kV circuit breaker which cleared the fault was 168kV (6.2pu) which is well above the requirement of 66kV (2.4pu) in IEC 62271-100:2001. Changing the location of the single phase fault within the array did not alter the TRV significantly.

The overvoltages in the array remained at a very serious level (with peak voltages of up to 6.9pu) until the wind turbines stopped generating. It would therefore be desirable for the wind turbines to stop generating before the circuit breaker is opened. The disconnection of an array whilst the wind turbines are still generating should be included in considerations for High Voltage Ride Through requirements.

A zig-zag grounding transformer was only effective if it was on the array side of the circuit breaker. This reduced the TRV to 88kV, but was still higher than the IEC requirements.

8.1.5. SWITCHING TRANSIENT STUDIES

The overvoltages in the offshore network of an offshore wind farm were generally more severe than those at the onshore connection point. The simulations indicated that these switching operations caused overvoltages of up to 3pu in the onshore network and up to 7pu in the offshore network. The rate of rise of voltage was also higher in the offshore network than in the onshore network.

The disconnection of an array produced the highest and most severe overvoltages, which exceeded the Lightning Impulse Withstand Voltage for 36kV equipment specified by IEC 60071. When the circuit breaker disconnected an array during normal operation, with the wind turbines still generating, the overvoltage within the array was almost 5pu. When the same circuit breaker disconnected an array during a single phase fault whilst the wind turbines were generating, the overvoltage reached almost 7pu. This value is well above the LIWV for 36kV equipment of 170kV peak (6.3pu) specified by IEC 60071.

Very fast front transients occurred during both energisation and disconnection, although they were more severe during disconnection. It was important to identify the location and instants when very high rates of change of voltage and very high frequency transients could occur in an offshore wind farm as they can cause transformer failures. The rate of change of voltage increased as the number of other arrays already connected increased. The highest rate of change of voltage was 85kV/μs. High frequency transients also occurred when a fault was applied at the base of a wind turbine, with a frequency of 350kHz.

Resonant overvoltages were shown to occur when an export cable and transformer were energised together. The energisation of the export cable and offshore transformer resulted in overvoltages which were lower than when the cable was energised separately, however the transient lasted for over a second due to the harmonics associated with the inrush current of the transformer. The overvoltage was more severe in terms of both magnitude and duration when the same network was energised from the high voltage side of an onshore transformer. If the resonant frequency of the network corresponds with a harmonic frequency, resonant overvoltages occur. A frequency scan of the offshore wind farm impedance should be carried out during the design stage of an offshore wind farm to identify if resonant overvoltages are likely to occur.

8.2. RECOMMENDATIONS FOR FURTHER WORK

8.2.1. FUTURE TRANSMISSION SYSTEMS

The majority of the work in this thesis has focused on AC radial transmission systems for offshore wind farms. It was shown that as offshore wind farms increased in size and moved further away from onshore connection points, DC transmission became more economical. Transmission systems for offshore wind farms could be

designed as an offshore grid instead of individual radial connections. Further work includes:

- A cost-benefit analysis of different multi-terminal DC grid topologies. Further work should be carried out on DC circuit breakers, including the operation time and the optimal number of DC circuit breakers required in different offshore grid configurations.

- A cost-benefit analysis taking into account other transmission technologies, particularly Gas Insulated Lines. Gas Insulated Line systems can transmit up to 3700MVA, which is about ten times more than an HVAC XLPE cable and over three times more than an HVDC VSC connection. Although the GIL is likely to have a higher capital cost, it has several advantages such as low losses and no requirement for reactive compensation.

- In some cases the cost of constrained energy was 30% of the total cost of the transmission system. The cost of constrained energy was calculated based on values of failure rate and Mean Time To Repair given in [53]. As the transmission systems of offshore wind farms are relatively new, data related to the failure rate and Mean Time To Repair is limited. It is also likely that as the distance from shore increases, the values of failure rate and in particular the Mean Time To Repair will increase. Further work should include the effect of these values on the cost of constrained energy.

8.2.2. MODELS FOR SWITCHING TRANSIENT STUDIES

In this thesis simulations of an offshore wind farm were compared with measurements during energisation. This enabled the models to be verified. Further work should include:

- A comparison with measurements at other offshore wind farms. This would enable the actual insulation and semiconductor thicknesses of different cables to be determined and compared with the manufacturer's data sheets. A tolerance value could then be given to the cable input parameters.

- Ideal circuit breaker models were used for the 132kV circuit breakers. Suitable models for SF_6 circuit breakers should be identified and developed. This should focus on the ability of these circuit breakers to interrupt the capacitive charging current of long cables.

- Simple 'voltage source behind a reactance' models were used to represent the wind turbines. Further work is required to develop more sophisticated models of the wind turbines for switching transient and fault studies.

8.2.3. SWITCHING TRANSIENT STUDIES

- Resonant overvoltages were shown to occur when an export cable and transformer were energised together. Further work should include the effect of export cable length and the addition of reactive compensation and harmonic filters. The resonant overvoltages were more severe when the export cable was energised by closing a circuit breaker on the high voltage side of an onshore transformer. It would be useful to identify if there are any other situations in which resonant overvoltages could occur.

- The disconnection of a single phase fault within a 33kV array caused very high overvoltages. Further work should involve the inclusion of more detailed wind turbine models in the simulations. This could include the analysis of High Voltage Ride Through requirements for wind turbines and the impacts on the overvoltages.

- The waveforms experienced within an offshore wind farm were significantly different to test waveforms specified by the IEC (specifically, they had a very high rate of change of voltage). This raises the question as to whether the standard waveforms are appropriate. It is expected that CIGRE Working Group C54-142 "Electrical Environment for Transformers" will be including recommendations on standards for waveforms.

- Further work is required on methods of mitigating very high rates of change of voltage and very high frequency transients. It is expected that the work of CIGRE Working Group A2/C4.39 "Electrical Transient Interaction between Transformers and the Power System" will provide some guidelines regarding this.

8.2.4. INSULATION COORDINATION AND THE REDUCTION OF OVERVOLTAGES

High maximum overvoltages occurred when an array was disconnected which exceeded the insulation level of equipment within the offshore wind farm.

- Surge arresters were not included in the simulations. Further work is required to include surge arresters. This should determine whether the overvoltages

can be reduced to an acceptable level. Studies should also be carried out to determine whether the energy rating of surge arresters is exceeded. This is likely to be an issue if an array (or the whole wind farm) is disconnected and the wind turbines continue to generate power.

- It was shown that a zig zag grounding transformer limited the overvoltages when it was located on the array side of the circuit breaker. Further work is required on the grounding of offshore wind farms.

REFERENCES

1. European Council, *Regulation (EC) No. 663/2009 "European Energy Programme for Recovery"*. July 2009.
2. UK Department of Trade and Industry, *Energy White Paper: Meeting the Energy Challenge*. 2007.
3. UK Department of Energy and Climate Change, *The UK Low Carbon Transitition plan*. 2009.
4. U.S. Department of Energy Office of Energy Efficiency and Renewable Energy Wind & Water Power Program, *A National Offshore Wind Strategy; Creating an Offshore Wind Energy Industry in the United States*. February 2011.
5. European Wind Energy Association, *Delivering Offshore Wind Power in Europe*, available from www.offshorewind2009.info accessed Sept 2008. 2007.
6. RWE npower renewables. *Greater Gabbard Wind Farm*, available from www.rwe.com, accessed September 2010. [cited.
7. BARD. *BARD Offshore 1*, available from www.bard-offshore.de/en, accessed September 2010.
8. Global Wind Energy Council, Chinese Renewable Energy Industries Association, and Greenpeace China, *The 2010 China Wind Power Outlook*. 2010.
9. Cape Wind Associates. *Cape Wind*, www.capewind.org. [cited October 2010].
10. Ofgem, *Offshore Electricity Transmission: Tender Rules, Version 1.1*, available from www.ofgem.gov.uk. September 2010.
11. The Crown Estate, *Offshore Wind Energy, Round 3*, available from www.thecrownestate.co.uk/round3, accessed September 2010. 2008.
12. Forewind. *Dogger Bank*, available from www.forewind.co.uk/dogger-bank, accessed February 2011.
13. National Grid, *Offshore Development Information Statement*, available from www.nationalgrid.com. September 2010.
14. ABB Power Technologies AB, *Submarine Cables for Inter-Turbine Connections*, available from www.abb.com/cables. 2004.
15. ABB, *XLPE Submarine Cable Systems, revision 5*, available from www.abb.com/cables. 2010.
16. Alstom T&D, *Network Protection & Automation Guide*. 1st ed. 2002.
17. A. Shafiu, A. Hernandez, F. Schettler, J. Finn, and Jorgensen, E. *Harmonic Studies for Offshore wind farms*. in *9th International Conference on AC and DC Power Transmission*. 2010. London, UK.
18. Koch, H. and Retzmann, D. *Connecting large offshore wind farms to the transmission network*. in *Transmission and Distribution Conference and Exposition, IEEE PES, pp 1-5, 19-22 April 2010*. 2010.
19. Siemens Energy. *Trans Bay Cable Project, USA*, available from www.energy.siemens.com. 2010, accessed December 2010.
20. Siemens Energy. *800MW offshore HVDC PLUS link BorWin2*, available from www.energy.siemens.com, accessed December 2010.
21. ALSTOM Grid, *Alstom Grid wins innovative offshore platform substation contract in Germany*, available from www.alstom.com/news-and-events. September 2010.

22. Cockerill, T.T., Kuhn, M., Bussel, G.J.W.v., Bierbooms, W., and Harrison, R., *Combined technical and economic evaluation of the Northern European offshore wind resource*. Journal of Wind Engineering and Industrial Aerodynamics, 2001. **89**(2001): p. 689-711.

23. Liebreich, M. and Young, W., *Offshore Wind: Europe's Eur 90 Billion Funding Requirement*. 2005, New Energy Finance: London.

24. Offshore Transmission Expert Group and GB-SQSS sub-group, *Voltage Limits and Planning and Operation of Offshore Transmission Networks*. 2006, DTI.

25. Anders, G.J., *Rating of Electric Power Cables, Ampacity Computations for Transmission, Distribution and Industrial Applications*. 1997: IEEE Press.

26. Insulated Conductors Committee Task Group 7-39, *Loss evaluation for underground transmission and distribution cable systems*. Power Delivery, IEEE Transactions on, 1990. **5**(4): p. 1652-1659.

27. Walling, R.A. and Ruddy, T., *Economic Optimization of Offshore Windfarm Substations and Collection Systems*: GE Energy.

28. Weedy, B.M. and Cory, B.J., *Electric Power Systems*. 4th ed. 1999: Wiley.

29. Anders, G.J. and Brakelmann, H., *Improvement in Cable Rating Calculations by Consideration of Dependence of Losses on Temperature*. IEEE Transactions on Power Delivery, 2004. **19**(3): p. 919-925.

30. Neher, J.H. and McGrath, M.H., *The Calculation of the Temperature Rise and Load Capability of Cable Systems*. AIEE Transactions, Part III, 1957. **76**: p. 752-772.

31. Burton, T., Sharpe, D., Jenkins, N., and Bossanyi, E., *Wind Energy Handbook*: John Wiley & Sons, Inc.

32. Masters, G.M., *Renewable and efficient electric power systems*. 2004, Hoboken, N.J.: [Chichester : Wiley-Interscience ; John Wiley].

33. Manwell, J.F., McGowen, J.G., and Rogers, A.L., *Wind Energy Explained, Theory, Design and Application*. 2005: Wiley.

34. Lazardis, L.P., *Economic Consideration of HVAC and HVDC Solutions for Large Offshore wind farms under Special Consideration of Reliability*, in *Electrical Engineering*. 2005, Royal Institute of Technology: Stockholm.

35. Norgaard, P. and Holttinen, H. *A Miulti-Turbine Power Curve Approach*. in *Nordic Wind Power Conference NWPC'04*. 2004. Chalmers University of Technology, Sweden.

36. Negra, N.B., Todorovic, J., and Ackermann, T., *Loss evaluation of HVAC and HVDC transmission solutions for large offshore wind farms*. Electric Power Systems Research, 2006. **76**(11): p. 916-927.

37. Rajapakse, A.D., Gole, A.M., and Wilson, P.L., *Approximate Loss Formulae for estimation of IGBT switching losses through EMTP type simulations*. IPST05, 2005.

38. Gole, A.M., Keri, A., Kwankpa, C., Gunther, E.W., Dommel, H.W., Hassan, I., Marti, J.R., Martinez, J.A., Fehrle, K.G., Tang, L., McGranaghan, M.F., Nayak, O.B., Ribeiro, P.F., Iravani, R., and Lasseter, R., *Guidelines for modeling power electronics in electric power engineering applications*. IEEE Transactions on Power Delivery, 1997. **12**(1): p. 505-14.

39. Backlund, B., Schnell, R., Schlapbach, U., Fischer, R., and Tsyplakov, E., *Applying IGBTs - Application Note. Available from www.abb.com. Accessed 08/08/07*. 2007, ABB.

40. Rajapakse, A.D., Gole, A.M., and Wilson, P.L., *Electromagnetic Transients Simulation Models for Accurate Representation of Switching Losses and*

Thermal Performance in Power Electronic Systems. IEEE Transactions on Power Delivery, 2005. **20**(1): p. 319 - 327.

41. Finney, S.J., Williams, B.W., and Green, T.C. *IGBT turn-off characteristics and high frequency application.* 1994. London, UK: IEE.

42. Winterhalter, C., Kerkman, R., Schlegel, D., and Leggate, D. *The effect of circuit parasitic impedance on the performance of IGBTs in voltage source inverters.* 2001. Anaheim, CA, USA: IEEE.

43. Petterteig, A., Lode, J., and Undeland, T.M. *IGBT turn-off losses for hard switching and with capacitive snubbers.* in *Industry Applications Society Annual Meeting, 1991., Conference Record of the 1991 IEEE.* 1991.

44. Mohan, N., Undeland, T.M., and Robbins, W.P., *Power Electronics. Converters, Applications, and Design.* 2nd ed. 1995: John Wiley & Sons, Inc.

45. Kuang, S., Williams, B.W., and Finney, S.J., *A review of IGBT models.* IEEE Transactions on Power Electronics, 2000. **15**(6): p. 1250-66.

46. Wong, C., *EMTP modeling of IGBT dynamic performance for power dissipation estimation.* IEEE Transactions on Industry Applications, 1997. **33**(1): p. 64-71.

47. Azuma, S., Kimata, M., Seto, M., Xinjian, J., Haiwei, L., Dewei, X., and Lipei, H. *Research on the power loss and junction temperature of power semiconductor devices for inverter.* 1999. Changchun, China: IEEE.

48. Jinrong, Q., Khan, A., and Batarseh, I. *Turn-off switching loss model and analysis of IGBT under different switching operation modes.* 1995. Orlando, FL, USA: IEEE.

49. ABB, *www.abb.com/hvdc* *Accessed 03/08/07.*

50. Jacobson, B., Karlsson, P., Asplund, G., Harnefors, L., and Jonsson, T. *VSC-HVDC Transmission with Cascaded Two-Level Converters.* in *CIGRE Session 2010.* 2010. Paris.

51. Trainer, D.R., Davidson, C.C., Oates, C.D.M., Macleod, N.M., Critchley, D.R., and Crookes, R.W. *A New Hybrid Voltage-Sourced Converter for HVDC Power Transmission.* in *CIGRE Session 2010.* 2010. Paris.

52. Balog, G.E., Christl, N., Evenset, G., and Rudolfsen, F., *Power Transmission Over Long Distances with Cables.* CIGRE session 2004; B1-306, 2004.

53. Djapic, P. and Strbac, G., *Cost Benefit Methodology for Optimal Design of Offshore Transmission Systems,* BERR, Editor. July 2008.

54. Econnect, *East Coast Transmission Network Technical Feasibility Study.* 2008, Crown Estate.

55. PB Power, *Concept Study: Western Offshore Transmission Grid.* 2002.

56. Valov, B., Lange, B., Rohrig, K., and Heier, S., *Long-term Concept for an Offshore Power Transmission System in the German North Sea,* in *7th International Workshop on Large Scale Integration of Wind Power and on Transmission Networks for Offshore Wind Farms.* 26 - 27th May 2008: Madrid, Spain.

57. Airtricity, *Building a more powerful Europe; Supergrid, the power to connect. Available from www.airtricity.com.* 2007.

58. Makanishi, K., *Switching Phenomena in High-voltage Circuit Breakers.* 1st Edition ed. 1991: CRC Press.

59. Andersson, D. and Henriksen, A. *Passive and active dc breakers in the three gorges-changzhou HVDC project.* in *ICPS2001, International Conference on Power Systems.* 2001. Wuhan, China.

60. Pauli, B., Mauthe, G., Ruoss, E., Ecklin, G., Porter, J., and Vithayathil, J., *Development of a high current HVDC circuit breaker with fast fault clearing capability.* IEEE Transactions on Power Delivery, 1988. **3**(4): p. 2072 - 2080.

REFERENCES

61. Podlesak, T.F., Singh, H., Fonda, K., Creedon, J., Schofield, G.L., and Johnson, F.O. *Megawatt high speed solid state circuit breaker for pulse power applications*. in *9th Pulsed Power Conference*. 1993.

62. Lange, G.B.D., Chol, A.M., and Ijumba, N.M. *Application of high-power semiconductor technology in dc traction circuit-breakers*. in *IEEE Power Engineering Society Inaugural Conference and Exposition*. 2005. Durban, South Africa.

63. Meyer, C., Kowal, M., and De Doncker, R. *Circuit breaker concepts for future high-power dc-applications*. in *Fourtieth IAS Annual Meeting Industry Applications Conference, Conference Record of 2005* 2005.

64. Oedegard, B., Stiasny, T., Carroll, E., and Rossinelli, M., *An application-specific asymmetric IGCT*. 2001, USA: ABB Semiconductors AG,.

65. Cigre Technical Brochure No. 269, *VSC Transmission, Working Group B4.37*. April 2005.

66. Long, W., *A study on some switching aspects of a double circuit HVDC transmission line*. IEEE Transactions on Power Apparatus and Systems PAS92, 1973. **2**: p. 734-741.

67. Flourentzou, V.G.A. and Demetriades, G.D., *VSC-based HVDC power transmission systems: An overview*. IEEE Transactions on Power Electronics, 2009. **24**: p. 592-602.

68. Greenwood, A., *Electrical transients in power systems. Second edition*. 1991: Wiley. xvi+751.

69. Lopez-Roldan, J., Herdt, H.D., Declercq, J., Sels, T., Dommelen, D.V., Popov, M., and Sluis, L.V.D., *Analysis, Simulation and Testing of Transformer Insulation Failures related to Switching Transients Overvoltages*. CIGRE Session 2002 12-116, 2002.

70. van der Sluis, L., *Transients in Power Systems*. 2001: John Wiley and Sons, Ltd.

71. CIGRE WG 33.02, *Guidelines for representation of network elements when calculating transients, CIGRE report no. 39*. 2000.

72. Povh, D. and Schultz, W., *Analysis of Overvoltages Caused by Transformer Magnetizing Inrush Current*. Power Apparatus and Systems, IEEE Transactions on, 1978. **PAS-97(4)**: p. 1355-1365.

73. Witte, J.F., DeCesaro, F.P., and Mendis, S.R. *Damaging long-term overvoltages on industrial capacitor banks due to transformer energization inrush currents*. in *Industry Applications Society Annual Meeting, 1993., Conference Record of the 1993 IEEE*. 1993.

74. *IEEE Guide for the Application of Insulation Coordination*. IEEE Std 1313.2-1999, 1999: p. i.

75. Qureshi, S.A. and Shami, T.A. *Effects of the GIS parameters on very fast transient overvoltages*. 1994. Antalya, TURKEY: IEEE, Piscataway, NJ, USA.

76. A. M. Sahni, C. Baliga, D. Raina, and J. K. Tiku, *Site Investigations and study of very fast transient overvoltages in 245kV GIS of Tata Electric companies*. CIGRE 1996: 15/21/33-01, 1996.

77. Das, J.C., *Transients in Electrical Systems, Analysis, Recognition, and Mitigation*. 2010: McGraw-Hill. 722.

78. Cornick, K.J. and Thompson, T.R., *Steep-fronted switching voltage transients and their distribution in motor windings. I. System measurements of steep-fronted switching voltage transients*. IEE Proceedings B (Electric Power Applications), 1982. **129(2)**: p. 45-55.

79. Cornick, K.J. and Kunji, A.M., *Nanosecond switching transients recorded in a mining transformer installation*. Power Delivery, IEEE Transactions on, 1993. **8**(3): p. 1130-1137.

80. Kondala Rao, B. and Gopal, G. *Development and application of vacuum circuit breaker model in electromagnetic transient simulation*. 2006. New Delhi, India: IEEE.

81. Liljestrand, L., Sannino, A., Breder, H., and Thorburn, S., *Transients in collection grids of large offshore wind parks*. Wind Energy, 2008. **11**(1): p. 45-61.

82. Popov, M. and Acha, E., *Overvoltages due to switching off an unloaded transformer with a vacuum circuit breaker*. IEEE Transactions on Power Delivery, 1999. **14**(4): p. 1317-26.

83. Greenwood, A. and Glinkowski, M., *Voltage escalation in vacuum switching operations*. IEEE Transactions on Power Delivery, 1988. **3**(4): p. 1698-706.

84. Popov, M. and van der Sluis, L., *Improved calculations for no-load transformer switching surges*. IEEE Transactions on Power Delivery, 2001. **16**(3): p. 401-8.

85. Eichenberg, J.P., Hennenfent, H., and Liljestrand, L. *Multiple re-strikes phenomenon when using vacuum circuit breakers to start refiner motors*. 1998. Portland, ME, USA: IEEE.

86. Li-Ming, Z. and Boggs, S., *Effect of shielded distribution cable on very fast transients*. Power Delivery, IEEE Transactions on, 2000. **15**(3): p. 857-863.

87. McNutt, W.J., Blalock, T.J., and Hinton, R.A., *RESPONSE OF TRANSFORMER WINDINGS TO SYSTEM TRANSIENT VOLTAGES*. IEEE Transactions on Power Apparatus and Systems, 1974. **PAS-93**(2): p. 457-467.

88. Stein, W., Muller, W., Moller, K., Brantl, U., Claudi, A., Glaninger, P., Kotschnigg, J., and Neinens, C.A. *Oscillatory switching voltages and relevant response of HV power transformers*. in *CIGRE Session 1984*. 1984. Paris.

89. Musil, R.J., Preininger, G., Schopper, E., and Wenger, S., *Voltage Stresses Produced by Aperiodic and Oscillating System Overvoltages in Transformer Windings*. Power Apparatus and Systems, IEEE Transactions on, Jan. 1981. **PAS-100**(no.1): p. 431-441.

90. Bayless, R.S., Selman, J.D., Truax, D.E., and Reid, W.E., *Capacitor switching and transformer transients*. IEEE Transactions on Power Delivery, 1988. **3**(1): p. 349-57.

91. Brierley, R.H. and Lishchyna, L. *CAPACITOR BANK SWITCHING SURGES AND POSSIBLE EFFECTS ON TRANSFORMER INSULATION*. 1983. Can: Canadian Electrical Assoc, Montreal, Que, Can.

92. Paul, D., *Failure analysis of dry-type power transformer*. IEEE Transactions on Industry Applications, 2001. **37**(3): p. 689-95.

93. Shipp, D.D., Dionise, T.J., Lorch, V., and MacFarlane, B.G. *Transformer failure due to circuit breaker induced switching transients*. in *Pulp and Paper Industry Technical Conference (PPIC), Conference Record of 2010 Annual*.

94. Gustavsen, B., *Study of Transformer Resonant Overvoltages Caused by Cable-Transformer High-Frequency Interaction*. Power Delivery, IEEE Transactions on, 2010. **25**(2): p. 770-779.

95. *IEEE Draft Guide to Describe the Occurrence and Mitigation of Switching Transients Induced by Transformer, Switching Device, and System Interaction*, in *IEEE Unapproved Draft Std PC57.142/D8*. Mar. 2010.

96.   CIGRE JWG A2-A3-B3.21, *Electrical Environment of Transformers, Impact of fast fast transients*. Electra, Feb. 2005. **No. 218.**

97.   Imbalance Settlement Group, *Review of Metering for offshore installations, available from* www.elexon.co.uk. 24th Nov. 2009.

98.   Energy Networks Association, *Engineering Recommendation P28, Planning Limits for Voltage Fluctuations Caused by Industrial, Commercial and Domestic Equipment in the United Kingdom.* 1989.

99.   Sorensen, T., *Email correspondance.* 2010.

100. Institution of Electrical Engineers, *Recommendations for the electrical and electronic equipment of mobile and fixed offshore installations, 2nd ed. ISBN 0 85296 528 1.* 1992 (and supplement 1995).

101. W. Sweet, Danish wind turbines take unfortunate turn, IEEE Spectrum, 2004, 41(11), p. 30-34.

102. J. Larsen and R. Singh Sagoo. *Replacement of Transformers on Middelgrunden Offshore Wind Farm.* in *European Offshore Wind conference.* Sept. 2009. Stockholm, Sweden.

103. Andersen, N., Marcussen, J.H., Jacobsen, E., and Nielsen, S.B., *Experience Gained by a major Transformer Failure at the Offshore Platform of the Nysted Offshore Wind Farm*, in *7th International Workshop on Large-Scale Integration of Wind Power into Power Systems as well as on Transmission Networks for Offshore Wind Farms.* 26 - 28th May 2008, Energynautics: Madrid, Spain.

104. Camm, E.H., Behnke, M.R., Bolado, O., Bollen, M., Bradt, M., Brooks, C., Dilling, W., Edds, M., Hejdak, W.J., Houseman, D., Klein, S., Li, F., Li, J., Maibach, P., Nicolai, T., Patino, J., Pasupulati, S.V., Samman, N., Saylors, S., Siebert, T., Smith, T., Starke, M., and Walling, R. *Wind power plant grounding, overvoltage protection, and insulation coordination: IEEE PES wind plant collector system design working group.* in *IEEE Power and Energy Society General Meeting, PES'09.* July 2009. Calgary, AB.

105. da Silva, F.F., Bak, C.L., Gudmundsdottir, U.S., Wiechowski, W., and Knardrupgard, M.R., *Methods to Minimize Zero-Missing Phenomenon.* Power Delivery, IEEE Transactions on. 25(4): p. 2923-2930.

106. Akhmatov, V., *Excessive over-voltage in long cables of large offshore windfarms.* Wind Engineering, 2006. 30(5): p. 375-83.

107. Wiechowski, W. and Eriksen, P.B. *Selected studies on offshore wind farm cable connections - challenges and experience of the Danish TSO.* 2008. Pittsburgh, PA, United states: Inst. of Elec. and Elec. Eng. Computer Society.

108. Akhmatov, V., Gellert, B.C., McDermott, T.E., and Wiechowski, W. *Risk of Temporary Over-Voltage and High-Voltage Fault-Ride-Through of Large Wind Power Plants.* in *9th International Workshop on Large-Scale Integration of Wind Power into Power Systems as well as on Transmission Networks for Offshore Wind Power Plants.* 18 - 19 October, 2010. Quebec City, Quebec, Canada.

109. Turner, R.A. and Smith, K.S. *Resonance Excited by Transformer Inrush Current in Inter-Connected Offshore Power Systems.* in *Industry Applications Society Annual Meeting, 2008. IAS '08. IEEE.* 2008.

110. Sorensen, P., Hansen, A.D., Sorensen, T., Nielsen, C.S., Nielsen, H.K., Christensen, L., and Ulletved, M. *Switching transients in wind farm grids.* in *European Wind Energy Conference and Exhibition.* 2007. Milan: EWEA, Brussels.

111. Christensen, L.S., Sorensen, P.E., Sorensen, T., Olsen, T., and Nielsen, H.K., *GPS Synchronized high voltage measuring system*. European Offshore Wind Conference, Berlin, 2007.

112. Aristi, I.A., *Modeling of Switching Transients in Nysted Offshore Wind Farm and a Comparison with Measurements; EMT Simulations with PowerFactory and PSCAD*. June 2008, Technical University of Denmark, DTU.

113. Arana, I., Holboll, J., Sorensen, T., Nielsen, A.H., Sorensen, P., and Holmstrom, O. *Comparison of Measured Transient Overvoltages in the Collection Grid of Nysted Offshore Wind Farm with EMT Simulations*. in *International Conference on Power System Transients (IPST2009)*. 2009. Kyoto, Japan.

114. Abdulahovic, T., *Analysis of High Frequency Electrical Transients in Offshore Wind Parks*, in *Department of Energy and Environment*. 2009, Chalmers University of Technology: Goteburg.

115. Daniel, A. and Gebre, S., *Analysis of Transients in Wind Parks: Modeling of System Components and Experimental Verification*, in *Department of Electric Power Engineering*. 2008, Chalmers University of Technology: Goteburg, Sweden.

116. Reza, M. and Breder, H., *Cable System Transient Study, Vindforsk V-110. Experiments with switching transients and their mitigation in a windpower collection grid scale model, Elforsk report 09:05. Available from* http://www.vindenergi.org/Vindforskrapporter/09_05_rapport.pdf Jan. 2009.

117. Reza, M., Srivastava, K., Sannino, A., Abdulahovic, T., and Thiringer, T. *Combining MV laboratory and simulation resources to investigate Transient Phenomena in Wind Cable Systems*. in *European Offshore Wind conference*. Sept. 2009. Stockholm, Sweden.

118. Larsson, A., *Practical Experiences gained at Lilgrund Offshore Wind Farm*, in *7th International Workshop on Large-Scale Integration of Wind Power into Power Systems as well as on Transmission Networks for Offshore Wind Farms*. 26 - 28th May 2008, Energynautics: Madrid, Spain.

119. Martinez, J.A., Mahseredjian, J., and Khodabakhchian, B., *Parameter determination for modeling system transients-Part VI: Circuit breakers*. Power Delivery, IEEE Transactions on, 2005. **20**(3): p. 2079-2085.

120. Glinkowski, M.T., Gutierrez, M.R., and Braun, D., *Voltage escalation and reignition behavior of vacuum generator circuit breakers during load shedding*. IEEE Transactions on Power Delivery, 1997. **12**(1): p. 219-26.

121. Cornick, K.J. and Tleis, A.N.D., *Computer simulation of three-phase prestriking transients in cable-connected motor systems*. IEE Proceedings-B, May 1991. **138**(3).

122. Wong, S.M., Snider, L.A., and Lo, E.W.C. *Overvoltages and Reignition Behaviour of Vacuum Circuit Breaker*. in *6th International Conference on Advances in Power System Control, Operation and Management*. 2003. Hong Kong.

123. Kosmac, J. and Zunko, P., *Vacuum Circuit Breaker models for calculation of Transient Overvoltages*. CIGRE Session 1996 : 13-203, 1996.

124. Kosmac, J. and Zunko, P., *Statistical vacuum circuit breaker model for simulation of transient overvoltages*. IEEE Transactions on Power Delivery, 1995. **10**(1): p. 294-300.

125. Chaly, A.M. and Chalaya, A.T. *Computer simulation of transformer magnetising current interruption by a vacuum circuit breaker*. 1996. Berkeley, CA, USA: IEEE, Piscataway, NJ, USA.

126. Vollet, C. and Metz-Noblat, B.d. *Vacuum Circuit Breaker Model: Application Case to Motors Switching*. in *International Power Systems Transients Conference*. 2007. Lyon, France.

127. Binnendijk, M., Merck, W.F.H., Smeets, R.P.P., Watanabe, K., and Kaneko, E., *High-current interruption in vacuum circuit breakers*. Dielectrics and Electrical Insulation, IEEE Transactions on, 1997. **4**(6): p. 836-840.

128. Helmer, J. and Lindmayer, M. *Mathematical modeling of the high frequency behavior of vacuum interrupters and comparison with measured transients in power systems*. 1996. Berkeley, CA, USA: IEEE, Piscataway, NJ, USA.

129. Watson, N. and Arrillaga, J., *Power systems electromagnetic transients simulation*. 1st ed. IEE Power and Energy Series 39, ed. A.T. Johns and D.F. Warne. 2003: IEE.

130. Bergeron, L., ed. *De coup de Belier en hydraulique au coup de foudre en electricite, (Water hammer in hydraulics and wave surges in electricity)*, ASME Committee. 1961, Wiley, New York.

131. Semlyen, A. and Dabuleanu, A., *Fast and accurate switching transient calculations on transmission lines with ground return using recursive convolutions*. Power Apparatus and Systems, IEEE Transactions on, 1975. **94**(2): p. 561-571.

132. Marti, J.R., *Accurate modelling of frequency-dependent transmission lines in electromagnetic transient simulations*. IEEE Transactions on Power Apparatus and Systems, 1982. **PAS-101**(1): p. 147-55.

133. Noda, T., Nagaoka, N., and Ametani, A., *Phase domain modeling of frequency-dependent transmission lines by means of an ARMA model*. IEEE Transactions on Power Delivery, 1996. **11**(1): p. 401-11.

134. Morched, A., Gustavsen, B., and Tartibi, M., *A universal model for accurate calculation of electromagnetic transients on overhead lines and underground cables*. Power Delivery, IEEE Transactions on, 1999. **14**(3): p. 1032-1038.

135. Kocar, I., Mahseredjian, J., and Olivier, G., *Improvement of Numerical Stability for the Computation of Transients in Lines and Cables*. Power Delivery, IEEE Transactions on. **25**(2): p. 1104-1111.

136. Gustavsen, B. and Semlyen, A., *Simulation of transmission line transients using vector fitting and modal decomposition*. IEEE Transactions on Power Delivery, 1998. **13**(2): p. 605-14.

137. Gustavsen, B., Martinez, J.A., and Durbak, D., *Parameter determination for modeling system transients-Part II: Insulated cables*. Power Delivery, IEEE Transactions on, 2005. **20**(3): p. 2045-2050.

138. IEC, *International standard of resistance of copper*. IEC 60028, 1925.

139. IEC, *Hard-drawn aluminium wire for overhead line conductors*. IEC 60889, 1987.

140. Gudmundsdottir, U.S., Gustavsen, B., Bak, C.L., Wiechowski, W.T., and Faria da Silva, F., *Field Test and Simulation of a 400kV Crossbonded Cable System*. IEEE Transactions on Power Delivery, unpublished, manuscript submitted in November 2009.

141. Gustavsen, B. *Panel session on data for modeling system transients insulated cables*. in *Proceedings of 2001 Winter Meeting of the IEEE Power Engineering Society*. 2001. Columbus, OH, USA: IEEE.

142. IEC, *Power cables with extruded insulation and their accessories for rated voltages above 30kV (Um = 36kV) up to 150kV (Um = 170kV) - Test methods and requirements*. IEC 60840.

143. IEC, *Power cables with extruded insulation and their accessories for rated voltages from 1kV (Um = 1.2kV) up to 30kV (Um = 36kV)*. IEC 60502.

144. De Leon, F. and Semlyen, A., *Reduced order model for transformer transients*. IEEE Transactions on Power Delivery, Jan. 1992. 7(1).

145. Martinez, J.A., Walling, R., Mork, B.A., Martin-Arnedo, J., and Durbak, D., *Parameter determination for modeling system transients-Part III: Transformers*. Power Delivery, IEEE Transactions on, 2005. 20(3): p. 2051-2062.

146. IEC 60909-0, *Short-circuit currents in three-phase a.c. systems - Part 0: Calculation of currents*. July 2001.

147. Samaan, N., Zavadil, R., Smith, J.C., and Conto, J. *Modeling of wind power plants for short circuit analysis in the transmission network*. in *IEEE PES Transmission and Distribution Conference and Exposition*. April 2008. Chicago, IL.

148. Kanellos, F.D. and Kabouris, J., *Wind Farms Modeling for Short-Circuit Level Calculations in Large Power Systems*. IEEE Transactions on Power Delivery, 2009. 24(3): p. 1687 - 1695.

149. Muljadi, E., Butterfield, C.P., Ellis, A., Mechenbier, J., Hochheimer, J., Young, R., Miller, N., Delmerico, R., Zavadil, R., and Smith, J.C. *Equivalencing the collector system of a large wind power plant*. 2006. Montreal, QC, Canada: Inst. of Elec. and Elec. Eng. Computer Society.

150. Western Electricity Coordinating Council Wind Generator Modeling Group, *WECC Wind Power Plant Power Flow Modeling Guide*, WECC Modeling and Validation Work Group, Editor. May 2008.

151. IEEE Std C37.011-2005, IEEE Application Guide for Transient Recovery Voltage for AC High-Voltage Circuit Breakers.

152. IEEE PES Switching Transients Task Force 15.08.09.03, *Task Force Report, Modeling Guidelines for Switching Transients*. 1997.

153. *IEEE Application Guide for Capacitance Current Switching for AC High-Voltage Circuit Breakers*. IEEE Std C37.012-2005 (Revision of IEEE Std C37.012-1979), 2005: p. 0_1-52.

154. Szewczyk, M. *Investigation on circuit breaker influence on transient recovery voltage*. in *42nd International Universities Power Engineering Conference (UPEC 2007)*. September 2007. Brighton, UK.

155. Zhou, Z., Wang, X., and Wilson, P. *Transient Recovery Voltage Assessment for 138kV Breakers with the New Addition of a Wind Farm*. in *International Conference on Power System Technology*. 2006. Chongqing.

156. Nanka-Bruce, O., Nurse, S., Jones, M., and Levi, V. *TRV Investigations to Assess the Suitability of 132kV Circuit Breakers for an Offshore Wind Farm Connection*. in *International Conference on Power Systems Transients (IPST2009)*. June 2009. Kyoto, Japan.

APPENDIX 1. LIST OF ABBREVIATIONS AND GLOSSARY

List of Abbreviations

AC	Alternating Current
BERR	Department for Business, Enterprise and Regulatory Reform
CIGRE	International Council on Large Electric Systems
DC	Direct Current
DECC	Department for Energy and Climate Change
DFIG	Doubly Fed Induction Generator
DTU	Technical University of Denmark
EES – UETP	Electric Energy Systems – University Enterprise Training Partnership
EMTP-RV	Electro-Magnetic Transient Program – Restructured Version
FRC	Fully Rated Converter
FSIG	Fixed-Speed Induction Generator
GIL	Gas Insulated Line
GIS	Gas Insulated Substation/Switchgear
HVAC	High Voltage Alternating Current
HVDC	High Voltage Direct Current
IEC	International Electrotechnical Commission
IGBT	Insulated Gate Bipolar Transistor
LCC	Line Commutated Converter
LF	Load Factor
LLF	Loss Load Factor
LIWV	Lightning Impulse Withstand Voltage
MTTR	Mean Time To Repair
NIS	Numerical Integration Substitution
pu	Per unit
PWM	Pulse-Width Modulation
rms	Root mean square
RRRV	Rate of Rise of Recovery Voltage
SF6	Sulphur Hexafluoride
SIWV	Switching Impulse Withstand Voltage
TRV	Transient Recovery Voltage
VCB	Vacuum Circuit Breaker
VSC	Voltage Source Converter
XLPE	Cross-Linked Polyethylene

Glossary

Array: A string of wind turbines which are connected in a radial fashion, either to shore or to an offshore platform.

Round 1: The Round 1 of UK offshore wind farm development was announced in December 2000. This gave developers the opportunity to construct wind farms of up to 30 turbines within the 12 nautical mile territorial limit. The majority of Round 1 offshore wind farms are connected by 33kV cables to shore and do not have offshore substations.

Round 2: In July 2003 the Crown Estate announced a competitive tender process for Round 2 sites. 15 projects amounting to 7.2GW were successful. Round 2 projects are significantly larger than Round 1 projects. They range in size from 240MW to 1200MW and are located further away from shore.

Round 3: The Crown Estate launched its Round 3 leasing programme in June 2008 with a goal to deliver up to 25GW of new offshore wind farm sites by 2020. Round 3 is split into 9 zones. The Dogger Bank zone is the largest of these zones with an agreed target of 9GW of installed offshore wind capacity. It is located 125 to 195km from the coast of Yorkshire.

AC/DC break-even point: The particular cable length above which HVDC transmission becomes more economic than HVAC transmission.

Cost of Constrained Energy: The capitalised cost of energy which is expected to be constrained per year due to failure of equipment. It is calculated based on the failure rate of equipment and the mean time to repair.

Vacuum Circuit Breaker: The contacts of a vacuum circuit breaker are in a vacuum container. Vacuum circuit breakers are generally used for voltages up to 36kV although vacuum circuit breakers have been developed for voltages above this level.

Transient Recovery Voltage: A Transient Recovery Voltage appears across the contacts of a circuit breaker immediately after the arc is extinguished.

SIWV: Electrical strength of insulation against switching overvoltages expresses as the crest value of a standard switching impulse.

LIWV: Electrical strength of insulation against lightning overvoltages expressed as crest value of a standard lightning impulse.

Pole-span: The time between the first pre-strike of one phase and the first pre-strike in another phase

APPENDIX 1A. OFFSHORE WIND FARM DEVELOPMENT

Year	Wind farm Capacity (MW)	Location	Offshore Substation?	Distance to shore (km)	Wind turbine rating (MW)
1991	5	Vindeby, DK	N	1.5 to 3	0.45 (11 x Siemens Bonus)
1994	2	Lely, NL	N	0.8	0.5 (4 x Nedwind)
1995	5	Tunø Knob, DK	N	3	0.5 (10x Vestas)
1996	16.8	Irene Vorrink, NL	N	0.8	0.6 (28x Nordtank)
1998	2.8	Bockstigen, SE	N	4	0.5 (5 x WindWorld)
2000	4	Blyth, UK	N	1.6	2 (2x Vestas)
2001	40	Middelgrunden, DK	N	2	2 (20x Bonus)
2001	10.5	Utgrunden, SE	N	7	1.5 (7 x GE)
2002	160	Horns Rev I, DK [2]	Y	14 - 20	2 (80 x Vestas)
2002	10	Yttre Stengrund, SE	N	5	2 (5 x NEG Micon)
2003	8	Frederikshavn, DK	N	3.2	2.3 to 3 (Nordex, Vestas, Bonus)
2003	60	North Hoyle, UK	N	6.5 - 8	2 (30 x Vestas)
2003	166	Nysted, DK	Y	10	2.3 (72 x Siemens Bonus)
2003	23	Samsø, DK	N	4	2.3 (10 x Siemens Bonus)
2003	17	Rønland	N	0.1	2 to 2.3 (4 x 2MW and 4 x 2.3MW)
2004	25	Arklow Bank, IE	N	10	3.6 (7 x GE)
2004	60	Scroby Sands, UK	N	2.5	2 (30x Vestas)
2004	1.2	Setana, JP	N	0.7	0.66 (2 x Vestas)
2005	90	Kentish Flats, UK	N	9-10	3 (30 x Vestas)
2006	90	Barrow, UK	Y	7	3 (30 x Vestas)
2006	108	Egmond aan Zee, NL	N	10-18	3 (36 x Vestas)
2007	10	Beatrice, UK	N	25	5 (2 x Repower)
2007	90	Burbo Bank, UK	N	6.4 - 7.2	3.6 (25 x Siemens)
2007	110	Lillgrund, SE	Y	10	2.3 (48 x Siemens)
2008	30	Kemi Ajos I + II, FI	N	2.6 - 6	3 (10 x WinWinD)
2008	194	Lynn and Inner Dowsing, UK	N	5	3.6 (54 x Siemens)
2008	120	Princess Amalia, NL	Y	23	2 (60 x Vestas)
2008	30	Thornton Bank I, BE	Y	27 - 30	5 (6 x Repower)
2009	60	Alpha Ventus, DE	Y	45	5 (6 x Repower, 6 x Multibrid)
2009	2	Hywind, NO	N	10	2 (**Floating** wind turbine, **220m** deep water)
2009	209	Horns Rev II, DK	Y (with separate accommodation platform)	31	2.3 (91 x Siemens)
2009	90	Rhyl Flats, UK	N	8	3.6 (25 x Siemens)
2010	180	Robin Rigg, UK	Y	11	3 (60 x Vestas)
2010	173	Gunfleet Sands, UK	Y	8.5	3.6 (48 x Siemens)
2010	102	**Shanghai Donghai Bridge, CN [3]**	N	8-13	3 (34 x **Sinovel**)
2010	6	Xianshui Intertidal Project, CN	N	3.5	2 (3 x Shanghai Electric)
2010	7.2	Avedøre Holme, DK	N	1.4	3.6 (2 x Siemens)
2010	30	Vindpark Vanern, SE	N	3.5	3 (10 x WinWinD & Dynawind)
2010	21	Sprogø, DK	N	10.6	3 (7 xVestas)

2010	12	Frederikshavn, DK	N	4.5	6 (test site)
2010	48	EnBW Baltic 1, DE		16	2.3 (21 x Siemens)
2010	207	Rødsand II, DK	Y	4	2.3 (92 x Siemens)
2010	300	Thanet, UK [4]	Y	12	3 (100 x Vestas)
2010	14	Kamisu, JP	N	0.1	2 (7 x Subaru)
2011	30	Rudong Intertidal Project, CN	N	3.5	1.5 to 3 (3 of 16 turbines - 2x UP82-1500 and 1x Mingyang - installed by the end of 2009.)
2011	315	Sheringham Shoal, UK	Y	17 - 23	3.6 (88 x Siemens)
2011	400	BARD Offshore 1, DE	Y (HVDC)	100 (200km total export cable)	5 (80 x BARD)
2011	184	Walney Phase 1, UK	Y	14	3.6 (51 x Siemens)
2011	45	Weihai Offshore wind farm, phase 1, CN			1.5 (30x)
2011	165	Belwind, BE	Y	45	3 (55 x Vestas)
2012	500	Greater Gabbard, UK [5]	Y (2 - Gabbard and Galloper)	45	3.6 (140 x Siemens)
2012	150	Ormonde, UK	Y	10	5 (30 x Repower)
2012	92	Tricase, IT [6]		20	2.4 and 3.5 (24 x Blue H, floating turbines in 118m water depth)
2012	184	Walney Phase 2, UK	Y	14	3.6 (51 x Siemens)
2012	248	Lincs, UK	Y	8	3.6 (69 x Siemens)

References for Appendix 1A

1. *4C Offshore.* [Online] [Cited: 08 06, 2010.] http://www.4coffshore.com.
2. [Online] [Cited: 08 06, 2010.] www.hornsrev.dk.
3. China Wind Power Newsletter. [Online] June 2010. [Cited: 08 11, 2010.] http://www.windpower.org/download/781/China_wind_power_newsletter_June.pdf.
4. *Thanet Offshore Wind Farm.* [Online] Vattenfall. [Cited: 08 12, 2010.] http://www.vattenfall.co.uk/en/thanet-offshore-wind-farm.htm.
5. *Greater Gabbard.* [Online] [Cited: 08 12, 2010.] http://www.scottish-southern.co.uk/SSEInternet/index.aspx?rightColHeader=30&id=15836.
6. [Online] Blue H Group. [Cited: 08 12, 2010.] http://www.bluehgroup.com/sitedevelopment.php.

APPENDIX 2A. CABLE AND TRANSFORMER SPECIFICATIONS

132kV Submarine Cable (System Base: S=100MVA and V=132kV)					
Conductor Area	mm²	500	630	800	1000
Maximum Continuous Load	MVA	169	187	203	217
Cable a.c. Resistance at max. temp, Rac	Ω/km	0.063	0.054	0.047	0.043
Capacitance, per phase	µF/km	0.192	0.209	0.217	0.236
Suseptance, per phase	mS/km	0.060	0.066	0.068	0.074
Inductive reactance, (star reactance)	Ω/km	0.122	0.117	0.114	0.110
R	p.u / km	3.62E-04	3.08E-04	2.70E-04	2.47E-04
X	p.u / km	7.00E-04	6.71E-04	6.54E-04	6.31E-04
Susceptance (p.u)	p.u / km	1.05E-02	1.14E-02	1.19E-02	1.29E-02

220kV Submarine Cable (System Base: S=100MVA and V=220kV					
Conductor Area	mm²	500	630	800	1000
Maximum Continuous Load	MVA	279	308	335	369
Cable a.c. Resistance at max. temp, Rac	Ω/km	0.066	0.056	0.049	0.045
Capacitance, per phase	µF/km	0.136	0.151	0.163	0.177
Suseptance, per phase	mS/km	0.043	0.047	0.051	0.056
Inductive reactance, (star reactance)	Ω/km	0.122	0.117	0.114	0.110
R	p.u / km	1.36E-04	1.17E-04	1.02E-04	9.26E-05
X	p.u / km	2.52E-04	2.42E-04	2.36E-04	2.27E-04
Susceptance (p.u)	p.u / km	2.07E-02	2.30E-02	2.48E-02	2.69E-02

Table 1. High Voltage XLPE cable specifications with Copper conductors [Alstom T&D, Network Protection & Automation Guide, 1st Ed. 2002].

Rating (MVA)	Primary kV	Primary Taps	Secondary kV	Z% HV/LV	X/R ratio	X (p.u on Rated base)	R (p.u. on Rated base)
60	132	10% - 20%	33	16.7	28	0.16689	0.00596
90	132	10% - 20%	33	24.4	60	0.24397	0.00407
180	132	10% - 10%	15	13.8	40	0.13796	0.00345
250	300	11.2% -17.6%	15	28.6	70	0.28597	0.00409
255	230	+10%'	16.5	14.8	43	0.14796	0.00344

Table 2. Transformer Specifications used in the models [Alstom T&D, Network Protection & Automation Guide, 1st Ed. 2002]

33kV Cable (System Base: S=100MVA, V=33kV)					
Conductor Area	mm²	185	240	300	400
Maximum Continuous Load (at 10°C seabed temp)	MVA	27.4	31.4	34.9	38.9
Series Resistance	Ω/km	0.127	0.098	0.08	0.064
Series Reactance	Ω/km	0.114	0.109	0.105	0.102
Susceptance	mS/km	0.068	0.075	0.081	0.089
R	p.u / km	1.17E-02	9.00E-03	7.35E-03	5.88E-03
X	p.u / km	1.05E-02	1.00E-02	9.64E-03	9.37E-03
Susceptance (p.u)	p.u / km	7.41E-04	8.17E-04	8.82E-04	9.69E-04

Table 3. 33kV XLPE sub-marine cable specifications with Copper conductors. MVA ratings from ABB [www.abb.com/cables], R,X and ωC values from [Alstom T&D, Network Protection & Automation Guide, 1st Ed. 2002]

132kV Cable data used in Chapters 6 and 7:

	132kV 800mm2					
	From data sheet - 15mm insulation/0 mm semiconductor screen	plus 1mm semiconductor screen both sides	plus 2mm semiconductor screen both sides	plus 1mm insulation+1mm semiconductor screen both sides	plus 1mm insulation	plus 2mm insulation
Outer insulation rad (mm)	33.25	35.25	37.25	36.25	34.25	35.25
Distance from centre (mm)	43.00	43.00	45.00	44.00	43.00	43.00
Rout (1) (mm)	16.85	16.85	16.85	16.85	16.85	16.85
Perm (1)	2.30	2.40	2.74	3.13	2.30	2.30
Semi thickness (mm)	0.00	1.00	2.00	1.00	0.00	0.00
Rin (2) (mm)	31.85	33.85	35.85	34.85	32.85	33.85
Rout (2) (mm)	32.07	34.07	36.07	35.07	33.07	34.07
Pipe Rin	91.50	91.50	91.50	91.50	91.50	91.50
Rout	94.00	94.00	94.00	94.00	94.00	94.00
Rext	97.00	97.00	97.00	97.00	97.00	97.00
Vdpth	1.00	1.00	1.00	1.00	1.00	1.00
C (uF/km)	0.20	0.19	0.20	0.24	0.19	0.18
Z (ohm)	25.16	26.98	27.33	24.63	26.38	27.57

	132kV 1000mm2		
	From data sheet - 15mm insulation/0 semiconductor screen	plus 1mm semiconductor screen both sides	plus 2mm semiconductor screen both sides
Outer insulation rad (m)	35.65	37.65	39.65
Distance from centre (m)	45.00	45.00	45.00
Rout (1) (mm)	18.95	18.95	18.95
Perm (1)	2.30	2.63	2.96
Semi thickness	0.00	1.00	2.00
Rin (2) (mm)	33.95	35.95	37.95
Rout (2) (mm)	34.17	36.17	38.17
Pipe Rin	97.30	97.30	97.30
Rout	100.00	100.00	100.00
Rext	103.00	103.00	103.00
Vdpth	1.00	1.00	1.00

$$C = (2pi*e0*er)/\ln(rin2/rout1)$$

$$Z = (138/sqrt(Perm(1)))*LOG10(Rin(2)/Rout(1))$$

Data sheet Reference:

[1] ABB, XLPE Submarine Cable Systems, Attachment to XLPE Land cable Systems - User's Guide, Rev 5 from www.abb.com/cables

APPENDIX 2B. FULL-LOAD LOSSES

Table 1. Full-Load losses for a 100MW wind farm

Transmission Voltage	Conductor Size	Transformer configuration	100MW Transmission via a single cable	_Transmission Distance (km)_								
				20	30	40	50	60	70	80	90	100
132kV	500mm²	One transformer (Z=24.4%, X/R=60, 90MVA), following OTEG guidelines	Transformer losses (MW)	0.44	0.44	0.43	0.43	0.43	0.42	0.41	0.41	0.40
			132kV offshore busbar voltage (p.u)	1.009	1.014	1.02	1.027	1.034	1.042	1.051	1.061	1.072
			132kV offshore busbar Δ(degree)	0.8	1.1	1.4	1.7	1.9	2.1	2.3	2.6	2.8
			Line Losses (MW)	0.72	1.08	1.46	1.84	2.24	2.67	3.16	3.68	4.27
			Reactive Power generated in cable (MVAr)	20	30	40	50	61	72	83	93	106
			Total Full Load losses (MW)	1.16	1.61	1.89	2.27	2.66	3.09	3.56	4.07	4.66
			Total Full Load losses (%)	1.16	1.51	1.86	2.27	2.66	3.09	3.53	4.07	4.66
132kV	630mm²		Transformer losses (MW)	0.44	0.44	0.43	0.43	0.43	0.42	0.41	0.41	0.40
			132kV offshore busbar voltage (p.u)	1.006	1.012	1.018	1.024	1.032	1.04	1.049	1.058	1.069
			132kV offshore busbar Δ(degree)	0.7	1	1.3	1.6	1.9	2.1	2.2	2.4	2.5
			Line Losses (MW)	0.61	0.92	1.25	1.59	1.97	2.37	2.81	3.27	3.84
			Reactive Power generated in cable (MVAr)	22	33	50	66	67	78	90	102	114
			Total Full Load losses (MW)	1.06	1.36	1.68	2.01	2.39	2.78	3.22	3.67	4.23
			Total Full Load losses (%)	1.06	1.35	1.68	2.01	2.39	2.78	3.22	3.67	4.23

Table 2. Full-load losses for a 150MW wind farm

150MW Transmission via a single cable

Transmission Voltage	Conductor Size	Transformer configuration		Transmission Distance (km)								
				20	30	40	50	60	70	80	90	100
132kV	500mm²	Two transformers (Z=24.4%, X/R=60, 90MVA)	transformer losses (MW)	0.49	0.49	0.48	0.47	0.46	0.46	0.46	0.44	0.43
			132kV offshore busbar voltage (p.u)	1.012	1.019	1.026	1.036	1.044	1.053	1.064	1.076	1.087
			132kV offshore busbar Z (degree)	1.1	1.7	2.2	2.6	3	3.4	3.8	4.1	4.2
			Line Losses (MW)	1.69	2.37	3.13	3.92	4.71	5.49	6.32	7.16	8.04
			Reactive Power generated in cable (MVAr)	18	28	37	47	57	67	77	88	99
			Total Full Load losses (MW)	2.08	2.86	3.61	4.39	5.17	5.94	6.76	7.59	8.47
			Total Full Load losses (%)	1.39	1.90	2.41	2.93	3.45	3.96	4.51	5.06	5.64
132kV	630mm²		transformer losses (MW)	0.50	0.48	0.48	0.48	0.47	0.46	0.46	0.44	0.43
			132kV offshore busbar voltage (p.u)	1.01	1.017	1.024	1.031	1.04	1.049	1.059	1.07	1.082
			132kV offshore busbar Z (degree)	1.1	1.6	2.1	2.6	2.9	3.3	3.7	4	4.2
			Line Losses (MW)	1.36	2.03	2.71	3.37	4.07	4.77	5.51	6.28	7.10
			Reactive Power generated in cable (MVAr)	20	30	41	52	63	74	85	97	109
			Total Full Load losses (MW)	1.85	2.52	3.19	3.85	4.54	5.23	5.96	6.72	7.54
			Total Full Load losses (%)	1.23	1.68	2.12	2.56	3.03	3.49	3.97	4.48	5.02
132kV	800mm²		transformer losses (MW)	0.50	0.49	0.48	0.48	0.47	0.46	0.46	0.44	0.44
			132kV offshore busbar voltage (p.u)	1.009	1.015	1.022	1.029	1.037	1.046	1.056	1.066	1.077
			132kV offshore busbar Z (degree)	1.1	1.6	2.1	2.5	2.9	3.3	3.6	4	4.2
			Line Losses (MW)	1.19	1.78	2.39	2.99	3.60	4.22	4.89	5.57	6.33
			Reactive Power generated in cable (MVAr)	21	32	43	54	65	77	89	101	113
			Total Full Load losses (MW)	1.69	2.27	2.87	3.46	4.07	4.68	5.35	6.02	6.77
			Total Full Load losses (%)	1.13	1.52	1.91	2.31	2.72	3.12	3.56	4.01	4.51

(Values in Red show that the cable is over-loaded)

Table 3. Full-Load Losses for a 200MW wind farm

200MW Transmission via a single cable												
Transmission Voltage	Conductor Size	Transformer configuration		Transmission Distance (km)								
				20	30	40	50	60	70	80	90	100
132kV	800mm²	Two parallel transformers (Z=24.4%, X/R=60, 90MVA), following OTEG guidelines	Transformer losses (MW)	0.87	0.86	0.85	0.84	0.82	0.81	0.79	0.78	0.76
			132kV offshore busbar voltage (p.u)	1.012	1.019	1.026	1.034	1.043	1.053	1.063	1.075	1.087
			132kV offshore busbar δ(degrees)	1.4	2.1	2.8	3.4	4	4.5	5	5.5	5.9
			Line Losses (MW)	2.10	3.13	4.14	5.13	6.13	7.14	8.14	9.19	10.23
			Reactive Power generated in cable (MVAr)	18.96	28.75	38.77	49.03	59.56	70.40	81.51	93.00	104.82
			Total Full Load losses (MW)	2.98	3.99	4.99	5.97	6.96	7.95	8.93	9.96	10.99
			Total Full Load losses (%)	1.49	2.00	2.49	2.99	3.48	3.97	4.47	4.98	5.50
132kV	1000mm²		Transformer losses (MW)	0.88	0.87	0.85	0.84	0.83	0.81	0.80	0.78	0.76
			132kV offshore busbar voltage (p.u)	1.011	1.018	1.025	1.033	1.042	1.051	1.061	1.073	1.085
			132kV offshore busbar δ(degrees)	1.4	2	2.7	3.3	3.8	4.4	4.8	5.3	5.7
			Line Losses (MW)	1.93	2.87	3.81	4.74	5.68	6.61	7.56	8.56	9.57
			Reactive Power generated in cable (MVAr)	21.21	32.13	43.27	54.87	66.34	78.30	90.57	103.23	116.23
			Total Full Load losses (MW)	2.80	3.74	4.66	5.58	6.51	7.42	8.35	9.34	10.33
			Total Full Load losses (%)	1.40	1.87	2.33	2.79	3.25	3.71	4.18	4.67	5.16
220kV	500mm²		Transformer losses (MW)	0.89	0.88	0.87	0.86	0.85	0.84	0.83	0.82	0.81
			offshore busbar voltage (p.u)	1.006	1.01	1.015	1.02	1.025	1.031	1.038	1.045	1.053
			offshore busbar δ(degrees)	0.5	0.8	1	1.2	1.4	1.6	1.7	1.8	1.9
			Line Losses (MW)	1.07	1.62	2.21	2.80	3.40	4.07	4.83	5.62	6.52
			Reactive Power generated in cable (MVAr)	39.62	59.67	79.89	100.31	120.93	141.79	162.90	184.29	205.98
			Total Full Load losses (MW)	1.96	2.50	3.08	3.66	4.25	4.91	5.66	6.44	7.33
			Total Full Load losses (%)	0.98	1.25	1.54	1.83	2.13	2.46	2.83	3.22	3.67
220kV	630mm²		Transformer losses (MW)	0.89	0.88	0.87	0.87	0.86	0.85	0.84	0.82	0.81
			offshore busbar voltage (p.u)	1.006	1.009	1.014	1.018	1.024	1.03	1.036	1.043	1.051
			offshore busbar δ(degrees)	0.5	0.8	1	1.2	1.3	1.5	1.6	1.7	1.8
			Line Losses (MW)	0.94	1.40	1.92	2.42	3.03	3.66	4.30	5.05	5.92
			Reactive Power generated in cable (MVAr)	44	67	89	112	135	158	182	205	229
			Total Full Load losses (MW)	1.82	2.28	2.80	3.28	3.88	4.50	5.14	5.87	6.73
			Total Full Load losses (%)	0.91	1.14	1.40	1.64	1.94	2.25	2.57	2.94	3.36

(Values in *Red* show that the cable is over-loaded)

Table 4. Full-Load losses for a 250MW wind farm

250MW Transmission via a single cable

Transmission Voltage	Conductor Size	Transformer configuration		Transmission Distance (km)								
				20	30	40	50	60	70	80	90	100
220kV	500mm²	Three parallel transformers (Z=24.4%, X/R=60, 90MVA)	Transformer losses (MW)	0.92	0.91	0.90	0.89	0.88	0.87	0.86	0.85	0.83
			offshore busbar voltage (p.u)	1.008	1.012	1.017	1.023	1.029	1.036	1.043	1.051	1.059
			offshore busbar δ(degrees)	0.7	1	1.3	1.6	1.8	2	2.2	2.4	2.6
			Line Losses (MW)	1.68	2.51	3.35	4.24	5.13	6.09	7.06	8.13	9.21
			Reactive Power generated in cable (MVAr)	39	58	78	98	118	139	160	181	202
			Total Full Load losses (MW)	2.60	3.42	4.26	5.13	6.01	6.96	7.92	8.98	10.05
			Total Full Load losses (%)	**1.04**	**1.37**	**1.70**	**2.05**	**2.40**	**2.78**	**3.17**	**3.59**	**4.02**
220kV	630mm²		Transformer losses (MW)	0.92	0.91	0.91	0.90	0.89	0.88	0.86	0.85	0.84
			offshore busbar voltage (p.u)	1.007	1.011	1.016	1.021	1.027	1.033	1.04	1.048	1.056
			offshore busbar δ(degrees)	0.6	1	1.2	1.5	1.7	2	2.2	2.3	2.5
			Line Losses (MW)	1.45	2.17	2.93	3.99	4.50	5.32	6.21	7.21	8.24
			Reactive Power generated in cable (MVAr)	43	65	87	110	132	155	178	202	226
			Total Full Load losses (MW)	2.37	3.09	3.83	4.88	5.38	6.19	7.08	8.07	9.08
			Total Full Load losses (%)	**0.95**	**1.24**	**1.53**	**1.95**	**2.15**	**2.48**	**2.83**	**3.23**	**3.63**
220kV	800mm²		Transformer losses (MW)	0.92	0.92	0.91	0.90	0.89	0.88	0.87	0.86	0.84
			offshore busbar voltage (p.u)	1.006	1.01	1.015	1.02	1.025	1.032	1.038	1.046	1.054
			offshore busbar δ(degrees)	0.6	0.9	1.2	1.5	1.7	1.9	2.1	2.3	2.4
			Line Losses (MW)	1.26	1.90	2.58	3.27	3.96	4.78	5.54	6.48	7.44
			Reactive Power generated in cable (MVAr)	47	71	95	119	143	168	193	219	244
			Total Full Load losses (MW)	2.19	2.82	3.49	4.17	4.85	5.65	6.41	7.33	8.28
			Total Full Load losses (%)	**0.87**	**1.13**	**1.40**	**1.67**	**1.94**	**2.26**	**2.56**	**2.93**	**3.31**

(Values in *Red* show that the cable is over-loaded)

Table 5. Full-Load losses for a 300MW wind farm

Transmission Voltage	Conductor Size	Transformer configuration	300MW Transmission via a single cable	Transmission Distance (km)								
				20	30	40	50	60	70	80	90	100
220kV	630mm²	Three parallel transformers (Z=24.4%, X/R=90, 90MVA), following OTEG guidelines	Transformer losses (MW)	1.32	1.31	1.30	1.28	1.27	1.25	1.23	1.22	1.20
			offshore busbar voltage (p.u)	1.008	1.013	1.018	1.024	1.03	1.037	1.044	1.052	1.061
			offshore busbar δ(degrees)	0.8	1.1	1.5	1.8	2.1	2.4	2.7	2.9	3.1
			Line Losses (MW)	2.07	3.10	4.13	5.20	6.26	7.38	8.50	9.70	11.02
			Reactive Power generated in cable (MVAr)	42	63	85	107	129	152	174	198	221
			Total Full Load losses (MW)	3.39	4.41	5.43	6.49	7.52	8.63	9.73	10.92	12.21
			Total Full Load losses (%)	1.13	1.47	1.81	2.16	2.51	2.88	3.24	3.64	4.07
220kV	800mm²		Transformer losses (MW)	1.33	1.31	1.30	1.29	1.27	1.26	1.24	1.22	1.20
			offshore busbar voltage (p.u)	1.007	1.012	1.016	1.022	1.028	1.035	1.042	1.05	1.058
			offshore busbar δ(degrees)	0.8	1.1	1.5	1.8	2.1	2.3	2.6	2.8	3.1
			Line Losses (MW)	1.81	2.73	3.62	4.58	5.54	6.57	7.61	8.73	9.87
			Reactive Power generated in cable (MVAr)	46	69	92	116	140	165	189	214	240
			Total Full Load losses (MW)	3.13	4.04	4.92	5.86	6.81	7.82	8.84	9.95	11.07
			Total Full Load losses (%)	1.04	1.35	1.64	1.95	2.27	2.61	2.95	3.32	3.69
220kV	1000mm²		Transformer losses (MW)	1.33	1.32	1.30	1.29	1.27	1.26	1.24	1.22	1.20
			offshore busbar voltage (p.u)	1.007	1.011	1.016	1.021	1.027	1.033	1.041	1.049	1.057
			offshore busbar δ(degrees)	0.7	1.1	1.4	1.7	2	2.3	2.5	2.7	2.9
			Line Losses (MW)	1.65	2.48	3.33	4.18	5.09	6.00	7.06	8.14	9.24
			Reactive Power generated in cable (MVAr)	50	76	101	127	153	180	207	234	262
			Total Full Load losses (MW)	2.98	3.79	4.63	5.47	6.36	7.26	8.30	9.36	10.45
			Total Full Load losses (%)	0.99	1.26	1.54	1.82	2.12	2.42	2.77	3.12	3.48

(Values in Red show that the cable is over-loaded)

Table 6. Full-load losses for a 350MW wind farm

350MW Transmission via a single cable												
Transmission Voltage	Conductor Size	Transformer configuration		Transmission Distance (km)								
				20	30	40	50	60	70	80	90	100
220kV	1000mm²	Four parallel transformers (Z=24.4%, X/R=60, 90MVA)	Transformer losses (MW)	1.35	1.34	1.33	1.31	1.30	1.28	1.26	1.24	1.22
			offshore busbar voltage (p.u)	1.006	1.012	1.017	1.023	1.029	1.036	1.044	1.052	1.061
			offshore busbar δ(degrees)	0.9	1.3	1.7	2	2.4	2.7	3	3.3	3.5
			Line Losses (MW)	2.24	3.34	4.46	5.60	6.74	7.94	9.21	10.50	11.88
			Reactive Power generated in cable (MVAr)	49	74	99	124	150	176	202	229	257
			Total Full Load losses (MW)	3.59	4.68	5.78	6.91	8.04	9.22	10.47	11.74	13.10
			Total Full Load losses (%)	1.03	1.34	1.65	1.97	2.30	2.63	2.99	3.35	3.74

(Values in *Red* show that the cable is over-loaded)

Table 7. Full-load losses for 33kV inter-array cables

5MW Turbines, 126m rotor diameter:								
Distance between Turbines (km)	No. of Turbines per array	7	6	5	4	3	2	1
0.63	Losses (MW)	0.195	0.150	0.100	0.055	0.026	0.009	0.002
0.63	Losses (%)	0.557	0.501	0.400	0.274	0.171	0.092	0.036
1	Losses (MW)	0.307	0.237	0.158	0.087	0.041	0.015	0.003
1	Losses (%)	0.877	0.790	0.632	0.434	0.271	0.145	0.058

4MW Turbines, 110m rotor diameter:									
Distance between Turbines (km)	No. of Turbines per array	9	8	7	6	5	4	3	2	1
0.55	Losses (MW)	0.212	0.171	0.131	0.093	0.056	0.031	0.014	0.005	0.001
0.55	Losses (%)	0.590	0.536	0.467	0.386	0.281	0.192	0.119	0.064	0.025
0.85	Losses (MW)	0.326	0.263	0.201	0.142	0.086	0.047	0.022	0.008	0.002
0.85	Losses (%)	0.905	0.822	0.718	0.593	0.432	0.296	0.184	0.099	0.040

3MW Turbines, 90m rotor diameter:						
Distance between Turbines (km)	No. of Turbines per array	12	11	10	9	8
0.45	Losses (MW)	0.237	0.204	0.169	0.133	0.095
0.45	Losses (%)	0.658	0.618	0.563	0.493	0.396
0.69	Losses (MW)	0.361	0.310	0.257	0.203	0.146
0.69	Losses (%)	1.003	0.939	0.857	0.752	0.608

Table 8. Full Load Losses for wind farms of 200, 500, and 1000MW rating located 60km from shore

Wind Farm Rating (MW)	Configuration	Transmission voltage (kV)	Cable Size (mm²)	Distance to shore = 60km Cable and Transformer Full Load Losses (%) cable	Cable, Transformer and Array Full Load Losses (%), 5MW turbines 400mm² cable	Cable, Transformer and Array Full Load Losses (%), 4MW turbines 400mm² cable	Cable, Transformer and Array Full Load Losses (%), 3MW turbines 400mm² cable	Cable, Transformer and Array Full Load Losses (%), 5MW turbines mixed 33kV cable
200MW	1 x 200MW	132	800	3.48	3.847	3.886	3.906	4.357
	1 x 200MW	132	1000	3.25	3.617	3.656	3.676	4.127
	2 x 100MW	132	500	2.66	3.027	3.066	3.086	3.537
	2 x 100MW	132	630	2.39	2.757	2.796	2.816	3.267
	1 x 200MW	220	500	2.13	2.497	2.536	2.556	3.007
	1 x 200MW	220	630	1.94	2.307	2.346	2.366	2.817
500MW	2 x 250MW	220	500	2.4	2.767	2.806	2.826	3.277
	2 x 250MW	220	630	2.15	2.517	2.556	2.576	3.027
	2 x 250MW	220	800	1.94	2.307	2.346	2.366	2.817
	3 x 167MW	132	800	3.03	3.397	3.436	3.456	3.907
	3 x 167MW	132	1000	2.85	3.217	3.256	3.276	3.722
	1 x 250MW + 2 x 125MW	1x220, 2x132	500	2.34	2.707	2.746	2.766	3.217
1000MW	5 x 200MW	132	800	3.48	3.847	3.866	3.906	4.357
	5 x 200MW	132	1000	3.25	3.617	3.656	3.676	4.127
	5 x 200MW	220	500	2.13	2.497	2.536	2.556	3.007
	5 x 200MW	220	630	1.94	2.307	2.346	2.366	2.817
	4 x 250MW	220	500	2.4	2.767	2.806	2.826	3.277
	4 x 250MW	220	630	2.15	2.517	2.556	2.576	3.027
	4 x 250MW	220	800	1.94	2.307	2.346	2.366	2.817
	2 x 300MW + 2 x 200MW	2x220, 2x132	800	2.75	3.117	3.156	3.176	3.627
	1 x 350MW + 2 x 250MW + 1 x 150MW	3 x 220, 1 x 132	1000, 630 + 630	2.33	2.697	2.736	2.756	3.207

Configuration	Transmission voltage (kV)	Cable Size (mm²)	60km Full Load Losses (%)	100km Full Load Losses
5 x 200MW	132	800	4.36	6.37
5 x 200MW	132	1000	4.13	6.04
5 x 200MW	220	500	3.01	4.54
5 x 200MW	220	630	2.82	4.24
4 x 250MW	220	500	3.28	4.90
4 x 250MW	220	630	3.03	4.51
4 x 250MW	220	800	2.82	4.19
2 x 300MW + 2 x 200MW	2x220, 2x132	800	3.63	5.29
1 x 350MW + 2 x 250MW + 1 x 150MW	3 x 220, 1 x 132	1000, 630 + 630	3.21	4.76

191

APPENDIX 2C. GUIDELINES FOR CALCULATING ANNUAL LOSSES

1. Calculate Full-Load Losses (W_{max}) and No-Load Losses (W_V). Find the full-load current dependent losses from: $W_{max,1} = W_{max} - W_V$.

2. Obtain values for k and the expected annual mean wind speed for the wind farm site.

3. Either

   a) Using the Weibull distribution, calculate the expected Load Factor (LF) as follows (see section 4.1 for further details):

   $$Energy = \sum_{i=1}^{i=n} H(i) \cdot P(i) \qquad (MWh)$$

   $$LF = Energy /(P_{rated} \cdot 8760)$$

   b) Find a value of Load Factor from the following graph:
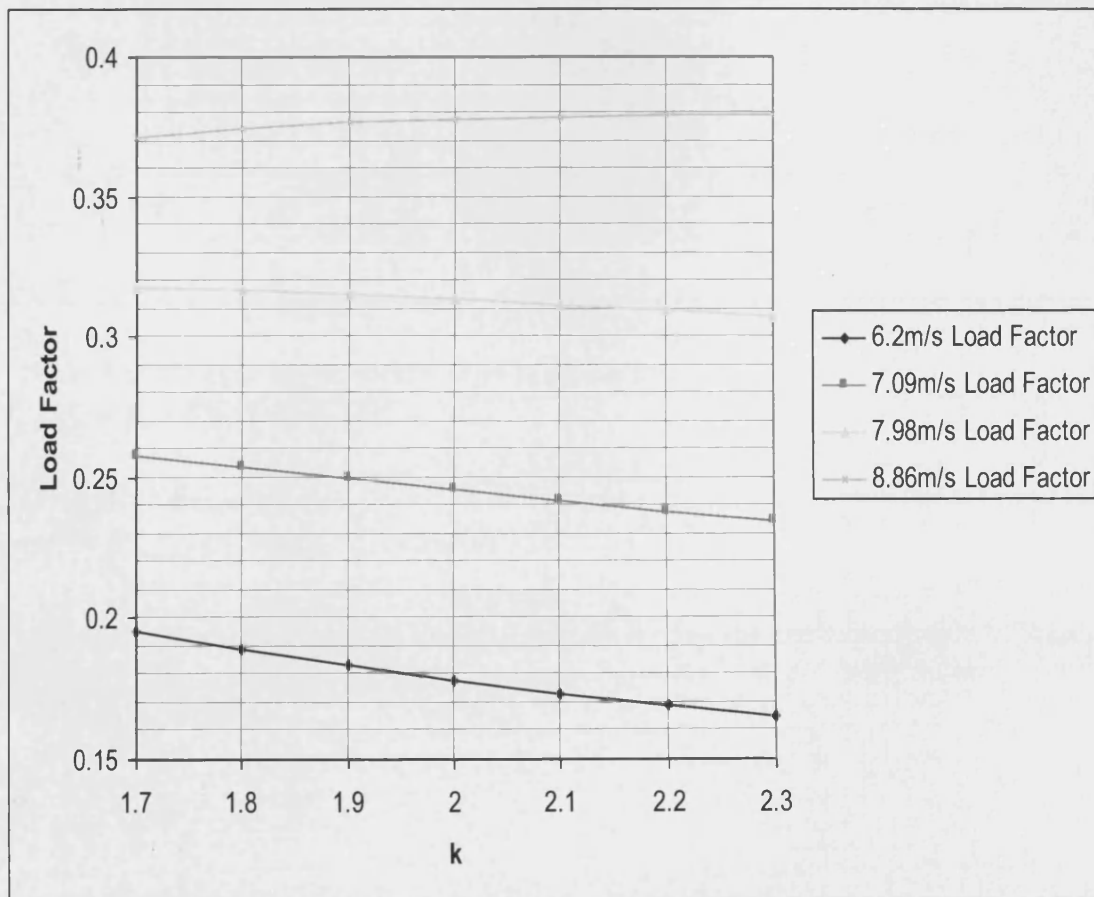
4. Find the value of p that corresponds to the value of k using the following graph:
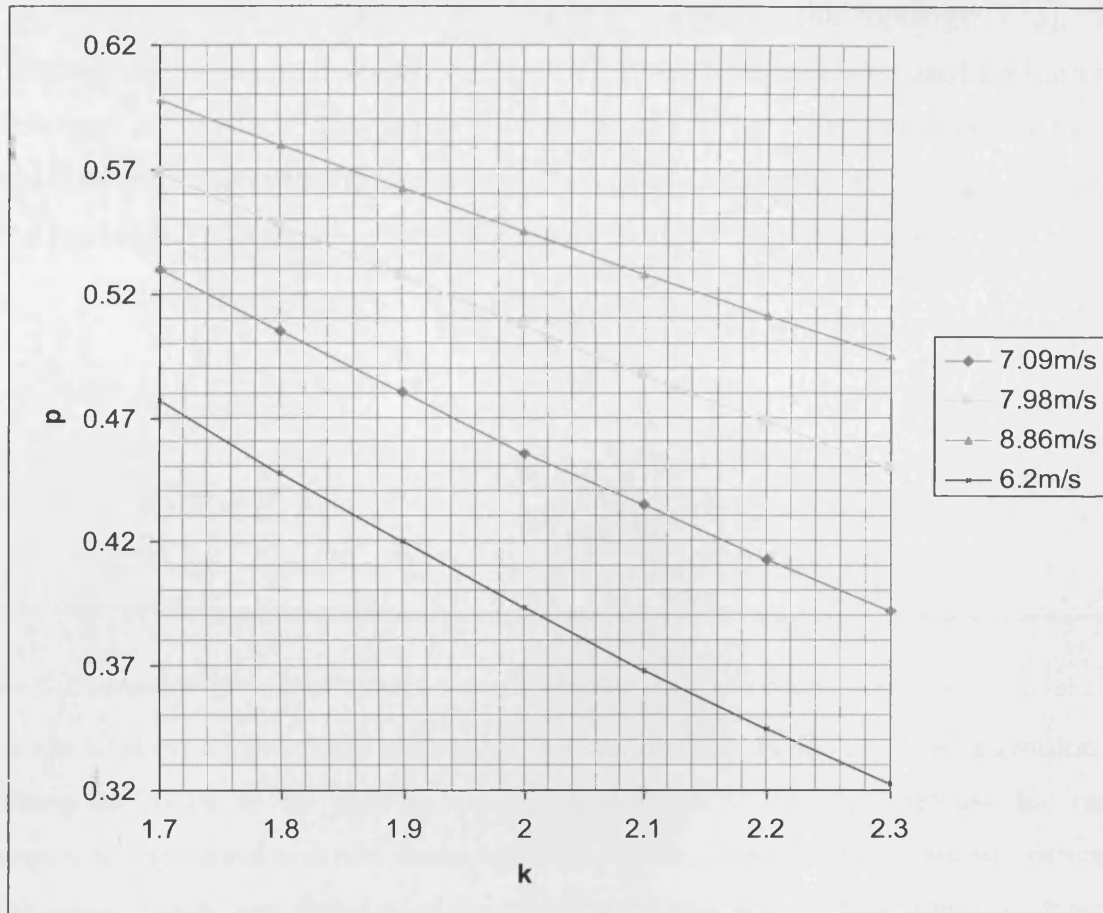
5. Calculate the current-dependent Loss-Load Factor:

$$\mu_{LF} = p \cdot LF + (1 - p) \cdot LF^2$$

6. Find the average losses:

$$\overline{W} = W_{max,l} \cdot \mu_{LF} + W_V \qquad \text{(MW)}$$

7. Calculate the expected annual losses as follows so that the capitalised value of losses can be found:

$$W_{annual} = \overline{W} \cdot 8760 \qquad \text{(MWh)}$$

APPENDIX 2D. HVDC VOLTAGE SOURCE CONVERTERS

The simplest HVDC-VSC converter comprises a conventional two-level three phase bridge [1], as shown in Figure 1. ABB's HVDC Light® is based on this topology [2, 3]. Three-level converters employing four switches for each phase have also been used for high power applications. A three-level VSC provides a significant improvement regarding total harmonic voltage distortion; however the converter system is more complex requiring a complicated control system and a larger footprint which results in higher investment costs.
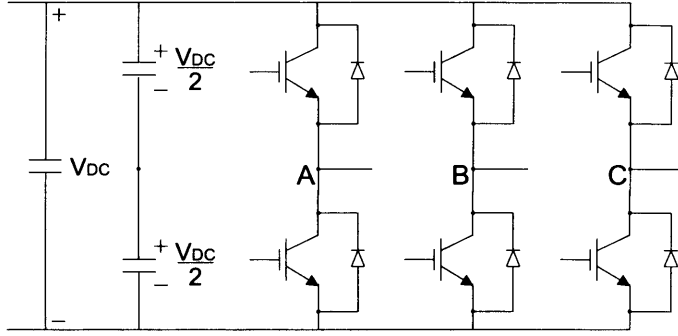
Figure 1. Conventional two-level Voltage Source Converter three phase topology.

There are a variety of switching techniques that can be used for HVDC VSC operation. The switching technique to be used is usually determined by the requirement for reduced harmonics at the output and low losses in the converter. Harmonics are mainly determined by the width, height and position of the converter output pulse. The switching losses are determined by the switching frequency and the number of switches used in the converter.

Pulse Width Modulation (PWM) involves very fast switching between two fixed voltages to create an AC voltage. In order to create this AC voltage, a sinusoidal control signal at the desired frequency is compared with a triangular waveform, as shown in Figure 2. The triangular waveform determines the switching frequency of the devices and its amplitude and frequency are generally kept constant. PWM enables almost any phase angle or amplitude to be created. The control signal is used to modulate the switch duty ratio. The amplitude modulation ratio m_a is defined as [4]:

$$m_a = \frac{\hat{V}_{control}}{\hat{V}_{tri}} \qquad (1)$$

where $\hat{V}_{control}$ is the peak amplitude of the control signal and $\hat{V}_{tri}$ is the amplitude of the triangular signal. The frequency modulation ratio m_f is defined as:

$$m_f = \frac{f_s}{f_1}$$

(2)

where f_s is the carrier frequency and f_1 is the control signal frequency.
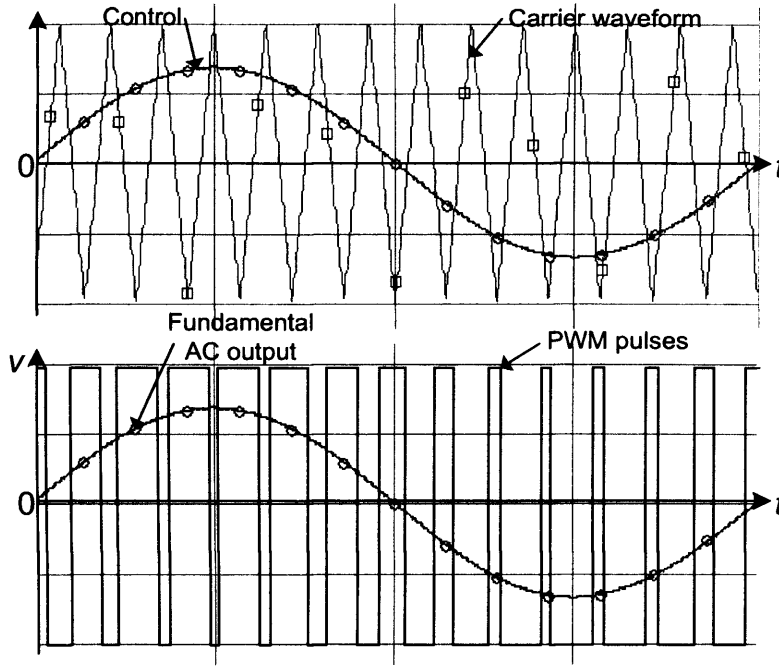
Figure 2. Pulse Width Modulation.

Figure 3 shows the power capability curve for HVDC VSC transmission. From a power system stability perspective, there are three factors that limit the power capability [5]. The first is the current rating of the IGBTs which gives rise to a maximum MVA circle in the power plane where the maximum current and nominal AC voltage is multiplied. The second limit is the DC voltage level. Reactive power transmission is mainly dependent on the difference between the AC voltage generated by the VSC DC voltage and the grid AC voltage. If the grid AC voltage is high, the difference between the AC and DC voltages will be low and so the reactive power capability will be reduced. The third limit is the maximum DC current through the cable.
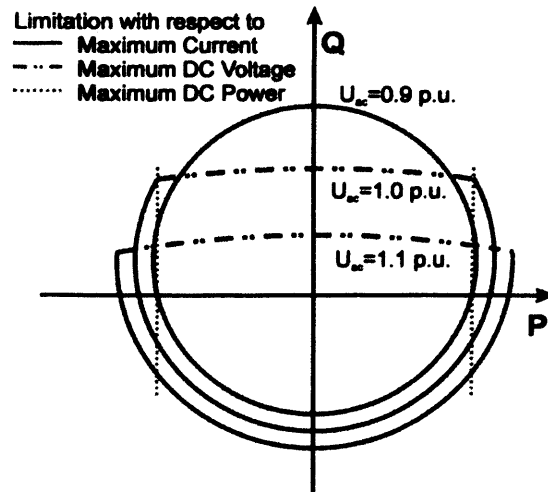
Figure 3. Capability curve for HVDC VSC [5].

REFERENCES

[1]   Agelidis, V. G., Demetriades, G. D. and Flourentzou, N., *Recent Advances in High Voltage Direct-Current Power Transmission Systems*.

[2]   Schettler, F., Huang, H. and Christl, N. *HVDC transmission systems using voltage sourced converters design and applications*. 2000. Seattle, WA, USA; IEEE.

[3]   ABB Power Technologies AB, *Its time to connect – Technical description of HVDC Light technology*, 2006.

[4]   Mohan, N., Undeland, T. M. and Robbins, W.P., *Power Electronics; Converters, Applications and Design*, 2nd ed. 1995: John Wiley & Sons, Inc.

[5]   Johansson, S.G., Asplund, G., Jansson, E. and Rudervall, R., *Power System Stability benefits with VSC DC-Transmission Systems*. CIGRE Session 2004; B4-204, 2004.

APPENDIX 2E. ROUND 3 CASE STUDIES

The Round 3 offshore wind farm sites have connection distances to the onshore grid varying from 40 to 230km as shown in Table 1. The additional capacity for each of the Round 3 regions ranges from 200MW to 15GW. Due to these differences, two regions have been chosen for the case study. The first region to be considered is the North West region, which has relatively short connection distances to the grid of 40km and a potential capacity of 2.5GW. The second region is Dogger Bank which has connection distances of around 210km and a potential capacity of 15GW.

Table 1. Offshore wind capacity – higher scenario [1].

Region	Round 1 + 2 - Under construction/ consented (MW)	Installed Capacity (MW) by 2020		Distance (km) to:	
		Higher Scenario	Additional to Rounds 1 + 2	shoreline	suitable grid connection
Wash	4,068	8,000	3,932	40 - 90	75 - 140
North West	2,588	5,000	2,412	30	40
Thames	1,954	2,800	846	50	50
Severn	108	108	0	-	-
North East	94	94	0	-	-
Scotland	10	10	0	-	-
Wales	0	2,500	2,500	40	40
Dogger	0	15,000	15,000	120 – 180	190 - 230
Total	8,822	33,512	24,690		

EXAMPLE 1. NORTH WEST REGION

A map of the North West region along with the National Grid system is shown in Fig. 1. A more detailed map of the National Grid transmission system is shown in Fig. 2.

Two wind farm options are considered in this region; option 1, 400MW capacity, and option 2, 1200MW capacity. For each of these options, an AC and a DC connection is considered. The DC connection in this case is chosen to be HVDC VSC.
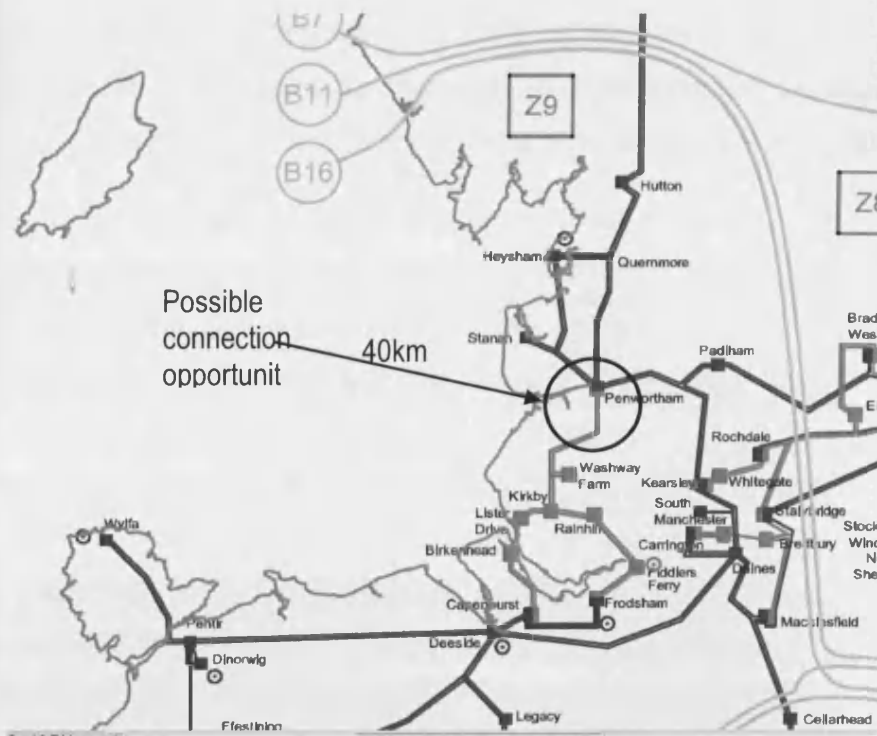
Fig. 1. The North West region and National Grid. Blue lines represent the 400kV network and red lines represent the 275kV network [2].
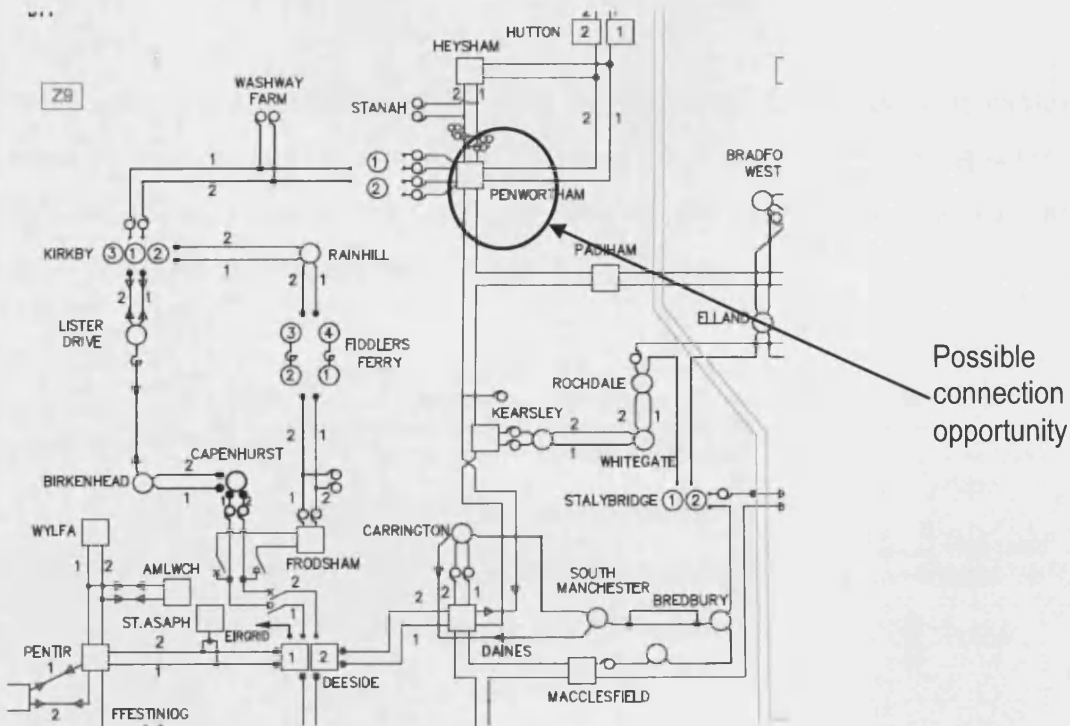
Fig. 2. Section of the North West National Grid transmission system in 2014/15 [2].

198

400MW WIND FARM IN THE NORTH WEST REGION

The cable route lengths for this wind farm are assumed to be similar to those given in the SKM study [46]. A specification of this wind farm is given in Table 2.

Table 2. Specification of 400MW wind farm in North West region.

Rating (MW)	400
Offshore cable route distance (km)	30
Onshore cable route distance (km)	10
Grid connection point	Penwortham?
Turbine Rating (MW)	5
No. of Turbines	80
Array cable spacing (km) average	1
No. of turbines per array	8
No. of array cables	10
Option 1:	HVAC 132kV
Option 2:	HVDC VSC, 150kV

ARRAY CABLING

It is assumed that the total array cabling, and therefore the cost of array cabling will be the same for both AC and DC connection options. The average array cable spacing is assumed to be 1km. This of course will vary depending on the site conditions and location. Tapered array cabling is chosen, as shown in Fig. 3.
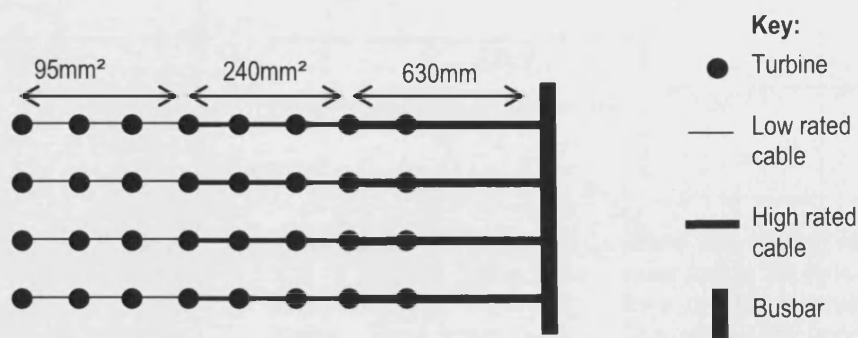
Fig. 3. Array cabling.

The amounts of cable required along with the costs are given in Table 3. This is based on the assumption that there would be 10 arrays. Each array would have 3km of 95mm² 33kV cable connecting the first three turbines in the array. The next three turbines are connected by a total of 3km of 240mm² 33kV cable. The last two turbines are connected to the offshore

199

platform busbar by a total of 2km of 630mm² 33kV cable. The costs for the 95mm² and 240mm² cables have been obtained from the SKM study [1], whilst the cost of the 630mm² has been estimated.

Table 3. Cost of array cabling for a 400MW wind farm.

Cable size (mm²)	Amount required (km)	Cost (£/km)	Total cost (£)
95	30	125000	3.75M
240	30	175000	5.25M
630	20	300000	6.00M
Overall Cost (£):			**15M**

AC SOLUTION (OPTION 1 – 400MW)

A HVAC solution for the connection of the 400MW offshore wind farm is shown in Fig. 4. A transmission voltage of 132kV is chosen. It is assumed that two 132kV cables, each with a capacity of around 200MVA will be required to transmit the power to shore.

HVAC 132kV Connection

There would be 10 array cable connections to the offshore platform. This assumes that the maximum rating of an array cable is around 40MVA.

Assuming that 132kV cables with a 200MVA rating are used, there could be 2 3-core cables. For a longer cable route, the reactive power generated in the cable increases, so an extra cable may be required.

When the cable reaches shore (before the substation), there will be a cable joint. This joins the submarine (usually 3-core cables) with the land cables (usually single-core cables).

Fig. 4. HVAC connection for a 400MW offshore wind farm.

The capital costs for the 400MW wind farm (when connected by HVAC) are given in Table 4. The cost data has been obtained from a SKM study [1] and the OTEG group study of the GB SQSS costs and benefits [3]. The majority of the data in the SKM study is taken from the GB SQSS study data, however there are some minor differences.

Fig. 5 shows the costs for each main section of the HVAC connection. The majority of the cost is due to the submarine cable.

Table 4. Capital costs for a 400MW wind farm connected by HVAC.

Array Cabling

Overall cost (£M)
15

Offshore Platform

Offshore Platform rating (MVA)	Fixed Platform cost (£)	Variable platform cost (£/MVA)	Total Platform cost (£M)
400	5000000	45000	23
2 x 200	5000000	45000	28

Submarine Cable

Rated Voltage (kV)	Conductor size (mm²)	Supply cost (£/m)	Lay and bury (£/m)	Total (£/m)	Cable length (km)	Total cost (£M)
132	800	440	300	740	60	44.4
132	1000	560	300	860	60	51.6

Onshore Cable

Rated Voltage (kV)	Conductor size (mm²)	Supply cost (£/m)	Lay and bury (£/m)	Total (£/m)	Cable length (km)	Total cost (£M)
132	800	440	600	1040	20	20.8
132	1000	560	600	1160	20	23.2

Onshore Substation

Rating (MVA)	Variable substation cost (£/MVA)	Reactive compensation (£/kVAR)	Reactive compensation required (kVAR)	Reactive compensation cost (£M)	Total cost (£M)
400	40000	15	20000	0.3	16.3

Option 1, HVAC Connection:

TOTAL (£M):	120
Cost (£k/MVA)	298.75
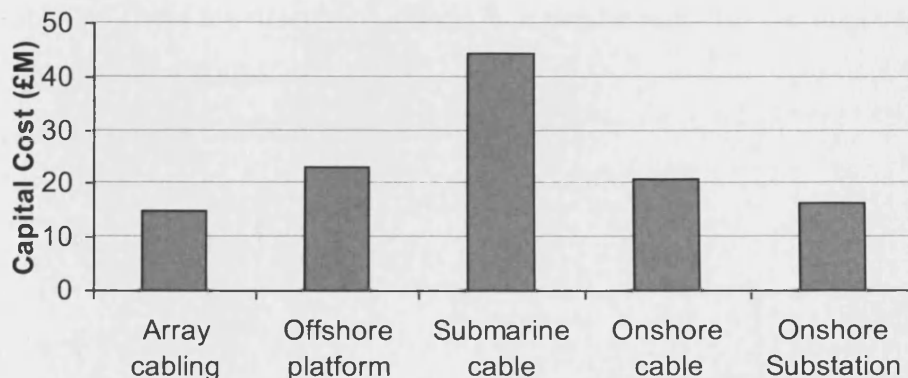
Fig. 5. Capital costs for a 400MW wind farm.

HVDC VSC SOLUTION (OPTION 2 – 400MW)

The HVDC VSC solution for the connection of the 400MW wind farm is shown in Fig. 6. There is a separate AC platform where the voltage is transformed up to 132kV. Two 132kV cables then connect the wind farm to an offshore HVDC VSC platform, where the AC is converted into DC. A pair of ±150KV HVDC cables (bipole) then transmit the power to shore. There is an onshore HVDC VSC platform where the DC is converted back to AC.
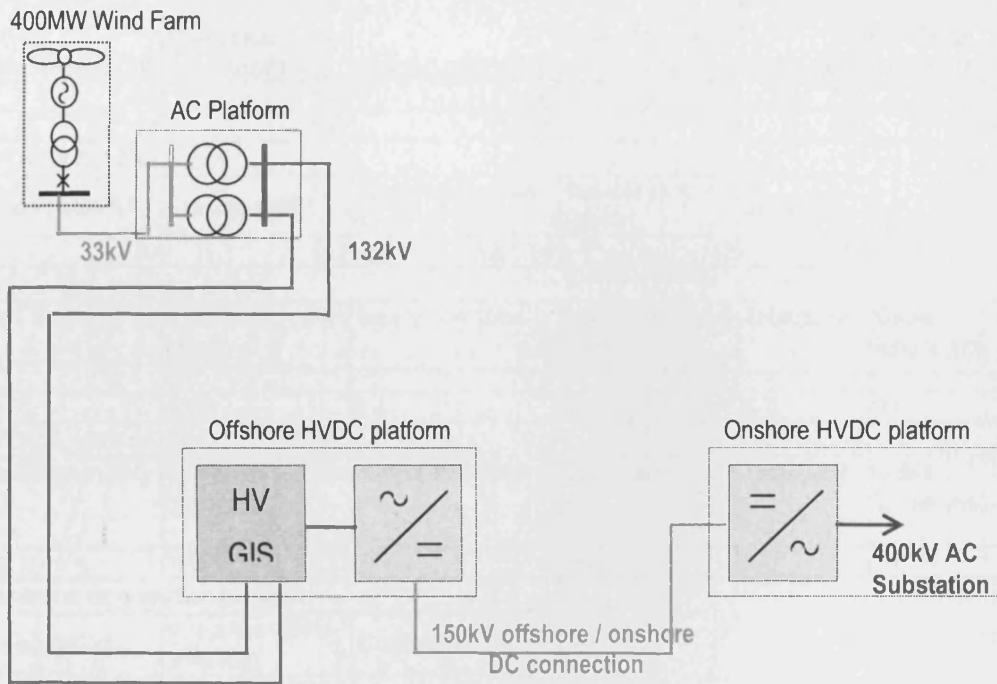
Fig. 6. HVDC connection of a 400MW offshore wind farm.

The capital costs for the 400MW wind farm when connected by HVDC VSC are shown in Table 5. These are illustrated in Fig. 7. It can be seen that the majority of the costs are due to the converter stations.
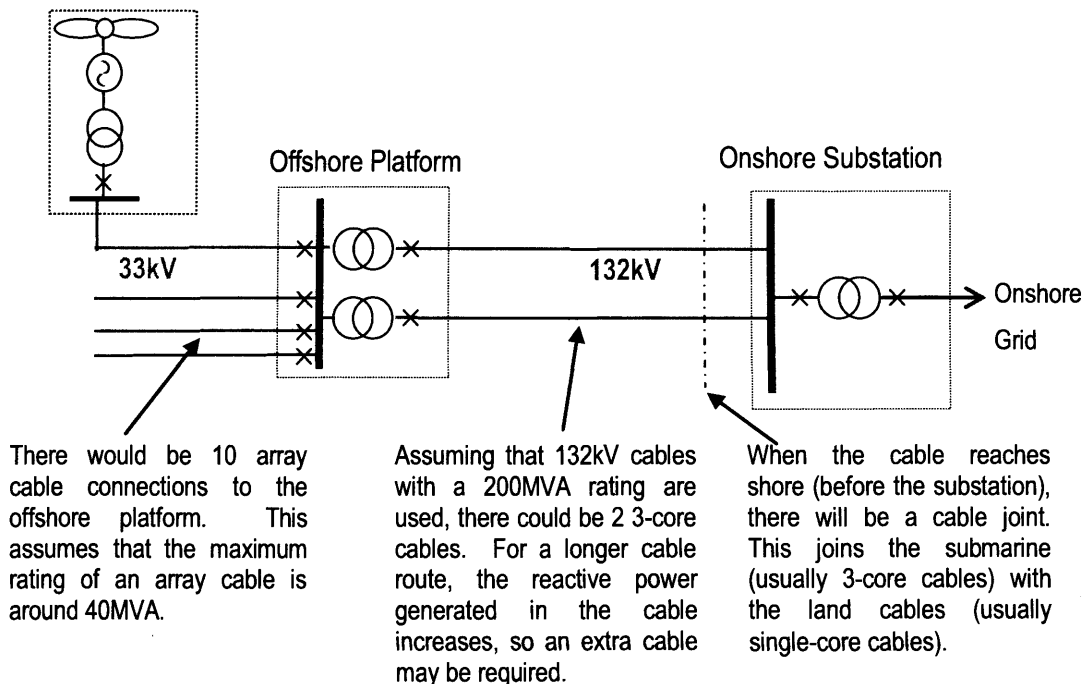
Table 5. Capital costs for a 400MW wind farm connected by HVDC VSC.

Array Cabling

Overall cost (£M)
15

Offshore Platform

Offshore Platform rating (MVA)	Fixed Platform cost (£)	Variable platform cost (£/MVA)	Total Platform cost (£M)
400	5000000	45000	23
2 x 200	5000000	45000	28

Submarine Cable

Rated Voltage (kV)	Conductor size (mm²)	Supply cost (£/m)	Lay and bury (£/m)	Total (£/m)	Cable length (km)	Total cost (£M)
132	800	440	300	740	4	2.96
132	1000	560	300	860	4	3.44

HVDC VSC Platform

Rated Voltage (kV)	Capacity (MW)	Fixed Platform cost (£)	Variable cost (£/kW)	Total (£M)
150	400	25000000	110	69

HVDC Submarine cable

Rated Voltage (kV)	Conductor size (mm²)	Supply cost (£/m)	Lay and bury (£/m)	Total (£/m)	Cable length (km)	Total cost (£M)
150	1000	310	360	670	30	20.1

HVDC Land cable

Rated Voltage (kV)	Conductor size (mm²)	Supply cost (£/m)	Lay and bury (£/m)	Total (£/m)	Cable length (km)	Total cost (£M)
150	1000	310	660	970	10	9.7

Onshore converter station

Rating (MW)	Variable costs (£/MVA)	Cost (£M)
400	110000	44

Option 1, HVDC Connection:

TOTAL (£M):	184
Cost (£k/MVA)	459.4
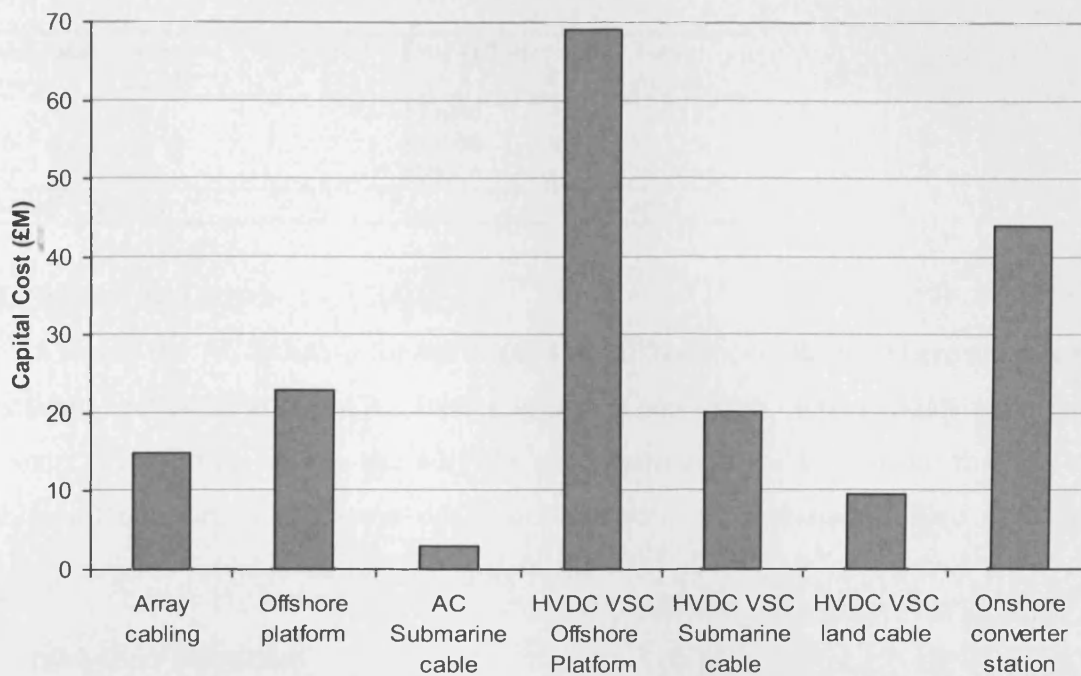
Fig. 7. Capital costs for a 400MW offshore wind farm connected by HVDC VSC.

1200MW WIND FARM IN THE NORTH WEST REGION

The connection options for a 1200MW offshore wind farm in the North West region are again considered to be either HVAC at 132kV, or HVDC VSC. The specification of the wind farm is given in Table 6.

Table 6. Specification for a 1200MW wind farm.

Rating (MW)	1200
Offshore cable route distance (km)	30
Onshore cable route distance (km)	10
Grid connection point	Penwortham?
Turbine Rating (MW)	5
No. of Turbines	240
Array cable spacing (km) average	1
No. of turbines per array	8
No. of array cables	10
Option 1:	HVAC 132kV
Option 2:	HVDC VSC, ±300kV

ARRAY CABLING

Again, it is assumed that the total array cabling, and therefore the cost of array cabling will be the same for both connection options. The average array cable spacing is assumed to be 1km. This of course will vary depending on the site conditions and location.

Table 7. Cost of array cabling for a 1200MW wind farm.

Cable size (mm²)	Amount required (km)	Cost (£/km)	Total cost (£)
95	90	125000	11.25M
240	90	175000	15.75M
630	60	300000	18.00M
Overall Cost (£):			46M

AC SOLUTION (OPTION 1 – 1200MW)

Fig. 8 shows the AC solution for the 1200MW offshore wind farm. There are three offshore platforms each rated at 400MW. Each platform is connected by two 132kV submarine cables to shore, in a similar way to the 400MW wind farm case. It is assumed that the submarine cables all connect to the same onshore substation. It is assumed here that there is no interconnection between the offshore platforms.

HVAC 132kV Connection
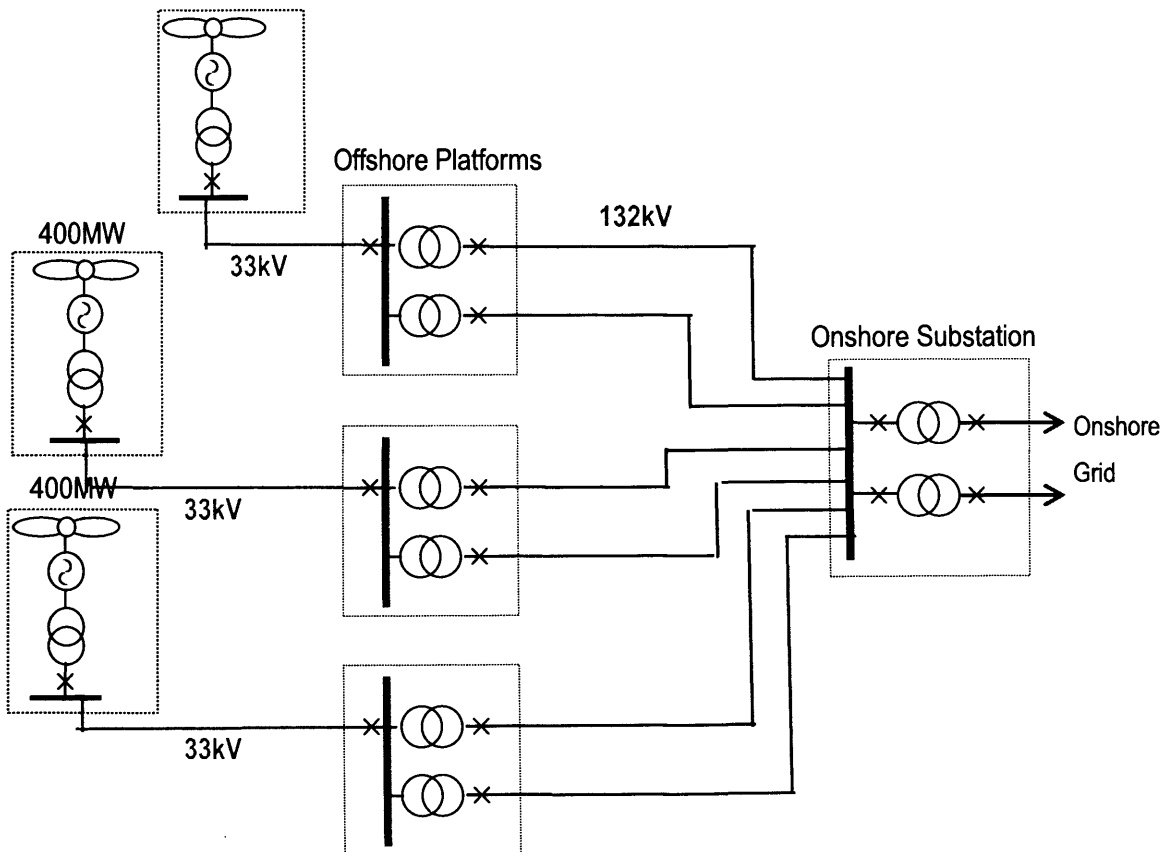
Fig. 8. HVAC connection of a 1200MW offshore wind farm.

The capital costs for the AC solution are given in Fig. 9 and Table 8. The majority of the costs are due to the HVAC submarine cables.

Table 8. Capital costs for a 1200MW wind farm connected by HVAC.

Array Cabling

Overall cost (£M)
46

Offshore Platform

Offshore Platform rating (MVA)	Fixed Platform cost (£)	Variable platform cost (£/MVA)	Total Platform cost (£M)
3 x 400	5000000	45000	69
6 x 200	5000000	45000	84

Submarine Cable

Rated Voltage (kV)	Conductor size (mm²)	Supply cost (£/m)	Lay and bury (£/m)	Total (£/m)	Cable length (km)	Total cost (£M)
132	800	440	300	740	180	**133.2**
132	1000	560	300	860	180	154.8

Onshore Cable

Rated Voltage (kV)	Conductor size (mm²)	Supply cost (£/m)	Lay and bury (£/m)	Total (£/m)	Cable length (km)	Total cost (£M)
132	800	440	600	1040	60	**62.4**
132	1000	560	600	1160	60	69.6

Onshore Substation

Rating (MVA)	Variable substation cost (£/MVA)	Reactive compensation (£/kVAR)	Reactive compensation required (kVAR)	Reactive compensation cost (£M)	Total cost (£M)
1200	40000	15	60000	0.9	**48.9**

Option 1, HVAC Connection:	TOTAL (£M):	360
	Cost (£k/MVA)	299.6
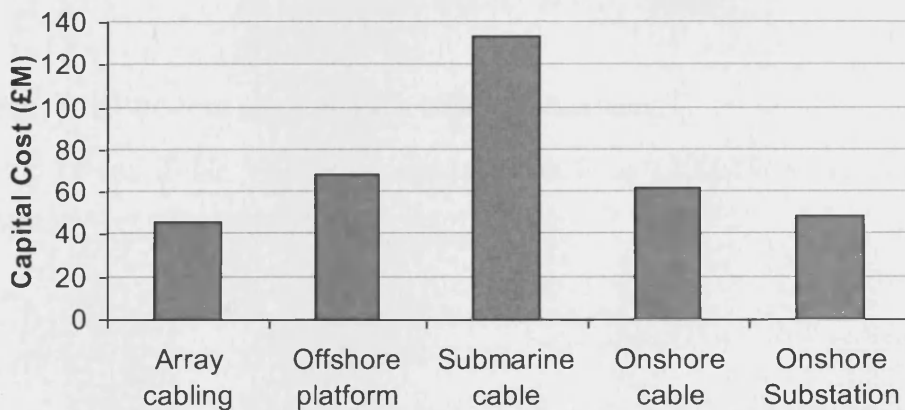
Fig. 9. Capital costs for a 1200MW wind farm connected by HVAC.

HVDC VSC SOLUTION (OPTION 2 – 1200MW)

Fig. 10 shows the connection of a 1200MW wind farm by HVDC VSC. Similarly to the 400MW wind farm, AC platforms will be required to transform the voltage up to 132kV. Each AC platform will then be connected by two submarine cables to the offshore HVDC VSC converter platform. Additional AC switchgear (HV GIS) will be required on the offshore converter platform. The capacity of a HVDC VSC bipole can go up to 1400MW

206

(assuming a transmission voltage of ±320kV), so it is assumed that a pair of HVDC VSC cables will be required to transmit 1200MW to shore. There will then be a converter station onshore.
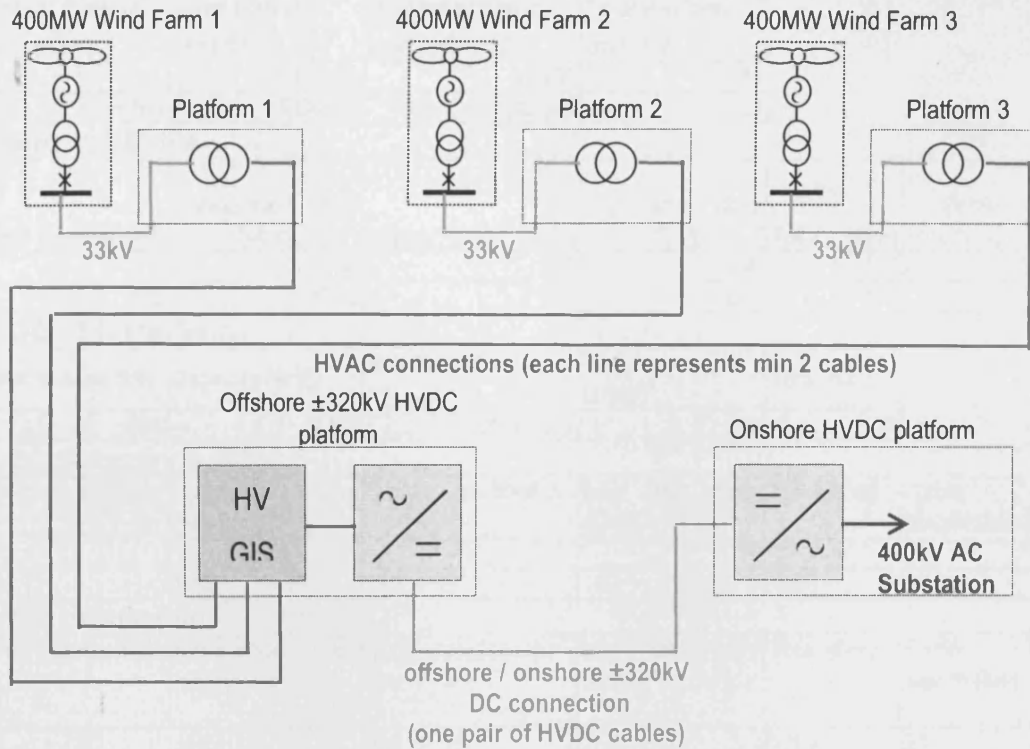
Fig. 10. HVDC VSC connection of a 1200MW wind farm.

Fig. 11 and Table 9 show the capital costs for a 1200MW wind farm connected by HVDC VSC.

Table 9. Capital costs for a 1200MW wind farm connected by HVDC VSC.

Array Cabling

Overall cost (£M)
46

Offshore Platform

Offshore Platform rating (MVA)	Fixed Platform cost (£)	Variable platform cost (£/MVA)	Total Platform cost (£M)
3 x 460	5000000	45000	69
6 x 200	5000000	45000	84

Submarine Cable

Rated Voltage (kV)	Conductor size (mm²)	Supply cost (£/m)	Lay and bury (£/m)	Total (£/m)	Cable length (km)	Total cost (£M)
132	800	440	300	740	12	8.88
132	1000	560	300	860	12	10.32

HVDC VSC Platform

Rated Voltage (kV)	Capacity (MW)	Fixed Platform cost (£)	Variable cost (£/kW)	Total (£M)
320	1200	25000000	110	157

HVDC Submarine cable

Rated Voltage (kV)	Conductor size (mm²)	Supply cost (£/m)	Lay and bury (£/m)	Total (£/m)	Cable length (km)	Total cost (£M)
320	1600	640	450	1090	30	32.7

HVDC Land cable

Rated Voltage (kV)	Conductor size (mm²)	Supply cost (£/m)	Lay and bury (£/m)	Total (£/m)	Cable length (km)	Total cost (£M)
320	1600	640	750	1390	10	13.9

Onshore converter station

Rating (MW)	Variable costs (£/MVA)	Cost (£M)
1200	110000	132

Option 2, HVDC Connection:

TOTAL (£M):	459
Cost (£k/MVA)	382.9
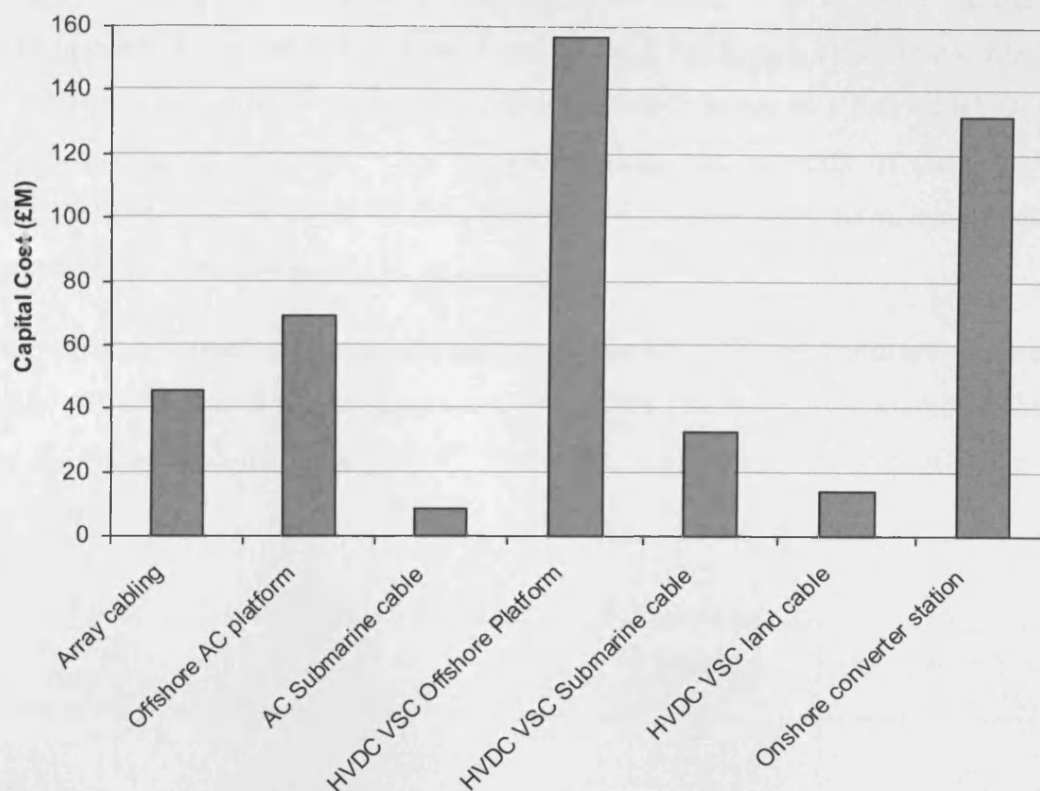
Fig. 11. Capital costs for a 1200MW wind farm connected by HVDC VSC.

The capital costs for a 1200MW wind farm connected by HVDC VSC are dominated by the cost of the HVDC converters.

COMPARISON OF CAPITAL COSTS

Table 10 gives a comparison between the capital costs for the AC and DC connection options of the 400MW and 1200MW wind farms.

Table 10. Comparison of capital costs for a 400MW and a 1200MW wind farm.

	AC capital cost (£M)	DC capital cost (£M)	AC cost (£k/MVA)	DC cost (£k/MVA)
400MW	120	184	298.8	459.4
1200MW	360	459	299.6	382.9

The AC solution is more economical for both wind farm sizes. The cost per rating for the AC solutions are the same for both wind farm ratings at around £300k/MVA. The capital cost for the 400MW DC solution is 53% greater than the AC solution. As the wind farm increases in size, the DC scheme becomes more competitive. For the 1200MW wind farm the capital cost

of the DC solution is 28% greater than the AC scheme. The reduction in the DC cost per rating is due to same amount of submarine DC cable (although a different cable rating is used for the two wind farms) being required for both wind farms, as a pair of HVDC VSC cables can transmit up to 1400MW. For the AC scheme, the capacity of the HVAC submarine cables is assumed to be 200MW, therefore, for a 1200MW wind farm, six cables are required to transmit the power to shore.

If the offshore cable route length is increased, the DC solution becomes more economically viable. This is due to the reduced total cost of the DC cables compared to the AC cables. Fig. 12 shows a comparison of DC versus AC capital cost as the offshore route length increases.
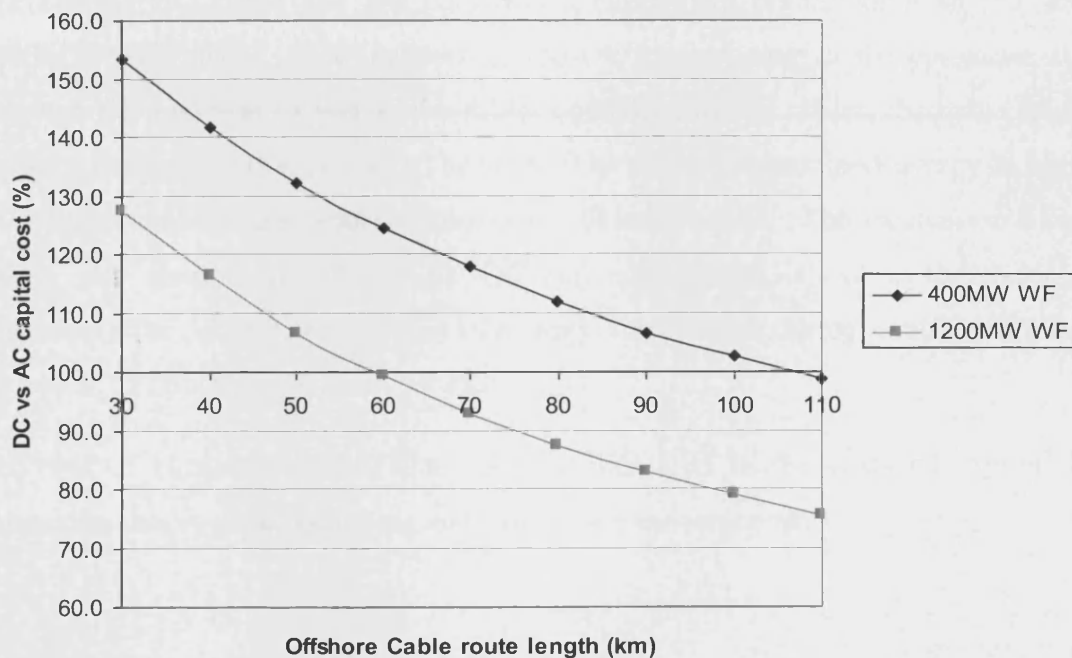
Fig. 12. DC versus AC capital cost for varying offshore cable route lengths.

The results show that the break-even point for AC and DC capital costs is 60km for a 1200MW wind farm whereas it is close to 110km for a 400MW wind farm.

INCLUSION OF LOSSES, MAINTENANCE AND CONSTRAINED ENERGY

Over the lifetime of the wind farm, the cost of losses, maintenance and constrained energy becomes important. Table 11 and Table 12 give a breakdown of the total costs for a 400MW and a 1200MW wind farm respectively.

210

Table 11. Comparison of total costs for a 400MW wind farm in the North West with AC or DC connections.

DC		AC	
Capital Cost (£M)	184	Capital Cost (£M)	120
Total Corrective Maintenance Cost (£M)	2.1	Total Corrective Maintenance Cost (£M)	1.8
Total Cost of Losses (£M)	31.9	Total Cost of Losses (£M)	13.6
Total cost of constrained energy (£M)	15.1	Total cost of constrained energy (£M)	7.3
TOTAL (£M)	**233**	**TOTAL (£M)**	**143**

Table 12. Comparison of total costs for a 1200MW wind farm in the North West with AC or DC connections.

DC		AC	
Capital Cost (£M)	459	Capital Cost (£M)	360
Total Corrective Maintenance Cost (£M)	5.1	Total Corrective Maintenance Cost (£M)	5.4
Total Cost of Losses (£M)	87.1	Total Cost of Losses (£M)	40.9
Total cost of constrained energy (£M)	51.0	Total cost of constrained energy (£M)	7.5
TOTAL (£M)	**602**	**TOTAL (£M)**	**414**

The cost of DC losses and DC constrained energy are higher for both the 400MW and 1200MW wind farms. The majority of the DC losses occur in the converter stations and although DC losses are lower in the cables compared to AC cables, the cable route length is not long enough for this benefit to be seen. The cost of constrained energy is higher for the DC solutions due to the reduced number of cables required. The calculation of constrained energy also assumes that the whole DC converter station is lost in the event of a fault, whereas on the AC solution the loss of a single transformer during a fault still allows half of the power to flow through the substation.

The cost of corrective maintenance is low compared to the costs of capital, losses and constrained energy and represents just over 1% of the total cost.

Example 2. Dogger Bank Region

A study by SKM states that there is a potential capacity of 15GW available in the Dogger Bank region [1]. The study also states that there is a clear case for extending transmission overland, as potential connection points closer to shore may have already been used for the wind farms in the Wash region.

A map of the Dogger Bank region along with the National Grid system is shown in Fig. 13. A more detailed map of the National Grid transmission system is shown in Fig. 14.

Fig. 13. Map of the Dogger Bank region and the National Grid transmission system [2].

Fig. 14. National Grid Transmission system in 2014/15 [47].

AC SOLUTION

It is unlikely that an AC solution will connect the wind farms in the Dogger Bank region. The reason for this is the limitations of HVAC submarine cables. Transmission by HVAC to shore may become viable if GIL is developed for submarine applications. A HVAC example is given here in order to indicate the reasons why a HVAC solution using submarine XLPE cables is not viable. A 1,200MW wind farm capacity is chosen, with the basic layout being the same as the 1,200MW wind farm solution given for the North West region shown in Fig. 8. The main difference is the cable route length. Here, the submarine cable route length is assumed to be 190km and the onshore cable route length is assumed to be 70km.

The capital costs for this wind farm are given in Table 13 and Fig. 15. The submarine cable represents the highest cost. In reality, the capacity of the HVAC cable is taken up by the

reactive power generated in the cable. Therefore, there would be a requirement for at least one extra cable per offshore platform. This would bring the costs up even further.

Table 13. Capital costs for a 1,200MW HVAC wind farm with a cable route length of 260km to the nearest available grid connection point. *This is indicative only, extra cables and offshore reactive compensation platforms would be required in addition to these costs.*

Array Cabling

Overall cost (£M)
46

Offshore Platform

Offshore Platform rating (MVA)	Fixed Platform cost (£)	Variable platform cost (£/MVA)	Total Platform cost (£M)	
3 x 400	5000000	45000	84	additional reactive compensation added
6 x 200	5000000	45000	84	

Submarine Cable

Rated Voltage (kV)	Conductor size (mm²)	Supply cost (£/m)	Lay and bury (£/m)	Total (£/m)	Cable length (km)	Total cost (£M)
132	800	440	300	740	1140	**843.6**
132	1000	560	300	860	1140	980.4

Onshore Cable

Rated Voltage (kV)	Conductor size (mm²)	Supply cost (£/m)	Lay and bury (£/m)	Total (£/m)	Cable length (km)	Total cost (£M)
132	800	440	600	1040	420	**436.8**
132	1000	560	600	1160	420	487.2

Onshore Substation

Rating (MVA)	Variable substation cost (£/MVA)	Reactive compensation (£/kVAR)	Reactive compensation required (kVAR)	Reactive compensation cost (£M)	Total cost (£M)
1200	40000	15	600000	9	**57**

Option 1, HVAC Connection:

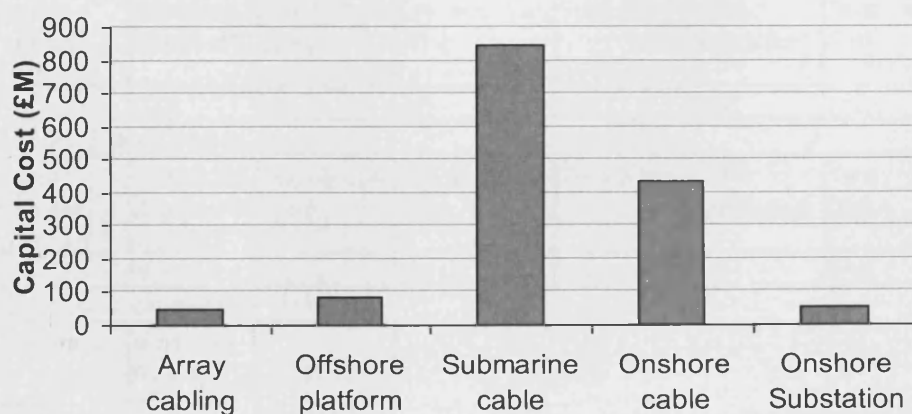| TOTAL (£M):	1467
Cost (£k/MVA)	1222.8

Fig. 15. Capital costs for a 1,200MW HVAC wind farm with a cable route length of 260km to the nearest grid connection point.

214

HVDC VSC SOLUTION

In order to compare the connection costs of the HVAC solution, a 1,200MW wind farm connected by HVDC VSC is considered. The connection principle is similar to that shown in Fig. 10. The main difference here is that the submarine cable route is increased to 190km and the onshore cable route is increased to 70km.

Table 14. Capital costs for a 1,200MW wind farm connected by HVDC VSC. The submarine cable route length is 190km and the onshore cable route length is 70km.

Array Cabling

Overall cost (£M)
46

Offshore Platform

Offshore Platform rating (MVA)	Fixed Platform cost (£)	Variable platform cost (£/MVA)	Total Platform cost (£M)
3 x 400	5000000	45000	69
6 x 200	5000000	45000	84

Submarine Cable

Rated Voltage (kV)	Conductor size (mm²)	Supply cost (£/m)	Lay and bury (£/m)	Total (£/m)	Cable length (km)	Total cost (£M)
132	800	440	300	740	12	8.88
132	1000	560	300	860	12	10.32

HVDC VSC Platform

Rated Voltage (kV)	Capacity (MW)	Fixed Platform cost (£)	Variable cost (£/kW)	Total (£M)
320	1200	25000000	110	157

HVDC Submarine cable

Rated Voltage (kV)	Conductor size (mm²)	Supply cost (£/m)	Lay and bury (£/m)	Total (£/m)	Cable length (km)	Total cost (£M)
320	1600	640	460	1090	190	207.1

HVDC Land cable

Rated Voltage (kV)	Conductor size (mm²)	Supply cost (£/m)	Lay and bury (£/m)	Total (£/m)	Cable length (km)	Total cost (£M)
320	1600	640	750	1390	70	97.3

Onshore converter station

Rating (MW)	Variable costs (£/MVA)	Cost (£M)
1200	110000	132

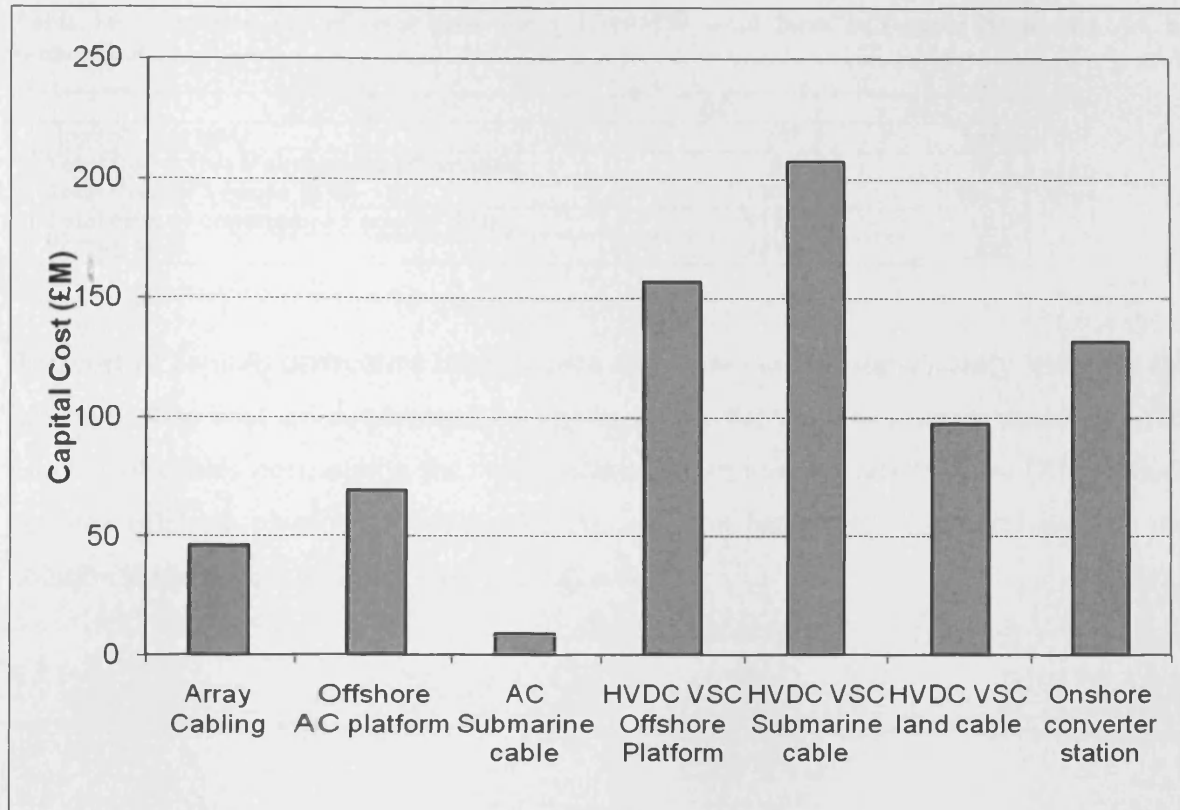| Option 2; HVDC Connection:	TOTAL (£M):	717
	Cost (£k/MVA):	598

Fig. 16. Capital costs for a 1,200MW wind farm connected by HVDC VSC with a submarine cable route length of 190km and an onshore cable route length of 70km.

A comparison between the capital costs for the connection of a 1,200MW wind farm with different cable route lengths is shown in Table 15. Although the HVDC VSC solution is less economical compared to the AC scheme when the cable route lengths are shorter (total 50km), when the cable route lengths are increased to a total of 260km, the HVDC VSC solution is significantly more economical.

Table 15. Comparison between capital costs for a 1,200MW wind farm with different cable route lengths. *The AC capital costs for the longer cable route length are likely to be much higher than this in reality. Extra cables and offshore reactive compensation platforms located at roughly 30km intervals along the cable length would be required in addition.*

Cable route length (km) offshore / onshore	AC capital cost (£M)	DC capital cost (£M)	AC cost (£k/MVA)	DC cost (£k/MVA)
40 / 10	404	470	337	392
190 / 70	1467*	717	1223*	598

Table 16 gives a comparison of the cost of capital, corrective maintenance, losses and constrained energy for the AC and DC solutions.

Table 16. Comparison of total costs for a 1,200MW wind farm in Dogger Bank with AC or DC connections.

	DC	AC
Capital Cost (£M)	717	1467
Total Corrective Maintenance Cost (£M)	6.0	10.5
Total Cost of Losses (£M)	130.8	184.7
Total cost of constrained energy (£M)	118.0	19.3
TOTAL (£M)	971.8	1682

The cost of capital, corrective maintenance and losses are all significantly lower for the DC solution. The cost of constrained energy is higher for the DC solution due to the reduced number of cables connecting the wind farm to shore and the fact that the DC solution only has one offshore platform whereas the AC solution has three. The total cost for the DC solution is significantly lower than the AC solution.

HVDC VSC SOLUTION – 1600MW WIND FARM

Here, a 1600MW wind farm is considered with two different types of connections as shown in Fig. 17. The first comprises four separate HVDC converters each rated at 400MW. The second comprises a single HVDC converter rated at 1600MW and with two bipoles connecting the offshore converter to shore.

A) Individual Connections:

Four AC substations each connected to a 400MW DC converter station. Each DC converter is connected by a single DC bipole to shore.

AC Substation

DC Converter Station

B) Shared Connections:

Four AC substations connected to a single 1600MW DC converter station. Two DC bipoles connect the offshore converter to a single onshore converter.
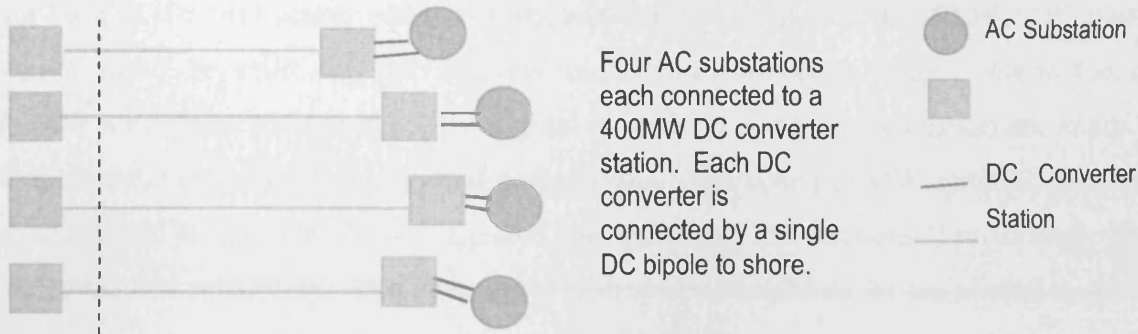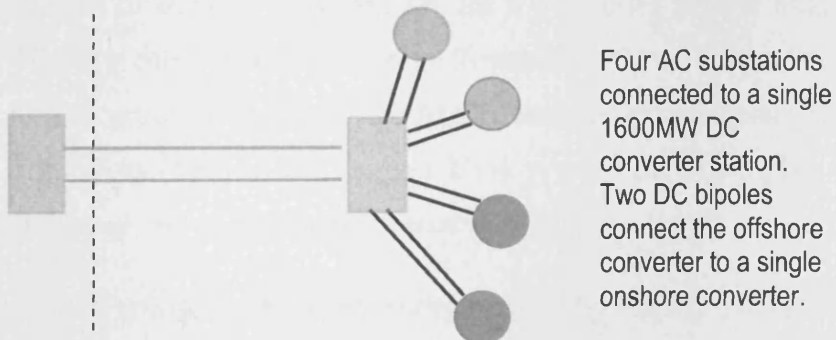
Fig. 17. Configurations for a 1600MW offshore wind farm.

The capital costs of the two solutions are given in Table 17. It is assumed that the wind farm is built in stages, with 400MW being built in the first stage.

Table 17. Comparison between capital costs for shared and individual HVDC VSC connections.

		400MW:	1600MW:
Shared Connections:	TOTAL (£M):	601.4	907.7
	Cost (£k/MVA)	1503.5	567.3
Individual Connections:	TOTAL (£M):	302.3	1209.0
	Cost (£k/MVA)	755.7	755.7

The capital cost for the shared connection is almost double that for the individual connections after the first 400MW has been built. This is due to the whole 1600MW offshore platform being built in the first stage, whereas only one out of a total of four offshore DC platforms would need to be built for the 400MW individual connection stage. Once the whole 1600MW wind farm is completed, the capital costs for the shared connection are much lower than the capital cost for the individual connections. The cost per MW remains the same for both the 400MW and 1600MW stages of the individual connections due to each 400MW being connected separately. The cost per MW drops by two thirds for the shared connection.

Table 18 gives a breakdown of the total costs for the individual and shared connections. The Mean Time To Repair (MTTR) represents the mean time required to repair a failed component or device. The MTTR for a converter is first assumed to be 1 month and the MTTR for a cable is assumed to be 2 months. These values are chosen as they are given by the OTEG group working on the SQSS cost benefit analysis [3]. The MTTR for equipment far from shore (such as the Dogger Bank region) may be higher than the values given by the OTEG group due to the reduced access to site.

The cost of constrained energy is determined by the MTTR values and is much higher for the shared connection solution. This is due to the reduced number of components. Since the cost of constrained energy is determined by the MTTR values, it is beneficial to consider various MTTR values and their effects. The results in Table show that when the MTTR for the converter is increased to 2 months, the cost of constrained energy increases by 14% for the individual connections and by 71% for the shared connections. If the MTTR of the converters is increased to 4 months, the cost of constrained energy becomes over 10 times more for the shared connections. As a result, the overall cost of the individual connection solution becomes more economical compared to the shared connections.

A 1600MW converter station may be modular, with separate 400MW converters operating on a single offshore platform. In this case, the probability of a whole 1600MW converter failure may significantly reduce and therefore bring the cost of constrained energy down.

Table 18. The effect of various MTTR for a 1600MW wind farm with individual and shared connections

		MTTRconv + MTTRcable	1month MTTRconv +1month MTTRcable 4month	4months MTTRconv +4months MTTRcable 2month	+2months MTTRconv +2months MTTRcable 2month	1month MTTRconv +2month MTTRcable 2month
Individual HVDC Connections:	Capital cost (£M)			1209.04		
	Cost (£k/MVA)			755.65		
	Losses (£M)			150.1		
	Corrective maint (£M)	10.5	10.5	10.5	10.5	
	Constrained energy (£M)	55	44.6	35.9	31.4	
	TOTAL (£M)	1424.64	1414.24	1405.54	1401.04	
	Total (£k/MVA)	890.4	883.9	878.5	875.7	
Shared Connections:	Capital cost (£M)			907.7		
	Capital Cost (£k/MVA)			567.3		
	Losses (£M)			114.4		
	Corrective maint (£M)	9.1	9	9.1	9.2	
	Constrained energy (£M)	206.7	483.3	274.8	161	
	TOTAL (£M)	1238.0	1514.6	1306.1	1192.3	
	Total cost (£k/MVA)	773.8	946.7	816.3	745.2	

References for Appendix 2E:

[1] SKM, *Growth Scenarios for UK Renewables Generation and implications for future developments and operation of electrcity networks* BERR, Editor. June 2008.

[2] National Grid, *GB Seven Year Statement*. 2008.

[3] Djapic, P. and Strbac, G., *Cost Benefit Methodology for Optimal Design of Offshore Transmission Systems*, BERR, Editor. July 2008.

APPENDIX 4A. VACUUM CIRCUIT BREAKER DATA

Rated Voltage [ref.]	High frequency quenching capability	Withstand electric field	Comments
13.8kV [1]	30 – 75A/us	2E7V/s	Contact speed = 1m/s with max gap = 5mm. Current chopping = 0.125A
36kV [2]	100 – 200A/us	2E7V/s – 5E7V/s	The following formulae are used: $$\frac{di}{dt} = C(t - t_{open}) + D$$ $$U = A(t - t_{open}) + B$$ $$U_{pre-strike} = TRV\_LIMIT - \left(A(t - t_{open}) + B\right)$$ The TRV limit is the maximum limit that the breaker can withstand: $$TRV\_LIMIT = k_{af} \cdot k_{pp} E\_MAG\sqrt{\frac{2}{3}}$$ Where k(af) is the amplitude factor = 1.4 K(pp) is the first pole to clear factor = 1.5 E_MAG is the breaker rated voltage.
6kV [3]	75A/us	2E7V/s	A 0.1us time step was used.
6kV [4]	100A/us	5E7V/s	The actual hf clearing capability and withstand voltage are found using a Weibull distribution. This is because they are of a statistical nature which depends on the contact material and shape: $$P(EV) = 1 - \exp\left(-\left(1.125\left(\frac{EV}{\overline{EV}} - 0.2\right)\right)^m\right)$$ The hf current clearing capability is represented in the same way, however some papers [9] have criticised this as it is affected by circuit parameters. The value of $m = 4$.
6kV [5]	(C = 0.34E5A/us² and D = 255A/us), (C = 0A/us² and D = 100A/us), (C = 0A/us² and D = 600A/us) and (C = 0.31E6A/us² and D = 155A/us)	(A = 2V/us and B = 0V), (A=2E7V/s and B = 0V), (A = 3E7V/s and B = 1E3V) and (A=5E7V/s and B=0V)	The paper uses these formulae: $$U = A(t - t_{open}) + B$$ $$\frac{di}{dt} = C(t - t_{open}) + D$$
11kV [6]	The number of high frequency current zero crossings before opening is set to 3	2E7V/s and 4E7V/s	Chopping current of either 5 or 8A.
6.3kV [7]	75A/us	2E7V/s	These are average values. A neural networking technique is used to calculate the points at which the arc ignites and extinguishes.
10.5 to 15.8kV [8]	High: C_C = 0.34E11A/s², D_D = 255E6A/s Medium: C_C = 0.31E12A/s², D_D = 155E6A/s Low: C_C = 1E12A/s², D_D = 190E6A/s	High: A_A = 1.7E7V/s, B_B = 3.4E3V Medium: A_A = 1.3E7V/s, B_B = 0.69E3V Low: A_A = 0.47E6V/s, B_B = 0.69E3V	Three typical characteristics are given (high, medium and low) for both the high frequency current clearing capability and the dielectric withstand. Combining these characteristics leads to nine different types of VCB. Three ranges of arc angle values are investigated: 0-10us, 10-50us and 50-100us.

References for Appendix 4A:

[1]   Popov, M. and Acha, E., *Overvoltages due to switching off an unloaded transformer with a vacuum circuit breaker*. IEEE Transactions on Power Delivery, 1999. 14(4): p. 1317-26.

[2]   Kondala Rao, B. and Gopal, G. *Development and application of vacuum circuit breaker model in electromagnetic transient simulation*. 2006. New Delhi, India: IEEE.

[3]   Kosmac, J. and Zunko, P., *Statistical vacuum circuit breaker model for simulation of transient overvoltages*. IEEE Transactions on Power Delivery, 1995. 10(1): p. 294-300.

[4]   Chaly, A.M. and Chalaya, A.T. *Computer simulation of transformer magnetising current interruption by a vacuum circuit breaker*. 1996. Berkeley, CA, USA: IEEE, Piscataway, NJ, USA.

[5]   Wong, S.M., Snider, L.A., and Lo, E.W.C. *Overvoltages and Reignition Behaviour of Vacuum Circuit Breaker*. in *6th International Conference on Advances in Power System Control, Operation and Management*. 2003. Hong Kong.

[6]   Vollet, C. and Metz-Noblat, B.d. *Vacuum Circuit Breaker Model: Application Case to Motors Switching*. in *International Power Systems Transients Conference*. 2007. Lyon, France.

[7]   Kosmac, J. and Zunko, P., *Vacuum Circuit Breaker models for calculation of Transient Overvoltages*. CIGRE Session 1996 : 13-203, 1996.

[8]   Glinkowski, M.T., Gutierrez, M.R., and Braun, D., *Voltage escalation and reignition behavior of vacuum generator circuit breakers during load shedding*. IEEE Transactions on Power Delivery, 1997. 12(1): p. 219-26.

[9]   Li, H.Q. and Smeets, R.P.P., *Gap-length Dependent Phenomena of High-frequency Vacuum Arcs*. 1993, Eindhoven University of Technology.

APPENDIX 4B. THE LONG TRANSMISSION LINE

Figure 1 shows one phase and the neutral connection of a three-phase line. Lumped parameters are not shown since the model takes into account uniformly distributed values of impedance and admittance.
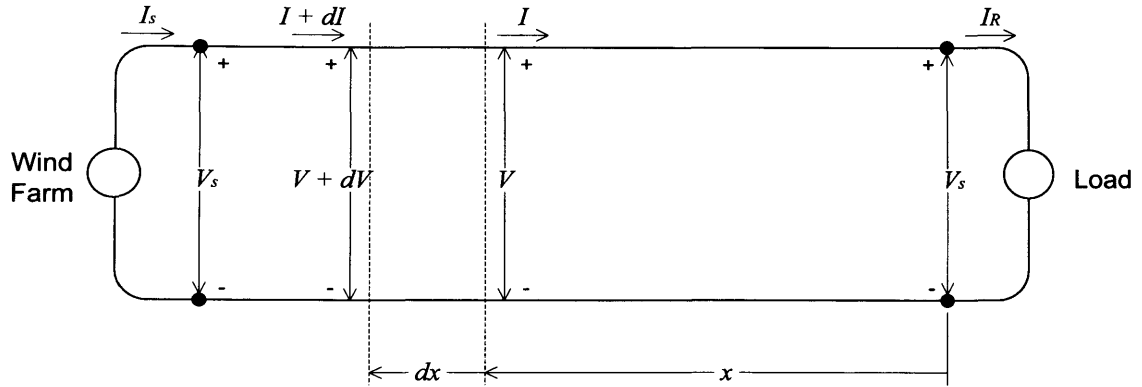

Figure 1. Schematic diagram of a transmission line showing one phase and the neutral return.

In Figure 1 a differential element of length dx in the line at a distance x from the receiving end of the line is considered. The series impedance and shunt admittance of the elemental section are zdx and ydx respectively. V and I are phasors which vary with x.

The average line current in the element is $(I + I + dI)/2$, and the increase of V in along the distance dx can therefore be expressed as:

$$dV = \frac{I + I + dI}{2} zdx \qquad (1)$$

Also,

$$dI = \frac{V + V + dV}{2} ydx \qquad (2)$$

Equations (1) and (2) result in the following equations if the products of the differential quantities are neglected:

$$\frac{dV}{dx} = Iz \qquad (3)$$

$$\frac{dI}{dx} = Vy \qquad\qquad (4)$$

Differentiating equations (3) and (4) with respect to x results in:

$$\frac{d^2V}{dx^2} = z\frac{dI}{dx} \qquad\qquad (5)$$

$$\frac{d^2I}{dx^2} = y\frac{dV}{dx} \qquad\qquad (6)$$

If the values in equations (3) and (4) are substituted into equations (5) and (6) respectively, the following equations are obtained:

$$\frac{d^2V}{dx^2} = yzV \qquad\qquad (7)$$

$$\frac{d^2I}{dx^2} = yzI \qquad\qquad (8)$$

Equation (7) contains the variables V and x and equation (8) contains only variables in I and x. The solutions of the equations for V and I respectively will be expressions which when differentiated twice with respect to x yield the original expression multiplied by the constant yz. This suggests an exponential form of solution, such as:

$$V = A_1 e^{\sqrt{yz}x} - A_2 e^{-\sqrt{yz}x} \qquad\qquad (9)$$

If equation (9) is now substituted into the value given by equation (3),

$$I = \frac{1}{\sqrt{z/y}} A_1 e^{\sqrt{yz}x} - \frac{1}{\sqrt{z/y}} A_2 e^{-\sqrt{yz}x} \qquad\qquad (10)$$

The constants A_1 and A_2 can be evaluated by using the conditions at the receiving end of the line; $x = 0$, $V = V_R$ and $I = I_R$. Substitution of these values yields:

$$V_R = A_1 + A_2 \quad \text{and} \quad I_R = \frac{1}{\sqrt{z/y}}(A_1 - A_2)$$

Substituting $Z_C = \sqrt{z/y}$ and solving for A_1 gives:

$$V = \frac{V_R + I_R Z_C}{2} e^{yx} + \frac{V_R - I_R Z_C}{2} e^{-yx} \qquad\qquad (11)$$

$$I = \frac{V_R / Z_C + I_R}{2} e^{\gamma x} - \frac{V_R / Z_C - I_R}{2} e^{-\gamma x} \qquad \text{(12)}$$

Where $\gamma = \sqrt{zy}$ is called the propagation constant, and Z_C is called the characteristic impedance of the line.

A more convenient form of the equations for computing current and voltage of a power line is found by introducing hyperbolic functions, as defined in equations (13) and (14):

$$\sinh \vartheta = \frac{e^{\vartheta} - e^{-\vartheta}}{2} \qquad \text{(13)}$$

$$\cosh \vartheta = \frac{e^{\vartheta} + e^{-\vartheta}}{2} \qquad \text{(14)}$$

By rearranging equations (11) and (12) and by substituting the hyperbolic functions for the exponential terms, the following equations are obtained which give voltage and current anywhere along the line:

$$V = V_R \cosh \gamma x + I_R Z_C \sinh \gamma x \qquad \text{(15)}$$

$$I = I_R \cosh \gamma x + \frac{V_R}{Z_C} \sinh \gamma x \qquad \text{(16)}$$

The sending end voltages and currents can now be found along with values of voltage and current anywhere along the length of the line.

APPENDIX 4C. CALCULATIONS FOR THE WIND TURBINE MODEL

The base values for all three wind turbine types were:

$$V_{base} = 0.69 \text{kV}_{LL}$$

$$S_{base} = 3\text{MVA}$$

$$I_{base} = S_{base} / \sqrt{3} \cdot V_{base} = 2.51\text{kA}$$

$$Z_{base} = \frac{|V_{base}|^2}{S_{base}} = 0.1587\Omega$$

The impedance value was then determined by the fault level contribution of the wind turbine. An example is shown here for the DFIG, where the fault level was 3pu. The corresponding impedance was then:

$$|Z_{th}|_{pu} = \frac{S_{base}}{S_{sc}} = \frac{1}{3}$$

$$|Z_{th}| = Z_{base} \times |Z_{th}|_{pu} = 0.0529\Omega$$

The positive sequence resistance was chosen so that the X/R ratio was 10:

$$R_0 = R_1 = R_2 = |Z_{th}|/10 = 0.00529\Omega$$

$$X_1 = |Z_{th}| = 0.0529\Omega$$

Using typical values in [8], the zero and negative sequence reactance was chosen:

$$X_0 = 1.6 \times |Z_{th}| = 0.08464\Omega$$

$$X_2 = 0.15 \times |Z_{th}| = 0.00794\Omega$$

APPENDIX 5A. NUMERICAL INTEGRATION SUBSTITUTION

Numerical Integration Substitution (NIS) constitutes the basis of Dommel's EMTP [1], which is now the most generally accepted method for the solution of electromagnetic transients.

Trapezoidal integration is used for NIS due to its stability, simplicity and reasonable accuracy in most circumstances. The trapezoidal rule is based on a truncated Taylor's series and so can cause some numerical oscillations under certain conditions due to the neglected terms.

Another characteristic of Dommel's method is the discretisation of the system components, given a pre-determined time-step. These are then combined in a solution for the nodal voltages. Branch elements are represented by the relationship which they maintain between the branch current and nodal voltage.

Discretisation of R, L, C elements

The simplest circuit element is a resistor connected between the nodes k and m. It can be represented by equation (1) and is shown in Figure 1

$$i_{km} = \frac{1}{R}\left(v_k(t) - v_m(t)\right) \qquad (1)$$
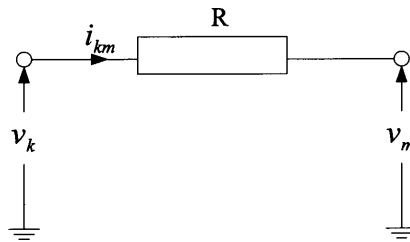

Figure 1. Resistor

Provided that R is not too small, resistors are accurately represented in this formulation. If the value of R is too small, its inverse in the matrix system will be large which results in poor conditioning of the solution at every step. The results then become inaccurate due to the finite precision of the numerical calculations.

The differential equation for the inductor shown in Figure 2 is:

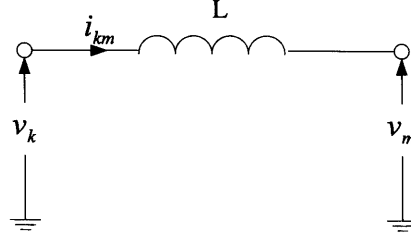$$v_L = v_k - v_m = L\frac{di_{km}}{dt} \qquad (2)$$

Figure 2. Inductor

Equation (2) can be rearranged to form:

$$i_{km(t)} = i_{km(t-\Delta t)} + \int_{t-\Delta t}^{t} (v_k - v_m) dt \qquad (3)$$

Applying the trapezoidal rule gives:

$$
\begin{aligned}
i_{km(t)} &= i_{km(t-\Delta t)} + \frac{\Delta t}{2L}\left((v_k - v_m)_{(t)} + (v_k - v_m)_{(t-\Delta t)}\right) \\
&= i_{km(t-\Delta t)} + \frac{\Delta t}{2L}\left(v_{k(t-\Delta t)} - v_{m(t-\Delta t)}\right) + \frac{\Delta t}{2L}\left(v_{k(t)} - v_{m(t)}\right)
\end{aligned}
\qquad (4)
$$

$$i_{km}(t) = I_{History}(t - \Delta t) + \frac{1}{R_{eff}}\left(v_k(t) - v_m(t)\right) \qquad (5)$$

Where:

$$I_{History}(t - \Delta t) = i_{km}(t - \Delta t) + (\Delta t / 2L)\left(v_k(t - \Delta t) - v_m(t - \Delta t)\right) \qquad (6)$$

And

$$R_{eff} = 2L / \Delta t$$

The term $2L / \Delta t$ is known as the instantaneous term as it relates the current to the voltage at the same time point (any change in one will instantly be reflected in the other). As an effective resistance, very small values of $2L / \Delta t$ can also result in poor conditioning of the conductance matrix.

Transforming equation (6) to the z domain gives:

$$I_{km}(z) = z^{-1}I_{km}(z) + \frac{\Delta t}{2L}\left(1 + z^{-1}\right)\left(V_k(z) - V_m(z)\right) \qquad (7)$$

Rearranging gives the following relationship between current and voltage in the z-domain:

$$\frac{I_{km}(z)}{(V_k(z) - V_m(z))} = \frac{\Delta t(1 + z^{-1})}{2L(1 - z^{-1})}$$ (8)
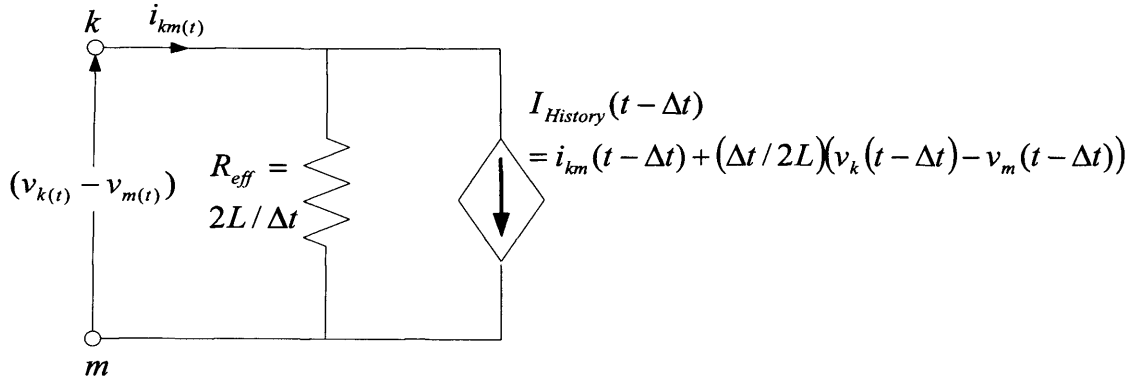

Figure 3. Norton equivalent of the inductor

The differential equation for the capacitor shown in Figure 4 is:
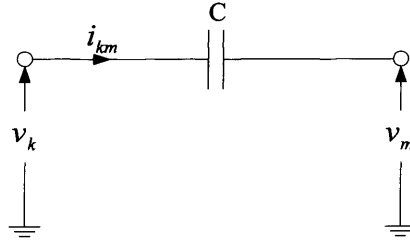
$$i_{km}(t) = C \frac{d(v_k(t) - v_m(t))}{dt}$$ (9)

Figure 4. Capacitor

Integrating and rearranging gives:

$$v_{km(t)} = (v_{k(t)} - v_{m(t)}) = (v_{k(t-\Delta t)} - v_{m(t-\Delta t)}) + \frac{1}{C} \int_{t-\Delta t}^{t} i_{km} dt$$ (10)

Applying the trapezoidal rule gives:

$$v_{km}(t) = (v_k(t) - v_m(t)) = (v_k(t - \Delta t) - v_m(t - \Delta t)) + \frac{\Delta t}{2C}(i_{km}(t) + i_{km}(t - \Delta t))$$ (11)

The current in the capacitor can be given by:

$$i_{km}(t) = \frac{2C}{\Delta t}(v_k(t) - v_m(t)) - i_{km}(t - \Delta t) - \frac{2C}{\Delta t}(v_k(t - \Delta t) - v_m(t - \Delta t))$$

$$= \frac{1}{R_{eff}}[v_k(t) - v_m(t)] + I_{History}(t - \Delta t)$$ (12)

Where

$$R_{eff} = \frac{\Delta t}{2C}$$

And

$$I_{History}(t - \Delta t) = -i_{km}(t - \Delta t) - \frac{2C}{\Delta t}\left(v_k(t - \Delta t) - v_m(t - \Delta t)\right) \tag{13}$$

This results in a Norton equivalent and is shown in Figure.

Transforming equation (13) into the z-domain gives:

$$I_{km} = -z^{-1}I_{km} - \frac{2C}{\Delta t}(V_k - V_m)z^{-1} + \frac{2C}{\Delta t}(V_k - V_m) \tag{14}$$

Giving a relationship between the current and voltage in the z-domain of:

$$\frac{I_{km}}{(V_k - V_m)} = \frac{2C}{\Delta t}\frac{(1 - z^{-1})}{(1 - z^{-1})} \tag{15}$$
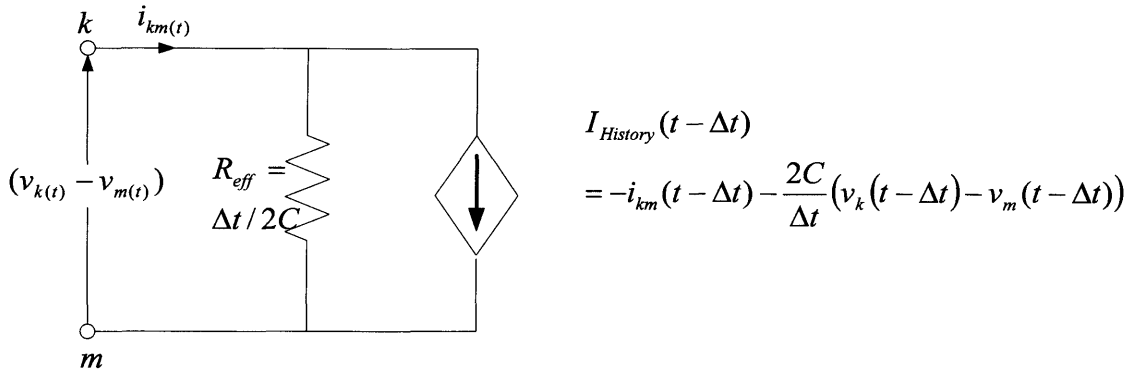

Figure 5. Norton equivalent of a capacitor

Any implicit integration formula can be substituted into a differential equation to form a difference equation and a corresponding Norton equivalent. A choice of three integration methods are given in EMTP-RV in the simulation options, they are; Trapezoidal, Trapezoidal and Backward Euler, and Backward Euler. The Norton equivalents described for the inductor and capacitor above were obtained using the Trapezoidal integration method.

Integration Method	R_{eq}	$I_{History}$
Inductor:		
Trapezoidal	$\dfrac{2L}{\Delta t}$	$i_{n-1} + \dfrac{\Delta t}{2L} v_{n-1}$
Backward Euler	$\dfrac{L}{\Delta t}$	i_{n-1}
Capacitor:		
Trapezoidal	$\dfrac{\Delta t}{2C}$	$-\dfrac{2C}{\Delta t} v_{n-1} - i_{n-1}$
Backward Euler	$\dfrac{\Delta t}{C}$	$-\dfrac{C}{\Delta t} v_{n-1}$

The Trapezoidal Integration option

This integration method behaves correctly in most EMTP simulation cases. The trapezoidal integration technique can occasionally result in numerical oscillations at state variable current or voltage discontinuities. This can be disputed as being a modelling choice problem since there is normally stray capacitance to ground providing current continuity.

A test case is shown to highlight the difference between the three integration options. The switch in Figure 6 is initially closed and opens at 5ms. A time step of $\Delta t = 10 \mu s$ is used.
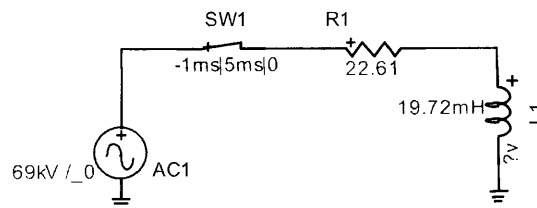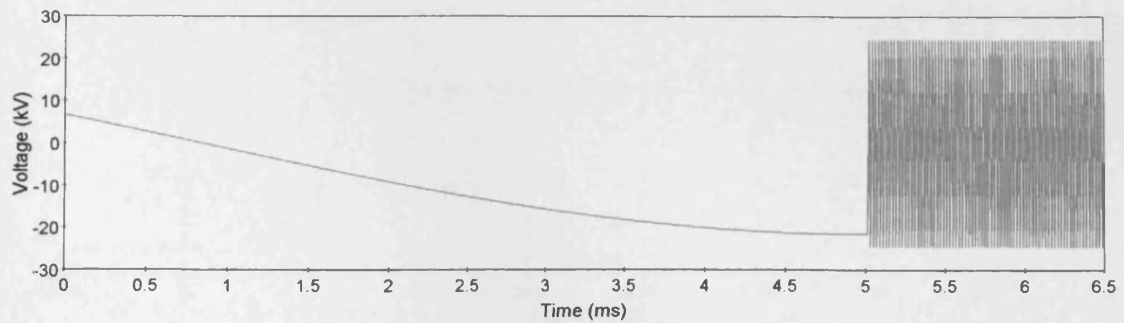

Figure 6. Test circuit.

Figure 7. Inductor voltage waveform starting from steady-state using the trapezoidal integration method.
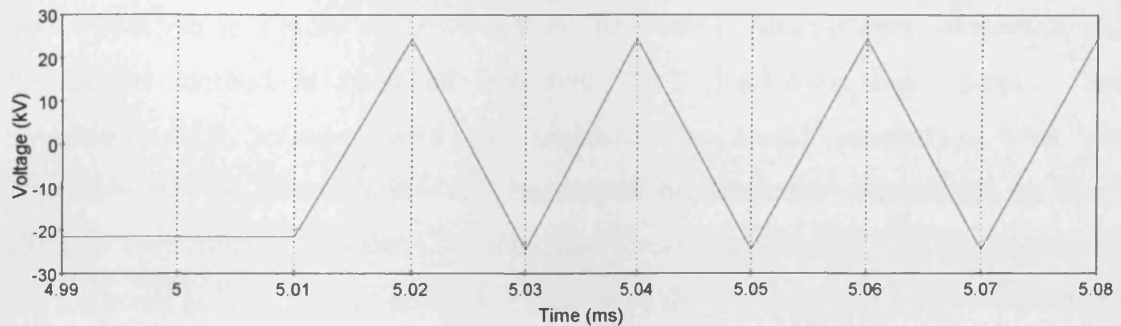

Figure 8. Numerical oscillations in the inductor voltage waveform due to the trapezoidal integration technique.

The configuration used in Figure 6 shows the numerical oscillation problem arising from using the trapezoidal integration technique. The oscillations can be seen in figures 7 and 8.

Trapezoidal and Backward Euler Integration option

The numerical oscillations occurring due to trapezoidal integration can be eliminated mathematically by reverting to the Backward Euler method once a discontinuity has been detected. The Backward Euler technique does not carry a non-state variable in its history, so the inductance has only current history and the capacitor only voltage history. This integration technique is the default option in EMTP-RV and is based on solving with the trapezoidal method and switching to Backward Euler only at discontinuities.
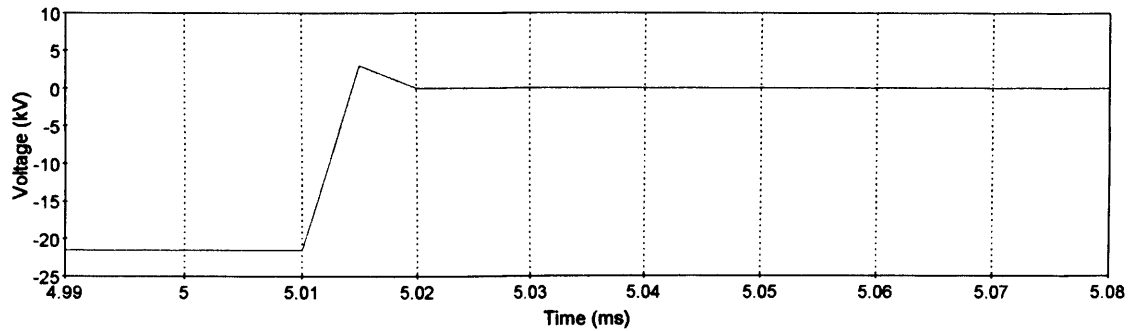
Figure 9. Elimination of numerical oscillations in the inductor voltage waveform using the Trapezoidal and Backward Euler Integration option.

The waveform in Figure 9 shows that at the point of discontinuity detection, the trapezoidal method is switched into two $\Delta t/2$ Backward Euler steps. The simulation then resumes with the standard trapezoidal integration after the discontinuity. A discontinuity can be caused by start-stop events and by slope changes in non-linear functions. In the current version of EMTP-RV, discontinuities are triggered only by power devices. If the same design has decoupled circuits, they are solved using the same matrix. Switching to Backward Euler in one circuit will force the other circuit to do the same even though only one circuit encounters the discontinuity.

Backward Euler integration option

The Backward Euler method does not have numerical oscillation problems, but is less precise than the trapezoidal method. This method is equivalent to the previous method except that the discontinuity method is carried out on a continuous basis and the apparent time-step is always $\Delta t/2$.

Reference:

[1]   Watson, N. and Arrillaga, J., *Power systems electromagnetic transients simulation*. 1st ed. IEE Power and Energy Series 39, ed. A.T. Johns and D.F. Warne. 2003: IEE.